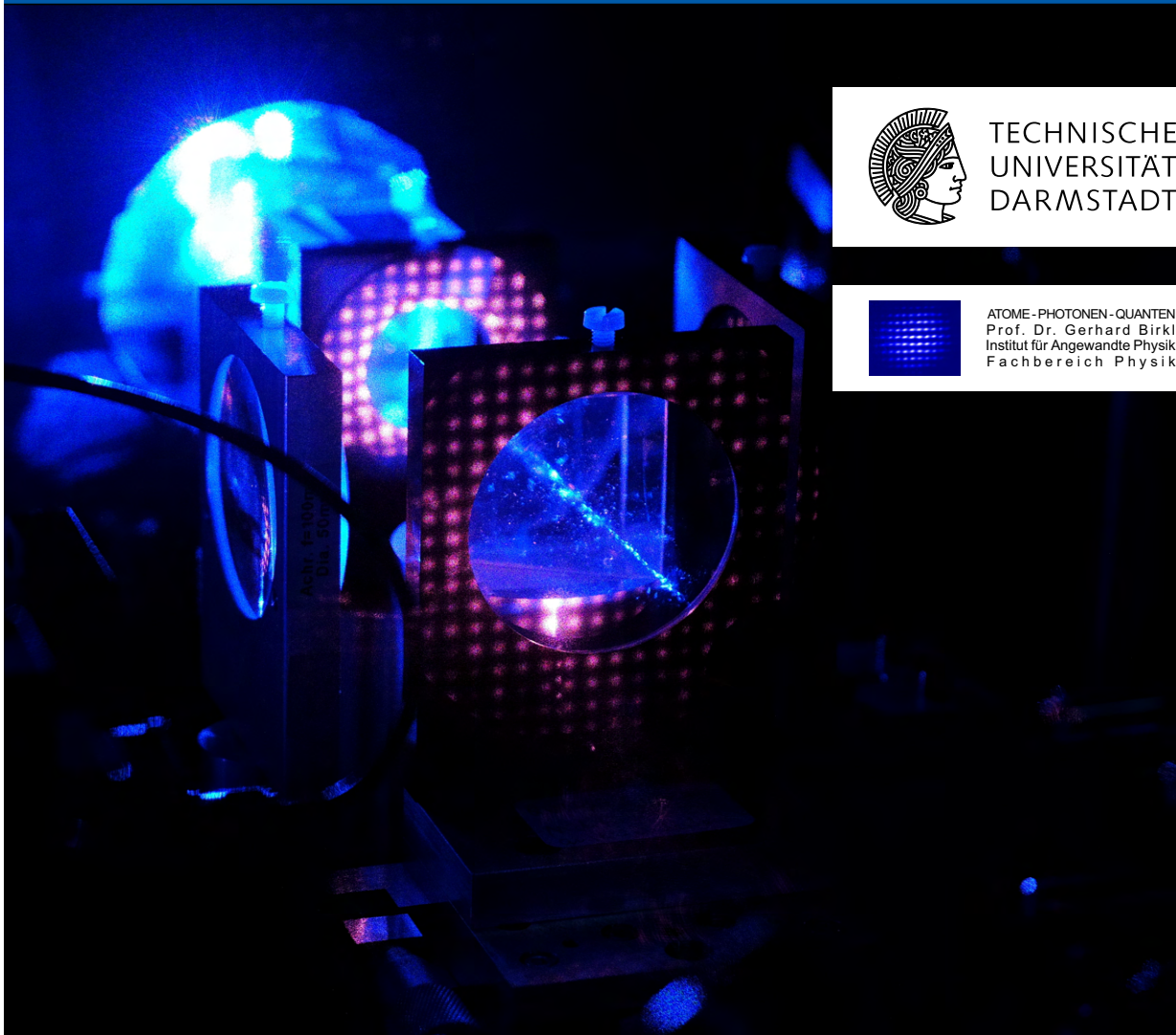


Rydberg interactions in a defect-free array of single-atom quantum systems

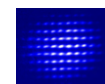
Rydberg-Wechselwirkungen in einem fehlstellenfreien Register aus Einzelatom-Quantensystemen

Zur Erlangung des Grades eines Doktors der Naturwissenschaften (Dr. rer. nat.)
genehmigte Dissertation von Daniel Ohl de Mello aus São Paulo, Brasilien
Tag der Einreichung: 28.01.2020, Tag der Prüfung: 17.02.2020
Darmstadt – D 17

1. Gutachten: Prof. Dr. Gerhard Birkel
2. Gutachten: Prof. Dr. Thomas Walther



TECHNISCHE
UNIVERSITÄT
DARMSTADT



ATOME - PHOTONEN - QUANTEN
Prof. Dr. Gerhard Birkel
Institut für Angewandte Physik
Fachbereich Physik

Rydberg interactions in a defect-free array of single-atom quantum systems
Rydberg-Wechselwirkungen in einem fehlerstellenfreien Register aus Einzelatom-
Quantensystemen

Genehmigte Dissertation von Daniel Ohl de Mello aus São Paulo, Brasilien

1. Gutachten: Prof. Dr. Gerhard Birkl
2. Gutachten: Prof. Dr. Thomas Walther

Tag der Einreichung: 28.01.2020

Tag der Prüfung: 17.02.2020

Darmstadt – D 17

Bitte zitieren Sie dieses Dokument als:

URN: [urn:nbn:de:tuda-tuprints-115040](https://nbn-resolving.org/urn:nbn:de:tuda-tuprints-115040)

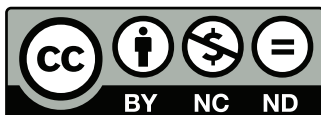
URL: <http://tuprints.ulb.tu-darmstadt.de/11504>

Dieses Dokument wird bereitgestellt von tuprints,

E-Publishing-Service der TU Darmstadt

<http://tuprints.ulb.tu-darmstadt.de>

tuprints@ulb.tu-darmstadt.de



Die Veröffentlichung steht unter folgender Creative Commons Lizenz:

Namensnennung – Keine kommerzielle Nutzung – Keine Bearbeitung 4.0 International

<https://creativecommons.org/licenses/by-nc-nd/4.0/legalcode>

Cover picture: Photograph of the experimental setup showing the beam paths of the dipole trap and blue Rydberg laser. Credit: J. F. Spindler.

Abstract

Neutral atoms trapped and manipulated by laser light provide experimentally well accessible quantum systems allowing for a high degree of control over external and internal degrees of freedom. Arrays of dipole traps in which the atoms are confined individually in a configurable geometry constitute a versatile platform for quantum simulation and information applications. By exciting these atoms into Rydberg states, interactions of variable strength and range can be introduced into the system, allowing for the implementation of entangling gate operations or spin Hamiltonians. A crucial requirement for these schemes to function in a reliable way is the ability to create defect-free arrays of single atoms. This is generally a challenge in these types of systems, as common atom loading schemes are limited to roughly 50% probability of filling each site.

In this work, a technique for the rearrangement of atoms within a scalable architecture based on micro-optical lens arrays was developed and implemented, resulting in the creation of uniformly filled regions containing more than 100 atoms, which represent the largest defect-free structures realized so far in systems of this kind. This was accomplished by filling the empty traps in a pre-defined pattern with an atom one by one using an optical tweezer. Thus, structures with up to 5×5 atoms could be rendered defect-free in more than 99% of attempts. Although the success rate drops below unity for larger clusters, a value of 3.1% for a 100-atom structure is still viable for experiments working with post-selection methods. The filling fraction of even the largest examined structures was observed to be higher than 88%, surpassing common loading schemes by a significant margin. The measurements presented in this thesis build on a region of the array containing 361 sites, being limited by available laser power. In contrast, the addressable range of the optical tweezer includes more than 1500 sites and microlens arrays with up to a million lenses are commercially available.

By implementing coherent Rydberg excitation of this assembled atom array, significant progress toward a universal quantum computer or flexible quantum simulator has been made. Using a two-photon excitation scheme, coherent dynamics between the ground and Rydberg state could be observed simultaneously in a 5×5 region of the array, with two-photon Rabi frequencies on the order of $\Omega = 2\pi \times 500$ kHz measured for a Rydberg laser beam waist of $\bar{w}_{0,B} = 18.7(10)$ μm . The choice of an appropriate Rydberg state and interatomic spacing led to the presence of strong nearest-neighbor interactions and allowed for the demonstration of the Rydberg blockade effect by observing a collective enhancement of the Rabi frequency consistent with the expected scaling $\propto \sqrt{N}$ as well as the suppression of multiple excitations. This mechanism represents the fundamental constituent of a two-qubit gate operation.

The architecture introduced in this work offers a scalability unique among quantum simulation platforms and the presented results underpin its potential to propel the atom-optical approach for quantum information processing beyond the threshold of quantum supremacy. Different approaches for scaling up the system have been explored, indicating that defect-free structures of more than 1000 atoms are within range with feasible experimental improvements. Through a detailed analysis of the factors limiting the coherence of the observed dynamics, strategies for future experimental improvements have been developed. Among these, increasing the coupling strength to the Rydberg state into the megahertz regime by increasing laser power and implementing single-site addressing represents the most straight-forward and promising approach.

Zusammenfassung

Neutrale Atome, die mithilfe von Laserlicht gefangen und manipuliert werden können, stellen experimentell gut zugängliche Quantensysteme dar, die ein hohes Maß an Kontrolle über externe und interne Freiheitsgrade erlauben. Optische Dipolfallenregister, in denen die Atome innerhalb einer konfigurierbaren Geometrie individuell gespeichert werden, bilden eine vielseitige Plattform für Quantensimulations- und -informationsanwendungen. Durch Anregung dieser Atome in Rydbergzustände können Wechselwirkungen variabler Stärke und Reichweite in das System eingebracht werden, was die Implementierung von Verschränkungsoperationen und Spin-Hamiltonians erlaubt. Eine wesentliche Voraussetzung für die zuverlässige Realisierung dieser Anwendungen ist die Möglichkeit, fehlerstellenfreie Register zu erzeugen. Dies stellt eine allgemeine Herausforderung für Systeme dieser Art dar, da übliche Atomladetechniken auf eine Besetzungswahrscheinlichkeit von etwa 50% pro Falle limitiert sind.

Innerhalb dieser Arbeit wurde ein Verfahren zur Umsortierung von Atomen innerhalb einer skalierbaren, auf mikrooptischen Linsenregistern basierenden Architektur entwickelt und umgesetzt. Dieses ermöglichte die Erzeugung von einheitlich gefüllten Regionen mit mehr als 100 Atomen, welche den größten bisher realisierten Strukturen in Systemen dieser Art entsprechen. Umgesetzt wurde dies durch das Auffüllen von Fehlstellen in einer vordefinierten Struktur mithilfe einer optischen Pinzette. So konnten Strukturen mit bis zu 5×5 Atomen in mehr als 99% der Versuche fehlerstellenfrei aufgebaut werden. Obwohl die Erfolgsrate für größere Strukturen abnimmt, erlaubt ein Wert von 3.1% für eine 100-Atom-Struktur die Durchführung von Experimenten, bei welchen die Auswertung auf Postselektionsmethoden zurückgreift. Die Füllfaktoren sogar der größten untersuchten Strukturen überschritten 88%, deutlich mehr als mit herkömmlichen Ladetechniken erreichbar ist. Die in dieser Thesis vorgestellten Messungen basieren auf einer Region aus 361 Registerstellen, welche nur durch vorhandene Laserleistung limitiert ist, während der adressierbare Bereich der optischen Pinzette mehr als 1500 Stellen beinhaltet und Mikrolinsenregister mit bis zu einer Million Einzellinsen kommerziell erhältlich sind.

Durch die Implementierung kohärenter Rydberganregungen der Atome in einem so zusammengesetzten Register konnte ein signifikanter Fortschritt in Richtung eines universellen Quantencomputers oder eines flexiblen Quantensimulators gemacht werden. Mit einem Zwei-Photonen-Anregungsschema konnte die kohärente Dynamik zwischen dem Grund- und Rydbergzustand von Atomen in einem 5×5 -Bereich des Registers simultan beobachtet werden, wobei Zwei-Photonen-Rabifrequenzen im Bereich von $\Omega = 2\pi \times 500$ kHz bei einer Strahltaile des Rydberglasers von $\bar{w}_{0,B} = 18.7(10)$ μm gemessen wurden. Die Wahl sowohl eines geeigneten Rydbergzustands als auch eine Anpassung des Atomabstands des Registers führte zum Auftreten von starken Nächste-Nachbarn-Wechselwirkungen und erlaubte den Nachweis des Rydberg-Blockade-Effekts durch Beobachtung einer kollektiv erhöhten Rabifrequenz im Einklang mit der erwarteten Skalierung $\propto \sqrt{N}$, sowie der Unterdrückung von Mehrfachanregungen.

Die in dieser Arbeit vorgestellte Architektur bietet eine für Quantensimulatoren einzigartige Skalierbarkeit und die hier dokumentierten Ergebnisse untermauern ihr Potential, den atomoptischen Ansatz für die Quanteninformationsverarbeitung über die Schwelle der Quantenüberlegenheit zu treiben. Die Untersuchung verschiedener Ansätze zur Skalierung der Sortiermethode ergab, dass fehlerstellenfreie Strukturen aus mehr als 1000 Atomen mit gangbaren experimentellen Verbesserungen möglich sind. Durch eine ausführliche Analyse der Faktoren, die die Kohärenz der beobachteten Rydberg-Dynamik limitieren, wurden Strategien für zukünftige experimentelle Verbesserungen entwickelt. Unter diesen ist die Erhöhung der Kopplungsstärke an den Rydbergzustand ins Megahertz-Regime durch Steigerung der Laserleistung und der Implementierung von Einzeladressierbarkeit der naheliegendste und vielversprechendste Ansatz.

Contents

1. Introduction	1
2. Enabling technologies for quantum simulation and computation in neutral-atom arrays	5
2.1. Optical traps for neutral atoms	6
2.1.1. Atom-light interaction	6
2.1.2. Creation of two-dimensional potential structures using microlens arrays . .	9
2.1.3. Preparation of single atoms	12
2.2. Rydberg atoms for quantum information and technology	19
2.2.1. Properties of Rydberg atoms	19
2.2.2. Lifetime of Rydberg states	21
2.2.3. Excitation schemes	22
2.2.4. Interactions between Rydberg atoms	23
2.3. Conclusion	27
3. Defect-free assembly of individual atoms in pre-defined structures	29
3.1. Introduction to atom assembly	29
3.1.1. State of the art in preparing defect-free single atom quantum systems . . .	29
3.1.2. Basic considerations regarding atom rearrangement	30
3.2. Deterministic assembly of defect-free structures	34
3.2.1. Experimental setup	34
3.2.2. Moving a single atom	36
3.2.3. Implementation of pattern assembly	38
3.2.4. Evaluation of performance	42
3.3. Future scalability	48
3.3.1. Scaling with improved experimental parameters	48
3.3.2. Interleaved reservoir grids	50
3.3.3. Parallelization of atom transport	51
3.3.4. 3D array via trapping in Talbot planes	52
3.4. Conclusion	53
4. Spatially resolved Rydberg excitations in assembled atom arrays	55
4.1. Theoretical background	55
4.1.1. Three-Level System	55
4.1.2. Transition strengths and Rabi frequencies in Rb atoms	58
4.2. The Rydberg laser system	59
4.2.1. High-finesse cavity for frequency stabilization	61
4.3. Coherent ground-to-Rydberg-state dynamics	63
4.3.1. Ground state preparation	63
4.3.2. Coherent two-photon excitation to Rydberg states	63
4.3.3. Parallel Rydberg excitation of an array of atoms	71
4.3.4. Site-selective control of coherent dynamics with an optical tweezer	73



4.3.5. Conclusion	74
5. Analysis of imperfections in the coherent Rydberg excitation	75
5.1. Static effects	75
5.1.1. Atom temperature and baseline loss	75
5.1.2. Efficiency of ground state preparation	77
5.1.3. Recapture of Rydberg atoms	80
5.2. Damping mechanisms	82
5.2.1. Spontaneous emission from the intermediate state	82
5.2.2. Dephasing effects	83
5.2.3. Other sources of noise	86
5.3. Combining the effects	87
5.4. Conclusion	90
6. Observation of Rydberg blockade and collective enhancement in the array	93
6.1. Rydberg interactions in the array	93
6.1.1. Angular dependence of the interaction	93
6.1.2. Collective enhancement through Rydberg blockade	94
6.1.3. Effect of imperfect blockade	96
6.2. Observation and analysis of partial and complete blockade	96
6.2.1. Analysis of blockade strengths	96
6.2.2. Experimental observation of Rydberg blockade	97
6.3. Analysis of imperfections	99
6.4. Conclusion	103
7. Discussion and Outlook	105
A. Properties of ^{85}Rb	111
B. Monte-Carlo simulation of atom-structure assembly	113
C. Simulation of Rydberg dynamics	119
D. List of publications	123
Bibliography	125

1 Introduction

At the time the founders of quantum mechanics formulated their revolutionary theory in the early 20th century, neither of them could envision that one day we would be able to directly observe these strange laws acting at the single particle level. Still in 1952 Erwin Schrödinger wrote [1]:

...we never experiment with just one electron or atom or (small) molecule. In thought experiments, we sometimes assume that we do; this invariably entails ridiculous consequences....

It seems likely that if he could visit a modern laboratory, E. Schrödinger would be more than a little surprised at the progress that has been made in the recent 70 years. The research on cold atoms and quantum optics, kickstarted by the invention of the laser, have long enabled scientists to study and manipulate single particle systems in myriad ways. The development of laser cooling and trapping techniques [2–4] allowed to advance into a regime where the laws of quantum mechanics cause transitions to previously unobserved phases of matter, such as Bose-Einstein condensates [5, 6], where a cloud of N atoms essentially behaves as a single quantum mechanical N -particle state. Enabled by tremendous progress in decoupling the studied systems from the environment, a regime could be reached where the entanglement between single particles, a uniquely quantum mechanical property, could be observed, while keeping the fragile quantum state intact. This was demonstrated in groundbreaking work both for single photons trapped in a cavity interacting with passing Rydberg atoms [7, 8] and for single trapped ions [9]. These advancements have since established atomic physics as a rich testbed for quantum mechanics and sprouted countless experiments that exploit the controlled entanglement of individual particles to explore exotic phases of matter, engineer radically new technologies and increase our understanding of the fundamental laws that govern nature.

The outstanding level of control over both external and internal degrees of freedom of these particles led to the emergence of a particularly exciting field of research: The simulation of quantum physical systems. This idea, first proposed by Richard Feynman almost 40 years ago [10], builds on the insight that the amount of information that needs to be stored and processed on a classical computer to solve a quantum mechanical problem scales exponentially with the number of particles. This makes the exact simulation of the behaviour of strongly interacting many-body systems, such as in condensed matter, unfeasible as soon as the system size exceeds a few tens of particles. At the same time, the small length scales present in these systems prevent the direct experimental observation of the behaviour at a microscopic level.

Quantum simulation offers an alternative approach for the study of these systems, namely their emulation on a well-controlled model system, designed to be governed by the same Hamiltonian as the simulated system. The quantum superposition of states in such a system results in its ability to contain an exponentially large amount of information without using an exponentially large amount of physical resources, thus outperforming classical simulations on a fundamental level [11]. Besides applications ranging from high-energy physics, nuclear physics and cosmology all the way to quantum chemistry and even biology, condensed matter problems such as quantum phase transitions, quantum magnetism and high- T_c superconductivity pose ideal candidates for this kind of simulation. Some of these systems can be efficiently modelled using spin Hamiltonians, which led to the first realizations of this approach being made using nuclear magnetic

resonance (NMR) techniques at the end of the previous century [12]. Since then, remarkable progress in quantum simulation has been made with ultracold atoms in optical lattices [13], among others.

Going one step further, it has been shown that the quantum properties of such systems can be exploited to build a generalized quantum simulator [14], on which an arbitrary quantum system can be emulated. By implementing a set of universal quantum gates, even abstract computational problems can be solved on such a machine [15]. Compared to a classical computer, where N classical bits can store N bits of information, N qubits on a quantum computer can store 2^N bits, illustrating the tremendous potential of these systems. Exploiting the fundamentally quantum properties of superposition, interference of quantum amplitudes and unitary quantum-state evolution, arithmetic operations then correspond to the coherent propagation of the initial input states. This quantum parallelism epitomizes the intrinsic supremacy of a quantum computer compared to a classical machine for a certain set of mathematical problems. Famous examples are Grover's algorithm for searching an unsorted database [16] and Shor's algorithm for prime factorization [17], which has the potential to void the security of the RSA cryptography method once universal quantum computers have grown to a sufficient size. This threshold, beyond which a quantum computer starts to outperform a classical one in these specific applications, is often termed as *quantum supremacy* and is estimated to lie around 50 qubits [18].

In the last two decades, the realization of a universal quantum computer has been progressed on numerous experimental platforms [19–22], while it is safe to say that systems using superconducting qubits [22], backed by the gigantic semiconductor industry, have demonstrated the most notable progress in recent years, including the first demonstration of quantum supremacy for a specifically tailored problem on a 53-qubit chip [23]. There is still a long way to go, however, before supremacy can be achieved on a truly universal quantum computer for a problem like prime factorization. This is mainly due to the fact that every quantum gate operation necessarily incorporates a finite amount of decoherence and thus introduces computation errors into the system. In order to perform complex algorithms, it is thus indispensable to implement a method to correct for these errors. This quantum error correction can be implemented by ancillary qubits protecting the state of the logical qubit through entanglement [24, 25]. The number of ancillary qubits needed to encode one logical qubit in a fault-tolerant quantum computer varies with different error correction codes, with the smallest possible code consisting of 5 physical qubits [26]. Factoring RSA-768, the largest number that has been factored on a classical computer so far [27], via Shor's algorithm on a quantum computer, requires 1154 logical qubits [28]. Empirically demonstrating capabilities beyond what is classically possible in this benchmark application will thus require thousands of physical qubits. Much advancement will be needed to scale existing platforms to this size.

This criterion of scalability presents a challenge for which cold atom system might prove to provide superior solutions. A quantum computer built of individual atoms trapped in potentials of light separated by only a few micrometers can host thousands of qubits within a cubic millimeter of space. The sophisticated atom-optical techniques developed in the past decades allow for the comprehensive fulfillment of the five criteria formulated by DiVincenzo [29], which have come to be generally recognized as the fundamental requirements for a quantum computer. They can be summarized as follows:

1. *A scalable physical system with well characterized qubits*
2. *The ability to initialize the state of the qubits to a simple fiducial state*
3. *Long relevant decoherence times, much longer than the gate operation time*

4. A "universal" set of quantum gates

5. A qubit-specific measurement capability

Neutral-atom arrays fulfil most of these criteria in a straightforward fashion [20, 30, 31]. Trapped in the well-separated potentials of an optical lattice or tweezer array, internal electronic states are typically used as a qubit basis. Optical methods allow for both the preparation and read-out of these states in an efficient manner and the ability for confinement in vacuum cells far away from any surface, enabled by optical traps, leads to long coherence times. The only thing that does not come naturally for neutral atoms is the entanglement of qubits that is entailed in the fourth criterion, as a universal set of quantum gates must necessarily contain at least one two-qubit operation, typically in the form of a controlled NOT (C_{NOT}) gate. Such a two-qubit gate was proposed in the form of a blockade interaction between atoms excited into high-lying Rydberg states [32, 33], whose large dipole moments introduce a significant interaction at the typical interatomic distance in these systems of otherwise non-interacting atoms. The first realizations of a two-qubit gate based on this method attested to the suitability of these systems for quantum computation and simulation [34, 35]. Apart from enabling universal quantum computers, harnessing the properties of Rydberg atoms also allows for the efficient simulation of the above-mentioned spin Hamiltonians in neutral atom quantum simulators [36, 37]. Both of these approaches have experienced rapid progress within the last years, such as a significant increase in scale and gate fidelities [38, 39] and the implementation of Ising and XY Hamiltonians in Rydberg atom simulators [13, 40, 41] up to the observation of quantum phase transitions [42] and topologically protected edge states [43].

Further progress is crucially dependent on the ability to scale up the system size even further, as well as on the reliable realization of defect-free structures in these systems. Since the initial loading of array sites always relies on more or less stochastic processes, assembly techniques have to be progressed in conjunction with growing system sizes.

The topic of this thesis is an inherently scalable architecture based on the massive parallelization of optical dipole traps enabled by micro-fabricated structures. Focusing a laser beam through an array of microlenses creates a homogeneous and stable potential surface containing thousands of sites ideally suited for the trapping of single atoms. The parallelized application of laser-based methods for qubit manipulation and detection makes this system an ideal platform for scaling quantum computation and simulation schemes to hundreds or thousands of atoms. Using the clock states of the ^{85}Rb ground state hyperfine splitting as qubit basis states $|0\rangle := |5S_{1/2}, F = 2, m_F = 0\rangle$ and $|1\rangle := |5S_{1/2}, F = 3, m_F = 0\rangle$, efficient single-qubit manipulation with coherence times on the order of 100 ms have been demonstrated [44–46], complemented by efficient state initialization and detection [45, 47]. This allows for thousands of operations before the system decoheres.

This thesis documents the advancement of the experimental setup in two areas: The creation of large defect-free structures of individual atoms is reported, as well as progress toward the realization of two-qubit gates or spin Hamiltonians through the first realization of Rydberg blockade in this setup. It is structured as follows:

Chapter 2 gives an overview of the atom-optical principles and techniques relevant for the work presented in this thesis. The first part reviews the fundamentals of optical trapping of neutral atoms and introduces the experimental setup, explaining the procedures necessary to provide an array of individually occupied sites. The second part gives an overview of the properties of Rydberg atoms, illustrating their appeal for quantum information applications and motivating the advancement of the experiment in this direction.

Chapter 3 describes the development of a technique for atom rearrangement, using an optical

tweezer to reorder initially half-filled atom arrays into pre-defined defect-free subarrays, demonstrates structures containing more than 100 atoms and analyzes the future scalability of this method.

Chapter 4 documents the implementation and detection of coherent Rydberg dynamics in the dipole trap array. The theoretical and experimental background of Rydberg excitation is discussed and the simultaneous excitation of an assembled array of atoms is demonstrated.

Chapter 5 is dedicated to the description and analysis of observed imperfections in the Rydberg excitation of atoms in the array. By assessing and characterizing the major sources of noise and errors individually, a deeper knowledge of the limiting factors present in the experiment is derived and strategies for improvement are developed, while the validity of the analysis is verified by Monte-Carlo simulations of the dynamics.

Chapter 6 presents an analysis of Rydberg interactions in the dipole trap array, demonstrating the presence of Rydberg blockade via the observation of collective enhancement of Rabi frequencies and the suppression of multiple excitations.

Chapter 7 then summarizes and discusses the obtained results and findings and gives an outlook on possible improvements and future developments of the experiment.

2 Enabling technologies for quantum simulation and computation in neutral-atom arrays

Experimental platforms for quantum simulation with individually trapped neutral atoms can be divided mainly into two categories: Ultracold atoms in optical lattices and arrays of individual dipole traps, often called tweezer arrays. While the physical effect confining the atoms in both of these geometries is the same, the interatomic spacing differs by roughly an order of magnitude, which has led to different experimental techniques and applications being developed in either of these approaches.

In both of these systems, sites can be made to be occupied by single atoms [13]. The challenge of providing a defect-free structure within these systems has been successfully tackled in optical lattices either by exploiting a superfluid-to-Mott insulator transition of a Bose Einstein condensate [48–50] or creating a strongly spin-imbalanced degenerate Fermi gas [51], and in tweezer arrays by reordering atoms one by one into the desired pattern [52–55].

The key features setting these two systems apart arise directly from their difference in geometric scale. Optical lattices, where the interatomic distance is typically in the sub-micrometer regime, allow trapping hundreds or thousands of atoms within a very small region, which, for example, allows the simultaneous coupling of a large number of atoms with excitation laser fields, as well as the study of many-body effects in large systems. Notable examples, among many others, are the observation of large Rydberg "superatoms" corresponding to a Rydberg excitation shared by more than 100 ground-state atoms [56] and the study of antiferromagnetic correlations by introducing short-range interactions via excitation into a low Rydberg state in a system of similar size [41]. Besides offering these obvious advantages, however, the close proximity of the atoms also has a drawback. For one thing, it makes single-site addressing extremely challenging, rendering the design unsuitable for universal gate operations. Secondly, restricting the interactions to short distances, as is necessary for studying most spin Hamiltonians, involves low-lying Rydberg states with short lifetimes. These short lifetimes can lead to strong dissipation and a quick relaxation of the system to the equilibrium [57, 58], preventing the observation of correlations on longer timescales.

Tweezer arrays offer an alternative approach that faces these limitations to a much lesser degree. Sacrificing to some extent the easily attainable system size and the homogeneous loading mechanism of optical lattices, they however allow for highly flexible geometries, where a model system can literally be assembled atom by atom and interatomic distances between a few and tens of micrometers can be easily accommodated [30, 37]. This allows for efficient single-site addressing of atoms, as well as the introduction of interactions between particles with exquisite control. The ability to use high-lying Rydberg states with long lifetimes for nearest-neighbor interactions, as well as technical improvements in reducing sources of noise [38, 59] have led to tremendous progress in the creation of entanglement between many qubits [39] and the study of topological phases [42, 43]. At the same time, these systems hold potential for the parallelization of universal gate operations en route to large-scale quantum computers [60].

This high degree of flexibility with regard to potential applications is what motivates the pursuit of the tweezer-array approach in the experiment on which this thesis was conducted. The

trapping geometry presented here, based on micro-fabricated arrays of refractive lenses, surrenders some of the complete flexibility present in similar setups [54, 61] by restricting itself to a periodic base pattern, for the benefit of a uniquely scalable and homogeneous architecture with the ability to provide hundreds and thousands of qubits, only being limited by available laser power. Through a choice of various available lens arrays and reimaging parameters, the range of available interatomic distances is equal to comparable setups.

This chapter will provide a discussion of the fundamental techniques common among atom-optical experiments, with an emphasis on the presented architecture. The first section contains a brief review of basic theoretical concepts relevant for the trapping of atoms with laser fields and introduces the experimental setup, discussing the preparation and detection of single atoms in a dipole trap array. The second section attempts to illustrate the appeal of highly-excited Rydberg states for quantum computation and simulation purposes.

2.1 Optical traps for neutral atoms

The trapping and storage of neutral atoms in one- or multidimensional arrays of optical potentials is an efficient and scalable way of providing a set of qubits for encoding, storing and retrieving quantum information in a single-site fashion. This section discusses the common way of creating such systems of individually stored atoms using common laser cooling and trapping techniques. As the experimental apparatus is already described in detail in [45], only a brief summary of the relevant experimental properties and procedures is given.

2.1.1 Atom-light interaction

The interaction between an atom and a light field is comprehensively discussed in various publications, such as [62–65]. This subsection will only give a brief summary of important relations and quantities relevant for this thesis. The following description is based on [64]. In a fully quantum-mechanical description, the Hamilton operator of the coupled system of atom and light field is given by

$$H_{\text{AL}} = H_A + H_L + H_{\text{Int}} \quad . \quad (2.1)$$

In a simplified description of the atom as a two-level system consisting of a ground state $|g\rangle$ and excited state $|e\rangle$ with an energy separation of $\hbar\omega_0$, the atomic term is given by $H_A = \hbar\omega_0\sigma^\dagger\sigma$ when neglecting the kinetic energy, with the two-level ladder operators $(\sigma^\dagger, \sigma) = (|e\rangle\langle g|, |g\rangle\langle e|)$. The light field is assumed single-mode and monochromatic with frequency ω_L and is similarly given by $H_L = \hbar\omega_L(a^\dagger a + \frac{1}{2})$. The energy scheme of this simple system is shown in Fig. 2.1 (a).

The most important term for the following considerations, however, is the atom-light interaction Hamiltonian H_{Int} . In the electric dipole approximation - which is valid as long as the wavelength of the light is much larger than the atomic charge distribution - it can be written as

$$H_{\text{Int}} = -\mathbf{d} \cdot \mathbf{E} \quad , \quad (2.2)$$

where \mathbf{E} denotes the electric field of the light and \mathbf{d} is the dipole operator. It is useful to decompose the field into positive- and negative-rotating components

$$\begin{aligned}\mathbf{E}(t) &= \epsilon \frac{E_0}{2} (e^{-i\omega_L t} + e^{i\omega_L t}) =: \mathbf{E}_0^{(+)} e^{-i\omega_L t} + \mathbf{E}_0^{(-)} e^{i\omega_L t} \\ &=: \mathbf{E}^{(+)}(t) + \mathbf{E}^{(-)}(t) ,\end{aligned}\quad (2.3)$$

where ϵ is the unit vector of the polarization. Similarly, the dipole operator can be written as

$$\begin{aligned}\mathbf{d} &= \langle g | \mathbf{d} | e \rangle (|g\rangle \langle e| + |e\rangle \langle g|) = \langle g | \mathbf{d} | e \rangle (\sigma + \sigma^\dagger) \\ &=: \mathbf{d}^{(+)} + \mathbf{d}^{(-)} ,\end{aligned}\quad (2.4)$$

where the first identity corresponds to the decomposition into the atomic basis and $\mathbf{d}^{(+)} \propto \sigma$, $\mathbf{d}^{(-)} \propto \sigma^\dagger$. Thus, the interaction Hamiltonian is given by

$$H_{\text{Int}} = -\mathbf{d}^{(+)} \cdot \mathbf{E}^{(+)} - \mathbf{d}^{(-)} \cdot \mathbf{E}^{(-)} - \mathbf{d}^{(+)} \cdot \mathbf{E}^{(-)} - \mathbf{d}^{(-)} \cdot \mathbf{E}^{(+)} . \quad (2.5)$$

Given the relations $\mathbf{E}^{(\pm)} \propto e^{\mp i\omega_L t}$ and $\mathbf{d}^{(\pm)} \propto e^{\mp i\omega_0 t}$ ¹, one can identify two terms oscillating rapidly as $e^{\pm i(\omega_L + \omega_0)t}$, while the last two terms oscillate slowly as $e^{\pm i\Delta t}$, with $\Delta = \omega_L - \omega_0$ being the detuning of the light field relative to the atomic resonance. For detunings $|\Delta| \ll \omega_L + \omega_0$, applying the *Rotating Wave Approximation* is valid, which corresponds to neglecting the fast oscillating terms, as they do not contribute significantly to the dynamics on the relevant timescale. Furthermore, transforming into the rotating frame of the light field, corresponding to changing into the interaction picture, allows to neglect H_L and eliminate an explicit time dependence in the problem. The resulting effective Hamiltonians can then be written as

$$\tilde{H}_A = -\hbar\Delta |e\rangle \langle e| \quad (2.6)$$

and

$$\tilde{H}_{\text{Int}} = \frac{1}{2} \hbar \Omega_0 (\sigma + \sigma^\dagger) , \quad (2.7)$$

introducing the Rabi frequency

$$\Omega_0 = -\frac{1}{\hbar} \langle g | \epsilon \cdot \mathbf{d} | e \rangle \cdot E_0 , \quad (2.8)$$

which is a measure of the coupling strength of the laser mode to the atomic transition and is proportional to the amplitude of the electric field E_0 .

¹ As σ corresponds to the time evolution of $|e\rangle$ under the free atomic Hamiltonian, it has the unperturbed time dependence $e^{-i\omega_0 t}$.

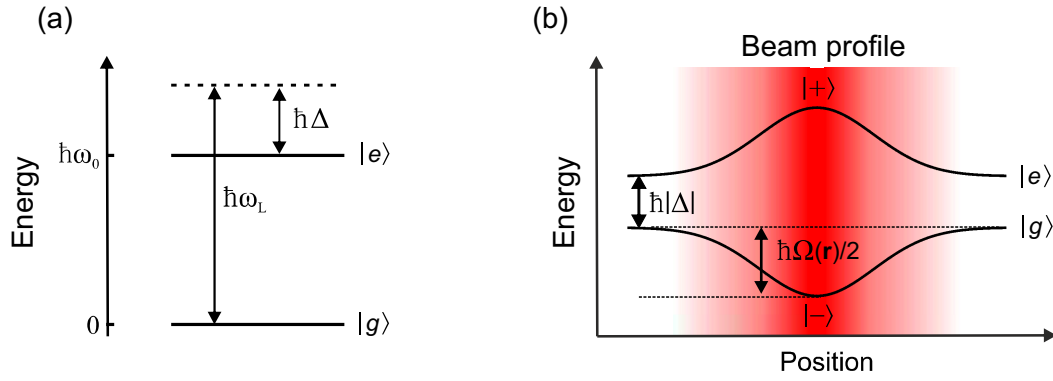


Figure 2.1.: Dipole force in the dressed atom picture. (a) Relevant properties in the uncoupled two-level system of the atom. The ground state $|g\rangle$ and excited state $|e\rangle$ are separated by an energy $\hbar\omega_0$ and the photons of the incident laser field have an energy $\hbar\omega_L$, corresponding to a detuning of $\hbar\Delta = \hbar(\omega_L - \omega_0)$. (b) Light shifting of the energy levels in the coupled basis. In the interaction picture, the atomic states $|g\rangle$ and $|e\rangle$ are merely separated by an energy $\hbar\Delta$ in the case of negligible coupling. In the presence of coupling by a position-dependent light field, the dressed eigenstates $|+\rangle$ and $|-\rangle$ experience an energy shift $\hbar\Omega(\mathbf{r})/2$. For the typical Gaussian profile of a focused laser beam, this corresponds to an approximately harmonic potential near the intensity maximum.

Dressed States

In this interaction picture, the eigenstates $|g\rangle$ and $|e\rangle$ of H_A are no longer eigenstates of the coupled system. Switching to the basis of the perturbed states corresponds to diagonalizing $\tilde{H} = \tilde{H}_A + \tilde{H}_{\text{Int}}$, represented by the matrix

$$\tilde{H} = \hbar \begin{pmatrix} -\Delta & \Omega_0/2 \\ \Omega_0/2 & 0 \end{pmatrix} \quad (2.9)$$

in the uncoupled energy basis. The new eigenvalues after diagonalization are

$$E_+ = -\frac{\hbar\Delta}{2} + \frac{\hbar\Omega}{2} \quad (2.10)$$

$$E_- = -\frac{\hbar\Delta}{2} - \frac{\hbar\Omega}{2} \quad (2.11)$$

where $\Omega := \sqrt{\Omega_0^2 + \Delta^2}$ is the generalized Rabi frequency.

The corresponding dressed eigenstates are given by an effective rotation of the original eigenstates

$$\begin{aligned} |+\rangle &= \cos \theta |e\rangle + \sin \theta |g\rangle \\ |-\rangle &= \cos \theta |g\rangle - \sin \theta |e\rangle \end{aligned} \quad (2.12)$$

by the mixing angle

$$\tan 2\theta = -\frac{\Omega}{\Delta} \quad (0 \leq \theta < \frac{\pi}{2}) \quad (2.13)$$

In order to use this effect to create an attractive potential for the atom, also known as a dipole potential, one typically uses a focused laser beam with detuning $\Delta < 0$. This introduces a spatial dependence of the electric field amplitude $E_0(\mathbf{r})$. Because of the proportionality of the Rabi frequency to the field amplitude mentioned above, the energy shift of the dressed states is maximized at the location of highest laser beam intensity. This is illustrated in Fig. 2.1 (b). For negative detuning $\Delta < 0$, the ground state evolves into the state $|-\rangle$ and is lowered in energy, which creates an attractive potential for the atom in the presence of the focused laser beam, which usually exhibits a Gaussian profile. This potential can be written as

$$U_{\text{dip}}(\mathbf{r}) = -\frac{\hbar\Delta}{2} - \frac{\hbar\Omega(\mathbf{r})}{2} \approx \frac{\hbar\Omega_0^2(\mathbf{r})}{4\Delta} = \frac{3\pi c^2\Gamma}{2\omega_0^3} \cdot \frac{I(\mathbf{r})}{\Delta}, \quad (2.14)$$

where Γ is the natural linewidth of the $|g\rangle \leftrightarrow |e\rangle$ transition and the approximation made holds for large detunings $|\Delta| \gg \Gamma, \Omega_0$. Taking into account the dissipative process of spontaneous emission, one arrives at a set of equations known as *Optical Bloch equations* (OBEs), the solutions of which yield an incoherent scattering rate. For large detunings and neglecting saturation effects, this can be written as

$$\Gamma_{\text{sc}} = \frac{3\pi c^2\Gamma^2}{\hbar\omega_0^3} \cdot \frac{I(\mathbf{r})}{\Delta^2}. \quad (2.15)$$

The dissipation associated with this scattering rate causes heating of the atom and should be aimed to be kept low. It is important to note the different scaling of U_{dip} and Γ_{sc} with the detuning Δ , meaning that a large detuning is preferable, as the scattering rate decreases quadratically with Δ , in contrast to the antiproportional scaling of the depth of the potential.

The relations and quantities introduced here provide a qualitative understanding of the interaction between the atomic system and a laser field. However, for a full quantitative description, the treatment of the atom as an idealized two-level system is not sufficient. Real alkali atoms, such as ^{85}Rb that is used in the presented experiment, exhibit a hydrogen-like level structure with fine structure and hyperfine structure, giving rise to a multitude of sublevels that can be populated by the valence electron. In order to perform accurate calculations of the potential depths, light shifts and scattering rates present in the experiment, one has to take into account all of the relevant states in H_A . For ^{85}Rb atoms, this has been done in [45] and will not be presented in detail here. One important result that should be noted here, however, is that in order to calculate the effective detuning of a far-off-resonance laser field trapping the ^{85}Rb ground state, one has to take into account contributions of both Rubidium D lines:

$$\frac{1}{\Delta_{\text{eff}}} = \frac{1}{3} \left(\frac{2}{\Delta_{\text{D2}}} + \frac{1}{\Delta_{\text{D1}}} \right). \quad (2.16)$$

2.1.2 Creation of two-dimensional potential structures using microlens arrays

Gaussian beam traps

As explained above, a focused laser beam with negative detuning constitutes a dipole trap for an atom, where the geometry of the trap is determined by the three-dimensional distribution of

light intensity around the focal point. The intensity distribution of a focused Gaussian laser beam of total power P is given by

$$I(r, z) = \frac{2P}{\pi w(z)^2} e^{-\frac{2r^2}{w(z)^2}}, \quad (2.17)$$

with the beam radius

$$w(z) = w_0 \sqrt{1 + \frac{z^2}{z_R^2}}, \quad w_0 = \frac{\sqrt{2}\lambda}{\pi \text{NA}}. \quad (2.18)$$

It is defined as the radial distance from the beam axis at which the intensity has dropped to $1/e^2$ times its central value. It reaches its minimal value, called *beam waist* w_0 , at the focal point. The *Rayleigh range* $z_R = \pi w_0^2/\lambda$ defines the axial distance after which the beam radius has increased by a factor of $\sqrt{2}$ and is a measure for the axial confinement of the dipole trap. The beam waist depends reciprocally on the numerical aperture of the focusing optics, given by $\text{NA} = a/f$, where a is the radius of the illuminated aperture and f the focal length. The relations introduced above are only strictly valid for a plane wave Gaussian beam of an incident size much smaller than a . In the case of micro-optical structures illuminated by a large beam, as is the case in the presented experiment, the second condition is not met, and the intensity distribution at the focus is modified by diffraction effects and exhibits a ring structure described with the use of Bessel functions (see [45, 66]). The central maximum, however, is well approximated by a Gaussian profile, with negligible deviations. In the scope of this thesis, it will thus be treated as being of Gaussian form (for a detailed discussion see [66]).

As can be seen from equation 2.14, the trap potential is proportional to $I(r, z)$. For cold atoms, whose wave function is significantly smaller than z_R and w_0 , it can be approximated as being harmonic. The corresponding axial and radial trap frequencies read

$$\omega_{\parallel} = \sqrt{\frac{2U_0}{mz_R^2}}, \quad \omega_{\perp} = \sqrt{\frac{4U_0}{mw_0^2}}. \quad (2.19)$$

Parallelization and scalability using micro-optics

In order to create potential geometries for the trapping of multiple individual atoms, different approaches can be pursued, with each having its own advantages and drawbacks. Using a microlens array allows the simultaneous creation of hundreds or thousands of spatially separated traps with the parameters introduced above. These micro-fabricated elements exist with varying geometries, numerical apertures and lens spacings. As the topology of the lens array is conserved by reimaging into the vacuum chamber, those parameters directly determine the waists and separation (pitch) of the dipole traps.

Table 2.1.2 lists parameters of the two microlens arrays and corresponding dipole trap arrays used within this thesis. The lens separation (pitch) d_0 is given by the manufacturer, as well as the lens diameter D_{ML} and radius of curvature, from which both f_{ML} and NA_{ML} are calculated. The other values denote parameters of the dipole trap array inside the vacuum chamber, created by a demagnifying reimaging ($M = 0.094(3)$) of the MLA's focal plane with a telescope consisting of a $f = 400$ mm achromatic lens and a $f = 37.5(10)$ mm lens system (see Fig. 2.4). This creates an array of diffraction limited spots of waist $w_{0,\text{exp}}$ with a pitch of d_{exp} , both measured experimentally by reimaging the trap array with known magnification onto a calibrated CCD camera.

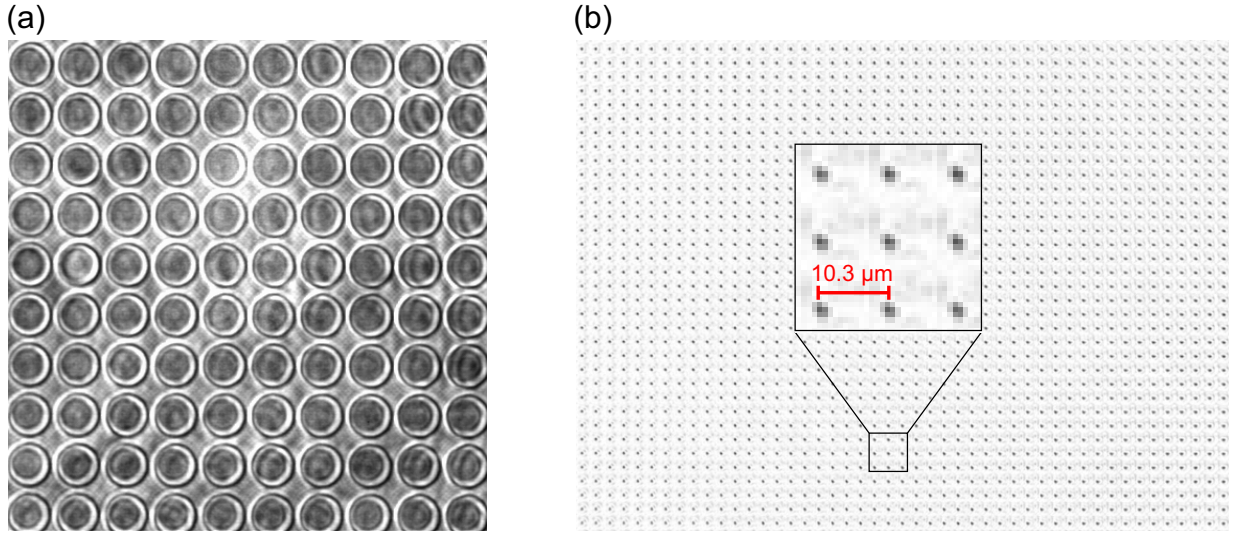


Figure 2.2.: Creating periodic potentials with a microlens array. (a) Microscopic image of a refractive MLA with a pitch of $30\ \mu\text{m}$. (b) Reimaged focal plane created with a $110\ \mu\text{m}$ -pitch array. Here, a 1500-site sub-region out of the total array containing more than 2500 focal spots is shown.

Talbot effect

When coherent laser light of wavelength λ is diffracted at a periodic object, self-images of the diffracting structure are created in the near field, called Talbot planes [67, 68]. These self-images are separated by the axial Talbot distance

$$z_T = \frac{2d^2}{\lambda}, \quad (2.20)$$

where d is the spatial period of the structure. In the case of a microlens array, this corresponds to the pitch of the array. In between these self-images, additional image planes (fractional Talbot planes) can be observed, exhibiting periodic structures with reduced spacing and varying intensity. For a more detailed analysis of this three-dimensional Talbot carpet, see [45, 69]. Most notably, this structure exhibits Talbot planes at half the Talbot distance which are self-images

Table 2.1.: Parameters of the microlens arrays (MLAs) used in this thesis (upper row). Both are manufactured by *SÜSS MicroOptics*. The bottom row lists the measured or calculated parameters of the dipole trap array (for details, see text). Calculated values assume a wavelength of $\lambda = 797\ \text{nm}$.

Name	Type	d_{ML}	D_{ML}	f_{ML}	NA_{ML}
ML1	11-1401-101-111	$110\ \mu\text{m}$	$106\ \mu\text{m}$	$1.894\ \text{mm}$	0.028
ML2	19-00021	$75\ \mu\text{m}$	$72\ \mu\text{m}$	$1.101\ \text{mm}$	0.033
Name	d_{exp}	$w_{0,\text{exp}}$	$z_{R,\text{exp}}$	z_T^*	
ML1	$10.3(3)\ \mu\text{m}$	$1.45(10)\ \mu\text{m}$	$8.3(12)\ \mu\text{m}$	$133(8)\ \mu\text{m}$	
ML2	$7.0(2)\ \mu\text{m}$	$1.45(10)\ \mu\text{m}$	$8.3(12)\ \mu\text{m}$	$61(4)\ \mu\text{m}$	

of the focal plane shifted by $d/2$ in each dimension. Integer as well as fractional Talbot planes can be harnessed for atom trapping, as will be shown in Section 3.3.4, yielding a sequence of experimentally relevant planes with a distance of

$$z_T^* = \frac{z_T}{2} = \frac{d^2}{\lambda} . \quad (2.21)$$

Unless otherwise indicated, however, all measurements presented in this thesis were made using only the original focal plane for atom trapping.

2.1.3 Preparation of single atoms

In order to prepare an atomic cloud cold enough to be trapped in the dipole trap array, a number of prior steps have to be made, as will be briefly discussed in the following.

Vacuum chamber

The central element and essential ingredient of the experimental setup is the vacuum apparatus. An ultra-high vacuum (UHV) is necessary to get the atoms sufficiently cold to be trapped in optical potentials, and provides a sufficient decoupling from the environment, which is crucial for quantum information processing. An insufficiently low pressure inside the chamber would lead to a significant amount of background collisions, causing a heating of the atoms and leading to their loss from the traps as well as causing decoherence on a timescale shorter than the time needed for the intended quantum operations. In the setup presented here, a pressure of around 2×10^{-9} mbar² is typically achieved, which is sufficiently low to not be the bottle-neck in terms of atom and coherence loss. A more detailed description of the chamber setup is given in [45, 47, 70]. Trapping and imaging single atoms requires tightly focussed traps and a high spatial resolution of the imaging system, which in turn requires an optical system with a high numerical aperture (NA). This has to be considered when designing the optical ports into the chamber. Figure 2.3 shows a computer-generated view depicting the vacuum apparatus and the coils used for magnetic field compensation (taken from [45]).

Magneto-optical trap and optical molasses

Since its first experimental demonstration [71, 72], the magneto-optical trap (MOT) has become a staple for the majority of cold atom experiments. It relies on the radiative force of three pairs of counter-propagating laser beams (nearly) orthogonal to each other, combined with a magnetic quadrupole field, in order to cool as well as spatially confine the atom cloud at the region of overlap of the beams. The typical minimum temperature which can be achieved in a MOT is given by the equilibrium between cooling and heating via spontaneous emission and is called Doppler limit:

$$T_D = \frac{\hbar\Gamma}{2k_B} \quad (2.22)$$

² This is assumed to be an upper bound given by the base level of the vacuum gauge being reached.

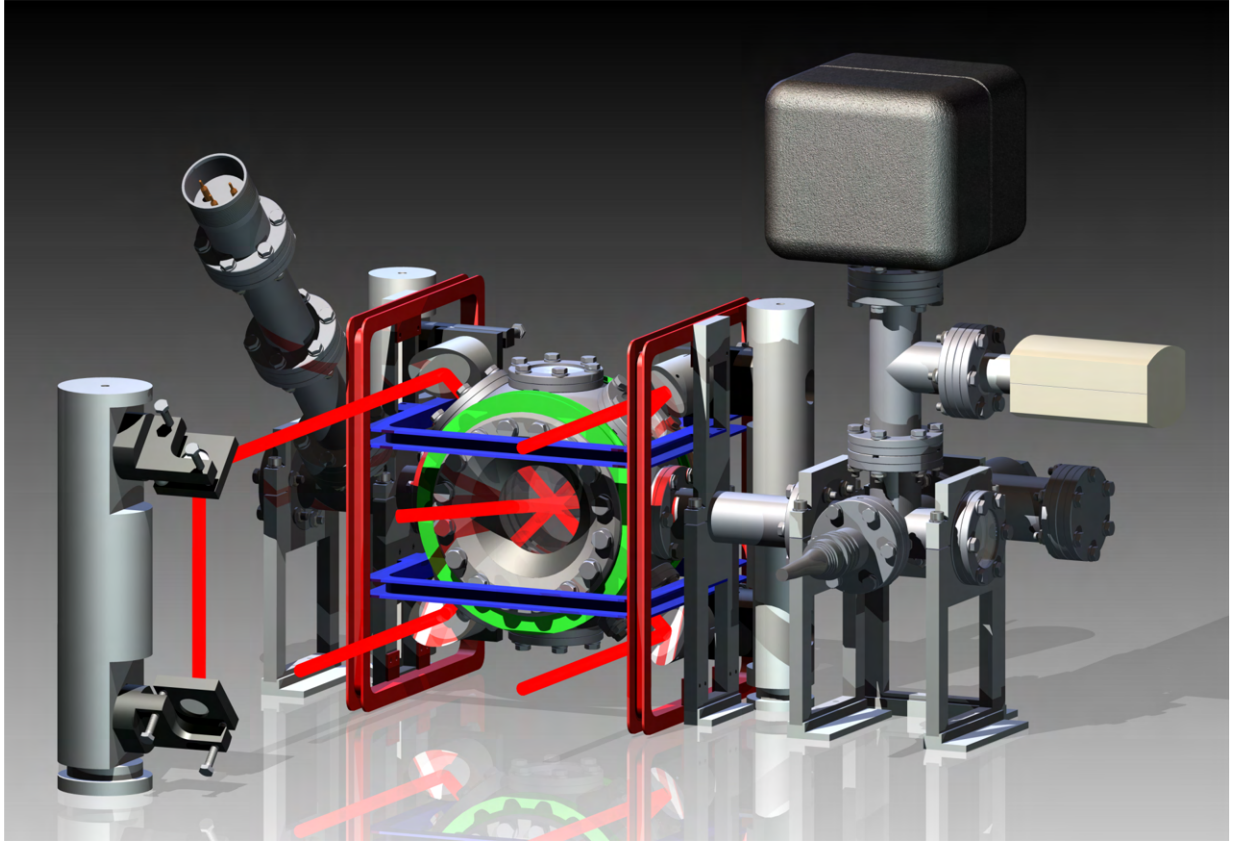


Figure 2.3.: Computer-generated image of the vacuum apparatus, magnetic field compensation coils and arrangement of the MOT beams through the chamber. Taken from [45]

Given the natural linewidth of $\Gamma = 2\pi \times 6.067\text{MHz}$ for the $5P_{3/2}$ level, the Doppler limit for cooling via the ^{85}Rb D2 line calculates to $T_D = 146\ \mu\text{K}$. This signifies the usual temperature that can be reached in a MOT. However, in the absence of the quadrupole MOT magnetic field, and taking into account the polarization of the laser beams as well as the magnetically sensitive Zeeman sublevels of the hyperfine splitting, it is possible to cool the atomic cloud below this temperature. This technique is called polarization gradient (or Sisyphus) cooling [73] and allows to reach the temperature corresponding to the momentum gained by the emission of a single photon, also called recoil temperature:

$$T_R = \frac{(\hbar k)^2}{mk_B} \quad (2.23)$$

With $k = 2\pi/\lambda$ and the atomic mass m , this yields a theoretical limit of $T_R = 370\ \text{nK}$ for the ^{85}Rb D2 line. An overview over the atomic properties of Rubidium relevant in this thesis, as well as a detailed level scheme, are given in Appendix A.

Figure 2.4 depicts a schematic image of the vacuum apparatus where the six MOT beams are shown. Each of the beams consists of cooling light red-detuned to the $|5S_{1/2}, F = 3\rangle \leftrightarrow |5P_{3/2}, F' = 4\rangle$ transition and repumping light slightly red-detuned to the $|5S_{1/2}, F = 2\rangle \leftrightarrow |5P_{3/2}, F' = 3\rangle$ transition, with the exception of the two diagonal beams, which consist only of cooling light. Also shown is the dipole trap beam, which propagates through the MLA coming

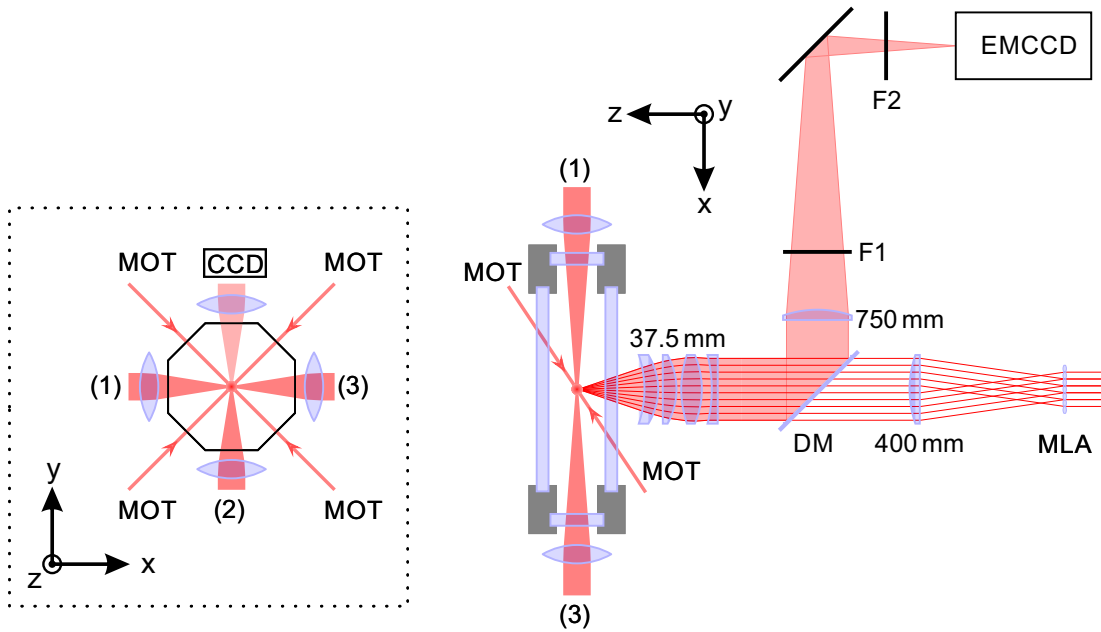


Figure 2.4.: Top view schematic (simplified and not to scale) of the vacuum chamber and relevant beam paths. The collimated dipole trap beam passes through the microlens array (MLA) from the right side, creating a focal pattern that is reimaged into the chamber by a demagnifying telescope consisting of a $f = 400$ mm achromatic lens as well as a $f = 37.5(10)$ mm objective. This same objective is used in conjunction with a dichroic mirror (DM) to image the fluorescence light onto the EMCCD camera, where filters F1 and F2 are used to suppress stray light from other sources. Inset: Front view of the chamber against the propagation of the dipole trap beam. The four MOT beams (as well as the two diagonal beams shown in the top view) are used for atom cooling and fluorescence imaging and are aligned to intersect at the position of the dipole trap array. Numbers (1) to (3) denote the available beam paths into the chamber for subsequent manipulation of the atoms, where (1) is used for the blow-away beam (see text). The CCD camera on top is used for additional monitoring of the MOT alignment.

from the right side and is aligned so that the reimaged focal plane coincides with the center of the MOT. The laser providing this light is a titanium-sapphire (Ti:Sa) ring laser (*Coherent 899-01*) optically pumped by a frequency-doubled Nd:YAG laser (*Coherent Verdi V18*) at 532 nm. The wavelength of the Ti:Sa can be tuned between 760 nm and 850 nm, which allows for a wide range of detunings to choose from. Since the goal for most of the measurements in this thesis was to trap as many atoms as possible, the wavelength was mostly chosen to be close to the D1 transition, with a value typically around 797 nm (for more details see Section 3.2.1). All other lasers used for atom cooling and manipulation, unless otherwise indicated, are external-cavity diode lasers (ECDL) with an interference filter as the frequency selective element [74]. They can be tuned via a piezo-electric element in the Gigahertz regime, and a modulation of the diode current allows for fast feedback-loop control. Via offset locks, the lasers are stabilized with tunable frequency offsets onto a master laser locked on a rubidium transition via Modulation Transfer Spectroscopy (MTS) [75]. The stabilized lasers exhibit a long-term linewidth below 500 kHz and an output power of up to 100 mW. After a MOT stage of typically 1 to 3 seconds, the MOT magnetic field is switched off and the detuning of the cooling light is changed from -9.6 MHz

(-1Γ) to -52MHz (-4Γ), cooling the atoms below the Doppler limit and allowing the cloud to expand in an optical molasses [71]. While letting the cloud expand to a size slightly larger than the dipole trap array, the latter is switched on. At this point, the typical temperature of the molasses is $5\ \mu\text{K}$, which is cold enough for the atoms to be trapped by the potential wells of the array, which typically have a depth of $U_0/k_B = 0.2\text{mK}$ to 1.7mK .

Single-atom preparation via collisional blockade

The atom density in the molasses leads to a large number of atoms occupying the volume of a single dipole trap at any given time during this loading process. Thus, this process can ideally be considered as a statistical series of capturing and loss events with constant loading rate R and molasses loss rate γ . In equilibrium, the atom number follows a Poissonian distribution with an average of $\bar{N} = R/\gamma$, with R and γ in general being experimentally accessible parameters [76]. In this model, the maximum rate of one-atom trap occupation events occurs at $\bar{N} = 1$ and lies at 36.8%.

In the case of small volume dipole traps, however, the statistics can deviate significantly from a Poisson distribution. It is modified by loss processes corresponding to light-induced two-body collisions, after which one or both impact partners have enough kinetic energy to leave the trap [77]. The collisional interaction couples the states of the colliding atom pair, leading to a modification of the two-atom eigenenergy according to the short range Van-der-Waals potential $U_{\text{vdw}} \propto 1/r^6$. In the presence of the light field of the optical molasses, the two approaching ground state atoms can be excited into a molecular state with a long-range dipole-dipole potential $U_{\text{DD}} \propto \pm 1/r^3$. If the involved photon is red-detuned, the atom pair experiences an attractive potential and gains kinetic energy while approaching each other, until the short-lived molecular state decays and the atomic interaction is again governed by the Van-der-Waals potential. The resulting energy gain is usually higher than twice the trap depth and both atoms can leave the trap. The temporal development of the atom number, taking into account the light-assisted loss processes, is given by the differential equation [78]

$$\frac{dN}{dt} = R - \gamma N - \beta' N(N - 1). \quad (2.24)$$

The loss rate γ takes into account collisions with the background gas as well as heating loss due to photon scattering; β' denotes the loss rate caused by two-body collisions. Again, the loading process leads to an equilibrium between atom capture and loss events. For small loading rates, the two-body collisions play a minor role and the average atom number corresponds to $\bar{N} \sim R/\gamma$. In the regime of high loading rates, the lifetime losses are negligible and one obtains $\bar{N} \sim \sqrt{R/\beta'}$. The transition between those two regimes is characterized by a critical atom number $N_c = \gamma/\beta'$ and the corresponding critical loading rate $R_c = \gamma^2/\beta'$. For loading rates higher than R_c , the increase of the atom number gets damped by two-body losses. The ideal regime for the preparation of single atoms lies at $N_c \ll 1$, where two-body losses dominate even at low atom numbers $\bar{N} < 1$, causing a plateau with $\bar{N} = 0.5$, which covers multiple orders of magnitude of the loading rate. Because the light-induced collisions lead to an almost immediate loss of atom pairs for atom numbers greater than one, in this case the trap is always populated by either one or zero atoms. This process is called *collisional blockade* [78].

For blue-detuned light the collisional potential is repulsive and the maximum energy gain is determined by the effective detuning of the light, making it easily controllable. If the detuning is less than half the trap depth, only one atom can be lost in the process. Taking into account collisions resulting in one-atom loss, the differential equation is modified by an additional term

$$\frac{dN}{dt} = R - \gamma N - \beta'_1 N(N-1)/2 - \beta'_2 N(N-1)/2, \quad (2.25)$$

with the total loss rate $\beta' = \beta'_1 + \beta'_2$ now consisting of the one and two atom loss rates β'_1 and β'_2 [79, 80], respectively. By modifying the parameters of the light used to catalyze the collisions such that the single-atom loss rate β'_1 begins to dominate the total loss rate, the average atom number can be pushed towards $\bar{N} = 1$. Experiments have shown that the loading efficiency of an atom in a single microtrap can be increased to 91 % [81]. An approximation of the loss rates present in an experimental implementation can be made via the effective trap volume [45, 76]

$$V_{\text{eff}} = \frac{\pi^2}{\lambda} w_0^4 \cdot \ln\left(\frac{1}{1-\eta}\right) \sqrt{\frac{\eta}{1-\eta}}. \quad (2.26)$$

The factor $\eta = k_B T / |U_0|$ denotes the ratio between atom temperature and trap depth. For the typical parameters present in the experiment, it amounts to $\eta \approx 1/5$ [82, 83], after the loaded atom has thermalized. The collision-induced loss rates in Eq. (2.24) follow the relation $\beta' \propto 1/V_{\text{eff}} \propto 1/w_0^4$, causing a strong increase of loss rates when reducing the trap size. For the typical trap waists in this thesis of $w_0 = 1.45(10) \mu\text{m}$, the effective trap volume evaluates to $V_{\text{eff}} \approx 6.1 \mu\text{m}^3$ for a wavelength of 797 nm. Following the approximations made in [45, 76], the two-body loss rate evaluates to $\beta'_2 \simeq 610 \text{s}^{-1}$, leading to a fast attainment of the collisional blockade. A detailed analysis of the occurring one- and two-body loss rates and the arising occupation dynamics for different trap sizes has been made in [45]. For all dipole trap arrays used in this experiment, the loading process is dominated heavily by two-body collisions induced by red-detuned light, resulting in a typical single-atom occupation probability of only slightly above 50%. While it is possible to increase the occurrence of single-atom loss events even for tight microtraps with waists of $1 \mu\text{m}$ or below [84, 85], thus allowing for single-atom occupations of around 80%, these techniques are challenging to scale up to large arrays. Thus, in order to achieve deterministic filling in a pre-defined region of the array, a different approach was chosen, which will be the topic of Chapter 3. Please note, however, that the technique introduced in [85], which uses Λ -enhanced gray-molasses to increase the loading efficiency, has the potential to provide a significantly better starting point for atom assembly and may become essential at some point.

Selection of the Talbot plane

As already mentioned above, atoms can not only be trapped in the focal plane, but also in other planes within the potential landscape created by the Talbot effect. Generally, this effect is undesired, as the fluorescence light emanating from these atoms during detection can not be sharply imaged due to the finite depth of field of the imaging system and appears as blurry background light on the camera, reducing detection contrast. A simple solution employed in this

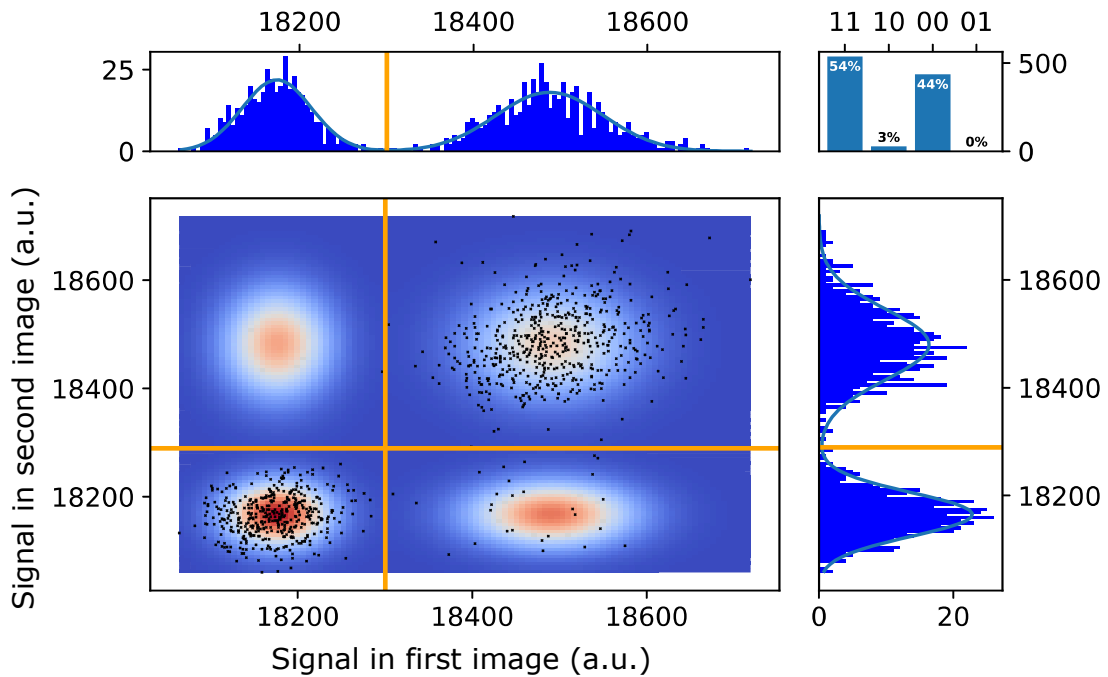


Figure 2.5.: Fluorescence signal from a single atom for two consecutive images. The histograms correspond to the sum signal in the trap region, for the first (top) and second (right) image. Well separated peaks ensure a near-unity detection fidelity. The scatter plot illustrates the correlation between an atom detection in the two images. The lower left and upper right quadrants correspond to zero or one atoms observed in both detections, respectively. Signal in the lower right quadrant corresponds to atom loss between the detections, while atom capture after the first image (upper left quadrant) is typically negligible. The probabilities of these respective events is given in the top right graph. By fitting a Gaussian to the signal distribution (blue curves or bright shaded regions), a threshold value for optimal detection fidelity can be obtained (for details, see [45, 86]).

experiment is to use a "blow-away" laser beam resonant to the cooling transition in combination with the shadow of a wire projected onto the focal plane, shielding only the atoms in this plane from the light. As the light only comes from one direction (beam path (1) in Fig. 2.4), the other atoms experience a strong directed force, ejecting them from the trap potentials and allowing for high-contrast imaging of the selected plane.

Site-resolved detection and loading statistics

As indicated in Fig. 2.4, the same objective used for reimaging the dipole trap array into the chamber is also used for fluorescence detection. For the excitation of the atoms, the cooling and repumping beams are used with similar power and detuning as in the molasses. Part of the scattered light thus emanating from the atoms is gathered by the $NA = 0.25(1)$ objective, corresponding to 2.2% of the isotropely emitted photons. A dichroic mirror (*Semrock FDi03-R785*) reflects the $\lambda = 780$ nm fluorescence light - while transmitting the trapping light from the opposite direction - after which a $f = 750$ mm lens focuses the light onto an EMCCD camera (*Andor iXon DV887DCS-BV*), creating an image of the atom plane magnified by a factor of 20. This allows for the clear spatial separation of the atoms and, due to the use of the dichroic mirror

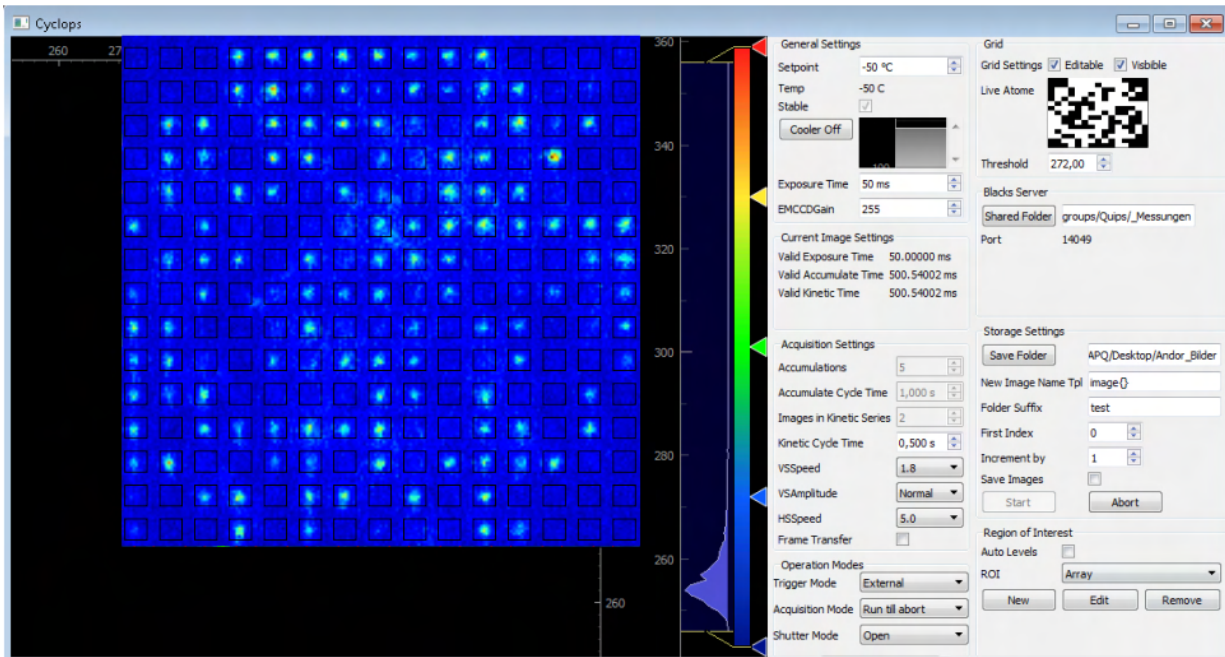


Figure 2.6.: Screenshot of the camera control software [86]. Having received the latest fluorescence image from the EMCCD, it is displayed with an overlay corresponding to the regions in which the signal pertaining to a particular trap is to be evaluated (black squares). Here, a 15×15 -site region of interest is used. At the same time, a boolean occupation array of the trap is generated (see text) based on an adjustable global threshold, displayed in the top right corner. As the software is implemented as a server, this array is then made available to other processes requiring the information.

reflecting more than 95% of the light instead of 50% using a polarizing beam splitter as in earlier work [45], an integration time of 50 to 75 ms is enough to ensure a detection fidelity well above 99%.

Figure 2.5 shows a histogram of the signal obtained from such an integration for a single trap after many repetitions of an experimental cycle, with the peaks corresponding to either no atom or one atom present in the trap, for two consecutive images. Figure 2.6 depicts a screenshot of the camera program developed in [86]. In any experimental repetition, the latest obtained fluorescence image is displayed in the left part of the window. This adjustable region, to which the analysis is restricted, is dubbed as "workspace" in the context of this thesis, as only atoms within this region are detected and manipulated in the scope of an experimental cycle. Here, the workspace contains 15×15 sites. The camera sensor's region of interest (ROI) is set so it only outputs the part of any image containing this workspace, speeding up image acquisition and further analysis.

An algorithm analyzes the histogram of the signal obtained from every trap in the ROI and determines a threshold which is then used to determine the atom occupation of the traps in each single image. This is illustrated in Fig. 2.5. For details on this procedure, see [45, 46, 86].

As there are experimental procedures requiring an in-shot analysis of the images (see Chapter 3), a simplified version of this algorithm calculates a boolean array containing the trap occupations as soon as the image is received from the camera and makes it available for other processes running on the computer. This is depicted in the top right corner of Fig. 2.6. Currently, it uses the same global threshold value for each trap, but more accurate methods can be implemented.

The stochastic loading discussed above leads to a random distribution of atoms in the array, which is an inadequate starting point for any quantum computation or simulation purpose, where the initial multi-particle state needs to be well-defined. Chapter 3 will tackle this problem and introduce a novel way of circumventing this limitation.

2.2 Rydberg atoms for quantum information and technology

Rydberg atoms have been the topic of extensive research throughout the twentieth century, due to their remarkable properties, which can be studied in vapor cell or atomic beam experiments and have been thoroughly mapped and charted over the course of several decades [87]. It is safe to say that the last 20 years have brought along a major resurgence of interest in these highly excited atomic states. The research areas that study and exploit Rydberg states now range from ultracold atoms in Bose-Einstein condensates [58, 88, 89], individually trapped Rydberg ions [90, 91] or exotic Rydberg excitons in cuprous oxide [92], through to experiments probing the interaction between a single photon and a Rydberg superatom [93] up to the observation of photonic bound states mediated by Rydberg blockade [94, 95]. A topical review of the potential of advancing quantum technologies enabled by the use of Rydberg atoms is given in [96].

A particular focus, motivating the research documented in this thesis as discussed in the introduction, is the utilization of Rydberg atoms to build a neutral-atom quantum computer [20, 30]. This section aims at providing an overview over the above-mentioned exceptional properties of Rydberg atoms and illustrating their enormous attractiveness for modern quantum-optical research.

2.2.1 Properties of Rydberg atoms

A comprehensive introduction to the topic of Rydberg atoms can be found in [87]. This section will provide a brief summary of important results obtained from the theoretical description of the Rydberg atom and important properties arising from it.

Alkali atoms are widely used in most cold atom experiments for their similarity to the hydrogen atom and the associated simplicity of the level scheme, with most relevant transition energies corresponding to convenient optical wavelengths. This is due to the fact that all electrons except the outermost one form closed shells effectively shielding that electron from all but a single nuclear charge. This similarity increases when the atom is excited into a Rydberg state, where the electron spends most of its time at a large distance from the core and the inner electrons, where it only experiences the net charge. For this reason, the formula for the binding energy

$$E_n = -\frac{Ry}{n^2} \quad , \quad (2.27)$$

found by J. R. Rydberg for the hydrogen atom in 1890 [97], is a fair approximation for an alkali Rydberg atom. In this equation, n is the principal quantum number and the Rydberg energy is given by

$$Ry = \frac{e^4 m_e}{32\pi^2 \epsilon_0^2 \hbar^2} \quad , \quad (2.28)$$

where m_e and e are the mass and charge of the electron, ϵ_0 the vacuum permittivity and \hbar the reduced Planck constant. In the semi-classical Bohr model, the radius of an electron orbit around the proton constituting a hydrogen core is given by

$$r = \frac{n^2 \hbar^2 \epsilon_0}{\pi \mu e^2} = n^2 \cdot a_0 \quad , \quad (2.29)$$

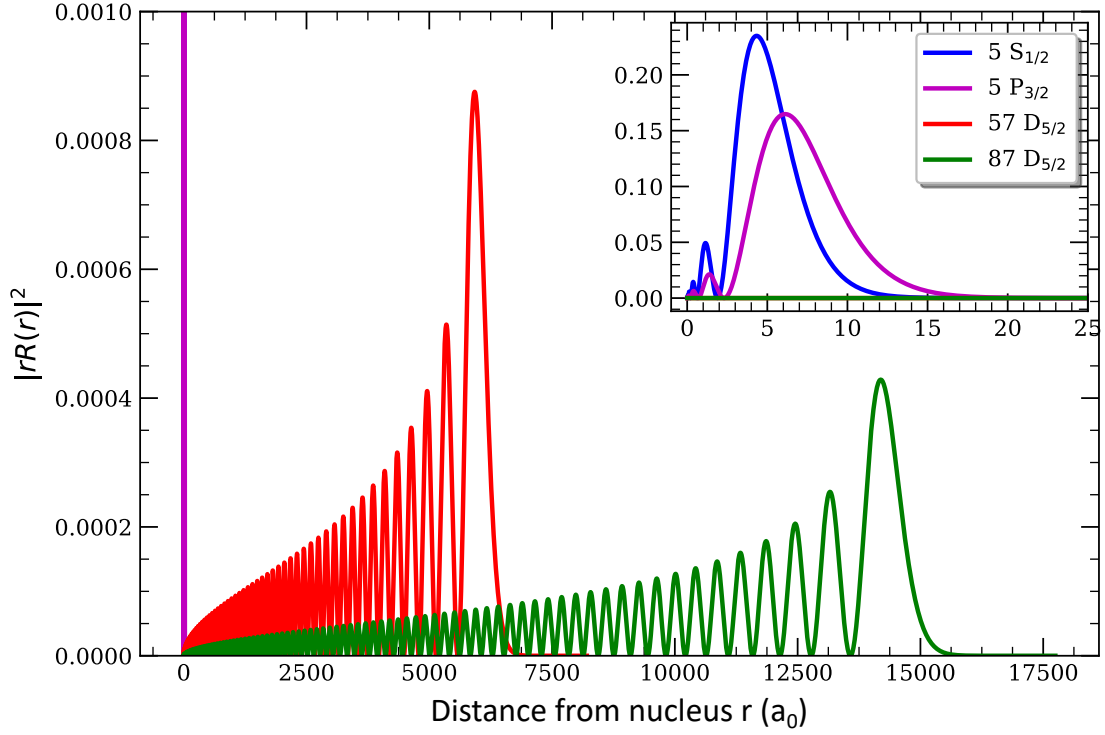


Figure 2.7.: Radial probability densities for the states relevant in this work. Values given in atomic units (a.u.)

with the reduced mass $\mu \approx m_e$ and the Bohr radius $a_0 = 4\pi\epsilon_0\hbar^2 m_e^{-1} e^{-2} = 52.9$ pm. This already illustrates the quadratic scaling of the atom size with the principal quantum number.

For Alkali atoms in Rydberg states of high orbital momentum, the differences to the corresponding hydrogen state are negligible. For low orbital angular momentum states ($l \leq 3$), however, the orbital of the Rydberg electron can penetrate the finite volume of the ionic core. This causes an exposure to the full nuclear charge and a polarization of the core, both increasing the binding energy of low- l Rydberg states, which is equivalent to a decrease in energy compared to the hydrogenic states. This difference can be modelled by introducing the quantum defects δ_{nlj} into the formula

$$E_{n^*} = -\frac{Ry}{(n - \delta_{nlj})^2} = -\frac{Ry}{(n^*)^2}, \quad (2.30)$$

which are given by the Rydberg-Ritz formula

$$\delta_{nlj} = \delta_0 + \frac{\delta_2}{(n - \delta_0)^2} + \frac{\delta_4}{(n - \delta_0)^4} + \frac{\delta_6}{(n - \delta_0)^6} + \dots \quad (2.31)$$

The coefficients δ_i depend on the element and can be determined from spectroscopic measurements. For Rubidium, they can be found in [98–100]. The properties of alkali Rydberg atoms are thus dependent on the effective principal quantum number $n^* = n - \delta_{nlj}$.

The scaling of many important properties with n^* is what makes Rydberg atoms such an interesting field of study and renders them ideal candidates for quantum information and simulation purposes. One example is the aforementioned scaling of the orbital radius $\langle r \rangle \propto (n^*)^2$, which is already evident from a semi-classical approach. Figure 2.7 illustrates this quadratic scaling. A Rubidium atom in the Rydberg state $57D_{5/2}$ already has an orbital radius of almost 5000 Bohr

Table 2.2.: Scaling laws $(n^*)^x$ of some important properties of Rydberg atoms adapted from [87]. The corresponding values for the $5P_{3/2}$, $57D_{5/2}$ and $87D_{5/2}$ states, which are relevant for the experiments presented in this work, can be found in [101] or calculated with formulas presented in this section.

Property	Expression	Scaling Law	Value for		
			$5P_{3/2}$	$57D_{5/2}$	$87D_{5/2}$
Binding energy	E_{n^*}	$(n^*)^{-2}$	2.59 eV	4.39 meV	1.85 meV
Level spacing ³	$E_{(n+1)^*} - E_{n^*}$	$(n^*)^{-3}$	32.9 THz	37.2 GHz	10.3 GHz
Orbit radius	$\langle r \rangle$	$(n^*)^2$	$7 a_0$	$4600 a_0$	$11000 a_0$
Eff. lifetime	τ_{eff}	$(n^*)^3$	26.4 ns	95.4 μs	267 μs
Trans. dip. moment ⁴	$\langle 5P \mathbf{d} nL \rangle$	$(n^*)^{-3/2}$	$4.227 ea_0$	$0.02 ea_0$	$0.01 ea_0$
vdW coefficient	C_6	$(n^*)^{11}$	—	$153 \text{ GHz} \cdot \mu\text{m}^3$	$14.1 \text{ THz} \cdot \mu\text{m}^3$

radii, which grows to 11000 Bohr radii for the $87D_{5/2}$ state, or $\approx 0.6 \mu\text{m}$. This huge orbital radius corresponds to a strong electric dipole moment, which can cause significant interaction between Rydberg atoms on a length scale of several micrometers, lying in the regime of interatomic distances that can be achieved in a microtrap array.

Table 2.2 gives an overview over some of the most relevant properties of Rydberg atoms and their scaling with effective principal quantum number, along with specific values for the excited states used throughout this thesis.

2.2.2 Lifetime of Rydberg states

The lifetime of Rydberg atoms is determined by radiative decay to lower-lying levels (Γ_0), as well as transitions to neighboring states (higher and lower in energy) induced by blackbody radiation (Γ_{BBR}). The effective lifetime of a Rydberg state is thus given by

$$\frac{1}{\tau_{\text{eff}}} = \Gamma_0 + \Gamma_{\text{BBR}} = \frac{1}{\tau_0} + \frac{1}{\tau_{\text{BBR}}} . \quad (2.32)$$

The spontaneous decay rate is determined by summing over the spontaneous transition rates from the Rydberg state nL ($L \in \{S, P, D, \dots\}$) with energy E_{nL} to all lower-lying states $n'L'$ [102]:

$$\Gamma_0 = \sum_{(n'L'): E_{nL} > E_{n'L'}} A(nL \rightarrow n'L') \quad (2.33)$$

The rate of BBR-induced depopulation is calculated by summing over all $nL \rightarrow n'L'$ transitions, where the transition rates are given by the Einstein coefficients multiplied by the number of BBR photons in the corresponding mode, given by the Planck distribution at temperature T ,

$$\Gamma_{\text{BBR}} = \sum_{n'} A(nL \rightarrow n'L') \cdot \frac{1}{e^{(\hbar\omega_{nn'}/k_B T)} - 1} , \quad (2.34)$$

³ Calculated for $nL_J \leftrightarrow (n+1)L_J$ transitions

⁴ For the $5P_{3/2}$ state, the $5S_{1/2} \leftrightarrow 5P_{3/2}$ transition is given. For all transitions, the beam polarization and sub-states with the maximum coupling strength are assumed.

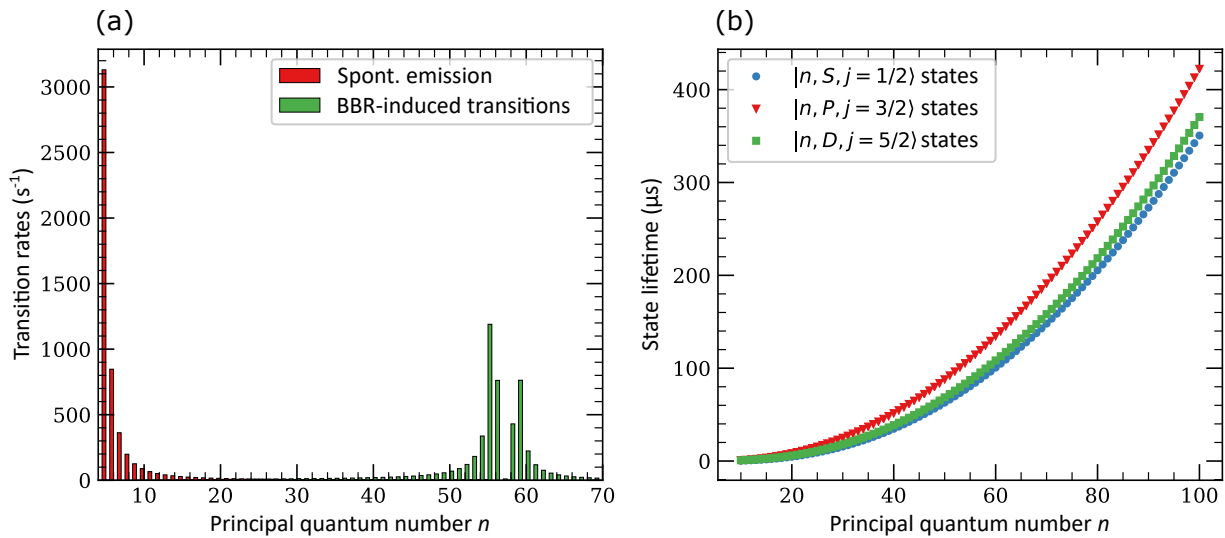


Figure 2.8.: (a) Transition rates from $57 D_{5/2}$ to $n P_{3/2}$, $D_{5/2,3/2}$, $F_{7/2,5/2}$ states, divided into spontaneous emission (red) and BBR-induced decay (green) at 300 K. The lifetime of the $57D_{5/2}$ state is reduced from $\tau_0 = 187.7 \mu\text{s}$ to $\tau_{\text{eff}} = 93.9 \mu\text{s}$ due to BBR. (b) Scaling of Rydberg state lifetimes with principal quantum number n (including BBR).

where k_B is the Boltzmann constant and $\omega_{nn'}$ the transition frequency between the states n and n' . Figure 2.8 (a) shows the transition rates caused by these two effects into all possible channels for the $57D_{5/2}$ Rydberg state⁵. Spontaneous decay is dominated by transitions with large $\omega_{nn'}$, whereas BBR-induced transitions mainly occur between neighboring Rydberg states. Figure 2.8 (b) illustrates the scaling of Rydberg state lifetimes with n for different orbital quantum numbers. As coherent dynamics and the study of interactions between Rydberg atoms typically takes place on a timescale of a few microseconds with Rabi frequencies in the MHz regime, lifetimes of tens of microseconds or longer provide enough time for several of these operations. Significantly higher lifetimes without changing the principal quantum number can be achieved by preparing the atom in a circular Rydberg state ($l = n - 1$). The lifetime of atoms in these states scales with $(n^*)^5$ and due to their large magnetic moments, they can be magnetically trapped, as has been demonstrated in [104], where a trapping time of several milliseconds for circular-state Rb atoms has been reported.

2.2.3 Excitation schemes

The Rydberg excitation of an atom initially in the ground state can be accomplished in different ways, each having distinct advantages and disadvantages. Figure 2.9 gives an overview over the possible excitation schemes for Rubidium atoms. While a direct single-photon excitation (Fig. 2.9 (a)) seems to be the straight-forward choice, the involved ultraviolet wavelength makes it challenging and resource-intensive to construct the required laser system. If implemented, however, it offers the advantage of eliminating an intermediate state, avoiding decoherence channels such as laser phase noise and photon scattering [105], making this scheme particularly relevant for systems using Rydberg-dressed atoms [57].

A coherent two-photon transition via an intermediate state offers the advantage of more convenient optical wavelengths that can be provided by commonly used EDCL systems. The schemes

⁵ Calculated using the ARC library [103].

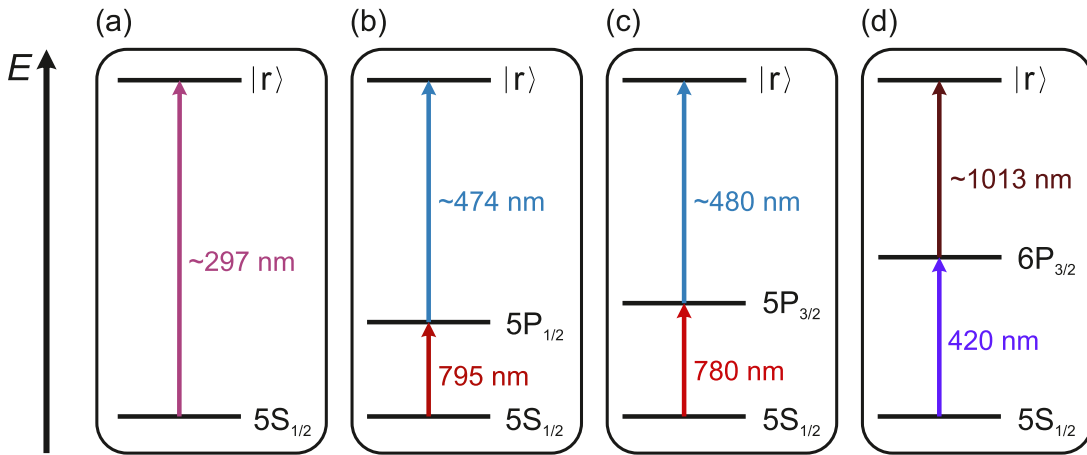


Figure 2.9.: Possible schemes for the Rydberg excitation of Rb atoms. While a direct single-photon excitation (a) avoids decoherence channels by eliminating the need for an intermediate state [41, 57, 105], the required ultraviolet wavelength makes it technically challenging to implement. Thus, most Rydberg experiments rely on a two-photon excitation scheme (b-d).

shown in Fig. 2.9 (b and c) are thus the ones most commonly applied in Rubidium Rydberg experiments. As the transition dipole matrix element decreases rapidly with increasing principal quantum number, the transition from the intermediate state to the Rydberg state couples much weaker than the lower transition, requiring a relatively large blue laser power to achieve similar Rabi frequencies for both transitions. As the blue light in this scheme is typically generated by a frequency-doubled ECDL system, this usually corresponds to a limitation of the maximally achievable Rabi frequency.

The scheme shown in Fig. 2.9 (d) mitigates this limitation to some extent by using the shorter wavelength for the strongly coupled transition and exciting to the Rydberg state with infrared light, where high laser powers are much easier to provide. Details on the excitation scheme chosen for the work presented in this thesis (Fig. 2.9 (c)) and the reasons for this choice are given in Chapter 4.

2.2.4 Interactions between Rydberg atoms

As already mentioned in the introduction, Rydberg atoms are prime candidates for studying quantum many body physics, as well as for the implementation of quantum information and computation schemes [20], due to their strong dipole-dipole interaction. As this interaction has an extremely strong dependence on principal quantum number and interatomic distance, varying these parameters enables the experimenter to tune its strength over several orders of magnitude. Together with a method for precisely exciting and de-exciting the atoms to and from Rydberg states, this allows for a comprehensive control of the dynamics of the quantum system, which is essential for applications such as two-qubit gates for quantum computation [20, 32, 34, 38, 106, 107] or the implementation of quantum Ising models [41, 108] and XY magnets [109, 110], to name just a few. In the following, a short qualitative introduction to the dipole-dipole interaction between Rydberg atoms is given, with a more detailed analysis performed in Chapter 6.

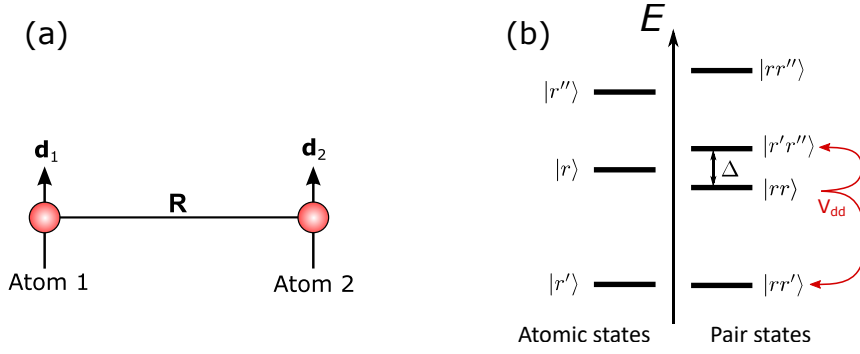


Figure 2.10.: Dipole-dipole interactions between two Rydberg atoms. (a) The dipole moments $\mathbf{d}_{1,2}$ of two atoms separated by a distance \mathbf{R} interact via V_{dd} . (b) Transformation from atomic to pair state basis reveals multiple pair states coupled by the interaction. In this case, the original pair state $|rr\rangle$ couples most strongly to the state $|r'r''\rangle$, with an energy defect of Δ .

Dipole-dipole interactions

Consider two atoms that are both prepared in a Rydberg state $|r\rangle$ initially, separated by a distance \mathbf{R} , as is illustrated in Fig. 2.10 (a). Due to the large dipole moment of a Rydberg atom, the dominant electrostatic interaction in this system for distances $|\mathbf{R}| \gg n^2 a_0$ is the dipole-dipole interaction. Its corresponding interaction operator can be written as

$$V_{\text{dd}}(\mathbf{R}) = \frac{1}{4\pi\epsilon_0} \left(\frac{\mathbf{d}_1 \cdot \mathbf{d}_2}{|\mathbf{R}|^3} - \frac{3(\mathbf{d}_1 \cdot \mathbf{R})(\mathbf{d}_2 \cdot \mathbf{R})}{|\mathbf{R}|^5} \right), \quad (2.35)$$

where $\mathbf{d}_{1,2}$ denote the electric dipole moment operators and the vector \mathbf{R} corresponds to the interatomic distance. As long as the Rydberg wavefunctions of the atoms do not overlap, which is always the case for the atom distances employed in this thesis, the Hamiltonian of this system can be written as

$$H = H_1 \otimes \mathbb{1} + \mathbb{1} \otimes H_2 + V_{\text{dd}}(\mathbf{R}), \quad (2.36)$$

with the free-atom Hamiltonians $H_{1,2}$. To calculate the energy shift caused by this interaction, a transformation from the atomic basis to a pair basis is necessary. The dipole-dipole interaction then couples the pair state $|rr\rangle$ to a state $|r'r''\rangle$, as is illustrated in Fig. 2.10 (b) ⁶. For simplicity, only the case where \mathbf{R} is parallel to the quantization axis shall be considered, making the problem one-dimensional. In the pair basis $\{|rr\rangle, |r'r''\rangle\}$, the system Hamiltonian can be written as

$$H = \begin{pmatrix} 0 & V(R) \\ V(R) & \Delta \end{pmatrix}, \quad (2.37)$$

with $\Delta = E_{r'} + E_{r''} - 2E_r$ being the energy difference and $V(R) = \langle rr | V_{\text{dd}}(\mathbf{R}) | r'r'' \rangle =: V_0/R^3$ the coupling strength between the two states. The eigenvalues of this Hamiltonian are

$$\lambda_{\pm} = \frac{\Delta \pm \sqrt{\Delta^2 + 4V_0^2/R^6}}{2}, \quad (2.38)$$

⁶ For an accurate calculation, the coupling to all nearby pair states has to be taken into account. As only a qualitative understanding is sought here, however, this is omitted.

illustrating the strong dependence of the pair state energy on the separation of the atoms. This leads to the emergence of two distinct limits of the spatial dependence:

i) Long range ($V/R^3 \ll \Delta$):

In this limit, also known as van der Waals (vdW) regime, the pair-state energy is shifted by

$$\Delta E = -\frac{V(R)^2}{\Delta} =: -\frac{C_6}{R^6} . \quad (2.39)$$

The sign of the interaction is determined by Δ and the interaction strength scales as $C_6 = V_0/\Delta \propto (n^*)^{11}$ (see Table 2.2 for a comparison between Rydberg states used in this thesis). This regime gives rise to the so-called Rydberg blockade mechanism [32, 111], as for the right choice of parameters, the interaction strength can become far larger than the coupling Ω of the laser fields to the Rydberg states. For the set of parameters (atomic distance and principal quantum number) typically employed within this thesis, the strength of this interaction ranges within four orders of magnitude (a few kHz to more than 20 MHz), allowing the study of both blockaded and unblockaded Rydberg physics.

ii) Short range ($V/R^3 \gg \Delta$):

This regime is known as the resonant dipole-dipole regime, as Δ is negligible compared to the interaction strength. The corresponding energy shift is given by

$$\Delta E = \pm V(R) = \pm \frac{C_3}{R^3} , \quad (2.40)$$

with $C_3 := V_0 \propto (n^*)^4$, exhibiting the typical R^{-3} scaling associated with a pair of static dipoles. As getting into this regime typically requires interatomic distances smaller than what can feasibly be achieved in a tweezer array without cross-talk between traps, this prohibits its utilization for most Rydberg states, which is the reason why all experiments performed so far in this experiment work in the long-range van der Waals regime. For the sake of completeness, however, two ways of observing resonant dipole-dipole dynamics in a tweezer array shall be noted.

1. For some specific Rydberg states, the initial pair state $|rr\rangle$ is near-degenerate with another $|r'r''\rangle$ state, which is known as a Förster resonance. Applying an external electric field can tune the two pair states exactly into resonance, allowing the observation of resonant dipole-dipole type interactions even for large interatomic spacings [112, 113]. This has been experimentally demonstrated for two atoms in optical tweezers in [114, 115].
2. Even in the absence of a Förster resonance, for a pair of atoms prepared in different Rydberg states corresponding to the pair state $|rr'\rangle$, this state is coupled to the degenerate state $|r'r\rangle$, resulting in a coherent excitation transfer between the two pair states mediated via the resonant dipole-dipole interaction. This has been demonstrated in [109].

The transition between these two regimes is characterized by the van der Waals radius, where $V(R_{\text{vdW}}) = \Delta$, given by $R_{\text{vdW}} = \sqrt[6]{C_6/|\Delta|} \propto (n^*)^{7/3}$.

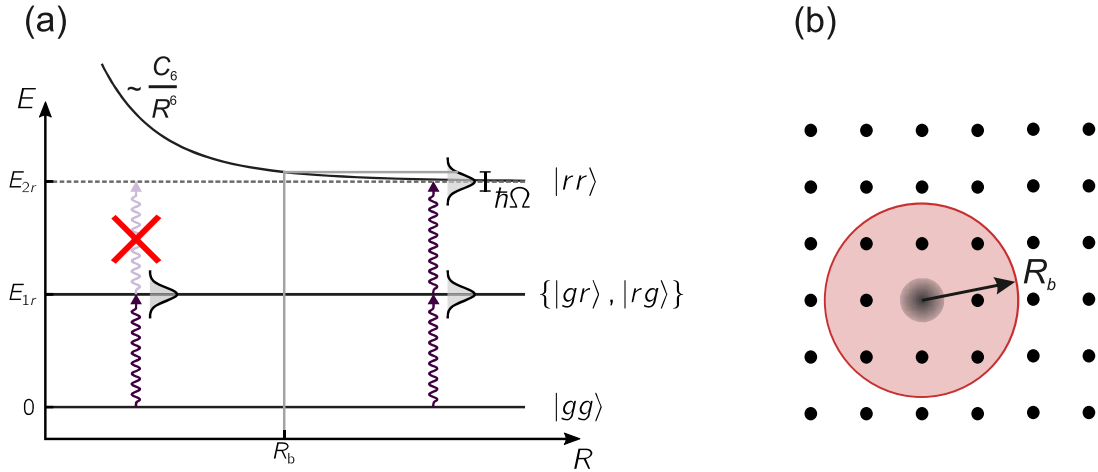


Figure 2.11.: Rydberg blockade in the van der Waals regime. **(a)** Blockade effect between two atoms. For small interatomic distances, the doubly excited state $|rr\rangle$ is shifted by $|\Delta E| = C_6/R^6$. When this shift becomes much larger than the Rabi frequency Ω driving the $|g\rangle \leftrightarrow |r\rangle$ transition, the simultaneous excitation of the two atoms gets suppressed. The critical distance for this effect is known as blockade radius R_b . **(b)** For isotropic interactions, the blockade can be visualized as a sphere of radius R_b around a Rydberg atom, within which no other atom can be excited into the same Rydberg state. Given the discrete distances in a periodic array, the radius can be tuned to affect only neighboring atoms, for example. Adapted from [116].

Rydberg blockade

As mentioned above, the van der Waals interaction can lead to a blockade of Rydberg excitations for distances on the order of typical trap spacings in a tweezer array. To picture this, one can consider the two-atom system introduced above, with each atom having a ground state $|g\rangle$ and a Rydberg state $|r\rangle$. Both are driven by a laser field Ω coupling to the $|g\rangle \leftrightarrow |r\rangle$ transition. Figure 2.11 (a) illustrates this system in the pair state basis. For large distances R , the two atoms can be considered as independent particles and they can both be simultaneously excited to the Rydberg state. For small distances, however, the interaction between the Rydberg states becomes noticeable and leads to an energy shift of the doubly excited state $|rr\rangle$. If this shift becomes much larger than the coupling strength Ω , the excitation of $|rr\rangle$ is suppressed, in other words, only one atom can be excited at the same time. This effect is known as Rydberg blockade. The characteristic blockade radius associated with the threshold $\Delta E = \hbar\Omega$ is given for the case of van der Waals interaction as

$$R_b = \sqrt[6]{\frac{C_6}{\hbar\Omega}}. \quad (2.41)$$

It scales proportional to $(n^*)^{11/6}$ and typically lies in the range of $5 \mu\text{m}$ to $20 \mu\text{m}$ for the experimental parameters in this thesis. For isotropic interactions⁷, the blockade can be visualized as a sphere with radius R_b . In the example of a tweezer array, choosing an appropriate combination of array spacing and Rydberg state allows the experimenter to control the number of atoms

⁷ Isotropy of the interaction is generally only a good approximation for $|nS\rangle$ states. For the $|nD\rangle$ states mostly considered in this thesis, C_6 has a significant angular dependence, which is discussed in Chapter 6.

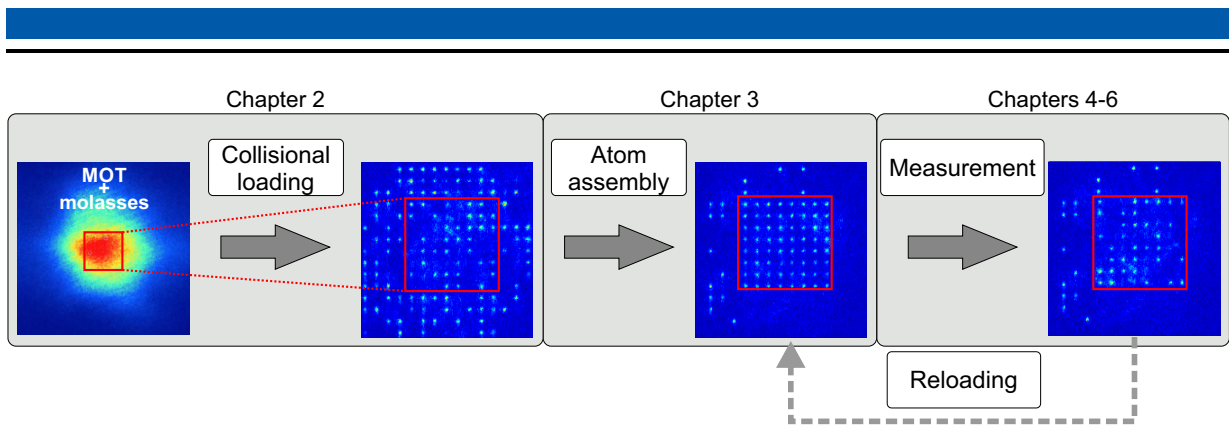


Figure 2.12.: Typical experimental cycle. A cloud of cold atoms created during a MOT and optical molasses phase is transferred into the dipole trap array, where the collisional blockade effect is exploited to ensure the presence of either zero or one atom in the traps. In the next step, the assembly technique developed during the course of this thesis is applied to rearrange the atoms into a predefined, defect-free structure within the array, documented in Chapter 3. This assembled array serves as a starting point for the measurements presented in the subsequent chapters, with the technique allowing for multiple measurement cycles within a single experiment enabled by a reloading of the initial array.

inside the blockade sphere, ranging from one (no blockade) up to tens or hundreds of atoms. Figure 2.11 (b) depicts a situation where only nearest neighbors of the Rydberg atom are blocked, corresponding to the regime typically considered within this thesis.

2.3 Conclusion

This chapter discussed two main technologies necessary for building a large-scale, neutral-atom quantum computer or simulator: A method for providing a large array of individually trapped atoms that can be individually addressed and detected, as well as the implementation of a controllable interaction mechanism between atoms in the array via Rydberg-state excitation. Reviewing the fundamental techniques for atom cooling and trapping, the application of these techniques to create a laser power efficient, inherently scalable architecture for individually trapped neutral atoms was presented. Rydberg-state mediated interactions will enable the implementation of quantum computation and simulation schemes in the presented architecture with unique prospects for qubit scaling. The following chapters document the progress towards this goal made on the experiment during the last years, namely the rearrangement of atoms into large defect-free structures, the implementation of coherent Rydberg excitation of the atomic array and the demonstration of Rydberg blockade. Figure 2.12 illustrates a typical experimental measurement cycle, illustrating the steps on which the individual chapters place their focus. While the experimental part of this chapter illustrated the steps leading to a stochastically occupied array of single atoms, the following chapter introduces a technique for creating fully-filled subarrays, which is then utilized for the measurements with Rydberg atoms documented in the subsequent chapters.



3 Defect-free assembly of individual atoms in pre-defined structures

When creating a large system of individual neutral atoms for quantum simulation or computation applications, most experiments aim at providing some form of periodic pattern in which the atoms are arranged. In the simulation of an interacting system of many particles, emulating for example the crystalline structure of a solid-state object, many emergent properties arise from the fundamental topology of the system [117], which makes it necessary to map this topology onto the experimental configuration. For quantum computation purposes, it is also convenient to rely on a periodic structure, be it a square lattice [118] or of other geometric shape [30]. In all of those cases, the initial configuration of the system for any set of operations one wishes to perform needs to be well-defined. In other words, each site of the initial structure needs to be deterministically filled with an atom, as defects can lead to the interacting system behaving in a fundamentally different way (in the case of a quantum simulator) or lead to quantum errors (in the case of a quantum computer). This chapter will give an overview of the techniques used for providing a system that meets these requirements, illustrating the state of the art for current experiments as well as fundamental considerations regarding atom rearrangement in Section 3.1. Subsequently, the method employed in the present experiment to achieve a defect-free array of more than 100 atoms will be presented, while analyzing its performance and discussing its scalability.

3.1 Introduction to atom assembly

3.1.1 State of the art in preparing defect-free single atom quantum systems

In recent years, many experimental efforts have been pursued to achieve defect-free filling in pre-defined target structures of neutral atoms. For the sub-micron spaced periodic potentials of optical lattices, the preparation of a central region with near-unity filling has been demonstrated in two-dimensional quantum gas microscopes [13, 41, 49, 50, 56, 119, 120]. Accurate repositioning of individual atoms has been implemented for four atoms in a one-dimensional polarization-synthesized optical lattice [121], but unrestricted individual atom transport remains a challenge in these lattices for higher atom numbers and dimensionality.

In focused beam micro-trap arrays with spacings in the micrometer regime, the preparation of individual atoms via collisional blockade, as described in the previous chapter, is the starting point for every experiment. Efficiencies can reach 90 %, as demonstrated for up to four traps [81, 122], but this enhanced blue-detuned loading requires trap depths roughly three times larger than standard red-detuned loading, making it more demanding to scale and typically imposing a limit to about 50 % filling on systems of larger size. Only recently, a novel loading scheme has been reported, using Λ -enhanced gray-molasses to cool the atoms into the traps and drive single-atom losses using the same blue-detuned light [85]. Thus, a 10×10 array with 80% loading efficiency could be demonstrated, requiring trap depths of not more than $U/k_B = 630 \mu\text{K}$.

While significantly enhancing the starting situation, this technique still fails to ensure defect-free filling in a large array. It is thus indispensable to implement some form of real-time atom

rearrangement procedure to eliminate defects. A 51-atom quantum simulator has been demonstrated based on a linear optical tweezer array generated by a multi-tone acousto-optic deflector (AOD) and atom-sorting through muting unoccupied sites and compressing the occupied ones [53, 123]. A similar technique has been used in [85] as a second stage after enhanced loading. A different approach is based on configuring a desired light field by the use of a 2D liquid-crystal spatial light modulator (SLM) [52, 54, 124]. This leads to holographically created trap arrays with adaptable geometries. Atom relocation has been demonstrated either by rearrangement of the traps themselves through the sequential altering of the pixel-based phase pattern [54] or by using a superposed moving optical tweezer [52]. The extension of this approach to pattern formation in three dimensions with up to 72 atoms [124] and the application of a large-spacing three-dimensional optical lattice for the creation of defect-free regions containing up to 50 atoms [55] have been reported recently.

All prospect applications of assembled-atom platforms in quantum science and technology will strongly benefit from scaling the system size to larger atom numbers. This section will introduce a method of atom sorting via an optical tweezer similar to [52]. Combined with the excellent scalability of the microlens approach, which is not limited by size restrictions due to the finite frequency spectrum of AODs and constraints in pixelation and laser power resistance of SLMs, this allowed for the creation of the largest defect-free structures demonstrated at the time of writing this thesis. The results presented in this chapter have been published in [125] and [69]. The following subsections will provide a thorough analysis of the challenges associated with atom sorting, the experimental implementation in the presented experiment and further scalability.

3.1.2 Basic considerations regarding atom rearrangement

As described in the previous chapter, the starting point in the present setup after loading the atoms from a molasses is a randomly occupied quadratic array of configurable size, depending on power and diameter of the dipole trap beam, with an average loading efficiency of about 50%. The latter also depends on available laser power and the size of the subarray one chooses to work with, as well as the alignment of the MOT and optical molasses. It is thus subject to fluctuations on a daily basis, which has to be taken into account when designing a sorting scheme.

Out of the techniques for atom rearrangement introduced in the previous subsection, using two perpendicularly oriented AODs, thereby implementing a movable optical tweezer able to address every point in the atom plane, is the obvious choice, as the rigidity of the microlens platform does not allow muting and compression of traps as applied in [53, 123].

Over the last years, there has been preliminary work done in this group exploring the possibility of using an optical tweezer for such a purpose [126, 127], as well as earlier measurements characterizing atom transport by shifting whole arrays of atoms using a galvo mirror [44, 128, 129] or an AOD [46, 130] to tune the angle of light incident on the MLA.

The first successful implementation of a two-dimensional atom-sorting scheme using an AOD [52] impressively demonstrated the viability of this approach, further motivating its implementation within the presented experiment.

Atom transport using an optical tweezer

In contrast to the above-mentioned preliminary work as well as the multi-tone tweezers approach, where the atoms stay in the same trap during the whole transport process, using a single optical tweezer for atom rearrangement within a static array requires the extraction of the atom

from a source trap, the transport in the movable tweezer and the subsequent deposition into a static target trap. For this method to work, that is, for the atom to smoothly transition from a shallow array trap into the tweezer and back, the tweezer trap depth needs to be ramped steadily from zero to a depth much larger than the array depth (a factor of 10 has been reported in [52]) and vice versa for the transition back into the target trap. This gives an estimate for the optical power requirement of the tweezer and induces the need for a synchronization of the tweezer's position and amplitude (see also [130]).

By using an AOD for the transfer of the atoms, timescales on the order of the inverse trap frequency can easily be reached. A lower limit for the transport speed is thus given by the requirement of adiabaticity. Non-adiabatic transport causes a non-negligible displacement of the atom wavefunction away from trap center at the end of the transport sequence, which induces an increase of the average vibrational quantum number $\langle \nu \rangle$ (i.e. heating), eventually leading to atom loss. In a harmonic approximation of the trap potential and assuming an optimal sine shaped transport function $x(t)$, the average number of added vibrational quanta for a transport time T and transport distance S is given by [131]

$$\langle \nu(T) \rangle_+ = \frac{m_{\text{Rb}} S^2 \pi^4 \omega_T \cos^2(\omega_T t/2)}{\hbar(\pi^2 - \omega_T^2 T^2)^2}, \quad (3.1)$$

with m_{Rb} being the mass of a ^{85}Rb atom. Given a transport in lateral direction, the trap frequency ω_T equals the radial trap frequency ω_{\perp} of the dipole potential.

Scalability of the approach

When estimating the temporal requirement for a series of atom rearrangements, Eq. 3.1 yields a lower bound for the time needed for a single atom move. Given the adiabaticity criterion $\langle \nu(T) \rangle_+ \leq 1$, it can be written as

$$T = \frac{\pi}{\omega_{\perp}} \sqrt{1 + S \sqrt{m \omega_{\perp} / \hbar}}. \quad (3.2)$$

With a typical radial trap frequency of $\omega_{\perp} \approx 2\pi \cdot 100 \text{ kHz}$ (which corresponds to a tweezer depth of $U_0/k_B \approx 2 \text{ mK}$ according to Eq. (2.19)), the minimum time needed for a displacement of one pitch ($\approx 10 \mu\text{m}$) is less than $50 \mu\text{s}$. As T only scales with \sqrt{S} , even for a transport over the whole array an allotted time of $T = 1 \text{ ms}$ is a conservative estimate. This means that even hundreds of moves can be performed in a time significantly smaller than the lifetime of an atom in the array (on the order of 10 s), which is sufficient for the current size of the array.

Please note that all considerations on atom transport in this section are concerned with single-atom moves, which means that a single optical tweezer is used to move one atom at a time. A parallelization of atom transport is much more challenging to implement in the given setup while its yield is limited for small to medium sized arrays. However, it may become crucial once the target array is scaled beyond a certain size, and will thus be discussed as a potential future improvement in Section 3.3.

Outlining the atom sorting scheme

Having asserted the basic feasibility of moving the atoms around within an acceptable timeframe, a scheme for the rearrangement of the atoms has to be defined. The basic principle of this scheme is quite simple. It generally involves three steps:

- (1) Choose a desired sub-grid within the array and define it as the target to be uniformly filled, as well as a second grid acting as a reservoir, from which atoms are to be taken.
- (2) Identify a set of trap pairs, each consisting of a filled reservoir trap and an empty target trap, so that a unique reservoir atom is mapped to each empty target site.
- (3) Perform a series of rearrangements so that each of the selected reservoir atoms is transported to its designated target site, thereby achieving a uniform filling of the target sub-grid.

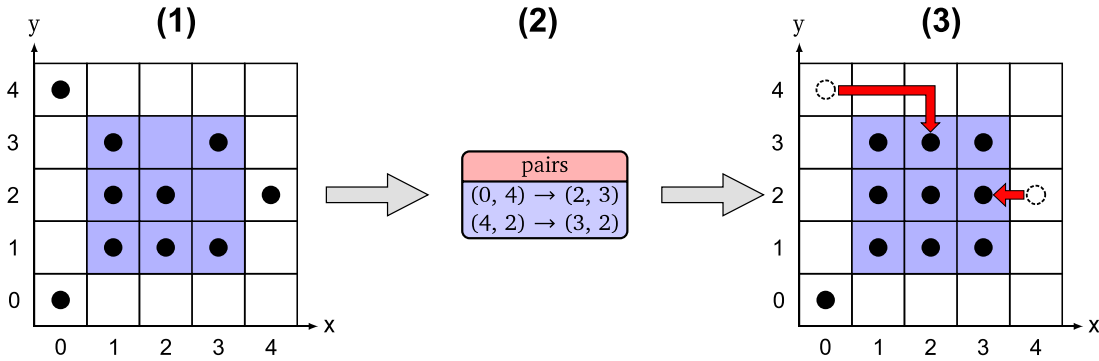


Figure 3.1.: Illustration of a generalized atom sorting scheme in a two-dimensional array. Adapted from [86].

An illustration of this scheme is given in Fig. 3.1. The blue area indicates the target sub-grid, while the white squares correspond to a reservoir grid. In the second step, two pairs of reservoir atoms and empty target sites are matched, before the rearrangement is performed in the third step.

Defining target and reservoir structures

The first step involves the decision whether a target structure should be pre-defined before the atoms are loaded, or whether it is to be chosen dynamically, favoring regions within the array exhibiting the highest occupation ratio, for any given experimental realization. The latter approach is more likely to find an optimal region in terms of the initial atom number contained within, but requires additional computational overhead. In [126, p. 35-40], different applicable algorithms for this purpose are explored. For the current experiment, the utilization of a static target grid was chosen, for two reasons: (1) For quantum computation and simulation purposes relying on single-site addressability, a pre-defined structure allows applying a hard-coded set of laser pulses without having to adjust the location of the beams in real-time for every experimental cycle, significantly reducing experimental complexity. (2) Because of the Gaussian distribution of trap depths within the array, the average atom loading efficiency also peaks in the center of the array, as atoms are more likely to be loaded and remain trapped in deeper potentials. Defining the target structure to be near the center thus is expected to provide a sufficiently good starting

situation, with the slight decrease in atom occupation rate being compensated by the increase in time efficiency gained by avoiding the additional algorithmic complexity.

Probability of success versus grid size

Given an initial array with each site randomly filled with a probability p , an estimate can be made regarding the ideal size and shape of the reservoir as well as the maximally feasible size of the target structure. For a first rough assessment, two simplifying assumptions are made:

- The loading probability p is the same for every trap in the array.
- Atom transport is performed with perfect efficiency and no atom is lost during the rearrangement (neither transported, nor static atoms).

Obviously these assumptions will not hold in a real experiment, but the simple estimate that can be made using them provides a good starting point for further considerations.

Given the first assumption, the number X of occupied traps in any experimental realization follows a binomial distribution. Under the second assumption, the probability of successfully filling a target structure of size M in a total array of size N is thus given by

$$\begin{aligned}
 P_{M,p}(X \geq N) &= \sum_{x=N}^M P_{M,p}(X = x) \\
 &= \sum_{x=N}^M \binom{M}{x} p^x (1-p)^{M-x} \\
 &= S_{M,p}(N-1) \quad , \tag{3.3}
 \end{aligned}$$

where $S_{M,p}$ is the survival function of a binomial distribution.

In this simplified model, the success probability for an idealized rearrangement is therefore equivalent to the probability of having loaded at least M atoms in any single experimental realization. Given a uniform loading rate of $p = 0.5$, the probability for successfully filling a target structure containing $N = 100$ atoms thus scales with M according to equation 3.3, as plotted in Fig. 3.2.

For the creation of defect-free structures of size N , the corresponding reservoir size M required for $> 99\%$ probability of success in this graph is to be seen as an absolute lower bound. For real experimental parameters, including various sources of atom loss, M will have to be significantly higher to achieve these results, as will be demonstrated in the following section. In the present experimental setup, there are in principle two approaches for providing a reservoir of atoms, given a finite amount of laser power to create traps. The first approach is to define any atoms in the array not included in the target structure as the reservoir and try to make the trap array as large as possible. The second approach is to use multiple interleaved reservoir arrays by illuminating the MLA with additional beams. This would significantly reduce the average transport distance of an atom and thus the average time needed for a move and might thus become essential at some point when scaling up the system. Given a fixed total beam power, this would, however, not appreciably increase the number of reservoir traps and thus the success probability, compared to the single grid approach (see [86, p. 42] for a comparison), while requiring a considerably more complex experimental setup. Therefore, the first approach was chosen for the work presented here, although the latter may significantly gain in appeal once different trap laser sources will be available for the respective sub-grids (see Section 3.3.2).

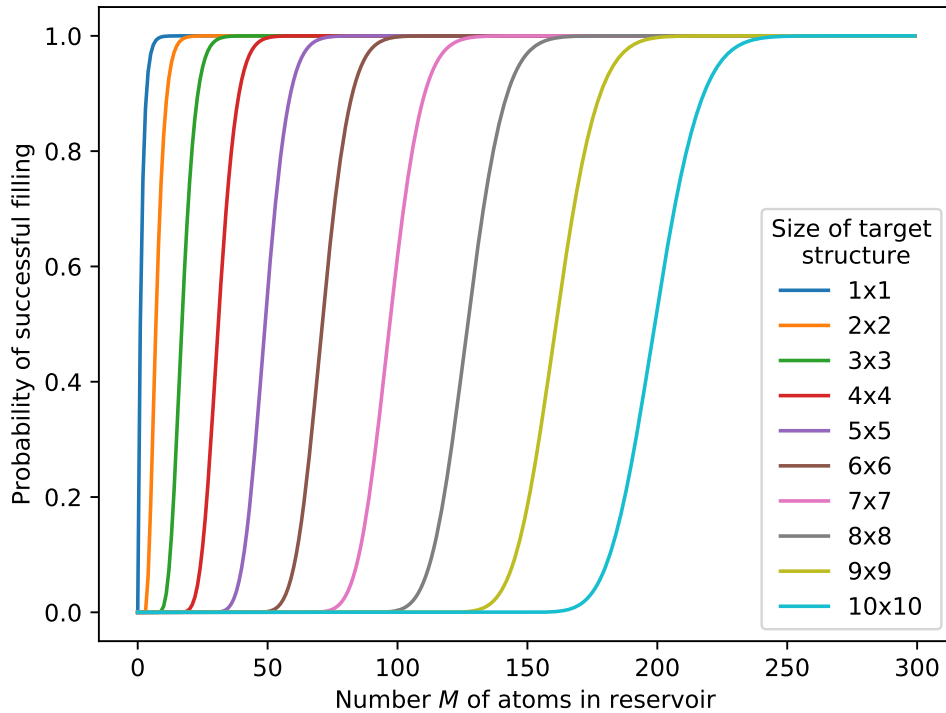


Figure 3.2.: Probability of creating a defect-free structure with total atom number M for various target structure sizes with N atoms, under the assumption of perfect transport efficiency and no atom loss.

3.2 Deterministic assembly of defect-free structures

With the viability of the approach asserted, the next step is to implement a system for atom rearrangement in the presented experiment. This section describes how this was achieved during the course of this thesis.

3.2.1 Experimental setup

For moving atoms from one trap to another, a single dipole trap beam passing through a 2D AOD is focused onto the atomic plane. This is most easily done by superposing it with the array beam before the objective focusing into the chamber. Thus, the beam position in the atomic plane can be controlled by altering the RF frequencies sent to the AOD. Figure 3.3 (a) shows a simplified schematic of this superposition. The AOD used in this setup (*DTSXY-400-780.800* by *AA Opto-Electronics*) actually consists of two deflectors joined to form one unit, with their planes of deflection aligned exactly perpendicular to each other. They will thus be treated as a single unit in the further description, accepting two frequencies ν_h and ν_v for horizontal and vertical displacement, respectively. When designing the complete optical setup to be integrated into the existing experiment, a number of constraints and experimental parameters have to be considered. These include, among others, the available space for the setup, power constraints given by the laser source as well as the laser power requirements for rearranging an array of a certain size, and the tweezer waist and addressable region one wishes to achieve. Considerations regarding

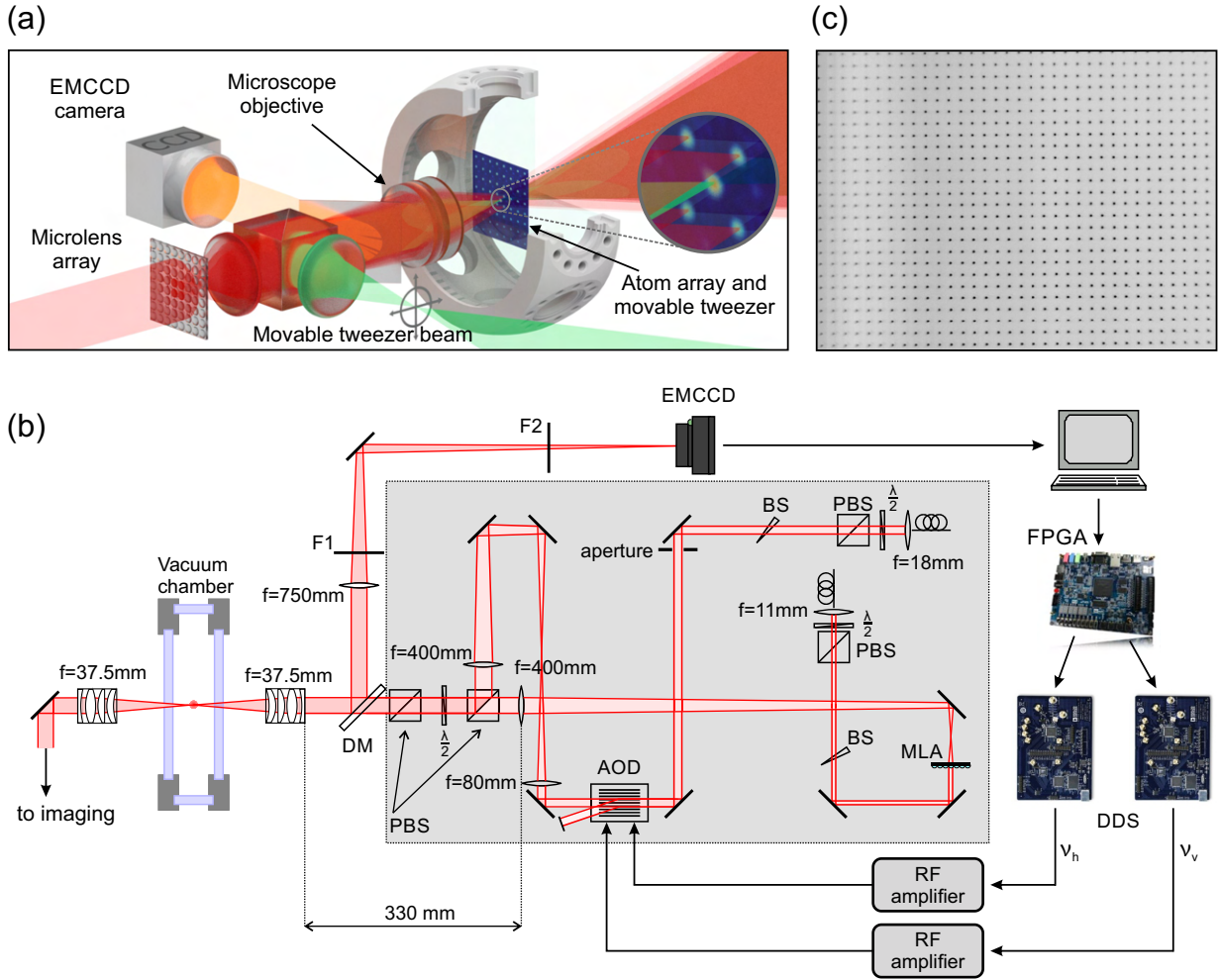


Figure 3.3.: A steerable, two-dimensional optical tweezer. (a) Simplified schematic of the experimental setup illustrating the superposition of array and tweezer beam and the reimaging of both into the vacuum chamber. (b) Top view of the optical setup and schematic of relevant electronic components. The tweezer beam is superposed with the array beam on a polarizing beam splitter cube (PBS). Beam samplers (BS) are used to pick off a small portion of the light for intensity stabilization. The light passing through the chamber is used to image the atom plane on a second CCD camera for alignment and calibration purposes. Fluorescence images obtained with the EMCCD are processed in the control computer, on which an algorithm calculates the frequency ramps corresponding to the rearrangement of atoms into a specified pattern. An FPGA converts these into DDS instructions. The RF frequencies output by the two DDS boards are amplified and sent to the AOD steering the tweezer beam. The modular design of the setup is indicated by the grey shaded area corresponding to a breadboard containing the array and tweezer beam paths. (c) 34×26 site section from the addressable region of the tweezer, obtained by reimaging the tweezer spot onto a CCD while stepwise tuning the AOD frequencies to overlap the tweezer spot with each array site in the region (array was turned off here). This illustrates the excellent homogeneity of the tweezer spots over the whole array.

tweezer waist versus addressable region, a detailed analysis of the power requirements taking into account losses on all of the optical elements, and a characterization of the setup is given in the Master thesis of Jan Werkmann [86], during the course of which this setup was designed and built. Figure 3.3 (b) displays a schematic drawing of the setup, showing array and tweezer beam paths, as well as a sketch of the electronic interconnection. The array beam path is equal to the one introduced in Fig. 2.4. The tweezer beam passes the AOD, where most of its power ($\approx 80\%$) is diffracted into the (1,1) order (horizontally and vertically), after which it is magnified using two achromatic lenses. The first $f = 80$ mm lens is placed such that its focal point corresponds to the pivot point of the diffraction, thus turning the diffraction angle into a lateral displacement. This displacement of the spot in the second focal plane of the lens is then reimaged with the second $f = 400$ mm lens and the $f = 37.5$ mm lens system into the atom plane. Scanning the AOD from 80 to 120 MHz, which corresponds to a range of nearly uniform diffraction efficiency $> 60\%$ [86], yields an addressable region exceeding $400 \mu\text{m} \times 400 \mu\text{m}$. This is equivalent to more than 1500 sites for a $10.3 \mu\text{m}$ pitch array and more than 3200 sites for a pitch of $7 \mu\text{m}$. A section of 34×26 sites from this addressable region is shown in Fig. 3.3 (c), indicating excellent homogeneity of the beam parameters over a large lateral area.

The light for both the array and tweezer beams is generated by the same Ti:Sa laser (see Section 2.1) at a wavelength of 797.3 nm. To avoid interference effects, they need to be slightly offset in frequency. Combining the AOD with the two AOMs used for fast intensity control, this shift is set to approximately 400 MHz by choosing the appropriate diffraction orders. Using a separate AOM for intensity control also allows to drive the AOD with a constant RF load, avoiding instabilities of the beam position due to thermal effects.

Moving an atom with the tweezer requires the ability to dynamically tune the AOD frequencies with a high update rate. This can be achieved, for example, by using a voltage controlled oscillator (VCO) and rapidly changing the reference voltage (as can be done with a fast DAC card integrated in the control computers). However, as the VCOs initially used in this setup proved insufficient for this purpose (causing atom loss because of frequency jitter, see [86]), a different approach was chosen, namely using direct digital synthesis (DDS) to create the frequencies. The two DDS systems used (*Analog Devices AD9915* evaluation boards) are able to execute frequency ramps with an update rate of 77 MHz [132] and are controlled by a field-programmable gate array (FPGA, *Terasic DE1-SoC*), which translates the frequency tuning words (FTWs) calculated on the control computer into DDS instructions. Thus, the tweezer can be integrated into the experimental control system and thus be synchronized with the rest of the experiment.

On the far side of the vacuum chamber, a magnifying telescope is set up to reimage the focal plane of the array and the tweezer onto a separate CCD camera. This allows a measurement of the beam waists (see below) and the calibration between AOD frequencies and array sites needed for atom rearrangement.

3.2.2 Moving a single atom

Before being able to assemble large arrays, a single atom move has to be implemented in order to characterize the efficiency and optimize parameters. This elementary atom move is outlined in Fig. 3.4 (a,b): The tweezer position is aligned with an array trap containing an atom and the tweezer depth is ramped up to its maximum value U_T . As the tweezer's potential is much deeper than that of the array trap, the atom is captured by the tweezer and extracted from the array trap. It is then moved in a sinusoidal trajectory to its destination, ensuring a smooth acceleration and deceleration. Finally, the amplitude ramp is reversed, thereby depositing the atom in the target trap. For rearranging large arrays, sequences of tens or hundreds of these single atom

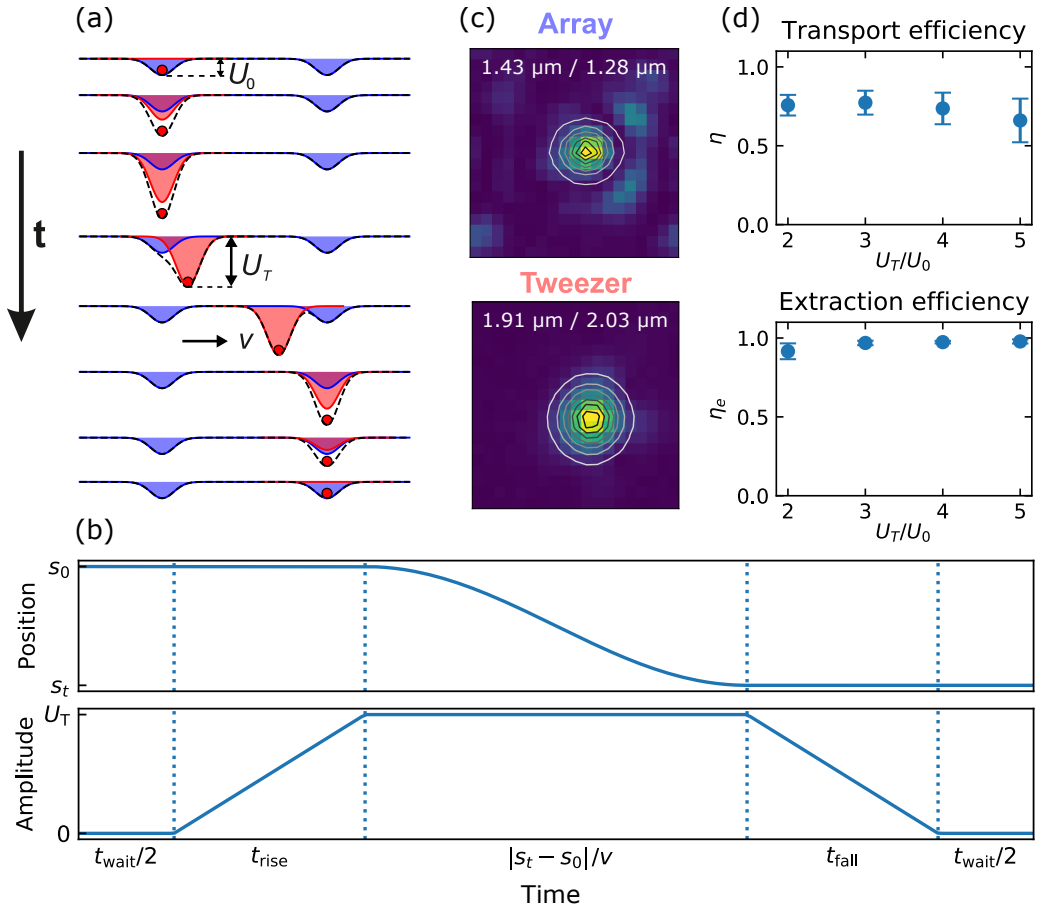


Figure 3.4.: Illustration and characterization of a single atom move. (a) Sketch of the tweezer capturing an atom from a source trap and transferring it to a target trap. (b) Corresponding ramps of tweezer amplitude and position during an atom move. (c) Typical measured beam waists of a central array trap and the tweezer obtained by reimaging (see text). (d) Transport and extraction efficiency versus tweezer depth U_T in units of the central array depth U_0 . Error bars correspond to the standard deviation when averaging over 11 rows in the array.

moves are needed, and time becomes a limiting factor as the total duration reaches a significant fraction of the atom lifetime. Therefore, it is paramount to keep the single atom move as short as possible without causing atom loss. Ramp times found to be optimal are $t_{\text{rise}} = t_{\text{fall}} = 200 \mu\text{s}$ and the fastest viable acceleration was determined to be $a_{\text{max}} \approx 400 \mu\text{m}/(\text{ms})^2$, corresponding to a transport speed of $\bar{v} \approx 21 \mu\text{m}/\text{ms}$ averaged over the sinusoidal ramp.

Figure 3.4 (c) shows a measurement of the waists of the tweezer and a central array trap in the atom plane, obtained by reimaging the focal plane with a magnifying telescope on a CCD camera on the far side of the vacuum chamber. Knowing the magnification ($M = f_2/f_1 = 13.3(4)$) and pixel size of the camera allows the extraction of an average tweezer beam waists of $2.0(1) \mu\text{m}$ and an average array waist of $1.45(10) \mu\text{m}$. Measuring the efficiency of atom extraction and transport as a function of the tweezer depth (see Fig. 3.4 (d)) yields an optimal tweezer to array depth ratio of $U_T/U_0 \approx 3$, typically corresponding to a tweezer depth of $U_T = 0.52(5) \text{mK}$, and suggests that the observed limitation of the transport efficiency to roughly $\eta = 0.75$ stems mainly from atom loss when depositing the atom into the target trap (the movement itself does

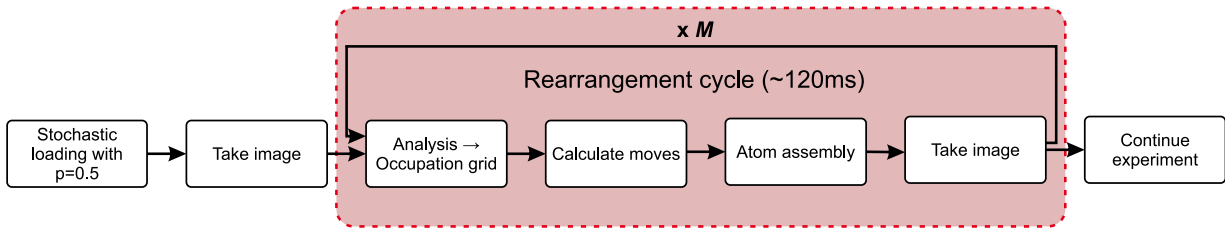


Figure 3.5.: Flow diagram of the assembly scheme. The steps highlighted by a red background constitute a single rearrangement cycle. This cycle is typically repeated multiple times to achieve a higher success rate.

not induce significant loss, as was verified in independent measurements). While the reason for this atom loss is not entirely clear, the most probable cause is the difference in waists of tweezer and array trap. As the tweezer waist is larger by a factor of approximately 40%, the atom occupies a larger volume, which can plausibly lead to the atom getting lost in some cases when trying to transfer it back into the smaller volume. In [52] however, where a quasi-perfect transport efficiency of 99.3% was reported, the tweezer waist is specified as 30% larger than the array traps. This suggests that, if this mismatch constitutes a significant limitation, it is likely not the only one. Other possible causes remain a subject of future investigation at the point of writing this thesis.

Thus, even though the waist mismatch could be corrected by modifying the optical setup, this would require a significant amount of time and does not guarantee a perfect efficiency. It was rather chosen to find a way to circumnavigate the rearrangement limitation associated with this imperfect transport, as will be discussed in Section 3.2.4.

3.2.3 Implementation of pattern assembly

The next step is to string together the single atom moves to rearrange larger structures and create defect-free arrays. The individual steps in this process are sketched in Fig. 3.5 and will be discussed in the following.

Analysis of the initial occupation

The experimental cycle starts with stochastic loading of atoms and a fluorescence imaging with the EMCCD camera. As described in Section 2.1.3, the camera software analyses this image as soon as it receives it and provides a boolean array corresponding to the trap occupations (0=empty, 1=occupied). As the program is implemented as a server, it can subsequently be queried by other processes needing this information. This analysis constitutes the first step in a rearrangement cycle, as illustrated in Fig. 3.5. The left arrow in Fig. 3.6 illustrates this abstraction. The corresponding boolean array serves as an input parameter for the algorithm calculating the atom moves.

Path-finding algorithm

For efficient rearrangement of atoms, an algorithm is needed to calculate a set of single-atom moves that lead to an ordered target structure. When designing such an algorithm, one can associate a cost with certain types of movements, distance travelled, and time needed, corresponding

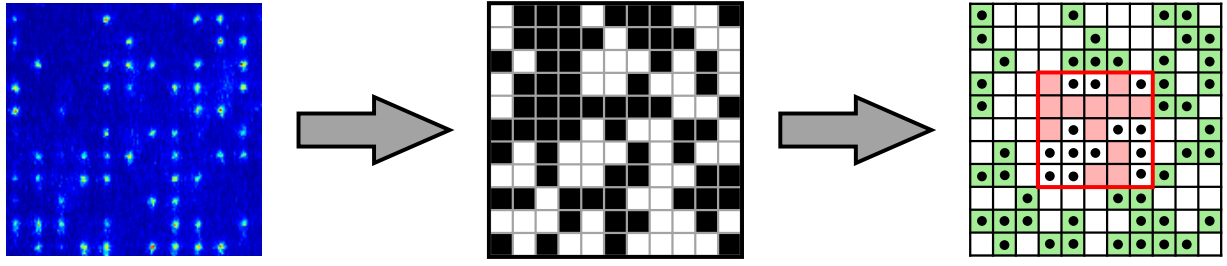


Figure 3.6.: Illustration of the abstraction from a fluorescence image of the atoms to a boolean occupation grid, with dark squares corresponding to an empty site (0) and white squares to an occupied site (1). This occupation grid is used by the algorithm to classify sites into overoccupied (reservoir sites containing an atom, colored green), underoccupied (empty target sites, colored red) and correctly occupied sites (white), shown in the image on the right. In this depiction, dots represent occupied traps for better visualization.

to the associated probability of atom loss. Different types of algorithms applicable to this problem are investigated in [126], all being variants of an A^* search, that, in its general form, uses a heuristic to efficiently find an optimal solution. All of these algorithms are tree-based, meaning they have to traverse a search tree that generally grows exponentially with the number of empty target traps, as the problem is similar to a travelling salesman problem in terms of complexity. Let M_{s_0} be the initial number of empty traps in the target structure and b the number of different source traps the algorithm considers for filling any given target trap. The time needed to execute the algorithm is proportional to the number of expanded nodes in the search tree. For an A^* search, the total number of nodes is then given by [126]

$$N_{\text{Nodes}, A^*} = \sum_{i=0}^{M_{s_0}} \frac{M_{s_0}!}{(M_{s_0} - i)!} \cdot b^i, \quad (3.4)$$

which would all have to be visited in the worst case. This becomes unfeasible very quickly, as even for a reasonably small target array with $M_{s_0} = 10$ and $b = 3$, Eq. 3.4 yields approximately $3 \cdot 10^{11}$ nodes. Assuming the expansion of one node takes on the order of a microsecond, it would thus already take more than 80 hours to traverse the whole search tree.

The modified A^* search, setting a strict order in which traps are to be filled, sacrifices optimality in favor of significantly reduced processing time. Thus, the number of maximally visited nodes shrinks to

$$N_{\text{Nodes}, \text{Mod. } A^*} = \sum_{i=0}^{M_{s_0}} b^i = \lfloor \frac{b^{M_{s_0} + 1} - 1}{b - 1} \rfloor. \quad (3.5)$$

For the same parameters as above, the processing time would now be less than 100 ms. As the number of nodes still grows exponentially with M_{s_0} , however, this algorithm is generally still not viable for larger arrays.

In order to achieve an execution time well below the atom lifetime, the criterion of finding an optimal solution has to be given up. The only case where this algorithm becomes feasible even for very large arrays, is if the number of considered source traps is limited to $b = 1$. This turns the modified A^* into a greedy algorithm with a linear time complexity of $\mathcal{O}(M_{s_0})$, as the search tree then only consists of a single branch of length M_{s_0} .

Ideally, this algorithm applies a shortest-move heuristic, meaning that it always chooses the

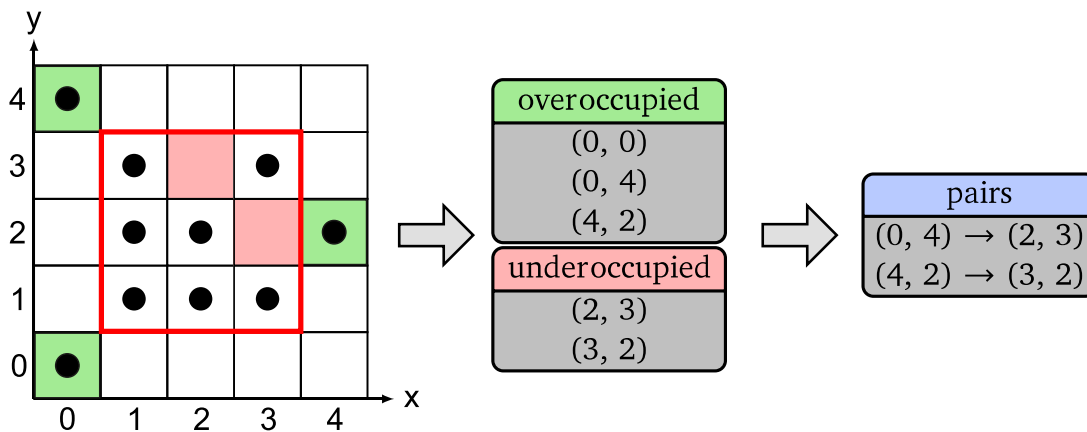


Figure 3.7.: Schematic of the algorithm matching overoccupied and underoccupied traps to form pairs. This is done employing a shortest-move heuristic, meaning that each empty target site is paired with the occupied reservoir site closest to it that has not been assigned yet.

nearest available source trap to fill any empty target trap. As it does so without considering consecutive options, this can lead to very long moves being forced later on in the sequence, which can yield solutions that take significantly longer to execute than the global optimum. It is, however, extremely fast (typically on the order of 1 ms) and, implemented correctly, very versatile with regard to target structure geometry. In pioneering work presented in [52], the group of Antoine Browaeys have demonstrated that this simple greedy-type algorithm is well-suited for the reordering of atoms, which is why this approach was also pursued within the work documented in this thesis. Its implementation was realized in [86].

In the first step, the process running this algorithm queries the camera server and receives the occupation grid. It then compares this grid with a pre-defined, target grid. Based on this comparison, a trap in the array can be either underoccupied (i.e. empty when it should contain an atom), overoccupied (i.e. occupied, but part of the reservoir), or correctly occupied. This is illustrated in Fig. 3.6. The goal now is to calculate paths from overoccupied traps to all underoccupied traps. Clearly, a successful rearranging is only possible when the number of overoccupied traps is equal to or larger than the number of underoccupied traps. However, even if this is not the case, the algorithm attempts to assemble the largest connected structure possible.

The coordinates of both over- and underoccupied traps are each stored in a list. The list of underoccupied traps is then ordered by their distance to the target structure's center of mass. This sets a strict order in which the algorithm tries to fill the structure, namely from the center outward, greatly reducing algorithmic complexity and minimizing the probability of encountering obstacles along the paths, which will be discussed later.

The next step is matching underoccupied with overoccupied traps, forming a new list of pairs. This is where the shortest-move heuristic comes into play. For each underoccupied trap in the list, starting from the top down, the algorithm calculates the euclidian distance to all traps in the overoccupied list, and then matches the pair with the shortest distance, adding it to the new list and removing it from the original lists. This is repeated until either of the lists is empty. This process is illustrated in Fig. 3.7.

Having matched all the traps, a route between each source and target trap has to be found. Here, complications arise from the fact that moving the loaded tweezer too close to an occupied array trap can lead to the loss of one or both atoms and therefore has to be avoided. There are two

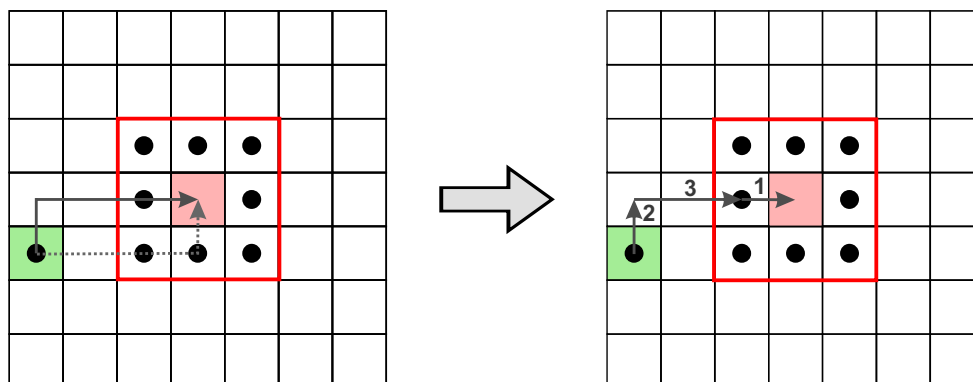


Figure 3.8.: Partitioning of paths to avoid atom collisions. For a given match between a source and target trap, there are two paths that contain only one turn. The algorithm chooses the one with fewer obstacles and, in the presence of obstacle atoms, divides the paths into segments until an obstacle-free set of moves is obtained.

types of path-finding that have been implemented and take this constraint into account. The first corresponds to moving the atoms between grid lines, displaced by half a pitch from any traps along the way. This ensures the absence of obstacles, but only works for arrays with a pitch large enough to allow the undisturbed passage of the tweezer. Another drawback is that this route includes two additional ninety degree turns of the tweezer with each requiring the deceleration and acceleration of the atom, resulting in longer move times. The other type of path avoids this problem by moving the tweezer directly along the grid lines. For this type of move, however, paths can include obstacles in the form of occupied traps along the way. The atoms in these traps will then have to be moved away first, requiring additional moves. As the latter type is more generally applicable and the overhead of extra moves manageable, it was chosen for all measurements presented in this work ¹.

The way the algorithm finds the optimal path and deals with obstacle atoms is sketched in Fig. 3.8. As it is advantageous to minimize the number of 90° turns, atoms are first moved in one dimension until they reach the target row or column, and then in the other dimension. This, in general, results in two possible paths the atom can take. For each pair in the matched list, the algorithm calculates the number of occupied traps along both of these paths and chooses the one with fewer obstacles. If it contains no obstacles, it is appended to a list of final paths and the next pair is processed. If it does, the path is segmented so that first the obstacle atom is moved to the target trap (again dealing in the same way with additional obstacles) and then the source atom is moved to the now empty obstacle trap. This recursive procedure continues until the list of pairs is empty and results in a list of all paths needed to assemble the target structure, each being obstacle-free.

The source code of this algorithm as well as an animation illustrating the procedure can be found in [133].

¹ Moving atoms along the grid lines obviously means that the tweezer can cross empty array traps while doing so. The temporary deepening of the potential experienced by the atoms in this case could cause some heating. A corresponding increase in atom loss could, however, not be observed in the experiment.

Assembly of the target structure

Once the path-finding algorithm returns the final list of paths, the process controlling the tweezer translates them into hardware instructions. Grid coordinates are converted into frequencies according to a calibration made using the reimaging system (see [86] for details), which are then passed to the FPGA as frequency tuning words (FTWs). The FPGA subsequently calculates corresponding sinusoidal frequency ramps that it passes on to the DDS, synchronizing their execution with tweezer amplitude ramps by simultaneously triggering an analog output card with pre-programmed ramp instructions. As this card has to be programmed at the beginning of an experimental run, at that instance the exact number of required ramps is not yet known. This is solved by just programming a much larger number of ramps than needed and aborting the execution once the rearrangement is completed. As a single atom move can consist of multiple paths, the first trigger, corresponding to a rising ramp, is sent when extracting the atom, and the second trigger for a falling ramp is sent when the tweezer has reached the target trap. Before the rearrangement starts, the array depth is ramped down by a factor of 4 to 5, facilitating extraction by the tweezer and rearrangement. Once all atom moves are executed, the array is ramped up again and a second image is taken to assess the result of the rearrangement. This concludes one rearrangement cycle, as indicated in Fig. 3.5.

Because of experimental limitations such as lifetime-related atom loss and imperfect transport, the larger the target structure is, the less likely it becomes that a defect-free filling is achieved after a single reordering. As long as there are still reservoir atoms present, however, this process can be repeated, significantly enhancing the probability of a successful filling, as will be characterized in Section 3.2.4.

Currently, the number of rearrangement cycles, like the rest of the experimental cycle, is pre-programmed and can not be changed dynamically, as all the hardware instructions would need to be reprogrammed, which takes hundreds of milliseconds. In a future extension, this could be solved by outsourcing all hardware instructions pertaining to atom assembly to separate devices and switching the control back and forth. This would allow to react in real-time to the array occupation and to abort the rearrangement and continue with the rest of the experimental cycle as soon as a defect-free target structure is achieved.

Duration of the rearrangement

As a single atom move takes roughly 1 ms, the duration of a complete rearrangement obviously depends on the size of the target structure, scaling more or less linearly with the number of empty target traps. Typical durations for the structures shown in this chapter are on the order of 50 to 100 ms. Factoring in the integration time of a fluorescence image, the readout time of the camera and the ramping times of the array, the duration of one complete rearrangement cycle (box in Fig. 3.5) adds up to an average of about 120 ms.

3.2.4 Evaluation of performance

In the following, the results that could so far be achieved with the current experimental setup are documented. These results have been published in [125].

The MLA used in this chapter has a pitch of $110\ \mu\text{m}$ (ML1, see Table 2.1.2). For the measurements presented here, a workspace of 361 atoms in a 19×19 grid was utilized. The trap depths of the array range from $U_0/k_B = 0.21(3)\ \text{mK}$ to $1.7(2)\ \text{mK}$ (grid corner to center), due to the

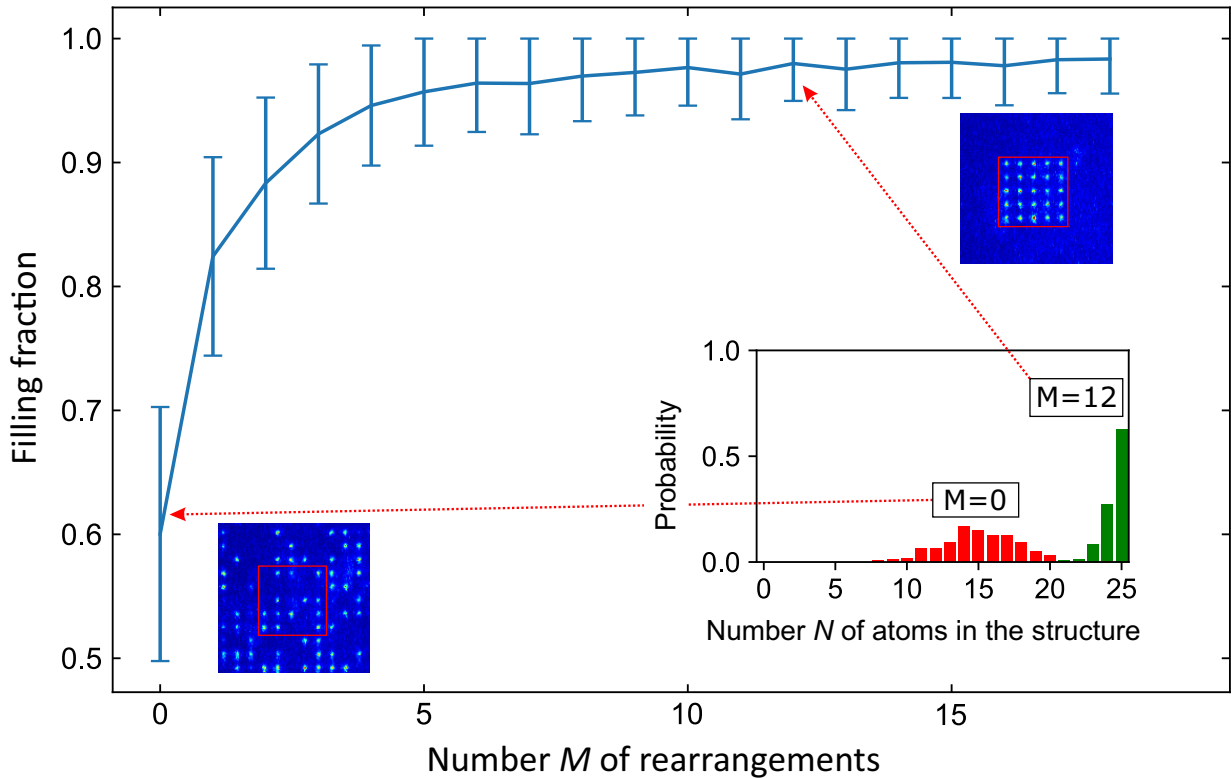


Figure 3.9.: Effect of multiple rearrangements on the filling fraction of a 5×5 cluster based on 500 experimental realizations. Error bars correspond to the standard deviation of the mean. The inset shows a histogram of the atom number in the target structure for two selected points in the sequence of rearrangements.

Gaussian profile of the beam illuminating the MLA. On average, 191(17) single atoms are initially loaded within this workspace. This corresponds to a loading efficiency of 53(5)%. Figure 3.9 illustrates the effect of a sequence of attempted assemblies of a 5×5 target cluster. Because of the limited transport efficiency and lifetime-related atom losses, a single rearrangement cycle is not enough to achieve a defect-free filling in any of the 500 experimental realizations. However, the repeated application of the rearrangement procedure quickly drives the filling fraction close to unity and yields a probability $> 60\%$ of detecting a defect-free cluster after 12 repetitions, as is shown by the histogram in the inset.

Scaling to larger arrays

With this procedure showing promising results for a medium-sized target cluster, this raises the question of the largest structure that can be assembled in the present experimental conditions. At the point of performing the experiments documented here, the largest structures demonstrated elsewhere so far contained 72 atoms [52].

In Fig. 3.10, results are presented that break this record by a significant margin. Figure 3.10 (a) shows a sequence of images corresponding to subsequent rearrangement cycles, resulting in a defect-free target structure containing 100 atoms. This is achieved after five cycles, taking 1.3 s in total. Especially for larger structures, the execution of multiple repetitions is vital for a successful assembly of the pattern, as is illustrated in Fig. 3.10 (b), where the cumulative success rate is plotted against the number of rearrangement cycles. Even as the probability to achieve a

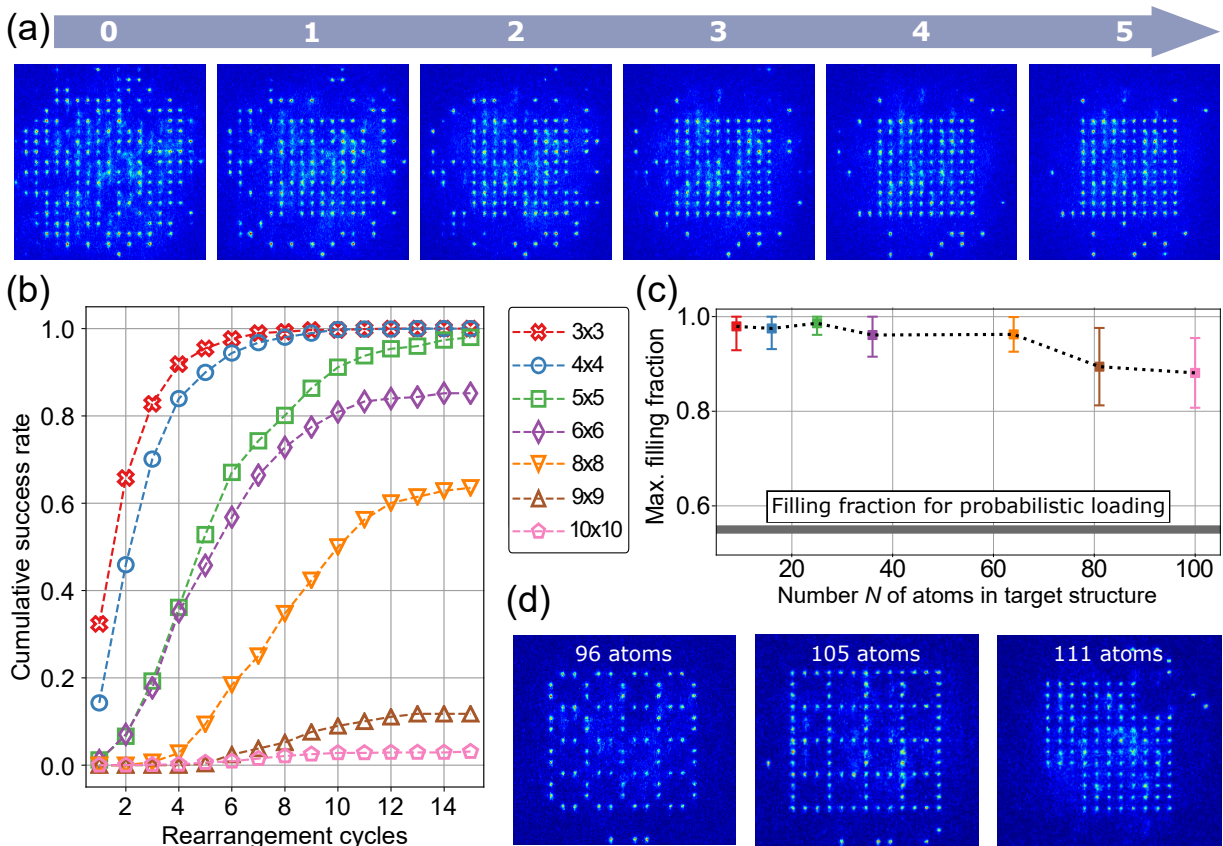


Figure 3.10.: Results of multiple rearrangements. (a) Atom distribution during a sequence of rearrangement cycles for a 10×10 target structure. Starting from an unsorted atom array, a defect-free cluster is generated within 5 cycles. (b) Measured cumulative success rates of achieving defect-free quadratic clusters of different sizes. For most clusters, the final value is reached after 10-15 rearrangement cycles. (c) Maximum filling fraction observed during rearrangement runs for different cluster sizes, which is typically reached after 7-9 cycles. Error bars correspond to a 1σ interval. The thick continuous line at 0.55 represents an upper bound to the filling fraction obtained via collisional blockade alone, i.e., the situation before the first rearrangement cycle. (d) Gallery of differently shaped defect-free clusters.

defect-free structure drops below 100% for clusters of more than 5×5 atoms, for measurements where a defect-free pattern is critical this would just mean that shots where the assembly did not succeed will have to be discarded in post-selection, which is still somewhat feasible for the 100 atom cluster with a 3.1% success rate. This number corresponds to the probability of creating a defect-free structure after any one of the rearrangement cycles and not necessarily after the last one, as atoms can get lost over time, creating new defects. In order to efficiently work with these large clusters, a method for aborting the rearrangement process once the structure is filled will have to be implemented.

For measurements that do not necessarily require a total absence of defects, but simply a near-unity occupation of a structure, the filling fraction is perhaps the more relevant number. It is shown in Fig. 3.10 (c) for the same clusters and exceeds 95% for all target clusters up to 8×8 atoms. Even the 10×10 cluster still exhibits a filling fraction of 88(7)%, which is significantly higher than the initial loading rate of $\approx 55\%$, drawn as a grey bar at the bottom of the graph.

Table 3.1.: Success rates and filling fractions for different structure sizes. The data in this table are plotted in Fig. 3.10 (b and c). For details, see text.

Structure size	Max. cumulative success rate	Max. filling fraction
3×3	100%	98(5)%
4×4	100%	98(5)%
5×5	99.8%	99(3)%
6×6	85.5%	96(5)%
8×8	63.5%	96(4)%
9×9	11.8%	89(8)%
10×10	3.1%	88(7)%

The *maximum filling fraction* plotted here corresponds to the highest observed value within each respective series of rearrangements. It typically peaks at around 7 rearrangements for the measurements presented here. For any given structure, it does not reach 100% in every repetition of the experiment, as during any specific rearrangement cycle, there is a finite probability of atom loss².

Table 3.1 lists the maximal cumulative success rates and filling fractions that could be achieved for the respective structures.

Figure 3.10 (d) depicts a gallery of differently shaped target structures, including the largest structure that could be assembled so far, containing 111 atoms. This illustrates the flexibility to create various topologies, which is essential in some quantum error correction schemes [134, 135] as well as for the observation of topological effects in a Rydberg quantum simulator [43, 136].

Reloading and reordering

The larger the target structure gets, the more the success of its assembly is limited by lifetime-related atom loss. But even for smaller clusters, it sets a boundary on the cluster lifetime after its successful assembly. Another source of atom loss in the cluster can be intentional, such as a destructive state detection, as will be utilized for the Rydberg measurements introduced in Chapter 4. In both of these cases, the reloading of atoms into the cluster would mean that the experimental cycle would not have to be started over, that is, with the loading of the MOT. Instead, the experimental segment requiring a defect-free cluster can be executed as many times within one cycle as there are enough reservoir atoms to reload the cluster.

Figure 3.11 (a) demonstrates this scheme for a 3×3 cluster. In between rearrangements, the target traps are depleted by extracting the atoms with the tweezer and depositing them in a region without a trapping potential, ensuring that for the subsequent assembly the atoms have to be taken again from the reservoir, as would be the case in the situations described above. The number of times this can be repeated obviously depends on target structure and reservoir size (here, only a 11×11 workspace was used), as well as transport efficiency, atom lifetime and

² This is to be seen in contrast to the cumulative success rate, which represents the probability of achieving defect-free filling in *any one* of the evaluated rearrangement cycles.

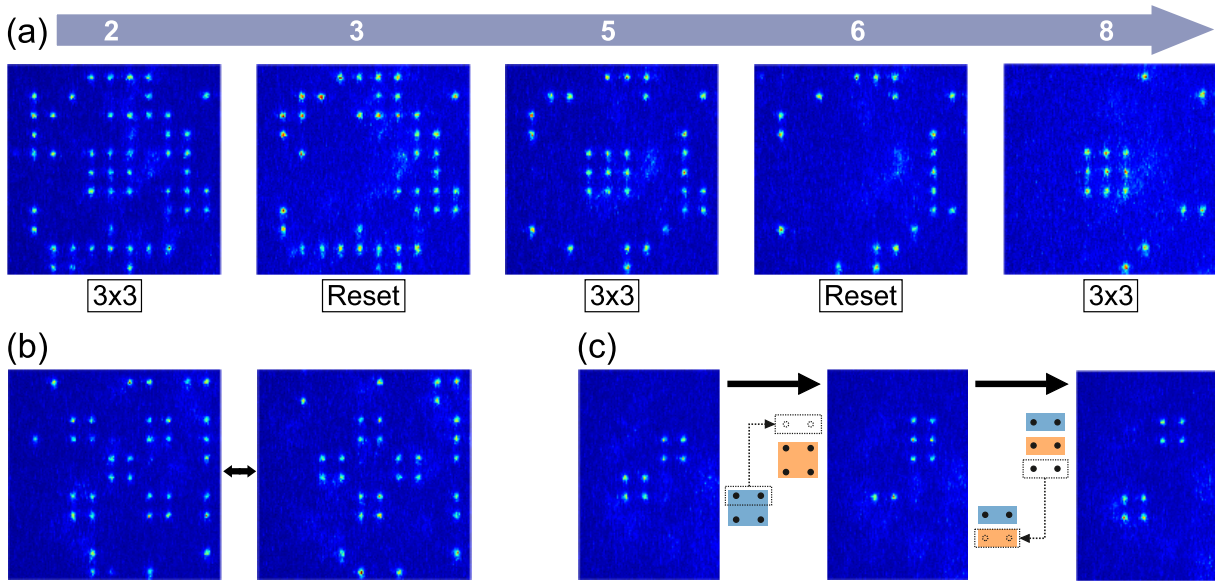


Figure 3.11.: Demonstration of reloading and reordering schemes. (a) Multiple reconstruction of a central 3×3 cluster after deliberate atom removal. The number of feasible repetitions within one experimental run scales with the size of the reservoir array. This demonstration is based on an 11×11 workspace with 96 reservoir sites. (b) Example of the transformation (inversion) of an atom arrangement within a single experimental run. Atoms lost during this procedure are replaced by atoms from the surrounding reservoir. (c) Demonstration of an atom exchange between two clusters: *Left*, An initial defect-free structure of two 2×2 clusters is created. *Middle and Right*, The atoms are relocated so that two atoms of each cluster are moved into the respective other cluster. The two colors in the schematic correspond to the respective original clusters. This procedure can be used for the distribution of entanglement [137].

initial loading rate. Especially the latter can fluctuate on a daily basis, so that the attempted number of reloadings has to be assessed and adapted routinely. This method was used for the measurements presented in Chapter 6.

Apart from reloading the same target structure multiple times, atoms can also be configured into different patterns within the same experimental run. Figure 3.11 (b) shows the inversion of a pattern. In that particular case, the transport efficiency is insufficient to allow a perfect reordering, so atoms lost during rearrangement were replaced by atoms from the reservoir. In a smaller arrangement, as shown in Fig. 3.11 (c), the efficiency is high enough to deterministically exchange particular atoms between clusters, as sketched in the schematic. Done adiabatically, this procedure preserves coherence [44, 130] and thus allows for the redistribution of quantum-correlated or entangled subarrays [137].

Extension of atom lifetime and perpetuation of structures

Because of the limitation in trapping laser power, the wavelength for the measurements presented here was chosen to be only 2 nm red-detuned from the D1 line (i.e. 797.3 nm). This close to the resonance, photon scattering plays a major role in limiting the atom lifetime in the trap,

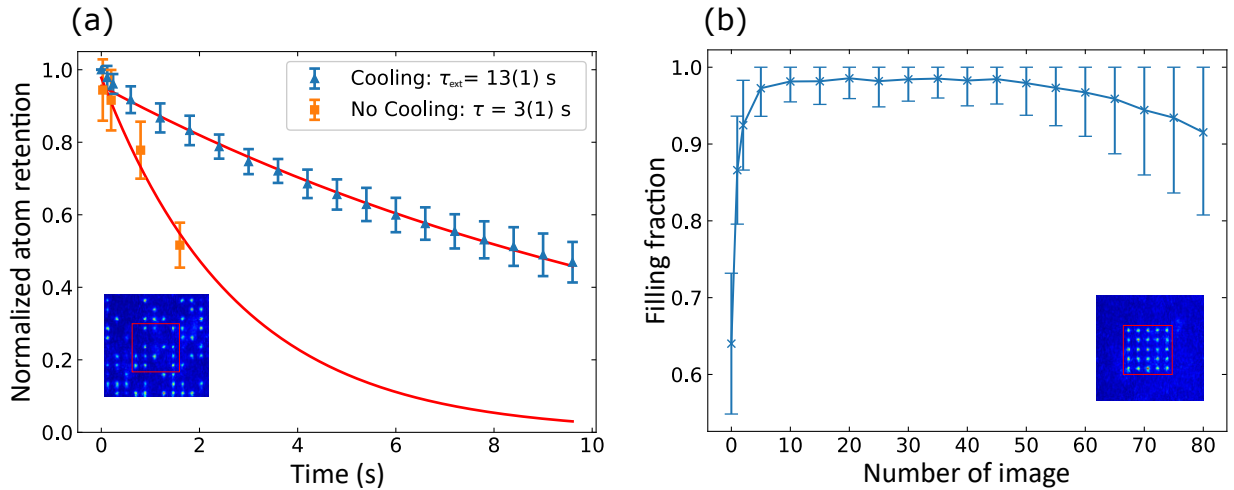


Figure 3.12.: Extension of the lifetime by repeated imaging and perpetuation of a cluster. (a) Periodically illuminating an unsorted atom distribution with detection light exerts a cooling effect counter-acting scattering-induced heating by the trapping laser. This significantly prolongs the lifetime of the atoms in the trap compared to a measurement without detection light. (b) Making use of this lifetime extension as well as reloading from the reservoir, a 5×5 cluster can be kept defect-free for up to 80 cycles, or approximately 10 s. Error bars correspond to the standard deviation of the mean.

which is expected to be significantly lower than the value of $\tau_{805\text{nm}} = 10.3(14)$ s measured for a Ti:Sa wavelength of 805 nm and trap depth of $U_0 = 3.2$ mK [138], which was shown to be limited by collisions with background atoms. Indeed, a similar measurement for $\lambda_{\text{Ti:Sa}} = 797.3$ nm yields a lifetime of only $\tau_{797\text{nm}} = 3(1)$ s, as is shown in Fig. 3.12 (a) (orange data points). Based on this lifetime, the assembly of defect-free structures of 100 atoms or more should not have been possible. However, during the repeated assembly attempts, the atoms seem to experience a boost in trap lifetime. This can be explained by the repeated illumination with the detection light, which periodically cools the atoms in the traps, analogous to an optical molasses stage. This effect becomes especially noticeable the larger the number of repetitions get. In a measurement consisting of 80 repetitions, with 120 ms between each image, the extension of the atom lifetime to a value exceeding the vacuum lifetime reported in [138] can be observed. The blue data points in Fig. 3.12 (a) illustrate this lifetime extension. For this measurement, the tweezer was disabled, so no rearrangement happens, isolating the effect of the imaging on a central 5×5 region of the array. The extended lifetime was measured to be $\tau_{\text{ext}} = 13(1)$ s.

Switching on the tweezer to assemble a defect-free 5×5 cluster in the same region demonstrates the combined effect of extended atom lifetime and reloading from a reservoir on the cluster lifetime. Figure 3.12 (b) illustrates how this allows to keep the cluster defect-free for several seconds. In an average of 49(13) of the 80 images taken in this series, the target structure was determined to be without defect, perpetuating the cluster for up to 10 s. This can be especially interesting for quantum sensing and metrology applications benefiting from long-lived atomic arrays. We infer that the lifetime of the target structure is limited by the lack of sufficient reservoir atoms for long rearrangement cycles and it could be further extended in a larger workspace.

3.3 Future scalability

The results presented in the previous section are to be seen as a current status quo, with numerous ways of expanding this procedure to even larger structures within reach, given the intrinsic scalability of the microlens platform. In this section, the potential for further scaling up the system will be evaluated. First, it will be explored how the currently implemented tweezer setup could perform with a feasible improvement of parameters such as transport efficiency or atom lifetime. After that, different possible extensions of the setup will be discussed.

3.3.1 Scaling with improved experimental parameters

Modelling the rearrangement procedure described in the previous section with a Monte-Carlo simulation allows to assess the effect of various experimental parameters on its performance. A finite transport efficiency and atom lifetime are easily modelled by introducing a stochastic loss after every rearrangement. For each repetition of the simulation, a randomly filled initial grid is created and the path-finding algorithm is applied to find a rearrangement sequence. The timings, which are relevant for simulating lifetime losses, are matched closely to the experimental values. The source code for this simulation can be found in Appendix B. To assert its validity, first a simulation with experimentally measured parameters is done. These parameters are:

- A single move transport efficiency of $\eta = 0.75(5)$
- An atom lifetime of $\tau = 6(6)$ s
- A site-specific loading rate with an average of $p = 0.53(5)$
- A workspace of 19×19 sites

The lifetime was obtained from the same measurement as plotted in Fig. 3.12 (a), but evaluated over the whole 19×19 workspace and only taking into account the initial 10 repetitions, as the atom loss tends to be slightly higher during these compared to later repetitions. The large error is due to significant variations over the whole workspace³.

Simulating 5000 experimental repetitions this way yields the result shown in Fig. 3.13 (red circles and shaded region), which agrees well with the experimental data.

Having a reliable method to simulate the outcome of a rearrangement attempt allows an extrapolation to improved experimental parameters. In the following, two sets of improved parameters will be analyzed.

1. $\eta = 0.95$, $\tau = 13$ s, $p = 0.5$, 19×19 site workspace:

These parameters represent experimental improvements that can feasibly be achieved in the existing setup without having to invest in a more potent laser or vacuum system. Since a transport efficiency of 99.3% has already been reported in [52], a value of 95% should be achievable with an improved optical setup, reducing the tweezer waist to match that of the array. To reach the vacuum-limited lifetime of 13 s over the whole array, the photon scattering of the array beam needs to be reduced by detuning the laser slightly further from resonance. The array trap depth lost this way can be compensated for by supplying

³ This would be more correctly modelled by introducing a site-specific lifetime in the simulation. As the corresponding modification of the simulation yielded no appreciable difference to using a global lifetime, the latter was chosen for all simulations presented here. This also facilitates extrapolations to improved parameters.

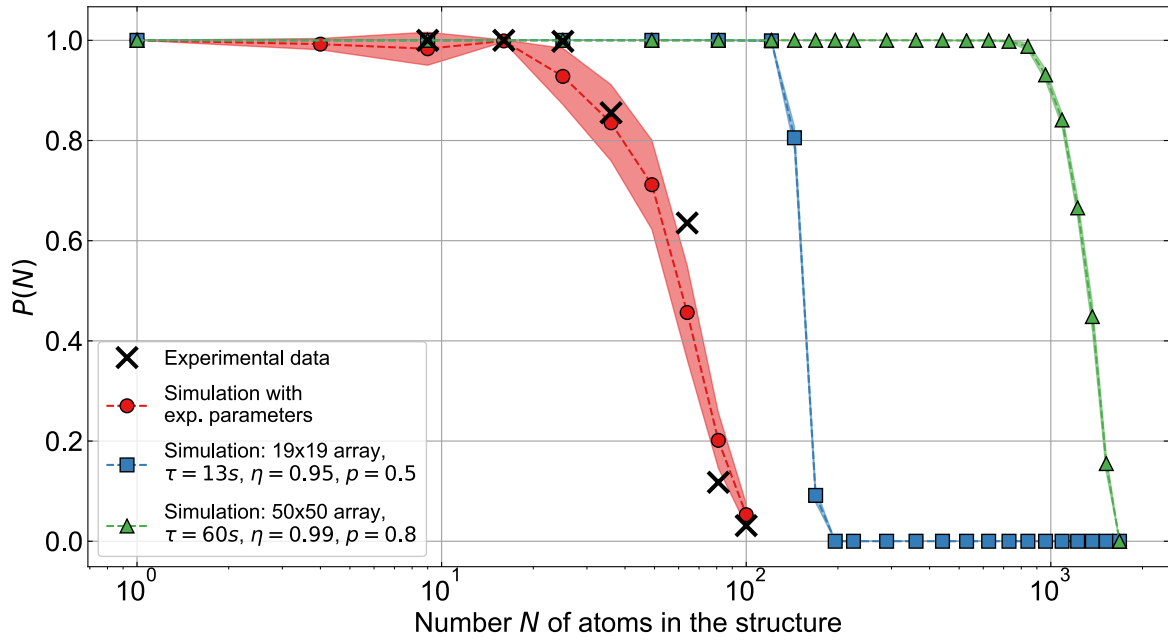


Figure 3.13.: Results of Monte-Carlo simulations of the rearrangement procedure. The graphs shows Monte-Carlo simulations of the cumulative success probability after 25 rearrangements for different parameter sets. The experimental data correspond to the maximum values of the curves in Fig. 3.10 (b) and is matched well by the simulation using experimentally obtained parameters. Shaded regions correspond to a 1σ confidence interval.

the tweezer beam from a different laser, so that all of the available Ti:Sa power can be used for the array (the amount of power needed for the tweezer can be provided by a diode laser). The result of the simulation for these parameters is represented by the blue curve in Fig. 3.13.

2. $\eta = 0.99$, $\tau = 60$ s, $p = 0.8$, 50×50 site workspace:

This simulation is still based on the same experimental methods, but with significant improvements of the setup. The parameters correspond to the best that have been demonstrated in comparable experiments so far. A lifetime close to a minute can be reached in alkali metal atoms setups with vacuum pressures an order of magnitude lower than in the current setup presented here [139]⁴, and an initial filling fraction of 80% in an array of 100 traps has recently been demonstrated [85]. Ensuring sufficient trap depths for a 50×50 array, while staying far-detuned enough to allow for the aforementioned parameters to be met, admittedly, requires significantly more laser power than is available in the current setup (by roughly a factor of 10), which is also more than can be provided by a single commercially available Ti:Sa laser. However, as each site in the trap array corresponds to a separate lenslet in the MLA, a microtrap array could be composed of multiple laser sources, thereby overcoming this limitation. The green curve in Fig. 3.13 shows that given these

⁴ Using a much narrower cooling transition in the alkaline earth metal Strontium, longer lifetimes under constant application of Sisyphus cooling have been reported [140, 141].

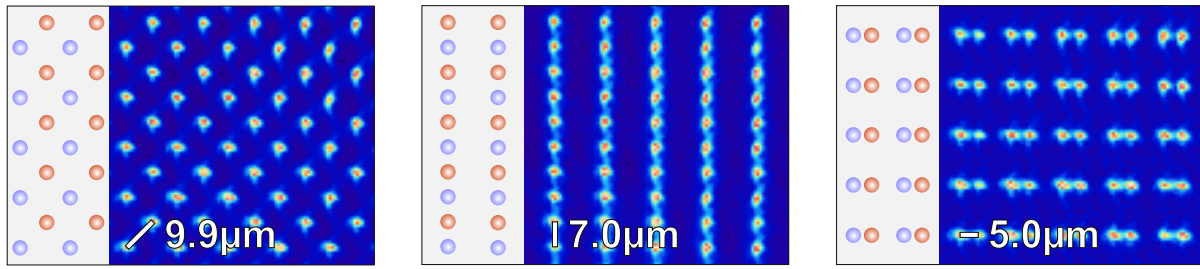


Figure 3.14.: Interleaved arrays with different geometries created by varying the relative angle of the illuminating beams on the MLA. The fundamental pitch here is $14.1 \mu\text{m}$. The pictures represent averaged fluorescence images. Taken from [69].

parameters, structures containing more than 1000 atoms could be assembled with high probability.

These simulations serve to illustrate the robustness and intrinsic scalability of the microlens approach combined with a single optical tweezer, the major limitation merely being optical power. These extrapolations were made based on the same rigid geometry as is currently in use in the setup, using a single trap array. Modifications of this geometry, such as interleaved grids, parallelization of transport and an expansion into the third dimension, are discussed in the following.

3.3.2 Interleaved reservoir grids

Due to the direct mapping of microlenses to focal spots, it is possible to create multiple trap arrays in the same focal plane by superposing two illuminating beams on the MLA in an angle. Trapping of atoms in these interleaved arrays has been demonstrated in [130] for atomic ensembles and in [46] for single atoms. Given a fundamental pitch of $10 \mu\text{m}$, an additional array in each dimension, shifted by half a pitch in horizontal and vertical directions, is feasible without noticeable cross-talk between the traps [46], thereby quadrupling the density of traps compared to the current setup. As each of the arrays could be sourced from a different laser, available laser power would not be a major limitation (the light for the additional arrays could be provided by Master Oscillator Power Amplifier (MOPA) systems, which are being actively developed and widely used in the group, and are relatively inexpensive to build). Averaged fluorescence images of an interleaved array created with two beams on the MLA are depicted in Fig. 3.14 (in this example, the fundamental pitch is $14.1 \mu\text{m}$). By changing the relative angle of the incident beams, various geometries can be created.

Using these additional arrays as a reservoir should yield similar results to increasing beam size and power in a single array, in terms of creating defect-free structures of larger sizes. This approach has the additional advantage, however, that the reservoir would not lie outside the target structure, as is typically the case in the current setup, but would be interleaved with it, yielding very short moving distances and significantly reducing the occurrence of obstacles in a path. An adaptation of the path-finding algorithm catering to this modified setup has already been implemented during the work reported in [86] and can thus be used to simulate the performance of this method. Figure 3.15 shows the result of a simulation using interleaved reservoir arrays, as illustrated schematically in the top part of the figure. All simulations are based on a 19×19 workspace, a loading rate of $p = 0.5$ and a transport efficiency of $\eta = 0.75(5)$, as measured in the experiment, as well as a global lifetime of $\tau = 13(1)\text{s}$, which corresponds to the

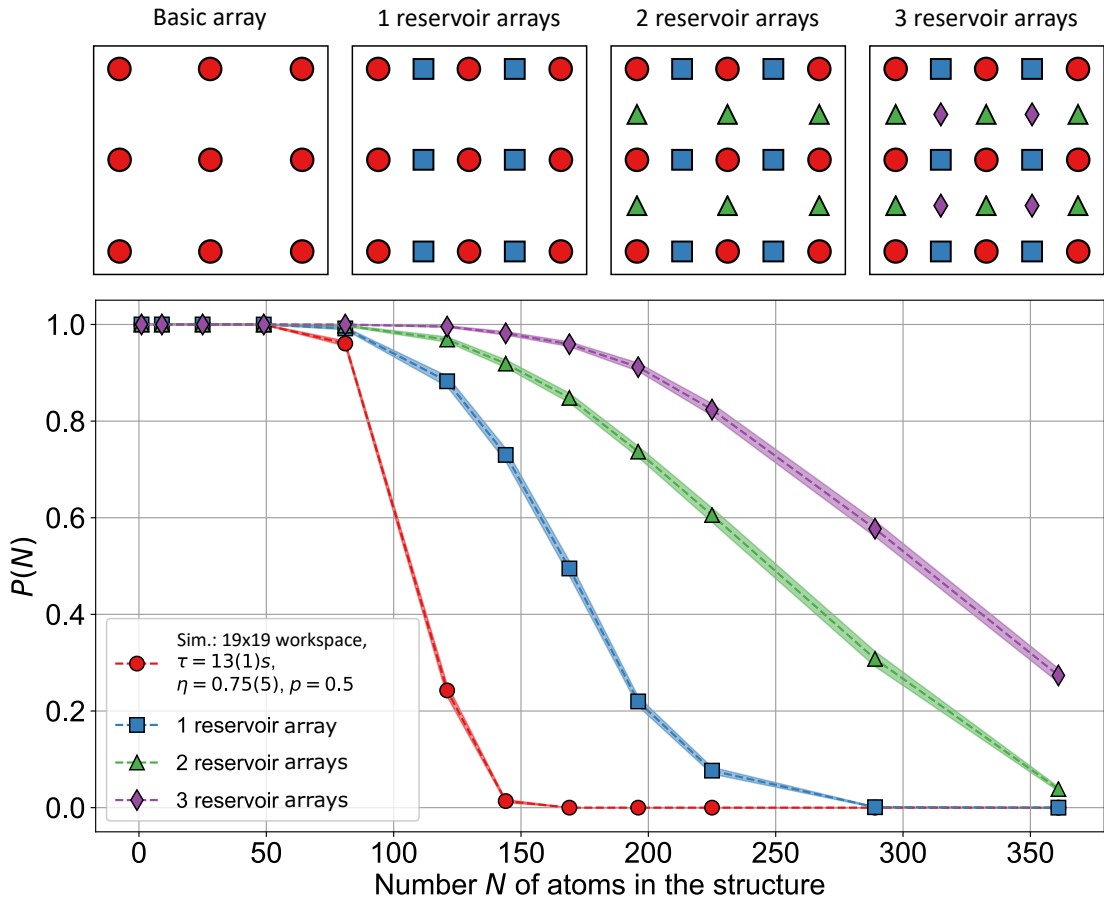


Figure 3.15.: Monte-Carlo simulations of the probability for generating large defect-free structures using interleaved reservoir arrays. All simulations are based on experimental parameters, but assume a vacuum-limited lifetime over the whole workspace. Adding interleaved arrays offset by half a pitch in horizontal, vertical, or both directions, respectively, would lead to an appreciable increase in feasible cluster size. Shaded regions correspond to a 1σ confidence interval. Lines are used to guide the eye.

vacuum-limited value measured in the central 5×5 traps under repeated cooling. Given these parameters, the graph shows that using two or three additional interleaved arrays, with similar laser power as the fundamental array, would allow for a complete filling of the workspace with a finite probability.

3.3.3 Parallelization of atom transport

As the atom lifetime in the presence of repeated cooling cycles is significantly longer than a sequence of movements, the use of a single optical tweezer for rearrangement is sufficient given the current array sizes. However, as one scales up the system according to the above-mentioned approaches, the time needed for a sequence of rearrangements grows rapidly as well. Improving the atom lifetime in the traps can somewhat mitigate the associated atom loss, but at some point this will nevertheless constitute a limitation when reaching a critical system size. In order to drastically cut back on the rearrangement time, one would have to implement some sort of parallelization. A promising approach for this is the use of multitone generation as introduced

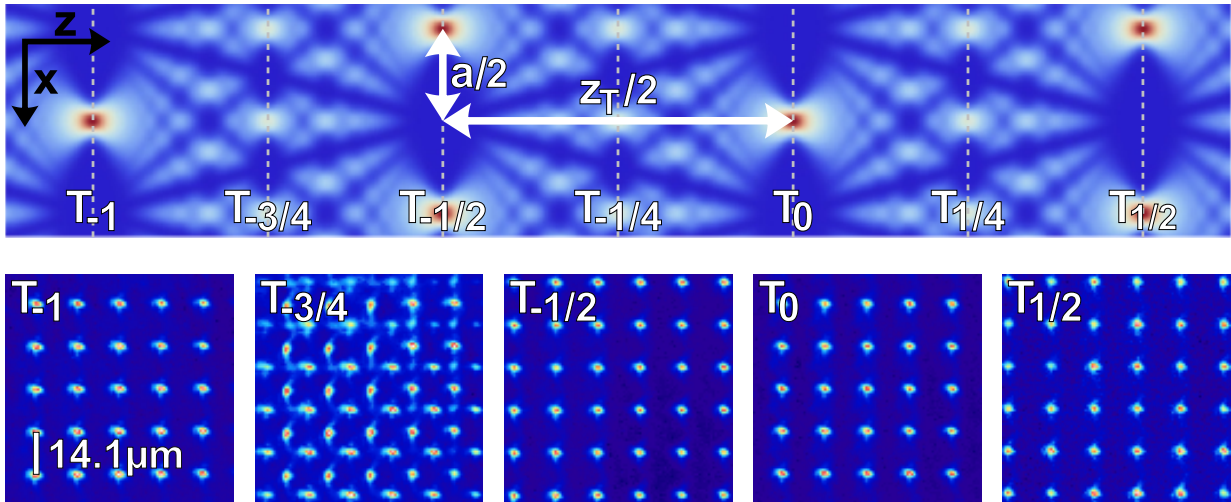


Figure 3.16.: Three-dimensional Talbot optical lattice created by reimaging the periodic pattern in the focal plane of the MLA. *Top:* Cut along the optical axis showing a 2D projection of the Talbot carpet with parameters similar to the current experiment ($\lambda = 798.6 \text{ nm}$, $d = 14.1 \mu\text{m}$, $w_0 = 1.45 \mu\text{m}$). *Bottom:* Averaged fluorescence image of single atoms trapped in the potential structure corresponding to fractional and integer Talbot planes [69].

in [53], with the obvious benefit that the current tweezer setup could still be used, but instead of a single spot, a hundred could be feasibly generated in a real-time fashion. Implemented appropriately, this would enable the transport of complete rows and columns at a time, thus significantly speeding up the rearrangement.

3.3.4 3D array via trapping in Talbot planes

In most of the experiments performed in the presented setup so far, the Talbot effect (introduced in Section 2.1.2) was treated as an undesirable side effect and atoms trapped in the self-images of the focal plane are usually removed by a resonant laser at the end of the initial loading process. However, the ability to control the axial spacing of the 3D Talbot carpet by tuning the array pitch, and the fact that all the additional trapping planes generated by this self-imaging come at no additional cost in laser power, makes the deliberate utilization of these planes for atom trapping a promising approach for extending atom assembly into the third dimension.

The implementation of a 3D assembled Talbot optical lattice faces two major challenges. The first is eliminating interference from unwanted fractional Talbot planes. While the integer and half-valued planes are typically spaced far enough from each other so that they do not cause a major reduction of contrast when imaging one of the planes while atoms are trapped in the other planes, the rest of the Talbot carpet constitutes a disrupting source of background light that can significantly impede the fidelity of atom detection. This can be seen in the axial plot of such a Talbot carpet illustrated in Fig. 3.16 (top). Figure 3.16 (bottom) illustrates how atoms can be trapped in planes of different geometries within the Talbot carpet. When working with multiple planes, the blow-away scheme using a string of wire is not applicable anymore, as it removes atoms from all but a single plane. Thus, a more sophisticated removal scheme will have to be implemented, for example by reimaging a periodic line structure on the atoms, whose periodicity can ideally be adapted to accommodate different Talbot lengths. This could be accomplished with a digital micromirror device (DMD), using the technique reported in [142] and illuminating the

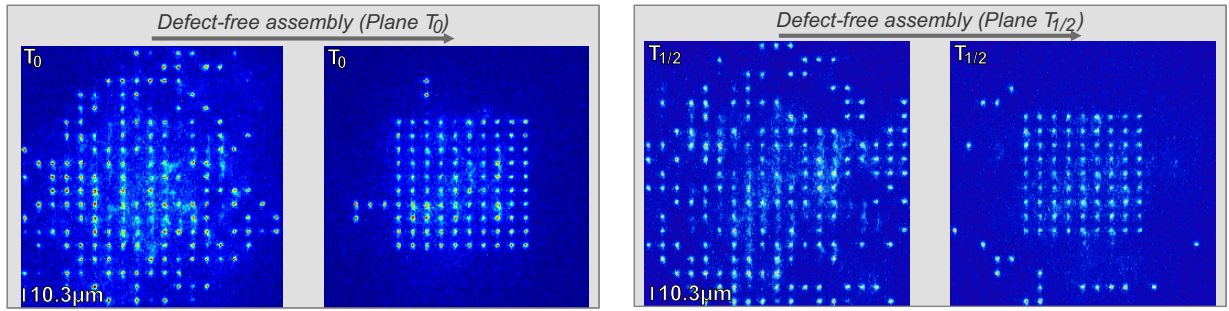


Figure 3.17.: Assembly of a defect-free 9×9 cluster in two adjacent half-integer Talbot planes separated by $133(8) \mu\text{m}$ [69].

Talbot carpet laterally. The second challenge is implementing a method for variable addressing and detection of atoms in multiple Talbot planes. So far, both of these are realized in a static fashion, so that changing the Talbot plane to be assembled involves manually displacing the array and tweezer in the axial direction by tuning the position of a lens, which can obviously not be done within a single experimental run. A solution for this problem has recently been demonstrated in [124], where electrically tunable lenses were used to dynamically adjust the tweezer and imaging plane, allowing for the sequential rearrangement of atoms in multiple trapping planes generated holographically with an SLM. Using these lenses, whose focal length can be tuned over a large range by controlling the curvature of a liquid-filled membrane with a driving current, adaptive addressing and imaging of various Talbot planes could be achieved in the current setup.

An analysis of the scalability gained by this approach, as well as first results of atom assembly in separate Talbot planes, has been published in [69]. Figure 3.17 shows the expansion of the atom sorting scheme presented in this thesis to an additional Talbot plane. Here, T_0 denotes the original focal plane of the array, while $T_{1/2}$ is the first fractional Talbot plane going along the optical axis. According to Eq. (2.21), their axial distance is $z^* = 133(8) \mu\text{m}$. The observed success probability for assembling a 9×9 cluster in the Talbot plane is comparable to the original plane. This demonstrates the excellent optical quality of the Talbot planes and hints at their potential for building large assembled 3D crystals.

3.4 Conclusion

The topic of this chapter was the experimental realization of an atom sorting scheme enabling the creation of large defect-free structures within an array of single-atom quantum systems. Utilizing an optical tweezer steered via a two-dimensional acousto-optical deflector, arbitrary atom transport within the focal plane of the dipole trap array introduced in Chapter 2 could be achieved. Combining the excellent homogeneity of both array and tweezer traps over a larger area with a fast method to calculate and execute sequences of atom moves needed for the assembly of the atoms into a predefined pattern, the formation of defect-free structures of more than 100 atoms could be demonstrated. The application of multiple assembly cycles within a single experimental realization was shown to both significantly boost the success probability for the initial assembly of a large structure and serve as an efficient way to reload atoms after deliberate or unintentional atom loss, while having the beneficial side effect of prolonging the atom lifetime in the traps. A Monte-Carlo simulation of the assembly process, validated by a comparison with experimental data, allows to access the scaling potential of this approach, indicating that defect-free structures of more than 1000 atoms could be constructed with feasible experimental parameters. Further

extensions of the technique enabled by intrinsic properties of microlens arrays, such as using interleaved grids or extending the system into the third dimension using the Talbot carpet, have been discussed and first results have been presented.

Large assembled arrays of neutral atoms have a multitude of potential applications, the most notable and actively pursued being quantum computation and simulation schemes relying on Rydberg-mediated interactions between the atoms [20, 30, 37], where remarkable progress has been achieved in the last years [38, 39, 42, 43, 60, 108, 143] even with smaller systems. Scaling up the atom number would allow the simulation of ever more complex systems, allowing the exploration of exotic quantum phase transitions [42] and topological effects [40, 43], as well as enabling the implementation of quantum error correction and topological quantum computing schemes [134, 135]. The latter is essential for the efficient implementation of quantum algorithms. The following chapters document progress towards these applications by implementing Rydberg-mediated interactions in the given experiment. While the experiments presented in this thesis were all conducted in a quadratic geometry, hexagonal microlens arrays are readily available and even arrays with completely arbitrary geometry can be custom-crafted, as has been reported in [142]. This gives full flexibility for the study of topological effects.

4 Spatially resolved Rydberg excitations in assembled atom arrays

In Chapter 2, the utilization of Rydberg states for the development of quantum information applications was motivated. A major part of the work documented in this thesis was the implementation of a coherent Rydberg excitation scheme into the experimental setup. While one-photon excitation to the Rydberg state has been realized in various experiments in the past years [41, 57, 105], the setup of the corresponding laser system is a cumbersome and resource-intensive task. For this reason, most of the experiments working with Rydberg atoms choose a two-photon excitation scheme with a large detuning from the intermediate state. As a frequency-doubled 960 nm laser system already existed in the experiment prior to the work conducted for this thesis, the adaptation of the scheme depicted in Fig. 2.9 (c) in the experiment was an obvious choice.

This chapter documents the implementation of spatially-resolved Rydberg excitations in an assembled atom array prepared according to the technique presented in Chapter 3, as well as an analysis of the dynamics arising from the coherent coupling to the Rydberg states.

In the first section, the theoretical background necessary to describe the coherent ground-to-Rydberg-state coupling will be discussed briefly, after which the laser system and experimental setup will be presented. Section 4.3 will then illustrate the experimental procedure for coupling the ground state to a desired Rydberg state and analyze the obtained Rabi oscillations.

4.1 Theoretical background

4.1.1 Three-Level System

In Chapter 2.1.1, the atom-light interaction in the *Dressed Atom* picture was discussed, where the atom is treated as a two-level system driven by a single-mode monochromatic light field. For a two-photon excitation scheme far-detuned from the intermediate level, the coherent drive of the transition from ground to Rydberg state can be well understood in this simplified picture. However, in order to describe effects such as electromagnetically induced transparency (EIT), as well as to fully understand the dampening that can be observed in the coherent dynamics when driving an atom to the Rydberg state via a two-photon transition, an intermediate state has to be included in the picture.

This atomic three-level system in a ladder scheme is illustrated in Fig. 4.1. It consists of a ground state $|g\rangle$, an intermediate excited state $|e\rangle$ and a Rydberg state $|r\rangle$ ¹. The transitions $|g\rangle \leftrightarrow |e\rangle$ and $|e\rangle \leftrightarrow |r\rangle$ are coupled by coherent laser fields $\mathbf{E}_{1,2}(t) = \mathbf{E}_{1,2} \cos(\omega_{1,2}t)$ ². The atom-light interaction can be described by the Hamiltonian

$$H_{\text{int}} = -\mathbf{d} \cdot (\mathbf{E}_1 + \mathbf{E}_2) , \quad (4.1)$$

¹ This nomenclature was chosen to reflect the given scenario of coupling a ground state to a Rydberg state. Other types of three-level system are of course possible, but not relevant here.

² A position dependency of \mathbf{E} is neglected here, as for the systems considered in this chapter, the spatial distribution of the atom is small compared to the intensity gradient of the laser field.

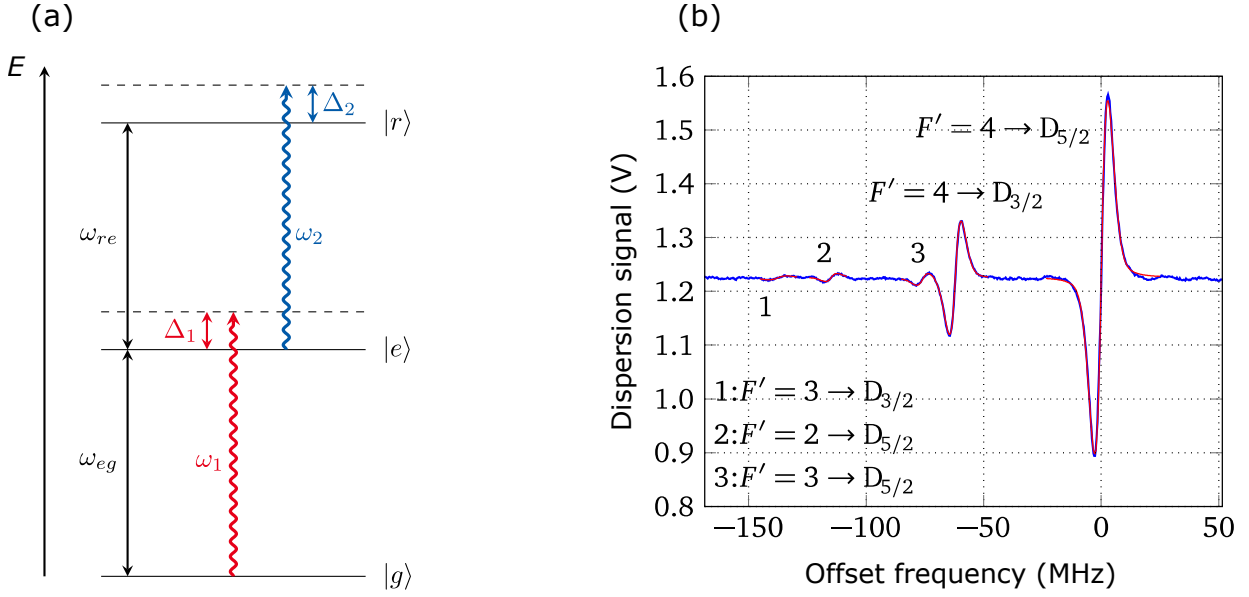


Figure 4.1.: (a) Three-level system in a ladder scheme. (b) EIT dispersion-like signal obtained by scanning the coupling laser across the $|5P_{3/2}\rangle \leftrightarrow |57D_J\rangle$ resonances, resolving the hyperfine structure of the intermediate state, as well as the fine structure of the Rydberg state. Taken from [144].

where the dipole operator can be expressed in the atomic basis as

$$\mathbf{d} = \mathbf{d}_{eg} \cdot (|e\rangle \langle g| + |g\rangle \langle e|) + \mathbf{d}_{re} \cdot (|r\rangle \langle e| + |e\rangle \langle r|) \quad (4.2)$$

with the matrix elements $\mathbf{d}_{ij} = \langle i|\mathbf{e}r|j\rangle$. Applying the dipole and rotating wave approximations³, the interaction Hamiltonian can be represented in the $\{|g\rangle, |e\rangle, |r\rangle\}$ basis as

$$H_{\text{int}} = \frac{\hbar}{2} \cdot \begin{pmatrix} 0 & \Omega_1 & 0 \\ \Omega_1 & -2\Delta_1 & \Omega_2 \\ 0 & \Omega_2 & -2(\Delta_1 - \Delta_2) \end{pmatrix}, \quad (4.3)$$

with the Rabi frequencies $\Omega_1 = -\mathbf{d}_{eg} \cdot \mathbf{E}_1/\hbar$ and $\Omega_2 = -\mathbf{d}_{re} \cdot \mathbf{E}_2/\hbar$ ⁴. The dynamics of the atomic system are thus governed by the Schrödinger equation

$$i\hbar\partial_t\psi = H\psi = (H_{\text{Atom}} + H_{\text{Int}})\psi, \quad (4.4)$$

where the state vector can be factored into external and internal components as

$$|\psi\rangle = |\psi_g\rangle |g\rangle + |\psi_e\rangle |e\rangle + |\psi_r\rangle |r\rangle. \quad (4.5)$$

Effective two-level system

Even in the absence of light, the excited states $|e\rangle$ and $|r\rangle$ couple to the vacuum mode of the radiation field, causing transitions to the ground state with rates Γ_e, Γ_r . This spontaneous emission occurs on a timescale of $\sim 1/\Gamma_i$. As only cases where $|r\rangle$ is a high- n Rydberg state shall

³ see Section 2.1.1

⁴ Compare to Eq. (2.8).

be considered here, Γ_r is typically at least three orders of magnitude smaller than Γ_e and small compared to the relevant Rabi frequencies, and will thus be neglected.

For a near-resonant two-photon drive ($\Delta_1 + \Delta_2 \ll \Delta_{1,2}$) far-detuned from the intermediate state ($\Delta_1 \approx -\Delta_2 \gg \Omega_1, \Omega_2, \Gamma_e$), one can adiabatically eliminate the excited state $|e\rangle$ from the picture. Specifically, if $1/\Gamma_e$ is fast compared to the relevant timescales governed by Ω_1 and Ω_2 , a valid approximation is that ψ_e damps to equilibrium instantaneously ($\partial_t \psi_e = 0$). Thus, the explicit dependence of ψ_e is removed from the equations of motion (Eq. (4.4)) describing ψ_g and ψ_r , and the time evolution of ground and Rydberg state is given by [64]

$$i\hbar\partial_t\psi_g = \frac{\Omega_1^2}{4\Delta}\psi_g + \frac{\Omega_1\Omega_2}{2\Delta}\psi_r \quad (4.6a)$$

$$i\hbar\partial_t\psi_r = \frac{\Omega_1\Omega_2}{2\Delta}\psi_g + \frac{\Omega_2^2}{4\Delta}\psi_r, \quad (4.6b)$$

where $\Delta = (\Delta_1 + \Delta_2)/2$. These equations are equivalent to the Schrödinger equation of a two-level system with an effective two-photon Rabi frequency

$$\Omega_{2\text{Ph}} := \frac{\Omega_1\Omega_2}{2\Delta} \quad (4.7)$$

and ac Stark shifts

$$\omega_{\text{AC},i} := \frac{\Omega_i^2}{4\Delta}. \quad (4.8)$$

With these Stark shifts and the definition $\delta_{2\text{Ph}} = \Delta_1 + \Delta_2$, the effective detuning of the light field from this two-level system is given by

$$\delta = \delta_{2\text{Ph}} - \left(\frac{\Omega_1^2}{4\Delta} - \frac{\Omega_2^2}{4\Delta} \right). \quad (4.9)$$

When working in this parameter regime, it is possible to transfer the population from the ground to the Rydberg state without significantly populating the intermediate state. Ideally, the coherence time of these dynamics would then only be limited by the decay rate Γ_r of the Rydberg state.

Electromagnetically induced transparency

Another coherent phenomenon that can be observed in a three-level system coupled by two laser fields is electromagnetically induced transparency (EIT). In the limit of a strong coupling and weak probe field ($\Omega_p := \Omega_1 \ll \Omega_2 := \Omega_c$), the atom becomes transparent for the probe light if the two-photon resonance condition is met ($\Delta_p = -\Delta_c = \Delta$).

For a comprehensive description of EIT, see [145]. A more Rydberg-specific treatment can be found in [146]. Here, only a brief discussion for the special case of a ladder system (as illustrated in Fig. 4.1 (a)) shall be given.

Diagonalizing the Hamiltonian (Eq. 4.3) for the resonance condition yields the eigenstates [145]

$$|+\rangle = \sin\theta \sin\phi |g\rangle + \cos\phi |e\rangle + \cos\theta \sin\phi |r\rangle \quad (4.10a)$$

$$|D\rangle = \cos\theta |g\rangle - \sin\theta |r\rangle \quad (4.10b)$$

$$|-\rangle = \sin\theta \cos\phi |g\rangle - \sin\phi |e\rangle + \cos\theta \cos\phi |r\rangle \quad (4.10c)$$

with mixing angles

$$\tan \theta = \frac{\Omega_p}{\Omega_c} \quad \tan 2\phi = \frac{\sqrt{\Omega_p^2 + \Omega_c^2}}{\Delta} . \quad (4.11)$$

As the state $|D\rangle$ only has contributions from the long-lived states $|g\rangle$ and $|r\rangle$, an atom prepared in $|D\rangle$ is unlikely to decay during the relevant timescales with the spontaneous emission of a photon. Hence it is called a *dark state*.

Assuming a weak-probe limit, as mentioned above, and light fields on resonance ($\Delta_p = \Delta_c = 0$), the mixing angles tend to $\theta \rightarrow 0$ and $\tan \phi \rightarrow \infty$ (or $\phi = \pi/2$). The eigenstates (Eq. 4.10) can then be expressed as

$$|+\rangle = \frac{1}{\sqrt{2}}(|r\rangle + |e\rangle) \quad (4.12a)$$

$$|D\rangle = |g\rangle \quad (4.12b)$$

$$|-\rangle = \frac{1}{\sqrt{2}}(|r\rangle - |e\rangle) . \quad (4.12c)$$

As the probe can only couple the ground state to the intermediate state, it now exhibits equal coupling amplitude from the dark state $|D\rangle$ to either of the states $|\pm\rangle$. Because of the opposite signs in the $|e\rangle$ terms, these two pathways interfere destructively, resulting in vanishing excitation and photon absorption. In other words, the atom becomes transparent for the probe light.

EIT is a powerful tool in Rydberg physics. For example, it can be used in cold atomic clouds to map the dipolar interaction between Rydberg atoms onto an optical transition, allowing the observation of a cooperative effect due to Rydberg blockade [146].

In the present experiment, a vapor cell setup for the detection of EIT signals is available and has been used in previous work to calibrate the laser system and tune it to a specific Rydberg state [144, 147]. The dispersion signal obtained from scanning the coupling laser across a Rydberg resonance is shown in Fig. 4.1 (b), where the fine structure of the Rydberg state, as well as the hyperfine structure of the intermediate state is resolved (taken from [144]). The inclusion of a highly stable reference cavity and subsequent calibration with a high-resolution wavemeter, as discussed in Section 4.2.1, removed the need for calibration with the EIT signal. As a tool for quick double-checking of the calibration, especially when switching to a largely different Rydberg state, it will however still be practical to have it available in the future.

4.1.2 Transition strengths and Rabi frequencies in Rb atoms

In order to accurately calculate the Rabi frequencies when coupling the atoms with the Rydberg laser fields in the experiment, the fine and hyperfine structure of the respective states have to be taken into account. The main interaction between different internal states is the dipole interaction, and as seen before, the Rabi frequency of a transition between an initial state $|i\rangle$ and a final state $|f\rangle$ is proportional to the dipole matrix element corresponding to this interaction

$$\Omega_{i \leftrightarrow f} = -\frac{\langle f | \mathbf{d} \cdot \epsilon E_0 | i \rangle}{\hbar} , \quad (4.13)$$

with the unit vector of polarization ϵ . The dipole matrix element between two internal states depends on the overlap of the wavefunctions of the two states, which intuitively explains why

the coupling from the ground state to a Rydberg state decreases with growing n , as the overlap of their wavefunctions gets smaller and smaller. Calculating the dipole matrix element is a nontrivial task, which however can be simplified by making use of rotational symmetries in the system. A comprehensive treatise on this subject can be found in [148]. Here, only the results of these derivations will be summarized. Transforming into a spherical basis exploits the rotational symmetry of the problem and the Rabi frequency between the states $|i\rangle = |n j m\rangle$ and $|f\rangle = |n' j' m'\rangle$ is given by

$$\Omega_{i \leftrightarrow f} = \frac{eE_0}{\hbar} \sum_{q=-1}^1 \epsilon^q \langle n' j' m' | \hat{r} C_q^1 | n j m \rangle \quad (4.14)$$

with spherical components $\epsilon^{q \in \{-1, 0, 1\}}$ of the polarization vector, the spherical tensor components C_q^1 and the position operator \hat{r} . The Wigner-Eckart theorem allows to split the matrix element into a factor containing the angular dependencies and a reduced radial part:

$$\langle n' j' m' | \hat{r} C_q^1 | n j m \rangle = \underbrace{(-1)^{j'-m'} \begin{pmatrix} j' & 1 & j \\ -m' & q & m \end{pmatrix}}_{\text{angular}} \underbrace{\langle n' j' || \hat{r} \mathbf{C}^{(1)} || n j \rangle}_{\text{radial}} \quad (4.15)$$

with the irreducible first order tensor $\mathbf{C}^{(1)}$. The angular part only contains a Wigner 3-j symbol constituting geometric consideration arising from the conservation of angular momentum, whereas the radial part describes the interaction between the states. It can be further broken down to the calculation of the radial integral

$$\mathcal{R}_{n'l'}^{nl} = \int R_{n'l'}^* r R_{nl} r^2 dr \quad (4.16)$$

with the radial wavefunctions $R_{nl}(r)$, which can be done numerically with the help of the Numerov algorithm. A Python implementation of this algorithm was developed in the group of Charles Adams [103]. This package, called *Alkali-Rydberg-Calculator* (ARC), provides methods to solve the radial Schrödinger equation and calculate the above matrix elements, as well as related properties, such as Rabi frequencies, transition probabilities, lifetimes, and simple interaction energies⁵. Throughout this thesis, this package was used to calculate these properties and make predictions for the experimental conditions. To calculate the expected Rabi frequencies, the experimental parameters of the laser field have to be included in Eq. (4.14) via the electric field amplitude

$$E_0 = \sqrt{\frac{4P}{\pi \epsilon_0 c w^2}} \quad , \quad (4.17)$$

where P denotes the total power of the beam and w the $1/e^2$ beam radius at the position of the atoms. These can be measured or approximated experimentally.

4.2 The Rydberg laser system

The current Rydberg laser setup consists of an interference-filter-stabilized ECDL at 780 nm and a frequency-doubled *Toptica TA-SHG 110* system with a fundamental wavelength of 960 nm. The

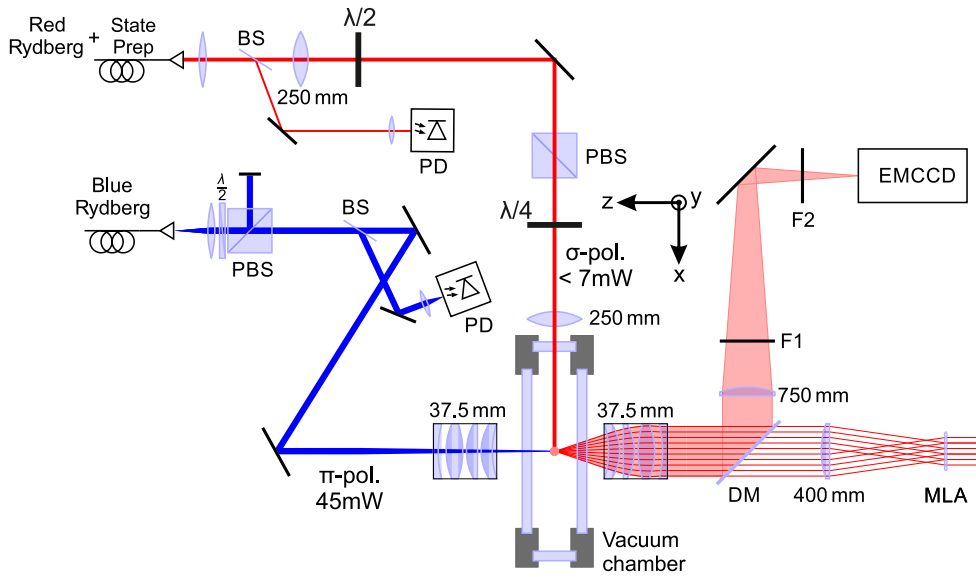


Figure 4.2.: Simplified schematic of the Rydberg beam paths into the vacuum chamber. The red Rydberg laser beam at 780 nm is superposed with the state preparation beam before the optical fiber with perpendicular polarizations, such that their relative intensities can be tuned with the half-wave plate ($\lambda/2$) and the polarizing beam splitter (PBS). Afterwards, they are both circularly polarized (σ^-) with a quarter-wave plate ($\lambda/4$) and have a collimated $1/e^2$ -radius of $550(50) \mu\text{m}$, with the red Rydberg beam having a power of up to $\sim 7 \text{ mW}$ at the position of the atoms. The 480 nm blue Rydberg beam is linearly polarized, illuminating the atoms with $\sim 45 \text{ mW}$ of optical power over a beam waist of $w_b \simeq 19 \mu\text{m}$. Beam samplers (BS) are used to direct a small portion of the power of each beam onto a photodiode (PD) for intensity stabilization. Beam paths are not drawn to scale.

light from the grating-stabilized ECDL passes a tapered amplifier and is subsequently frequency-doubled to 480 nm in an external doubling cavity. Figure 4.2 shows a top-down view of the Rydberg laser beam paths on the experiment table. The beams are polarized such that they excite the atoms to a Rydberg state via a $\sigma-\pi$ scheme. This is not the ideal scheme for achieving maximal coupling strength, as it does not allow to couple with the stretched $|nD_{5/2}, m_J = -5/2\rangle$ state. However, driving a $\sigma-\sigma$ -scheme necessary for the stretched transition would require the beams to be co- or counterpropagating, which is difficult to implement in the current optical setup. An advantage of a σ -coupling to the intermediate state is the fact that spontaneous decay can only occur back to the initially prepared ground state, and not to other hyperfine states. The red Rydberg laser beam has a power of up to 7 mW and the blue laser beam has maximum value of 45 mW, which is typically kept constant. Both are measured before entering the vacuum chamber, with the values given here corrected for transmission losses on the windows, so they correspond to the expected values at the position of the atoms. Please note that these values are not given with an uncertainty here, as they are difficult to quantify in a general manner. Estimated shot-to-shot fluctuations are on the order of 5% for the blue laser beam and 2% for the red one. The effect of this fluctuation is analyzed in Chapter 5.

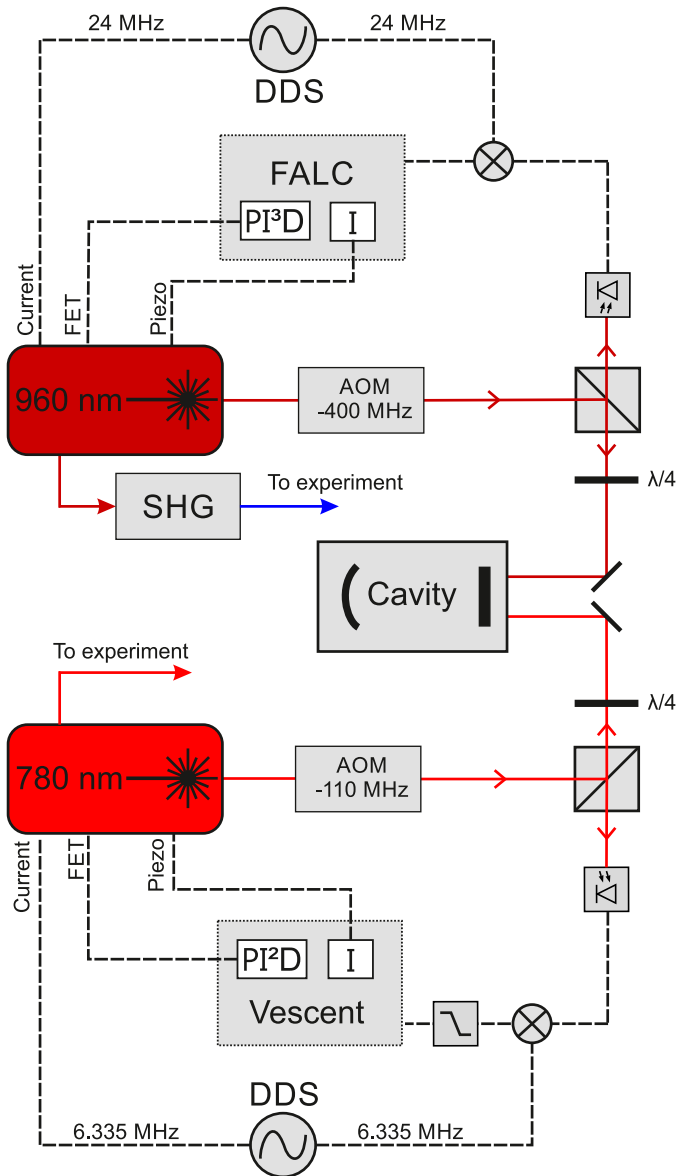


Figure 4.3: Simplified schematic of the Pound-Drever-Hall lock of the Rydberg lasers onto the ultra-stable reference cavity. The frequency generated by a local oscillator is used to modulate the laser current and is mixed with the signal obtained by a fast photodiode monitoring the light reflected on the cavity mirror, thus generating the error signal used for frequency stabilization. The latter is implemented in a slow feedback loop acting on the piezoelectric element controlling the resonator length of the laser and in a fast loop acting on the diode current via a FET circuit. AOMs are used to offset the laser frequency with regard to the cavity modes.

4.2.1 High-finesse cavity for frequency stabilization

During this thesis, the Rydberg laser system was modified to enable locking onto a new ultra-stable reference cavity (*SLS VH-6020-4*). Previously, both lasers have been locked onto a transfer cavity, which was itself indirectly locked onto a Rubidium spectroscopy (see [144, 147]). This allowed for large frequency scans well suited for applications such as the spectroscopy of highly charged ions and the cartography of molecular tellurium resonances in vapor cells [147]. Preliminary results could be achieved with this cavity, such as a first verification of a two-photon Rydberg excitation of atoms in the dipole trap array [83, 144]. For the observation of coherent dynamics, however, the finesse of the transfer cavity ($\mathcal{F} = 55$) proved insufficient, as it only allowed for laser linewidths orders of magnitude larger than the natural linewidth of Rydberg states. The new reference cavity was included to overcome this limitation. It is custom-coated to achieve a finesse above 10000 for wavelength windows around 420 nm, 480 nm, 780 nm,

⁵ For a detailed documentation, see: <https://arc-alkali-rydberg-calculator.readthedocs.io>

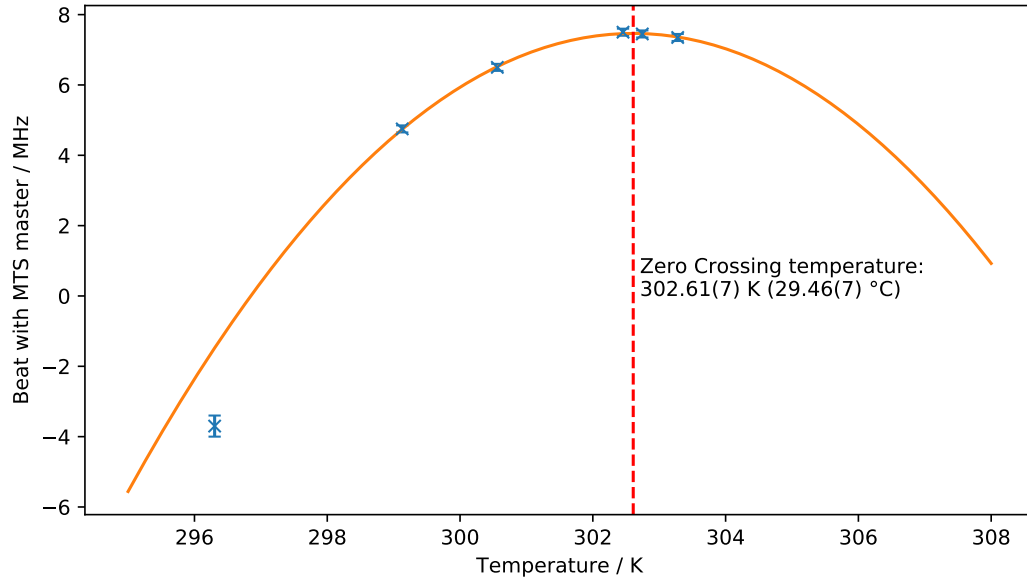


Figure 4.4.: Measurement of the zero crossing temperature of the reference cavity.

960 nm, 1015 nm and 1188 nm ($4 \cdot 297$ nm), which correspond to different Rydberg excitation schemes (see Fig. 2.9). The lasers are locked onto the cavity using the Pound-Drever-Hall (PDH) technique [149, 150]. The sidebands required for this method are created by modulating the diode current of the lasers. The frequency stabilization consists of a fast feedback loop controlling the diode current and a slow loop to compensate for drifts controlling the resonator length of the diode lasers with a piezo-electric actuator. Figure 4.3 shows a schematic illustration of this locking scheme. In the case of the blue Rydberg laser, a second PDH loop locks the frequency doubling cavity onto the laser to ensure maximum doubling efficiency (not drawn). The cavity finesse for 780 nm and 960 nm was determined experimentally with a ring-down measurement to be $\mathcal{F}_{780} = 31500(100)$ and $\mathcal{F}_{960} = 46700(120)$, given a measured free spectral range of $\text{FSR} = 1496.923(2)$ MHz. With the relation

$$\mathcal{F}_\lambda = \frac{\text{FSR}}{\Delta \nu_\lambda}, \quad (4.18)$$

the full width at half maximum (FWHM) linewidths of the cavity fringes evaluate to $\Delta \nu_{780} = 47.6(4)$ kHz and $\Delta \nu_{960} = 32.1(1)$ kHz. Knowing the cavity linewidths and analyzing the transmission signal when locking the lasers to the cavity, an upper bound on the laser linewidths can be estimated. Thus, a linewidth of < 11 kHz for the 780 nm laser and < 4.5 kHz for the 960 nm laser (< 9 kHz for 480 nm) on a timescale of milliseconds was obtained.

Temperature drift of the cavity

To minimize temperature effects, the cavity is housed in a vacuum chamber with a pressure of $4(1) \times 10^{-5}$ mbar. This decouples the cavity from fast temperature fluctuations in the laboratory, as the thermalization rate with the environment is on the order of days. Long-term drifts of the temperature regulation, however, can still cause an expansion or contraction of the cavity, and thus a drift in absolute frequency of the locked lasers. To keep this drift as low as possible, the

cavity is designed so that its coefficient of thermal expansion has a zero-crossing at a certain temperature. A respective temperature somewhere between 25 and 50°C is specified by the manufacturer. In order to find this working point and characterize the frequency drifts associated with residual expansion, a series of measurements was performed, as shown in Fig. 4.4. For each data point, the controller regulating the temperature of the cavity housing was set to a new value, and the beat frequency of the 780 nm Rydberg laser locked on the cavity with a spectroscopy master was measured after a settling time of at least two days, to ensure a complete thermalization. Thus, the zero crossing temperature was measured to be 302.61(7) K. Around this point, a temperature drift of (1 K, 0.1 K) would result in a shift of the cavity resonance of (~ 220 kHz, ~ 2 kHz). As the fluctuations of the temperature with the current controller are estimated to be significantly less than 0.1 K, this renders the residual frequency drift from this source negligible, especially considering a resonance drift of up to 50 kHz per day due to relaxation of the spacer material, as specified by the manufacturer.

4.3 Coherent ground-to-Rydberg-state dynamics

4.3.1 Ground state preparation

In order to excite the atom into the selected Rydberg state with high efficiency, it has to be prepared in a well-defined ground state. The $\sigma^- - \pi$ scheme used for Rydberg state excitation for all measurements presented in this thesis is illustrated in Fig. 4.5. To ensure a well-defined quantization axis, a $|\mathbf{B}| = 2.748(3)$ G magnetic field is applied along the x-axis, which lifts the degeneracy of the Zeeman sublevels m_F, m'_F of the hyperfine structure of ground and intermediate state, as well as the fine structure sublevels m''_J of the Rydberg state⁶. Maximal coupling, and thus a maximal Rabi frequency, for the given beam polarization is then achieved for the transition $|g\rangle = |5S_{1/2}, F = 3, m_F = -3\rangle \rightarrow |e\rangle = |5P_{3/2}, F' = 4, m'_F = -4 \hat{=} m'_J = -3/2\rangle \rightarrow |r\rangle = |nD_{5/2}, m''_J = -3/2\rangle$. The atoms thus have to be prepared in the $|F = 3, m_F = 3, m_F = -3\rangle$ ground state, which is accomplished by a σ^- -polarized laser beam near-resonant to the $|5S_{1/2}, F = 3\rangle \leftrightarrow |5P_{3/2}, F' = 3\rangle$ transition in conjunction with weak MOT repumping light. This ensures that the atomic population is optically pumped to the desired state and gets trapped in it, as there is no coupling to any other states via these two laser fields. As shown in Fig. 4.2, the state preparation beam is superimposed with the red Rydberg laser beam before being coupled into the fiber going to the experiment, matching pointing and polarization of these two beams and facilitating the alignment of the red Rydberg beam on the atoms.

4.3.2 Coherent two-photon excitation to Rydberg states

The coupling to a Rydberg state via the two-photon transition can be described with an effective two-level system introduced in Section 4.1.1, with

$$\Omega_{\text{eff}} = \frac{\Omega_R \Omega_B}{2\Delta}, \quad \delta = \delta_{2\text{ph}} - \left(\frac{\Omega_R^2}{4\Delta} - \frac{\Omega_B^2}{4\Delta} \right) \quad (4.19)$$

denoting the effective Rabi frequency and detuning of the coupling, the latter being modified by the AC Stark shift caused by the laser beams. Ω_R and Ω_B represent the single-photon Rabi fre-

⁶ The large orbital radius of a Rydberg electron leads to a very weak coupling of its total orbital angular momentum \mathbf{J} with the nuclear spin \mathbf{I} , which is why the hyperfine structure of a Rydberg state is not resolvable with typical laser linewidths. For this reason, the Rydberg state manifold is expressed in the fine structure basis.

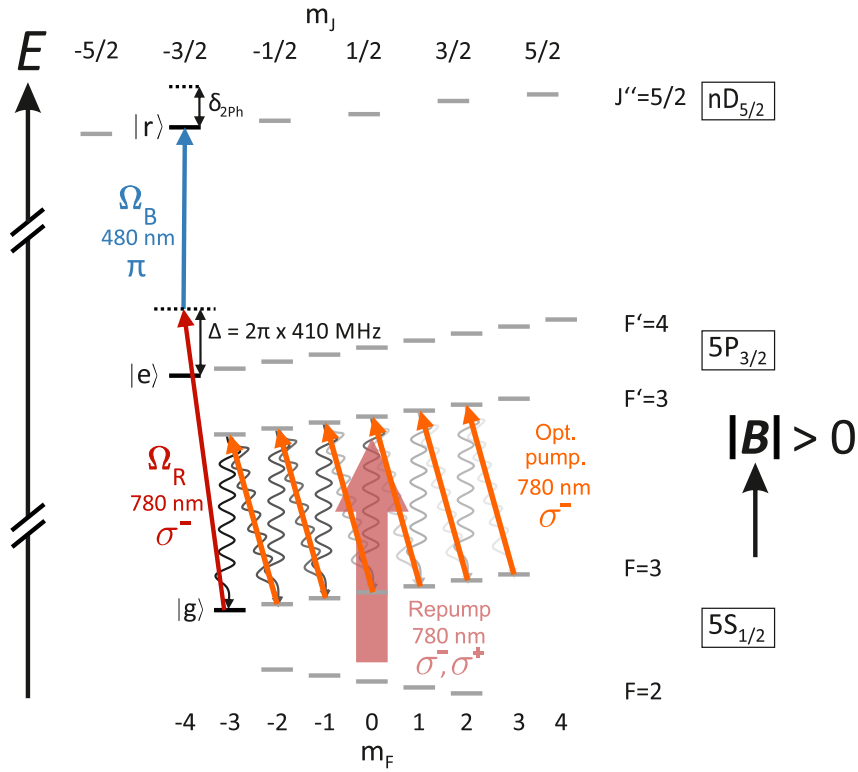


Figure 4.5.: Level scheme for ground state preparation and Rydberg state excitation. Applying an external magnetic field B lifts the degeneracy of the hyperfine manifold, shifting the Zeeman levels in energy. The $\sigma^- - \pi$ -polarized optical pumping field (orange arrows) and the repumping light having both circular polarizations (pink arrow) cause a passage of the Zeeman population in the direction of negative m_F states. Atoms decaying into either of the ground states are kept in this cycle until they decay into the $|F = 3, m_F = -3\rangle$ state, which corresponds to a dark state in this scheme. This is indicated by the grey arrows (decay channels to the $F = 2$ ground state are not drawn for the sake of clarity). Once an atom is prepared in this ground state $|g\rangle$, it is excited into an $nD_{5/2}$ Rydberg state via the depicted two-photon transition. As F is not a good quantum number for a Rydberg state, a switch to the J basis is made.

quencies of the red and blue laser fields, respectively. These quantities are illustrated in Fig. 4.5. The scattering rate due to spontaneous emission from $|e\rangle$ is given by

$$\Gamma_{\text{sc},|e\rangle} = \Gamma_e \cdot \frac{\Omega_R^2 + \Omega_B^2}{4\Delta^2}, \quad (4.20)$$

with $\Gamma_e = 6.07\text{MHz}$ being the radiative decay rate of $|e\rangle$. Ideally, one would choose Δ to be as large as possible to minimize scattering on the intermediate state, but it has to be kept in mind that larger detuning also reduces the available effective Rabi frequency. This can be compensated by increasing the laser power, which is possible for the red laser. For the blue Rydberg laser, however, the coupling between the intermediate and Rydberg states is so low that all available laser power is applied typically. Only increasing Ω_R also leads to increased scattering, as is evident from the quadratic scaling in Eq. (4.20). Lacking a more powerful blue laser, this means that a compromise has to be found between Rabi frequency and scattering. The latter results in an expected damping of the Rabi oscillation amplitude, as the assumption of the far-detuned

two-level system is not completely valid. Within this chapter, all observed damping effects will be taken into account by introducing a phenomenological damping rate γ , while in Chapter 5 a more thorough analysis of the underlying mechanisms will be provided.

Typical experimental parameters

The detuning Δ from the intermediate state was chosen to be positive to minimize scattering on lower lying hyperfine states. The light from the red Rydberg laser is shifted via AOMs by a fixed value of 410 MHz with regard to the cavity resonance, yielding a frequency of $\nu_{780} = 3.842\,296\,50(10) \times 10^{14}$ Hz⁷ for the light going to the experiment. This corresponds to a blue detuning of $\Delta = 410(10)$ MHz with regard to the $|5S_{1/2}, F = 3\rangle \leftrightarrow |5P_{3/2}, F' = 4\rangle$ transition⁸. Given a beam waist of $w_{0,R} = 550(50)$ μm and using Eqs. (4.13) and (4.17), this results in a calculated Rabi frequency of

$$\frac{\Omega_R}{2\pi} = \frac{|\langle g|\mathbf{d} \cdot \boldsymbol{\epsilon}|e\rangle|}{\hbar} \cdot \sqrt{\frac{4P_R}{\pi\epsilon_0 c w_{0,R}^2}} \simeq 48(5) \sqrt{\frac{P_R}{1 \text{ mW}}} \text{ MHz} , \quad (4.21)$$

where the dipole moment $\langle g|\mathbf{d} \cdot \boldsymbol{\epsilon}|e\rangle \simeq 2.99ea_0$ for the cycling transition driven with σ -polarized light is taken from [101]. For the measurements presented in this work, the power of the red Rydberg beam, measured before the vacuum window, was varied between 175 μW and 760 μW . Analogously, the Rabi frequency of the blue laser field is given by

$$\frac{\Omega_B}{2\pi} = \frac{|\langle e|\mathbf{d} \cdot \boldsymbol{\epsilon}|r\rangle|}{\hbar} \cdot \sqrt{\frac{4P_B}{\pi\epsilon_0 c w_{0,B}^2}} \simeq 3.6(7) \left(\frac{57 - 1.35}{n^*}\right)^{3/2} \sqrt{\frac{P_B}{1 \text{ mW}}} \text{ MHz} , \quad (4.22)$$

for a waist of $w_{0,B} = 20(5)$ μm . Here, the quantum defect $\delta_{57,2,5/2} \simeq 1.35$ and the dipole element $\langle e|\mathbf{d} \cdot \boldsymbol{\epsilon}|57D_{5/2}, m_J'' = -3/2\rangle \simeq 0.0081ea_0$ for a π transition were calculated with the ARC library and the known scaling with effective principal quantum number $n^* = n - \delta_{nlj}$ allows to extrapolate to different Rydberg states (see Table (2.2)). For the maximally available beam power of $P_B = 45$ mW at the position of the atoms, the blue Rabi frequency evaluates to $\Omega_B = 2\pi \times 24(5)$ MHz.

Although the frequency of the red Rydberg laser can be tuned dynamically with the AOM in a double-pass configuration, it was kept constant for all measurements presented here. Frequency tuning of δ is done with the double-pass AOM in the 960 nm beam path to the stabilization cavity, as the subsequent frequency doubling allows for larger frequency ranges. For a given shift in AOM frequency $\Delta\nu_{\text{AOM}}$, the shift in detuning is given by

$$\Delta\delta = 2\Delta\nu_{\text{AOM}} \frac{\nu_{480\text{nm}}}{\nu_{960\text{nm}}} = 4\Delta\nu_{\text{AOM}} . \quad (4.23)$$

As the AOM has an approximately uniform diffraction efficiency for a tuning range of ~ 20 MHz, this allows for a variation in two-photon detuning of 80 MHz⁹.

⁷ A frequency of $3.842\,296\,48(2) \times 10^{14}$ Hz was measured with a *High Finesse WS02* wavemeter for a different temperature setpoint of the cavity. Comparing the respective beats with the MTS master allows to calculate the current frequency based on this reference measurement. Since the setpoint was varied slightly for different measurements presented in this thesis, an uncertainty of 10 MHz is assumed to cover this range of frequencies.

⁸ The fact that the cavity resonance exactly matches the frequency of this transition is purely coincidental.

⁹ Larger ranges are possible, but the associated drop in diffraction efficiency modifies the error signal of the cavity lock and can thus hamper frequency stability, which is why this is typically avoided. However, for auxiliary measurements and searching for resonances, larger ranges are routinely utilized.

Since the FSR of the stabilization cavity is known to an accuracy of 2 kHz and the absolute frequency was measured for one of the fringes with a single MHz accuracy (by measuring the frequency of the 960 nm laser with a high-precision wavemeter), the position of any cavity fringe within ~ 500 FSRs can be estimated with a MHz accuracy, which corresponds to a frequency range of ± 750 GHz. For comparison, the transition frequency between the $57D_{5/2}$ state and the $87D_{5/2}$ state is only 614 GHz, equivalent to 307 GHz for the undoubled 960 nm light. Thus, the sum frequency of the two Rydberg lasers required for exciting an atom into any desired Rydberg state can be predicted to an accuracy far below the available scan range.

Alignment of the Rydberg beams

The red Rydberg beam is superposed with the laser beam used for optical pumping before the respective transfer fiber, thus exactly matching size and alignment of the two beams. Since the pumping laser is near-resonant to the $|5S_{1/2}, F = 3\rangle \leftrightarrow |5P_{3/2}, F' = 3\rangle$ transition, alignment on the atom array can be done with a "blow-away" measurement. In this scheme, the atoms are removed from the traps via radiation pressure with an efficiency depending on the intensity of the light and, thus, beam alignment. As more than 100 atoms are typically loaded into the array, this procedure yields enough resolution to give immediate feedback after a single shot, making the beam alignment simple.

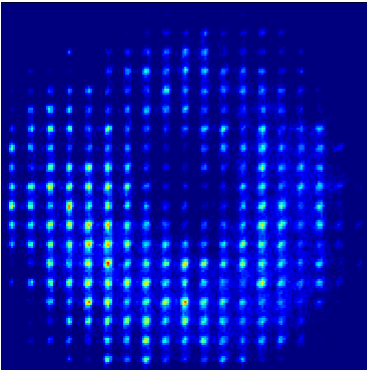


Figure 4.6.: Illustration of the alignment of the blue beam.

Alignment of the blue Rydberg beam is not as straight-forward, as it is not superposed on any resonant laser beam. The position of the beam can be obtained via the distribution of Rabi frequencies during a coherent two-photon drive, but as such a measurement takes several hours, it is unfeasible to use for alignment.

Since the double-pass AOM in the 960 nm beam allows for flexibility in the laser frequency, however, one can search for a Rydberg state $|nL_J\rangle$, where the combination of an appropriate cavity fringe and AOM frequencies yield a situation where the blue laser is resonant to the $|5P_{3/2}, F' = 4\rangle \leftrightarrow |nL_J\rangle$ transition. If such a state is found, an illumination of the atoms with the blue laser beam and the MOT cooling beams causes significant atom loss over the area of the blue beam¹⁰, allowing for an alignment procedure similar to the red beam. Since the cavity fringes are known and the Rydberg transition frequencies can be calculated,

a simple algorithm can be used to find an appropriate state. Ideally, this state should be as near as possible to the target state for coherent excitation, so that adjusting the driving current of the laser diode is sufficient to reach it without having to manually tune the grating of the 960 nm master laser.

In the case of the $|57D_{5/2}\rangle$ state, there is such a state nearby, namely the $|56D_{3/2}\rangle$ state. Tuning the laser current and changing the frequency of the double-pass AOM by ~ 20 MHz constitutes a quick way to tune the laser to a resonance for an alignment on the atoms. Figure 4.6 shows an averaged fluorescence image obtained after performing this alignment procedure. The blue laser beam "shoots a hole" into the $7\ \mu\text{m}$ pitch array, illustrating the relative size of array and laser spot. It is typically aligned such that the center of the beam approximately corresponds to the central trap of the array.

¹⁰ This likely stems from a combination of radiation pressure, heating and anti-trapping of the Rydberg state by the dipole trap.

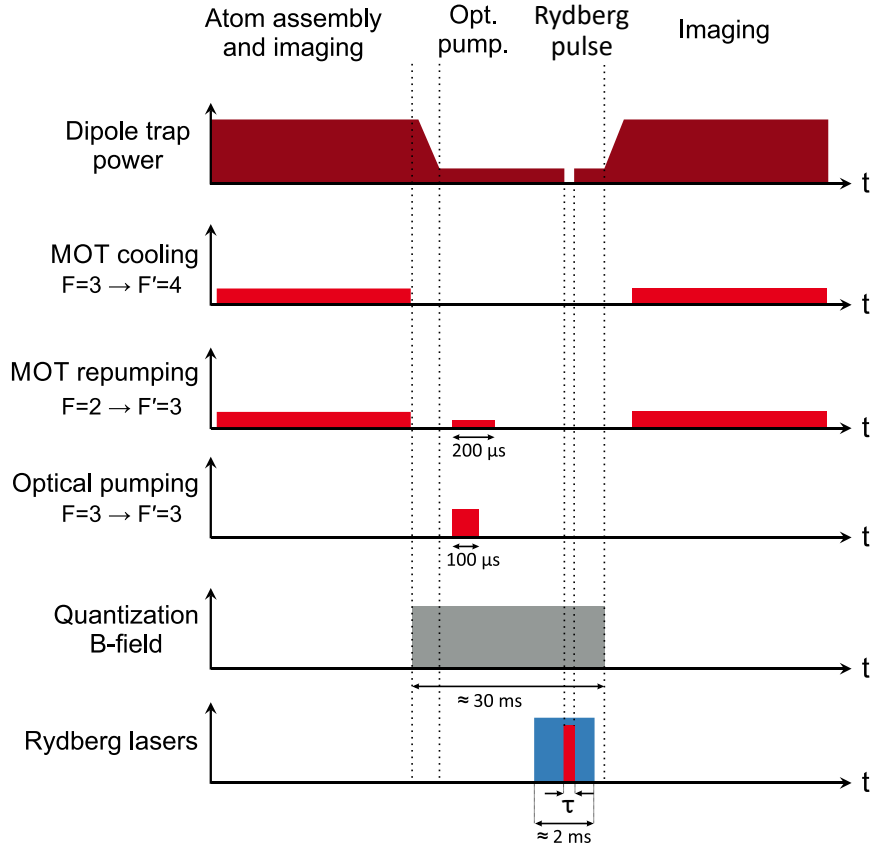


Figure 4.7.: Experimental sequence of a Rydberg excitation measurement.

Experimental sequence

All Rydberg experiments performed in this thesis excite the atoms into the Rydberg state by suddenly switching on both coupling fields¹¹. The Rydberg state used for all measurements presented in this chapter is the $|57D_{5/2}\rangle$ state. A typical experimental sequence is shown in Fig. 4.7, starting with the imaging phase following the assembly of a target structure (typically consisting of multiple rearrangement cycles). The trap occupation obtained from this image serves as a reference to determine atom loss after a Rydberg excitation. After taking this initial image, the magnetic quantization field is switched on and the atoms are optically pumped into the desired Zeeman sublevel. Directly afterwards, an excitation to the Rydberg state is performed by switching on the Rydberg beams, with the blue beam being turned on significantly longer (~ 2 ms) than the red beam ($\sim \mu$ s) due to the lack of a fast switching method for the blue laser. The red Rydberg beam is pulsed with an AOM with switching times of 50 ns to 100 ns. The pulse duration of the red laser thus defines the length of the coupling to the Rydberg state, during which the traps are switched off to avoid having to account for the inhomogeneous AC Stark shift caused by the trapping laser field, ensuring the same Rydberg resonance for all atoms¹². During the optical pumping and Rydberg phase, the trap depth is ramped down by a factor of

¹¹ Another way to prepare a desired Rydberg state is to apply adiabatic sweeps of the laser frequency and intensity, as utilized in STIRAP schemes [151].

¹² According to Eq. (4.19), the lightshifts caused by the Rydberg laser fields themselves still have to be taken into account, especially considering the strong spatial dependence of the blue Rabi frequency. As the magnitude of these shifts is typically smaller than the linewidth of the transition, they are accounted for by slightly tuning the laser frequency.

five. This adiabatically cools the atoms and increases the recapture probability after switching the trap off and on.

Finally, the trap depth is ramped up again and an image is taken to assess the remaining trap occupations.

Rydberg state detection

The detection of Rydberg excitation relies on the loss of excited atoms due to the fact that the dipole trap does not represent an attractive potential for the Rydberg state, causing the atom to drift out of the trap volume. In fact, the Rydberg state does experience an anti-trapping effect due to a positive lightshift and a ponderomotive potential [152], which further accelerates the expulsion. Within the lifetime of the Rydberg state, the atom thus moves far enough to not be recaptured by the trap most of the time. This leads to the signals shown in Fig. 4.8 (a,b), obtained by varying the Rydberg pulse duration τ or the two-photon detuning δ , respectively.

Other possible detection schemes, such as ionization of Rydberg atoms by a laser pulse or an electric field and subsequent detection of the free electrons via microchannel plates have been reported [87, 153]. This is, however, extremely challenging to implement in a single-site selective fashion and not feasible for the given experiment. When exciting atoms to different Rydberg states (in order to observe spin exchange dynamics, for example), the detection method may need to differentiate between the two states, which can be accomplished by coupling one of the states back to a ground state, which is then detected [109]. Such a positive Rydberg state detection can also be performed in the present experiment, with a resonant pushout beam removing all ground state atoms in between two Rydberg π pulses. For all measurements presented in this thesis, however, the atom loss scheme was used because of its efficiency and simplicity.

Repeating a measurement a large number of times and counting the events where the atom was lost versus when it was recaptured, one can extract the probability P_{recap} of recapture. From this quantity the probability of excitation into the Rydberg state can be inferred via $P_r = 1 - P_{\text{recap}}$. Note that this does not take into account detection errors such as false positives (a ground state atom was lost) and false negatives (the Rydberg atom decayed back to the ground state before moving out of the trap, thus being recaptured). The influence of these errors will be analyzed thoroughly in Chapter 5 and shall be ignored at this stage.

Spectroscopy of the Rydberg state

In order to perform a measurement probing the coherent dynamics between ground and Rydberg state, it is essential to know the exact resonance frequency of the transition. For this reason, the first measurement is typically a spectroscopic measurement of the Rydberg line: For a fixed pulse length (typically a value close to a π pulse length is chosen to maximize the excitation probability), the recapture probability of the atom is measured as a function of the two-photon laser detuning δ . Such a measurement for a single atom is shown in Fig. 4.8 (a). The finite length of the Rydberg pulse causes the observed signal to be broadened, as the Fourier width of the pulse is larger than the linewidth of the transition (~ 10 kHz)¹³. This results in a pulse shape described by a squared spherical Bessel function:

$$P_r(\delta) = A \cdot \frac{\Omega^2}{\Omega^2 + \delta^2} \sin\left(\sqrt{\Omega^2 + \delta^2} \cdot \frac{\tau}{2}\right) + B, \quad (4.24)$$

¹³ This also means that the laser linewidth can be significantly larger than the linewidth of the transition while still achieving maximum coupling.

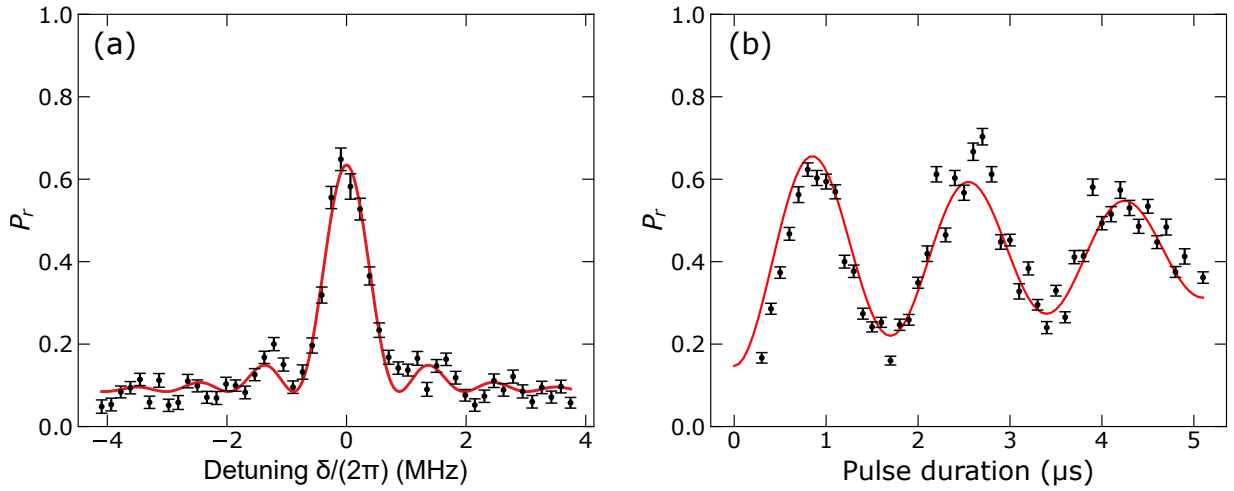


Figure 4.8.: Coherent excitation dynamics of a single atom. (a) Spectroscopy on the $|57D_{5/2}\rangle$ state. Excitation of the atom is detected via a dip in recapture probability $P_{\text{recap}} = 1 - P_r$ after the Rydberg pulse and inverting the retention signal yields the excitation probability P_r . Variation of laser detuning δ reveals a spectral shape limited by the Fourier width of the pulse. The red solid line is a fit of the formula in Eq. (4.24) to the data used to obtain the exact position of the resonance peak. (b) Rabi oscillations on resonance obtained by varying the Rydberg pulse duration τ . The red solid line is a fit to Eq. (4.25), yielding an effective Rabi frequency of $\Omega = 2\pi \times 0.59(1)$ MHz. Each data point is based on an average number of 70 experimental realizations where an atom was initially present, with error bars corresponding to a statistical uncertainty.

where τ is a parameter corresponding to the pulse duration and A, B are fit parameters used to account for a reduced amplitude and an offset caused by baseline atom loss. The red solid line in Fig. 4.8 (a) corresponds to a fit of this function to the data. The value $\tau = 0.97(3)$ μs obtained by setting it as a free parameter for the fit matches well the length of the Rydberg pulse for this measurement ($t = 1$ μs). The Rabi frequency obtained from the fit is $\Omega = 2\pi \times 0.56(5)$ MHz.

Rabi oscillations

After the resonance frequency is determined, setting the detuning to $\delta = 0$ and varying the duration τ of the Rydberg pulse causes the system to coherently oscillate between the ground and Rydberg state, an effect called Rabi oscillation. The result of such a measurement is shown in Fig. 4.8 (b). The rate with which the amplitude of the oscillation decays is a measure of the system's coherence time. As discussed at the beginning of this section, a noticeable damping is expected due to the relatively small detuning from the intermediate state. Solving the optical Bloch equations for the effective two-level system, with the spontaneous emission from the excited state introduced by the quantity γ , results in a damped oscillation [154]

$$P_r(t) = \frac{\Omega^2}{\gamma^2 + 2\Omega^2} \left[1 - \left(\cos(\tilde{\Omega}t) + \frac{3\gamma}{4\tilde{\Omega}} \sin(\tilde{\Omega}t) \right) e^{-\frac{3\gamma t}{4}} \right], \quad (4.25)$$

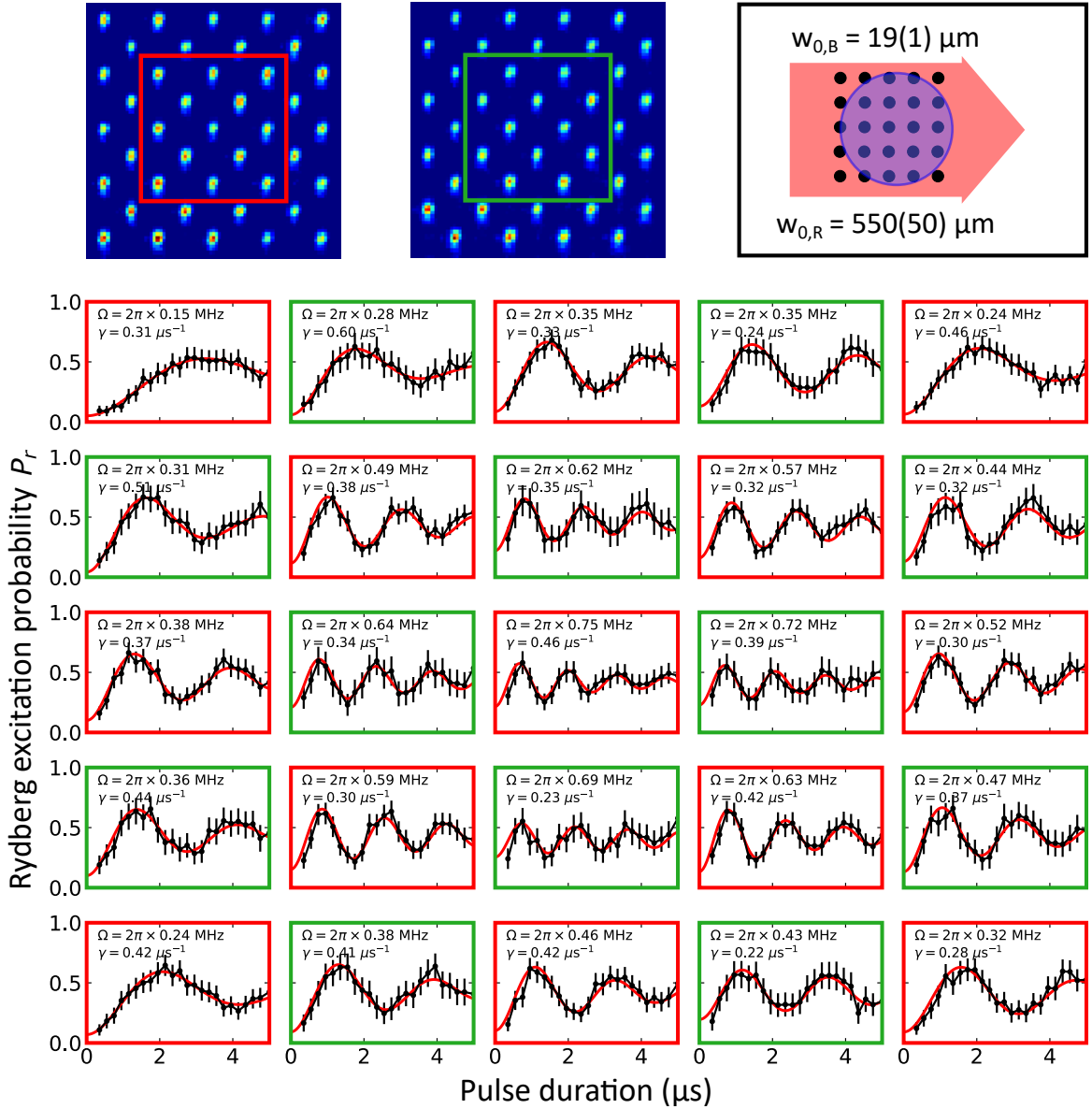


Figure 4.9.: Simultaneous Rabi oscillations in a $d = 7 \mu\text{m}$ pitch array. (Top) In two separate measurements, the atoms are prepared in a checkerboard pattern to avoid nearest-neighbor interactions when excited to the Rydberg state, which would quickly dephase the oscillations. As the patterns in the two measurements are inverted, the data can then be combined for analysis. The red and green frames distinguish the data obtained from the two measurements. (Bottom) For each trap in the 5×5 squares marked above, the function in Eq. (4.25) was fit to the data and fit parameters Ω and γ are given. Error bars correspond to statistical uncertainties.

with $\tilde{\Omega} = \sqrt{\Omega^2 + \gamma^2/16}$ corresponding to an effective Rabi frequency modified by the damping constant γ . Note that this is a simplified picture, treating the decay from the intermediate state in the same way as decay from the excited state in a two-level system¹⁴. As $\Gamma_e \gg \Gamma_r$, this is a useful empirical approximation to qualitatively describe the dynamics and obtain appropriate quantitative estimates of the relevant parameters.

Fitting this function to the data (red solid line in Fig. 4.8 (b)) yields a Rabi frequency of $\Omega = 2\pi \times 0.59(1)$ MHz, in excellent agreement with the value obtained from the resonance scan.

It should be noted that the array site that was evaluated for this analysis does not correspond to the site with maximum Rydberg beam intensity. An analysis of the distribution of Rabi frequencies across the array as well as a comparison with ab initio calculations will be given in the next subsection.

4.3.3 Parallel Rydberg excitation of an array of atoms

Having implemented an effective way of extracting information about the coupling of an atom to a Rydberg state from the analysis of the Rabi dynamics, the next step is to use this method to study the simultaneous coupling of multiple atoms within the beam radius of the Rydberg lasers. For this purpose, the 110 μm pitch MLA (ML1) is replaced with a 75 μm pitch MLA (ML2, see Table 2.1.2), yielding a pitch of $d = 7.0(2)$ μm for the dipole trap array. This increases the number of atoms coupling to the Rydberg fields. However, it also increases the van der Waals interaction between neighboring Rydberg atoms by an amount where it becomes detectable and leads to a quick dephasing if multiple neighboring traps are occupied. The resulting interaction physics will be the subject of Chapter 6. Here, the influence of this interaction is largely suppressed by only filling the traps in an alternating fashion. The atom assembly scheme introduced in Chapter 3 is utilized to prepare a 5×5 checkerboard of atoms with near-unity filling fraction, after which the Rydberg beams are switched on for a variable time. The atom retention rate after the pulse is analyzed for all atoms in the cluster, leading to the observation of Rabi oscillations with differing amplitude and frequency across the structure. Comparison with a measurement loading only a single trap reveals no significant influence of the remaining diagonal interactions on the dynamics. In a second measurement, the checkerboard is inverted and the data obtained from the two measurements are merged for analysis. Averaged fluorescence images of these two patterns are shown in Fig. 4.9 (Top).

Measuring waist and light shift of the blue Rydberg beam

Figure 4.9 (Bottom) shows the result of such a measurement, superposed with a fit of Eq. (4.25) to every trap. From the distribution of Rabi frequencies obtained this way, information about the spatial distribution of the intensity of the blue Rydberg laser beam is obtained. From the design of the beam paths and measurements of the beam waists before demagnification into the vacuum chamber, the beam waists could be estimated to be $w_{0,R} = 550(50)$ μm and $w_{0,B} \simeq 20$ μm . The spot size of the red Rydberg beam is thus significantly larger than the typically used array size and can thus be treated as having a homogeneous intensity in the region where the blue beam illuminates the array. The distribution of Rabi frequencies is thus determined by the intensity of the blue Rydberg field, which is proportional to Ω^2 (see Eq. (4.22)). Figure 4.10 (a) shows a 3D

¹⁴ If the detuning could be chosen so that $\Delta \gg \Omega_R, \Omega_B$, then $\Gamma_{sc|e}$ would vanish according to Eq. (4.20), rendering spontaneous emission from the Rydberg state as the dominant decay channel. The system would then be equivalent to the one considered in [154].

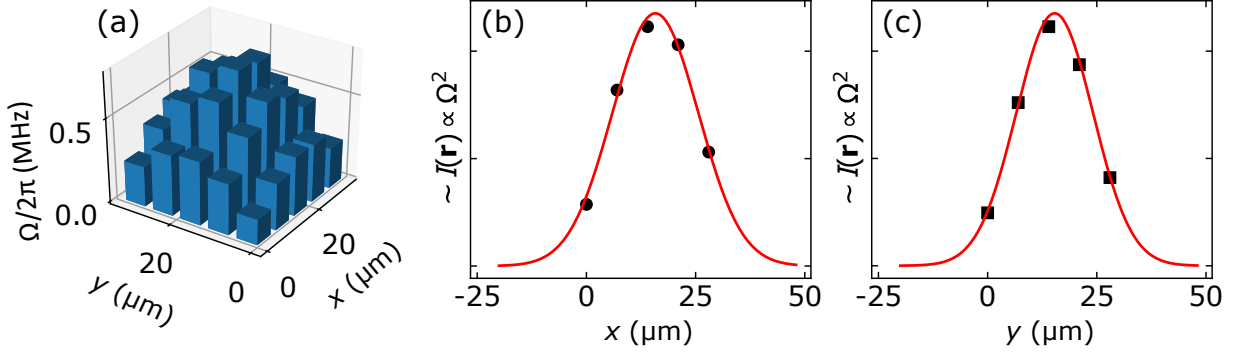


Figure 4.10.: Distribution of Rabi frequencies within a central 5×5 cluster of atoms (see Fig. 4.9). (a) 3D plot of Ω as a function of the atom position. (b),(c) Projections of a 2D Gaussian fit to the square of the measured Rabi frequencies, yielding the blue beam waist as $w_{0,B}^{(x,y)} = (19.7(3) \mu\text{m}, 17.6(2) \mu\text{m})$ (see text for details). Uncertainties are smaller than the plot symbols.

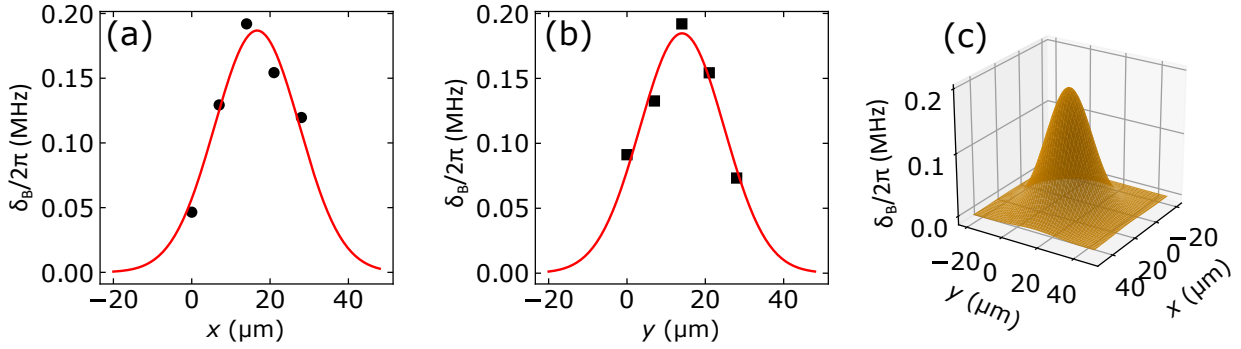


Figure 4.11.: Light shift distribution within the central 5×5 cluster. (a),(b) Projections of the normalized resonance shift caused by the blue laser beam in x and y direction, respectively, superposed with a Gaussian fit. (c) 3D plot of a two-dimensional Gaussian fitted to the data. The maximum value $\delta_{B,\text{max}} = 2\pi \times 189(4) \text{kHz}$ yields a maximal blue Rabi frequency of $\Omega_B \simeq 2\pi \times 18 \text{MHz}$ (see text for details).

plot of the squared Rabi frequencies over the atom array. Fitting a two-dimensional Gaussian on the data (projections to the x and y dimension are shown in Fig. 4.10 (b)) yields a blue beam waist of $w_{0,B}^{(x,y)} = (19.7(3) \mu\text{m}, 17.6(2) \mu\text{m})$, revealing a slight ellipticity. For further calculations of peak Rabi frequencies, the average of these values $\bar{w}_{0,B} = (w_{0,B}^x + w_{0,B}^y)/2 = 18.7(2) \mu\text{m}$ will be used.

A similar procedure can be applied to characterize the light shift of the blue Rydberg laser beam. Analysis of the site-resolved atom-loss signal from a frequency scan yields the resonance frequency as a function of the trap index. Comparing these frequencies reveals a shift to positive values, scaling linearly with laser intensity. This is expected from Eq. (4.19), where the AC Stark shift of the blue laser light has a positive sign and scales with $\delta_B := \Omega_B^2/4\Delta \propto I_B(\mathbf{r})$.

Figure 4.11 shows the distribution of these shifts across the array, again with a two-dimensional Gaussian fit to the data. The baseline of the Gaussian corresponds to the absence of blue light and is thus normalized to zero. The peak value $\delta_{B,\text{max}} = 2\pi \times 189(4) \text{kHz}$ corresponds to the intensity maximum, yielding a maximal blue Rabi frequency of $\Omega_B = \sqrt{\delta_{B,\text{max}} \cdot 4\Delta} = 2\pi \times 17.9(4) \text{MHz}$,

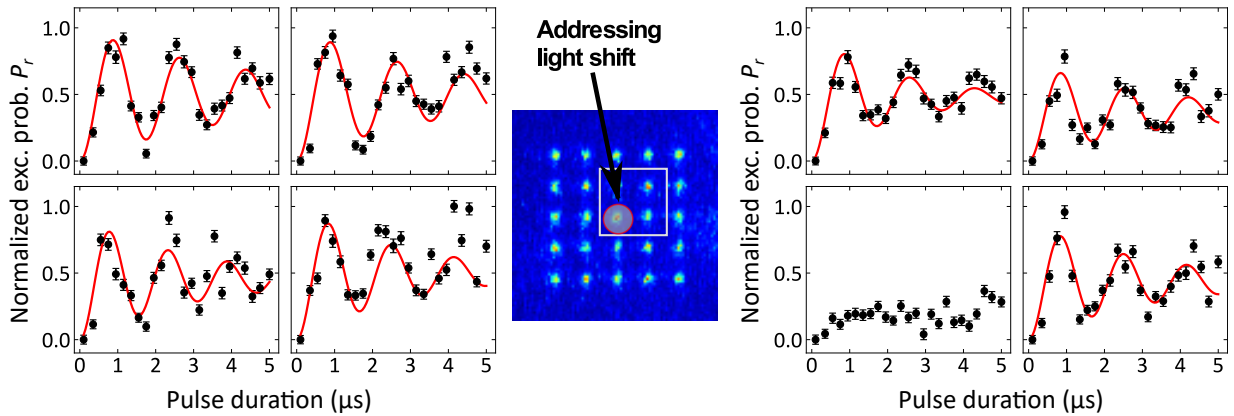


Figure 4.12.: Suppression of Rabi oscillation through a light shift applied via the optical tweezer. (Left) Rabi oscillations in a 2×2 sub-cluster of the array. (Right) Illuminating the lower left trap with the optical tweezer shifts the resonance for the corresponding atom by ≈ 4 MHz, largely inhibiting excitation to the Rydberg state. The data are normalized to the maximum value among the respective cluster and red solid lines are fits of Eq. (4.25). Error bars correspond to statistical uncertainties.

with $\Delta = 2\pi \times 417$ MHz. This is roughly 30% less than what was expected from the calculation in Eq. (4.22) for a laser power of 45 mW, suggesting that the transmission loss through the window of the vacuum chamber is higher than the expected value of $\sim 35\%$ based on previous transmission measurements.

4.3.4 Site-selective control of coherent dynamics with an optical tweezer

A crucial requirement for the comprehensive control of quantum states in the system is the manipulation of individual qubits in a site-selective fashion. Local control of the qubit basis states $\{|0\rangle, |1\rangle\}$ via a spatial light modulator has already been demonstrated in the present experiment [155]. A similar approach can be realized for the Rydberg lasers, albeit at a significant loss of optical power associated with using an SLM. A simple, yet effective alternative to a local excitation laser beam is the use of an off-resonant addressing laser beam to introduce a local light shift that selectively tunes single sites out of resonance for the global excitation laser field. This scheme has been demonstrated in optical lattices [156, 157] and, more recently, for Rydberg excitation in a tweezer array [158], where it was used to switch a pair of atoms between a blockaded and unblockaded regime.

The given setup is well suited for the integration of this scheme into the experimental repertoire. The optical tweezer introduced in Chapter 3 already has the ideal properties for this purpose, as the local addressing with a light shift is essentially the same procedure as extracting an atom from the trap, though at different laser intensities. In Fig. 4.12 a proof-of-principle measurement is presented, where the tweezer was used to shift one of four neighboring traps out of resonance for the Rydberg light, thereby suppressing the excitation for that trap. The light shift applied corresponds to approximately a third of the trap depth used for atom rearrangement, or ~ 4 MHz, which is roughly 4 times the measured linewidth of the resonance. The residual excitation probability, especially noticeable for longer pulse times, can be most likely attributed to Rydberg interactions between neighboring atoms, leading to a non-negligible excitation probability due to a shifting of the Rydberg levels. In Chapter 6 this will be discussed in detail.

4.3.5 Conclusion

In this chapter, the first observation of coherent Rydberg Rabi oscillations in the present experiment is documented. Utilizing the versatility of configurable atom geometries provided by the atom assembler introduced in Chapter 3, simultaneous excitation in a 5×5 site region of the array could be realized and studied effectively, allowing an accurate mapping of the individual Rabi frequencies and light shifts. Careful selection of the atom structure and Rydberg state parameters allows to minimize effects of atom-atom interactions at this stage. Using the optical tweezer to induce an additional light shift on a selected trap can shift the corresponding atom out of resonance and thus block its Rydberg excitation to a large extent, which has been demonstrated in a proof-of-concept measurement. The observed damping and reduced contrast of the oscillation amplitude, however, points to a short coherence time of the dynamics and imperfect excitation and/or detection of Rydberg states, which needs to be improved in order to perform high-fidelity gate operations or an efficient mapping of spin Hamiltonians to the system. The following chapter is thus dedicated to understanding and modelling the effects that contribute to this limitation, which is crucial if they are to be eliminated, or at least diminished.

5 Analysis of imperfections in the coherent Rydberg excitation

In the previous chapter, the observation of coherent dynamics between ground and Rydberg states has been demonstrated. All of these measurements, however, exhibit a reduced contrast and strong damping. A simplified, empirical model of these effects was applied in order to perform fits to the data and extract information such as Rabi frequencies and light shifts. As discussed in Chapter 2, the goal of the present experiment is to use this system for quantum computation and simulation purposes. Both of these applications require high fidelities for the excitation into a Rydberg state as well as decoherence on timescales longer than a π pulse duration. To get into this regime, the parameters of the system have to be significantly improved. As there is a multitude of effects contributing to the observed deficiencies of the signal, a careful analysis has to be applied to isolate these effects and understand their respective influence. Only then appropriate measures can be taken to address experimental shortcomings and improve the system. This chapter aims to study and quantify these limiting effects and model their influence on the Rabi oscillations. The goal is to replace the empirical fit function from the previous chapter with an ab-initio numerical simulation, taking into account all major limiting factors.

These effects can be classified into two categories. The first contains effects that result in a reduced initial amplitude and limit the contrast of the oscillations, such as imperfect state preparation, detection errors and baseline atom loss. They usually do not depend on the coherent dynamics and shall thus be called static effects.

The second type summarizes effects that lead to a time-dependent damping of the oscillations. They will be called dynamic effects and include spontaneous emission from the intermediate state, Doppler broadening, and other sources of noise that can cause a loss of coherence. These two categories will be discussed in the following two sections, after which they will all be combined in a comprehensive model. A detailed analysis of most of the effects considered here, for a similar setup, can also be found in [59, 159].

5.1 Static effects

Given an atom prepared in the appropriate ground state and having precisely measured the Rabi frequency of the oscillation arising when driving the atom with the laser field, it should be possible to execute a π pulse into the Rydberg state with near-perfect efficiency, as has been demonstrated in [38]. Despite the existence of imperfections limiting the efficiency of the excitation itself, there are several effects restricting the detection efficiency of a Rydberg excitation, which means that even for a perfect π pulse fidelity, the observed signal would still exhibit a reduced global amplitude. In the following, these effects will be discussed and quantified.

5.1.1 Atom temperature and baseline loss

The finite temperature of the atoms trapped in the array comes into play in different ways. The Rydberg detection scheme used in this experiment relies on the conditions for an atom to have a mean velocity large enough for it to leave the trapping volume within the lifetime of the Rydberg

state, whereas a larger temperature also increases the probability of ground state atoms getting lost from the traps, as well as broadening the laser beam linewidth seen by the atoms due to the Doppler effect.

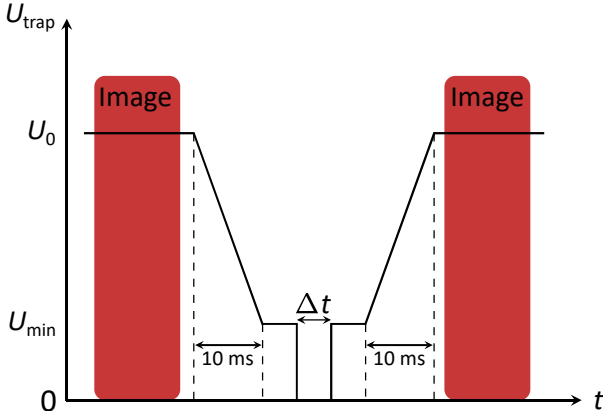


Figure 5.1.: Experimental sequence of a "release and recapture" measurement. As it is almost identical to a Rydberg measurement, it serves as a benchmark for baseline atom loss as well as a measurement of the atomic temperature.

In order to quantify the influence of all these effects, knowing the atom temperature to a fair amount of accuracy is essential. For this purpose, a "release and recapture" measurement is performed, which is described in detail in [160] and has been introduced in the context of this experiment in [83]. Figure 5.1 illustrates the experimental sequence corresponding to this technique. The only difference to a Rydberg measurement is the lack of a Rydberg pulse and the variation of the time Δt during which the traps are switched off (for the Rydberg measurements conducted for this thesis, this time was kept constant for all pulse durations). Thus it serves as a good benchmark for baseline atom loss for all Rydberg measurements¹ in addition to yielding information about the atom temperature.

As Rydberg measurements are typically performed in the central 5×5 traps of the array, only this region is analyzed, averaging the sig-

nal obtained from these 25 traps with a mean lowered trap depth of $U_{\min}/k_B = 300(50) \mu\text{K}$. The probability of atom recapture after a varying release time Δt is plotted in Fig. 5.2. A fit to the data is made by performing Monte-Carlo simulations of the recapture probability for different temperatures and minimizing the weighted least squares value (χ^2) obtained from comparing the simulations with the data (shown in the inset of the graph). The underlying model assumes a Maxwell-Boltzmann distribution of atom position and velocity in the trap and simulates trajectories based on this thermal motion, counting an atom as ejected from the trap if a threshold energy is exceeded during the release time (for details, see [83, 160]). The best fit yields an average temperature for atoms in this central region of $52(1) \mu\text{K}$, about a factor of six lower than the trap depth. This is consistent with earlier measurements [82, 83].

As can be seen in the graph, the recapture rate is nearly constant for the first $\approx 10 \mu\text{s}$. During this time, the atoms can not travel enough distance to leave the center of the trap and are thus always recaptured. The finite probability of detection in the second image for this initial plateau of ≈ 0.95 is likely to stem from other sources than loss during release time. The most probable source is atom loss during fluorescence detection or while adiabatically ramping down the trap depth from $U_0 = k_B \cdot 1.7(2) \text{mK}$ to U_{\min} , where a finite survival probability is associated with the truncation of the Boltzmann distribution [160]. The baseline atom loss can thus be quantified as $\epsilon_0 = 0.05$ and the obtained temperature of the atoms will be used for the analysis of further limiting effects later on.

¹ Loss induced by the Rydberg laser fields themselves is not included here. It can be neglected, as was confirmed in a separate measurement.

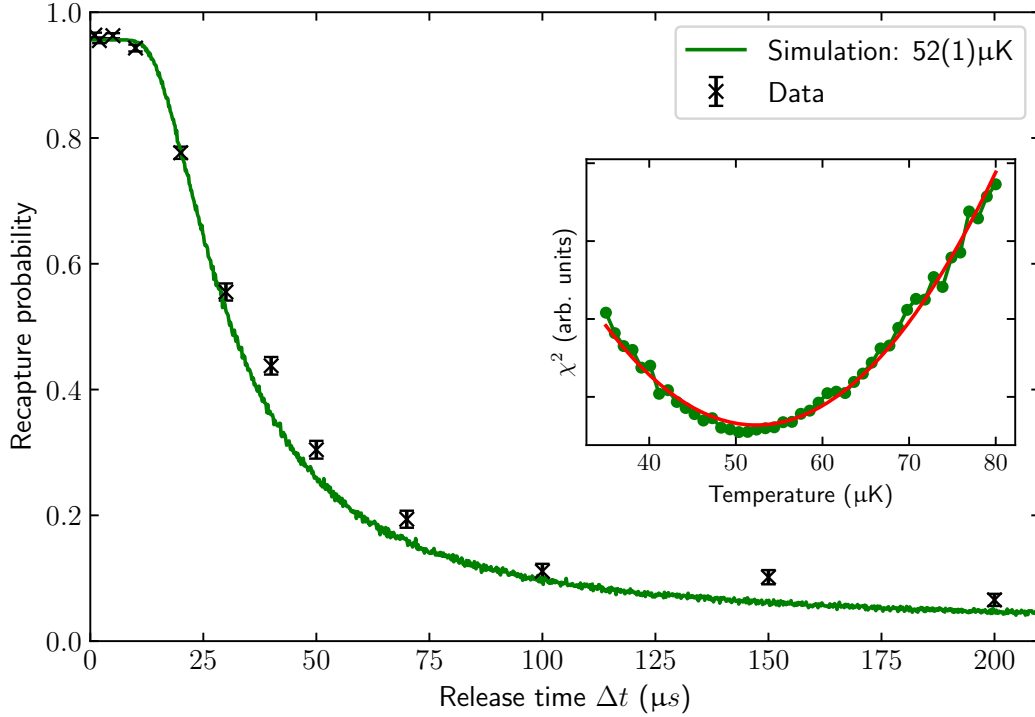


Figure 5.2.: Recapture probability for a lowered trap depth of $U_{\min}/k_B \approx 300(50) \mu\text{K}$, averaged over the central 5×5 traps. The data are superposed with the best fit obtained from Monte-Carlo simulations of the recapture for different temperatures. This best fit is found by minimizing the weighted least-squares values (χ^2) between data and simulation through harmonic approximation (inset).

5.1.2 Efficiency of ground state preparation

A further source of reduced Rydberg detection efficiency is an imperfect preparation into the correct ground state. The scheme used for trapping the population in the stretched $|5S_{1/2}, F = 3, m_F = -3\rangle$ state (see Section 4.3.1) is relatively robust against imperfections in polarization and fluctuations of laser power, as the target state essentially constitutes a dark state for the pumping laser field, which means that the population should always gather in this state as long as the correct polarization is dominant. The main influence of a slightly non-optimal polarization of the pumping or repumping laser beam should therefore be the number of excitation cycles the atoms have to undergo before gathering in the target state. This can lead to an associated increase in temperature, which could cause some atom loss. This loss, however, was measured to be almost negligible and is already included in the baseline atom loss quantified in Section 5.1.1, where the pumping cycle was already applied before releasing the atom. There is, however, a small chance that the atom gets excited out of the target state by a photon with a σ^+ polarization right before the end of the pumping sequence, which would result in the atom decaying into the wrong ground state with a small probability. Another possible source of error is the shift of the Zeeman sublevels by the applied quantization field. At a B-field strength of $|\mathbf{B}| = 2.75 \text{ G}$, the two outermost states $m_F = (3, -3)$ are shifted relative to each other by $\approx 10 \text{ MHz}$, which is more than the linewidth of the transition, thus having a non-negligible

impact on the relative detuning of the various sublevels.

To quantify the state-preparation efficiency, the population of the hyperfine manifold can be probed by coupling a driving field to the hyperfine transition ($|F = 2\rangle \leftrightarrow |F = 3\rangle$) of the ground state. As the hyperfine splitting for ^{85}Rb has a frequency in the microwave spectrum of $\nu_{\text{HFS}} = 3.036\text{ GHz}$, the transition can be driven by an appropriate microwave, or by a two-photon Raman transition with two 780 nm laser fields far-detuned to the $|5S_{1/2}\rangle \leftrightarrow |5P_{3/2}\rangle$ transition. The latter has been used extensively before in this group, primarily for optimizing preparation into the clock states ($m_{F,F'} = 0$) as well as performing single-qubit gate operations [45, 47]. For the preparation into a stretched state, as required here, the situation is slightly different. As the current setup only allows for $\Delta m_F = 0$ coupling of the hyperfine sublevels, it precludes the direct probing of the stretched state populations, as is illustrated in Fig. 5.3 (a) ². The stretched state populations after the optical pumping stage can thus not be directly observed and have to be inferred by careful analysis of the other populations and how they change when increasing the time of optical pumping. The laser system used for these measurements as well as the phase-stabilized locking scheme is described in [161, 162]. The dynamics arising when driving the transition with the Raman laser fields can again be derived by considering a three-level system, but this time in a Λ -scheme. Because of the relatively large detuning from the excited state of $\Delta \simeq 10\text{ GHz}$, all allowed hyperfine transitions contribute equally to the Rabi frequencies of the respective transitions. A detailed description can be found in [45]. As transitions from and to states with smaller values of $|m_{F,F'}|$ can couple via a larger number of paths than the stretched states, the Rabi frequencies decrease for increasing $|m_{F,F'}|$. This can be seen in Fig. 5.3 (b), where Rabi oscillations for all available transitions are plotted. First, a short repumping pulse ensures that all atoms are initially in $|F = 3\rangle$. The measurements consist of a Raman pulse directly followed by a blow-away pulse resonant to the cycling transition that removes all atoms in the $|F = 3\rangle$ ground state. By fits to the data, the exact Rabi frequencies and corresponding π pulse durations can be extracted. These values can then be used to perform a spectroscopic measurement where the respective π pulse is applied to all transitions, thus ensuring that the observed peak amplitudes correspond to the underlying state populations $|F = 3, m_F\rangle$. Varying the duration of optical pumping, one can observe a passage of populations in the direction of negative m_F states, as illustrated in Fig. 5.3 (c), as expected for pumping with σ^- -polarized light.

Let P_i denote the population in the respective state $m_F = i$. From the top graph corresponding to an absence of optical pumping, a linear decrease of P_i with increasing i can be observed ³. A linear fit to $P_{-2,\dots,2}$ thus yields the population P_3 . As $m_F = -3$ is a dark state, P_{-3} is expected to be higher than what one would obtain from the same linear regression. However, as all other populations are now known, it can be estimated via

$$P_{-3} = 1 - \sum_{i=-2}^3 P_i . \quad (5.1)$$

² This is due to the requirement of colinear propagation of the Raman laser beams, as other angles would introduce a significant Doppler broadening much larger than the linewidth of the transition and larger than the Fourier width of the pulse, causing a reduction of contrast. Colinear propagation with different polarizations can be used for $\Delta m_F = \pm 1$ coupling to the stretched states, but this would require a considerable modification of the setup and was thus avoided.

³ The non-uniformity of this distribution can likely be attributed to four of the six MOT beams being slightly out of balance, resulting in a dominance of σ^- over σ^+ photons when initially preparing the atoms in the $|F = 3\rangle$ state.

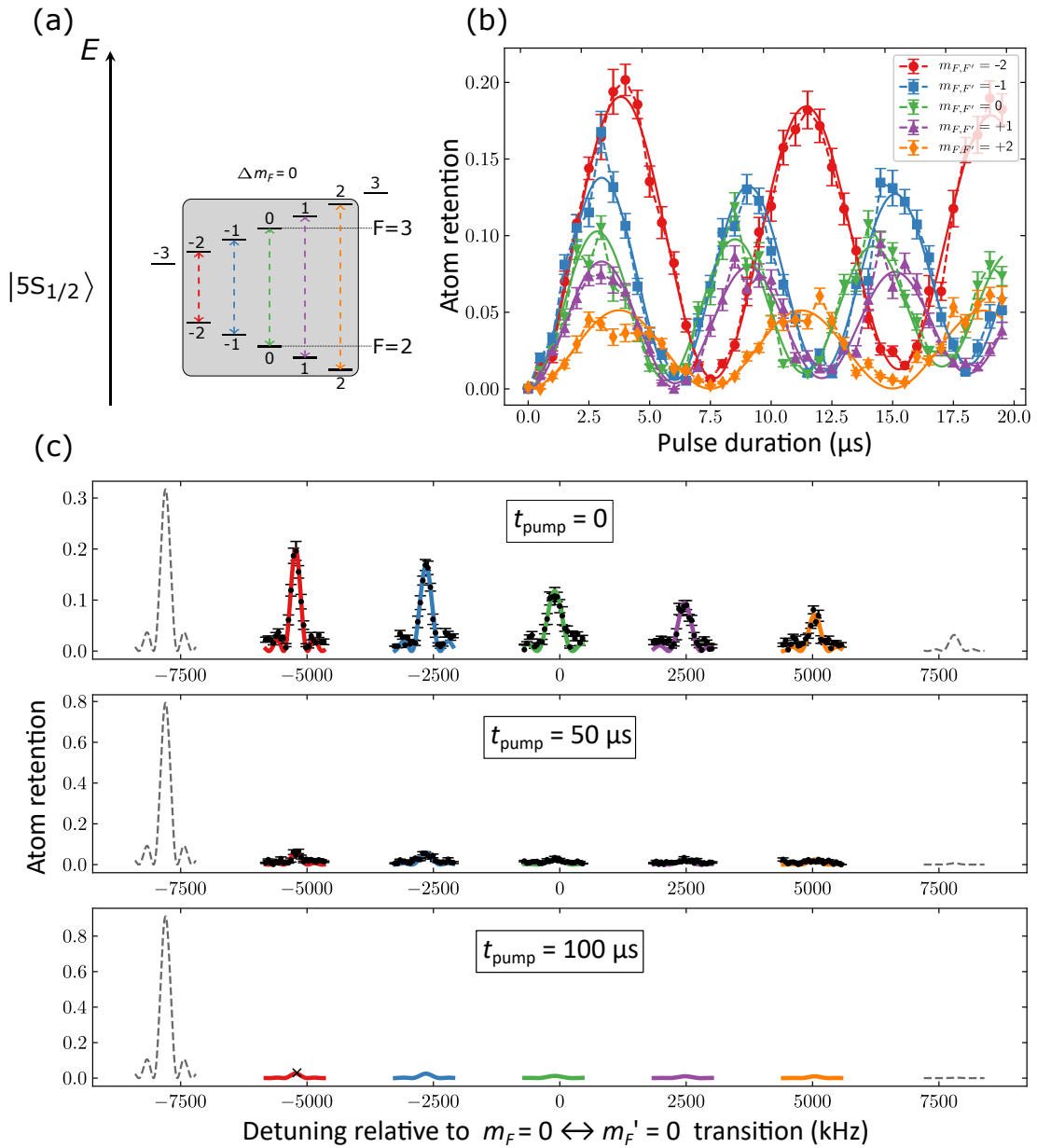


Figure 5.3.: Analysis of ground state preparation efficiency. (a) Schematic of the transitions that can be probed by the $(\sigma^- - \sigma^-)$ Raman laser beams, in the presence of a magnetic field lifting the degeneracy of the Zeeman sublevels. Since only $\Delta m_F = 0$ coupling is available, the stretched states can not be directly coupled (for details, see text). (b) Rabi oscillations measured on all of the 5 transitions with fits to determine the exact π pulse duration for the respective drives. (c) Spectroscopic scan on all the transitions to measure the effect of optical pumping on the relative amplitudes of the resonances. The small global shift to negative detunings relative to the theoretical $m_F = 0 \leftrightarrow m_{F'} = 0$ transition frequency corresponds to the Raman laser light shift. For all transitions, the respective π pulse duration obtained from (b) was applied. Via linear extrapolation, the corresponding populations in the stretched states can be inferred and the efficiency of the optical pumping quantified (see text). Error bars correspond to statistical uncertainties.

Factoring in the baseline atom loss measured in the previous subsection, the corrected population is then obtained via

$$\tilde{P}_{-3} = \frac{P_{-3}}{1 - \epsilon_0} = \frac{P_{-3}}{0.95} . \quad (5.2)$$

The extrapolated populations P_{-3} and P_3 are plotted as dashed grey lines in the graphs, to differentiate them from the measured data. The initially estimated dark state population is $P_{-3} \simeq 0.32$ (Fig. 5.3 (c, top)), having increased to 0.79 after 50 μs of optical pumping (Fig. 5.3 (c, center)). For the final value of $t_{\text{pump}} = 100 \mu\text{s}$ (Fig. 5.3 (c, bottom)), all states but the target state are almost completely depleted, making a spectroscopy impossible. Only for P_{-2} , a residual peak value of 0.03 can be measured, indicated as a single data point. From this point, the same extrapolation as before is applied to estimate the final populations. Thus, a baseline atom-loss corrected efficiency $\tilde{P}_{-3} \simeq 0.96$ of preparation in the $|5S_{1/2}, F = 3, m_F = -3\rangle$ ground state is obtained. Obviously, atom loss caused by the pumping laser would significantly hamper the accuracy of this method. For this reason, it was confirmed in a separate measurement that this loss is negligible for the pulse durations applied here.

5.1.3 Recapture of Rydberg atoms

As discussed in Section 4.3.2, the detection of Rydberg excitation relies on the assumption that the Rydberg atom leaves the trapping volume, and thus gets lost, before it decays back to the ground state, where it would see the trapping potential again and could get recaptured. Depending on the Rydberg state, however, this assumption is not always entirely valid. As the $57D_{5/2}$ state used for the measurements in Chapter 4 has an effective lifetime of $\tau_{\text{eff}} \simeq 95 \mu\text{s}$, a comparison with the recapture measurement presented in Fig. 5.2 reveals a significant chance of recapture after a decay from the Rydberg state, if only the atom's thermal motion is considered. The false-negative error associated with this recapture (the Rydberg excitation is not detected even though the atom was excited) shall be denoted as ϵ_r and will be estimated in the following.

Ponderomotive potential

Considering only thermal motion of the atom while in the Rydberg state already yields an upper bound for ϵ_r . There is, however, an additional potential acting on the Rydberg atom in the presence of the focused trap laser beam. As the valence electron in a Rydberg state is very weakly bound, it can be considered as a free electron and its interaction with the light field can thus be described by the ponderomotive potential [152, 163]

$$U_p(\mathbf{r}) = \frac{e^2 |\mathbf{E}(\mathbf{r})|^2}{4m_e \omega_L^2} , \quad (5.3)$$

where $-e$ and m_e are the electron charge and mass, and $\omega_L/2\pi$ is the frequency of the trap laser. As U_p is always positive, it constitutes a repulsive potential for every Rydberg state. Because of its scaling with ω_L^{-2} , longer wavelengths yield a stronger repulsion, especially considering the increase in power needed to achieve the same trap depth for larger detunings, which manifests itself in the $\sim |\mathbf{E}(\mathbf{r})|^2$ scaling of the potential. The time a Rydberg atom stays in the trap region thus strongly depends on the wavelength of the trapping light. This is illustrated in Fig. 5.4, showing a simulation of the recapture probability over time, given different wavelengths, while

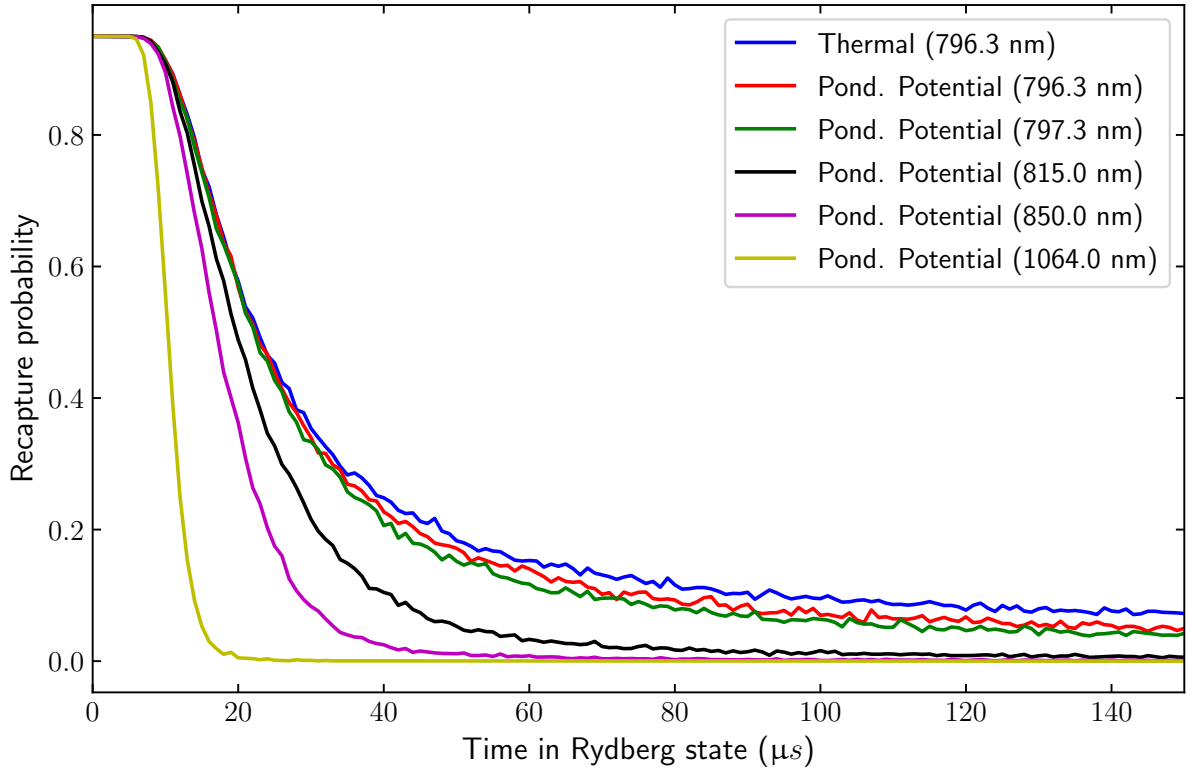


Figure 5.4.: Monte-Carlo simulations of Rydberg atom recapture for different trap laser wavelengths. The curve corresponding to thermal motion (blue) is obtained from a fit to experimental data (see Fig. 5.2). For all other curves, the repulsive ponderomotive potential experienced by a Rydberg atom is included in the simulation. Apart from the laser power, which has to be adjusted to assure a constant trap depth of $300 \mu\text{K}$, all other parameters are kept constant and correspond to experimentally measured values.

keeping the trap depths constant at $300 \mu\text{K}$. All other simulation parameters correspond to experimentally measured values. The curve for $\lambda = 796.3 \text{ nm}$ (for thermal motion) is thus identical to the one shown in Fig. 5.2. The red and green curves correspond to the two wavelengths used for all measurements presented in this thesis. The acceleration of Rydberg atom loss by the ponderomotive potential in this case is only minimal. Earlier measurements on this setup have been conducted with the Ti:Sa laser set to $\lambda = 815 \text{ nm}$ (black curve), where the difference already becomes noticeable. The requirement of large arrays currently precludes a significant increase in wavelength, however. The curves for 850 and 1064 nm serve as a comparison to other dipole trap wavelengths typically used. The probability of Rydberg atom recapture can thus be expressed as an integral over [59]

$$\epsilon_r = \int_0^{\infty} P_{\text{recap}}(t) \dot{p}_g(t) dt , \quad (5.4)$$

where $P_{\text{recap}}(t)$ can be obtained from the simulations and $\dot{p}_g(t) = \Gamma_0 \exp(-t\Gamma_0)$ denotes the time derivative of the ground state population, given that the atom is initially in $|r\rangle$ and decays to the ground state by spontaneous emission with a rate Γ_0 (see Section 2.2.2). Blackbody-induced transitions can be neglected, as transferring the atom to a neighboring Rydberg state would still

lead to its loss. Given the n^{-3} scaling of the radiative decay rate with principal quantum number n , this detection error decreases the higher n gets. Evaluating the above integral for the states $|57D_{5/2}\rangle$ and $|87D_{5/2}\rangle$ used in this thesis yields the error rates $\epsilon_{r,57} = 0.19$ and $\epsilon_{r,87} = 0.06$. As all measurements presented in Chapter 4 were performed on the $|57D_{5/2}\rangle$ state, this error constitutes by far the most significant cause of the finite amplitude observed in these measurements.

5.2 Damping mechanisms

Having analyzed the experimental imperfections that lead to an overall reduction in contrast in the oscillations, the goal of this section is to understand and quantify the mechanisms that cause a damping of the oscillations. Although they can already reduce the amplitude of the first oscillation period, thereby also having an effect on the total contrast, these effects mainly cause a time-dependent decay of the amplitude. Because the measurement of Rabi oscillations necessarily includes averaging over many experimental cycles, it is not possible to distinguish between effects damping a single Rabi oscillation and damping effects only arising when averaging over various cycles (like shot-to-shot fluctuations of experimental parameters). Both of these types will be treated in the same way, with most of the studied effects belonging to the latter type. So far, the damping has been accounted for by introducing a phenomenological damping rate γ , which allowed for fits to the data. This phenomenological approach does, however, not distinguish between different sources of damping and is thus insufficient for understanding and quantifying the underlying limitations. In the following, the main sources for oscillation damping will be analyzed, after which all of the considered effects will be combined in a comprehensive numerical simulation.

5.2.1 Spontaneous emission from the intermediate state

As already mentioned in the previous chapter, the relatively small detuning of $\Delta = 2\pi \times 417$ MHz necessary to achieve high enough Rabi frequencies in the current setup causes non-negligible spontaneous emission from the intermediate state. The effective scattering rate associated with this decay is given in Eq. (4.20). Generally, all possible decay channels have to be considered here, as was done in [164] for a π transition to the intermediate state. Since the current scheme in the presented setup uses σ^- -polarized light to couple to the stretched state, there is only one possible decay channel, namely the $|5P_{3/2}, F' = 4, m'_F = -4\rangle \rightarrow |5S_{1/2}, F = 3, m_F = -3\rangle$ transition. Coupling to other Zeeman sublevels of the intermediate state caused by imperfect polarization would introduce additional decay channels, but is neglected here, as the probability of these transitions happening is small compared to the decay via the dominant channel. A schematic of this simplified process is shown in Fig. 5.5 (a). This decay can thus be considered by keeping the three-level model, but switching to a density-matrix formalism and solving the Master equation.

Master equation approach

As soon as spontaneous decay is introduced into the system, it can no longer be considered as in a coherent superposition of the pure states $|g\rangle$ and $|r\rangle$, as was previously done in the idealized two-level scheme. The random decay causes decoherence in the system, which can be accounted for by including the intermediate state in the picture. The system can then be treated as a

superposition of the three pure states $|g\rangle$, $|e\rangle$ and $|r\rangle$ described by introducing the density matrix operator [154]

$$\rho = \sum_{(i,j) \in \{g,e,r\}} \rho_{ij} |i\rangle \langle j| . \quad (5.5)$$

The time evolution of the system is then governed by the master equation in Lindblad form [164]

$$\frac{d\rho}{dt} = -\frac{i}{\hbar} [H, \rho] + \mathcal{L}[\rho] , \quad (5.6)$$

where the Hamiltonian H describes the unitary part of the dynamics. Spontaneous emission causes dissipative damping, expressed by the Lindblad \mathcal{L} dissipator. Both operators are given in the $\{|g\rangle, |e\rangle, |r\rangle\}$ basis as

$$H = \hbar \begin{pmatrix} 0 & \Omega_R/2 & 0 \\ \Omega_R/2 & -\Delta & \Omega_B/2 \\ 0 & \Omega_B/2 & -\delta \end{pmatrix} \quad (5.7)$$

and

$$\mathcal{L}[\rho] = \begin{pmatrix} \Gamma \rho_{ee} & -\frac{\Gamma}{2} \rho_{ge} & 0 \\ -\frac{\Gamma}{2} \rho_{eg} & -\Gamma \rho_{ee} & -\frac{\Gamma}{2} \rho_{er} \\ 0 & -\frac{\Gamma}{2} \rho_{re} & 0 \end{pmatrix} , \quad (5.8)$$

where decay from $|r\rangle$ was neglected as the corresponding decay rate is three orders of magnitude smaller than Γ and thus has a negligible impact on the dynamics for the short timescales considered here. Defining an initial state of the system and solving this Master equation for various time steps yields the time-dependent population of the Rydberg state. A Python implementation of this solver is given via the *QuTiP* library [165], which was used for the simulation of Rabi oscillations presented in this chapter. The corresponding code is shown in Appendix C.

Figure 5.5 (b) shows the effect of different detunings Δ on the damping of the amplitude. For better comparability, the effective Rabi frequency Ω was kept constant throughout the simulations by adjusting Ω_R ⁴. The influence of spontaneous decay in the current experimental realization is represented by the red curve, with larger and smaller detunings given for comparison.

5.2.2 Dephasing effects

While spontaneous emission causes an immediate dissipative loss of coherence in the system, there is a multitude of effects whose influence on the amplitude of the oscillations manifests via averaging over multiple realizations. Shot-to-shot variations of laser frequencies and laser power, fluctuations of the atomic resonance via external fields or the Doppler effect lead to the oscillations having a slightly different Rabi frequency and amplitude in every repetition, causing the individual oscillations to drift out of phase with each other, which is why this effect is referred to as dephasing. In the following, the different sources of dephasing will be quantified and included in the model.

⁴ This was done to match the experimental situation, where Ω_B is always set to the maximal value and only Ω_R is varied to adjust the Rabi frequency.

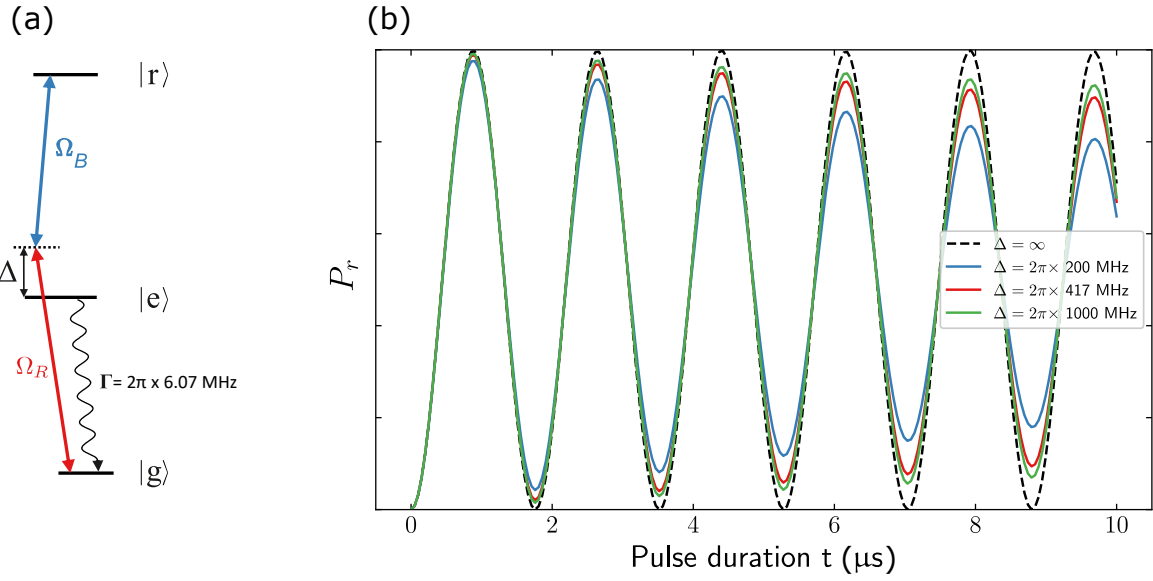


Figure 5.5.: Simulation of amplitude damping via spontaneous emission from the intermediate state. (a) Schematic of the simplified damping process. As the stretched intermediate state $|e\rangle$ can only decay to one Zeeman sublevel, only this one channel has to be modelled. (b) Monte-Carlo simulations for different detunings Δ . The red curve corresponds to the value present in the experiment.

Doppler effect

One of the largest contributors to dephasing is the Doppler effect. Due to its finite temperature, the atom oscillates in the trap, while its velocity is described by a Maxwell-Boltzmann distribution. For every repetition of the experiment, the atom can be treated as having a fixed velocity drawn randomly from this distribution⁵, with a standard deviation of $\sigma_v = \sqrt{k_B T/m} \simeq 0.07 \mu\text{m}/\mu\text{s}$ for the measured temperature of $T \approx 50 \mu\text{K}$. The Doppler effect thus gives rise to a corresponding distribution of frequency shifts $\sigma_\delta = |\mathbf{k}_{\text{eff}}| \sigma_v \simeq 2\pi \times 170 \text{ kHz}$, where $\mathbf{k}_{\text{eff}} = \mathbf{k}_R + \mathbf{k}_B$ is the effective wave vector, taking into account that the laser beams are orthogonal to each other (see Fig. 5.6 (a)). This frequency distribution can be included in the model by treating the effective detuning δ in Eq. (5.7) as a Gaussian distributed random variable with a mean given by the AC Stark shift caused by the laser fields and standard deviation σ_δ . The effect of this is illustrated in Fig. 5.6 (b). In the Bloch sphere picture, a drive on resonance is represented by a rotation about the x axis. A small detuning δ introduces an angle $\theta \approx \delta/\Omega$ between the axis of rotation Ω and the x axis, reducing the amplitude of a π pulse when making a projection measurement on $|r\rangle$. Having the detuning δ fluctuate randomly for different experimental repetitions further causes a dephasing of the individual Bloch vectors, which is observed as a damping of the amplitude when averaging over these repetitions⁶. The strength of this effective damping

⁵ For the relatively slow Rabi oscillations achievable in the current setup, the interaction time with the Rydberg laser fields lies on the order of the inverse trap frequencies, which means that the atom can actually change its direction of movement during a single oscillation, causing dephasing even in a single experimental realization. As this effect is indistinguishable from the simplified model due to the necessary averaging, the latter suffices for a quantitative analysis.

⁶ Note that this does not correspond to an inherent decoherence, as the individual systems remain in a pure state (represented by the Bloch vectors staying on the surface of the sphere) as opposed to the mixing of states caused by spontaneous decay. The randomness of the underlying process, however, makes it impossible to rephase the system.

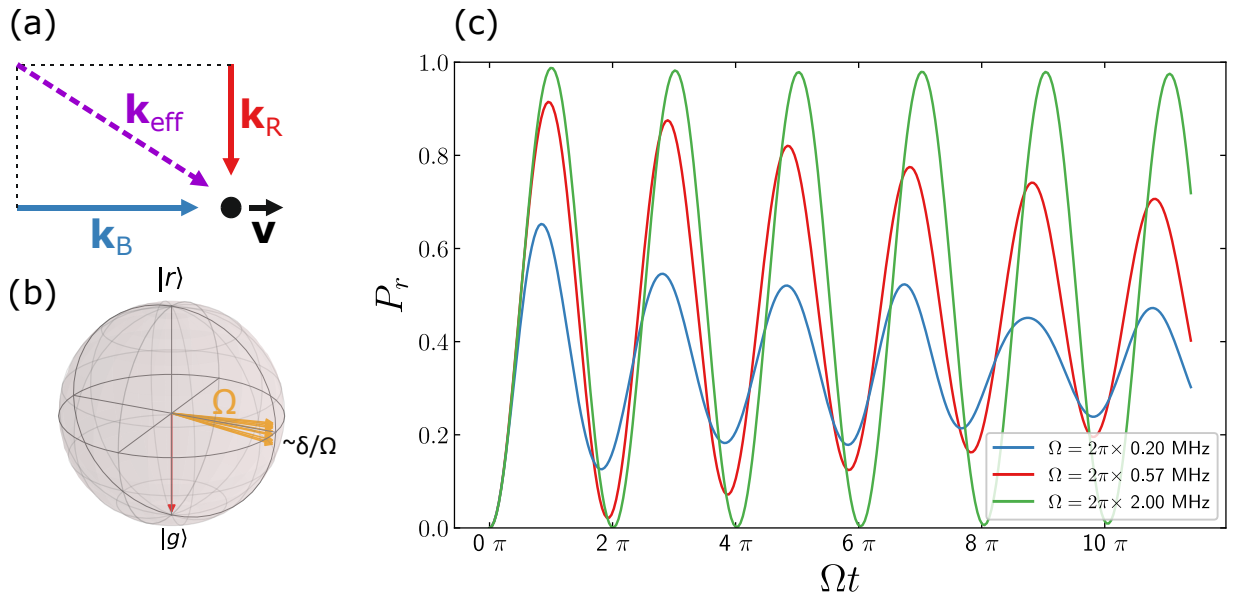


Figure 5.6.: Influence of Doppler broadening on the dephasing of Rabi oscillations. (a) The effective wave vector of the Rydberg laser beams is given by vectorial addition of the perpendicular components. Multiplied by the standard deviation of atom velocity, this results in a distribution of frequencies, from which δ is sampled for each experimental repetition (b). This is represented by a shift of the Bloch vector corresponding to Ω by an angle $\sim \delta/\Omega$. The state vector (red) is then rotated about a varying axis, leading to a dephasing of the system. (c) Simulation of the effect of the experimentally estimated Doppler broadening of $\sigma_\delta \simeq 170$ kHz on Rabi oscillations with different Ω , illustrating that strong couplings are much less vulnerable to this effect than weak ones. For better comparability between different timescales, the oscillations are plotted as a function of the pulse area Ωt . The red curve corresponds to a typical experimental value of Ω .

scales with the ratio δ/Ω , as is illustrated in Fig. 5.6 (c). The stronger the coupling, the weaker this effect becomes. Looking at the red curve corresponding to current experimental values, it becomes evident that the Doppler effect has a noticeably stronger influence on the signal than spontaneous decay (see Fig. 5.5 (b)).

Fluctuations of the magnetic quantization field

During the excitation to the Rydberg state, a $B_x = 2.75$ G magnetic field is applied to lift the degeneracy of the Zeeman levels. The stretched states which are then excited by the laser fields are especially sensitive to this magnetic field, with the ground state experiencing an energy shift of $\simeq -3.9$ MHz. As the Rydberg state experiences a similar shift of $\simeq -6.9$ MHz, the effective shift of the transition frequency between these states caused by the magnetic field is $\delta_B/2\pi \approx -3$ MHz⁷. A variation of this shift, as could be caused by fluctuations of the current sent to the coils creating the magnetic field, would thus have the same effect as the Doppler broadening. In order to be in a comparable order of magnitude as the latter, and thus have a noticeable influence on the oscillation, this current would have to fluctuate by $\simeq 5\%$. This would translate to a

⁷ As the magnetic field did not change for all measurements presented in this thesis, this shift was not explicitly introduced, but is rather implicitly included in the resonance frequency of the transition

fluctuation of the resonance peak in the Raman measurements (see Fig. 5.3 (c)) greater than the Fourier width, which was clearly not observed. There is furthermore no reason to assume that the high-precision power supply ($\Delta I/I < 2 \times 10^{-4}$, according to specifications) used to provide the current should fluctuate in this magnitude. Smaller variations can still have an effect on the oscillations on longer timescales and should be taken into account once the dominating effects are reduced, but for the current situation, the influence of magnetic field fluctuations can be neglected.

Fluctuations of laser power

Both Rydberg lasers are stabilized in intensity via a *Sample and Hold* scheme to ensure pulses with constant laser power over the course of a measurement. Small variations are, however, still possible and have been observed. The effect of such a variation is that it slightly modifies the coupling strength Ω and, via the Stark shift, the effective detuning δ . This also results in a dephasing and thus in an observed damping of the oscillation amplitude. As Ω scales with the square root of the laser power P , this can be included in the simulation by treating $\Omega_{R,B}$ as a random variable with standard deviation $(\Delta P_{R,B}\Omega)/2P_{R,B}$ for each repetition of the simulation. The respective laser power uncertainties are estimated as $\Delta P_R/P_R \approx 0.02$ and $\Delta P_B/P_B \approx 0.05$.

5.2.3 Other sources of noise

Electric fields

In contrast to the magnetic field sensitivity of Rydberg atoms, which is independent from the principal quantum number, the electric polarizability of a Rydberg atom scales as $\alpha_0 \propto n^{*7}$, making it extremely sensitive to electric fields, a property which can be harnessed for high-precision electric field sensing [166, 167]. In the present experiment, no external electric fields are applied. However, as even very small fields can cause an energy shift according to $\Delta E = -1/2\alpha_0|\mathbf{E}|^2$, stray fields and buildup of static charge on the sides of the vacuum windows can have a noticeable influence (in [168], a significant shift was observed caused by static charge on the surface of lenses placed inside the vacuum chamber). So far, no observations have been made in this experiment that would clearly point to an influence of such stray fields and since the magnitude of a hypothetical electric field is hard to gauge, it is difficult to include in a simulation. However, especially when working with higher-lying Rydberg states - the $|87D_{5/2}\rangle$ state also studied within this thesis is roughly 20 times more sensitive than the $|57D_{5/2}\rangle$ state - this effect has to be kept in mind as a potential source of damping.

Laser phase noise

As the Rydberg lasers exhibit a stabilized linewidth far below the Fourier width of the excitation pulses, it does not constitute a limitation of the observed signal. There is, however, another quantity associated with the laser fields that can represent a source of noise. If the phases $\Phi_R(t)$ and $\Phi_B(t)$ fluctuate in time, the effective Rabi frequency is given by $\Omega = |\Omega|e^{i(\Phi_R(t)+\Phi_B(t))}$, which corresponds to an azimuthal displacement of Ω on the Bloch sphere. A strong modulation of $\Phi_{R,B}(t)$ with a frequency on the order of Ω can thus lead to a strong damping of the Rabi oscillations. Precisely measuring the magnitude of these fluctuations is not an easy task, however. It can be estimated by analyzing the PDH error signal to measure the voltage noise spectral density $S_V(f)$, from which the related spectral density of phase noise $S_\Phi(f)$ can be estimated

Table 5.1.: Simulation parameters obtained from the individual measurements presented in this chapter.

Error source	Quantity	value	type
Efficiency of optical pumping	η_p	0.96	static
Baseline loss	ϵ_0	0.05	static
Rydberg detection error	ϵ_r	0.19 ($n = 57$)	static
Spontaneous decay	$\Gamma_{sc, e\rangle}$	0.08 / μ s	damping
Doppler effect	σ_δ	$2\pi \times 170$ kHz	dephasing
Laser power fluctuations	$(\Delta P_R, \Delta P_B)$	(2%, 5%)	dephasing

with the knowledge of the PDH parameters and the cavity linewidth, as described in [59, 159]. As the parameters of the laser system reported therein are similar to the system presented in this thesis ⁸, these results suggest that in the current setup, laser phase noise does not represent a major limitation, as long as the PDH parameters are set to optimal values (too much gain, for example, can significantly increase the phase noise). Once other limitations are reduced, this effect will however become noticeable, and a more thorough analysis should be performed. An effective way to reduce phase noise is to use the light transmitted through the cavity, which serves as a passive low pass filter for frequency noise, to inject another laser diode. Light from this injection seeded laser then exhibits an enhanced spectral purity and can be used to excite the atoms. This technique has been successfully applied in [38], among other improvements, leading to a reported Rydberg Rabi coherence time of 27 μ s.

5.3 Combining the effects

After having analyzed the main sources of reduced contrast and amplitude damping in the current experiment, all these effects can be combined in a comprehensive simulation of the dynamics. Table 5.1 lists the individually obtained experimental parameters that are included in the simulation. The simulation relies on the same Master equation solver as introduced in Section 5.2, only this time all damping effects are combined and the obtained Rydberg state population is modified according to the static effects. The combination of these effects can be factored in as:

$$P_r = \epsilon_0 + \eta_p(1 - \epsilon_0 - \epsilon_r)\tilde{P}_r, \quad (5.9)$$

where \tilde{P}_r denotes the "real" Rydberg state population and P_r corresponds to the population one would measure in the experiment, given these static sources of finite contrast. The *Python* implementation of this code is given in Appendix C. Figure 5.7 shows the result of averaging over 100 such simulations for a selected trap, each time stochastically sampling the fluctuating parameters from a Gaussian distribution ⁹. The values of Ω_R and Ω_B are set as the measured values from Chapter 4. For this trap, the simulation is in good agreement with the experimental data. Comparison with a simulation including only static effects confirms the strong influence of the damping effects as well as an increase of the oscillation frequency. The latter

⁸ Our cavity linewidth for red light of $\Delta\nu = 47$ kHz is even smaller than the linewidth of 75 kHz reported in [159].

⁹ These include the effective detuning δ due to the Doppler effect and the laser powers P_R and P_B according to the uncertainties given in Table 5.1.

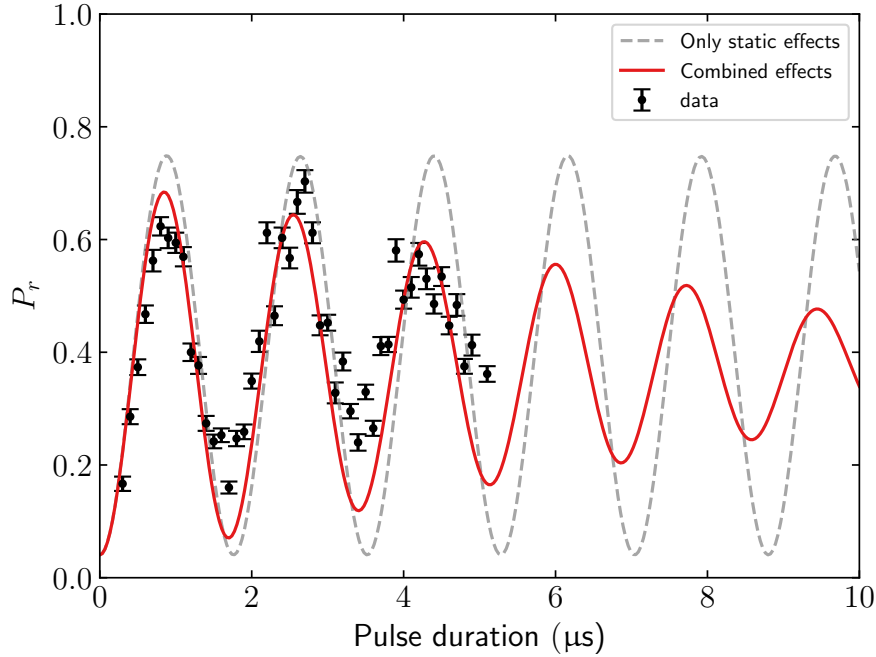


Figure 5.7.: Combined simulation of Rabi oscillation in a single trap using the individually obtained experimental parameters given in Table 5.1 (red curve), showing good agreement with the experimental data (black dots with errorbars). Comparison with a simulation including only static errors (grey dashed line) shows the increase in oscillation frequency through amplitude damping and dephasing. The combined result is based on 100 repetitions of the simulation.

is associated with a slight detuning from the resonance due to the fluctuating Doppler shift and laser power, increasing the effective Rabi frequency according to $\Omega_{\text{eff}} = \sqrt{\Omega^2 + \delta_{\text{eff}}}$. On top of this predicted behaviour, however, there appears to be a slight asymmetry in the damping (the minima are damped stronger than the maxima) that is not accounted for in the simulation. The cause of this is unclear. A hypothetical coupling to other intermediate states and corresponding decay to other (dark) ground states would manifest itself as an asymmetry in opposite direction.

Simulation for the array

Having compared the simulation result to a single trap, the obvious question is how it holds up against the measurement of simultaneous Rabi oscillations in the array. To make an appropriate comparison, the variation in the coupling of the light fields over the array has to be taken into account in the simulation. For this purpose, the Rabi frequencies obtained from the measurement shown in Fig. 4.9 are used to seed the simulation of the dynamics for each trap individually. Figure 5.8 shows the result of this site-selective simulation. While it matches the data well for some traps, in others a discrepancy of varying degree is visible. It appears that the simulation generally overestimates the damping and reduction of contrast for traps at the edge of the prepared cluster, while underestimating it for some of the central traps. A natural interpretation of this is that the dynamics are influenced by a non-negligible interaction between the diagonal

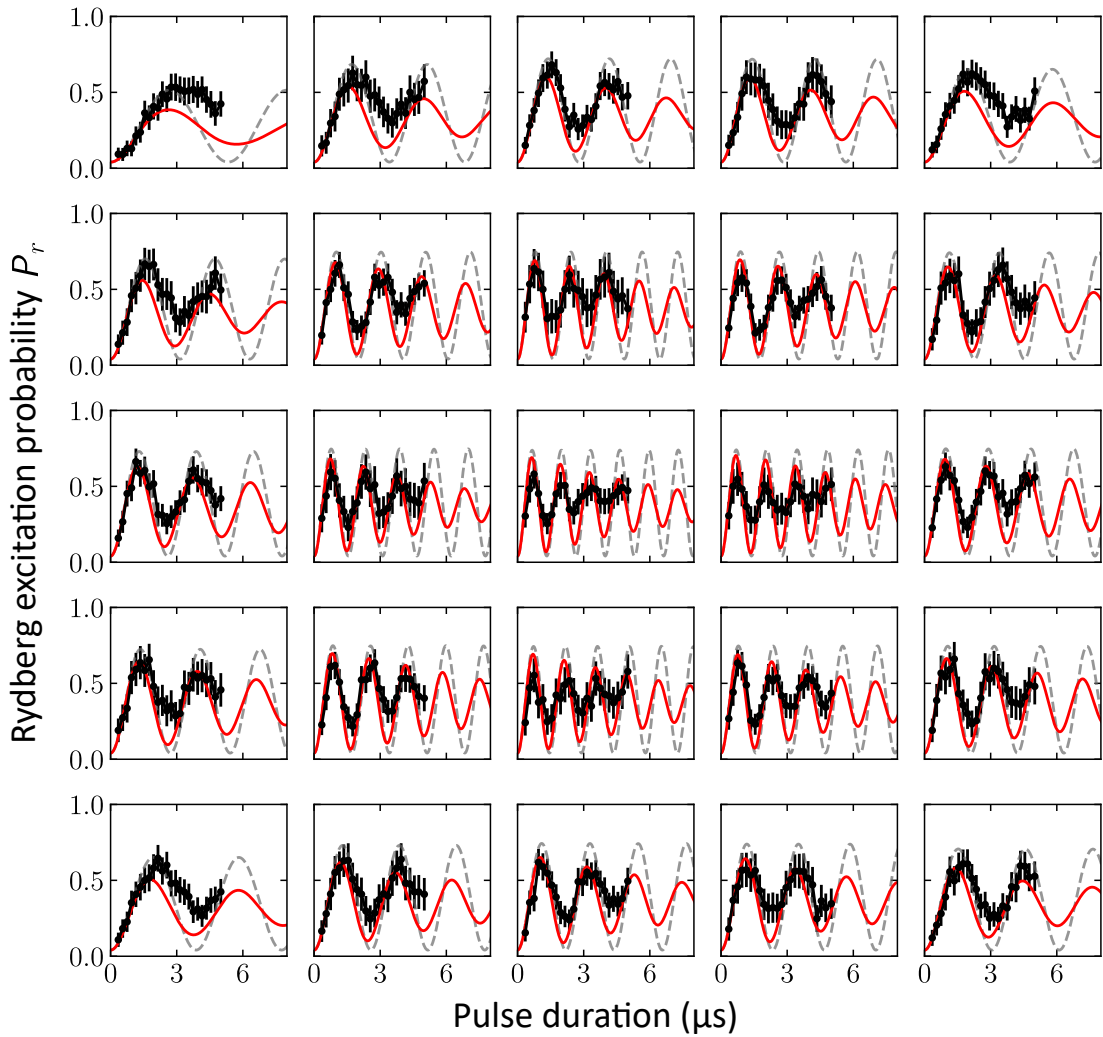


Figure 5.8.: Combined simulation of Rabi oscillations in the trap array. Rabi frequencies used for the simulations are obtained from the measurement shown in Section 4.3.3. The simulation for each trap is performed in the same way as for Fig. 5.7. It is apparent that it matches the data well for some traps, while generally overestimating the damping for outlying traps and underestimating it for central traps.

neighbors¹⁰. A calculation of the expected interaction strength, taking into account a distance of $\sqrt{2}d = 9.9 \mu\text{m}$ and an angle of 45° to the quantization axis defined by a 2.75 G magnetic field, yields an effective energy shift on the order of $\Delta E/h \simeq 75 \text{ kHz}$. As the central traps have four diagonal neighbors, these interactions can add up to a significant portion of the Rabi frequency, which would lead to a reduced amplitude, as is the case for an off-resonant drive. A varying number of diagonal neighbors would also explain additional damping. This is plausible, as the data was not post-selected for a fixed number of neighbors and a finite preparation efficiency of the checkerboard cluster causes these fluctuations. Accurately modelling the interaction with multiple neighbors is a non-trivial task and would exceed the scope of this chapter. An analysis of how interactions affect the coherent dynamics when driving to Rydberg states is given in Chapter 6.

¹⁰ As explained in Section 4.3.3, the experimental data consists of two separate measurements utilizing an inverted checkerboard pattern, so that no next neighbors along the grid lines are present.

In addition to a reduced contrast and increased damping, the signal in the central traps also appears to be offset to higher values. A higher baseline atom loss in these traps could explain this behavior, although it is not clear why this should be the case, as this baseline loss was explicitly measured for these traps. As the two measurements lie several months apart, however, it might be possible that some other parameter led to a higher loss in the case of the oscillation measurement. The slight asymmetry in the damping discussed for the single trap is observable in most of the traps, leaving room for further investigation.

Furthermore, it is not clear what leads to the signal in outer traps not being as strongly damped as what one would expect from the considerations made in this chapter. It appears, however, that the inclusion of the measured static effects, indicated by the grey dashed curve in the graphs, yields an accurate prediction of the initial amplitude in these traps, especially for the corner traps that only have at most one relevant interaction partner. Thus, assuming the perfect isolation of an atom driven to the Rydberg state, normalizing the measured signal P_r by these static errors should result in a good estimate of the real probability \tilde{P}_r . Accordingly, inverting Eq. (5.9) yields

$$\tilde{P}_r = \frac{1}{\eta_p} \frac{P_r - \epsilon_0}{1 - \epsilon_r - \epsilon_0} . \quad (5.10)$$

This equation will thus be used for normalizing the data in the following chapter.

5.4 Conclusion

This chapter analyzed the various sources of reduced contrast and amplitude damping observed when driving the atoms coherently to a Rydberg state. This was done using ab-initio calculations and independent measurements to isolate each limiting effect and quantify it. Combining all these effect into a comprehensive simulation of the dynamics yields good agreement with experimental data, with some residual discrepancies mostly attributed to non-negligible interaction between Rydberg atoms. As mentioned in the introduction of this chapter, the goal of this study was to derive knowledge about the relative influence of the limitations, so they can be specifically targeted and diminished. To sum up what could be learned, these are the parameters with the most potential for improvement:

- **Rabi frequency Ω and detuning Δ :** Increasing Ω by an appreciable amount, while keeping Δ constant or decreasing it, would yield the most significant improvement, as it would render the system less vulnerable to both spontaneous decay from the intermediate state and a fluctuating two-photon detuning. It can be achieved in the present system by focusing the blue beam down to a significantly smaller waist. As it would then only be able to effectively couple a single atom, a site-selective addressing will have to implemented at the same time, for example with a two-dimensional AOD as used in the atom assembly board. Multi-tone generation as introduced in [53, 123] could then be used for parallelized addressing.
- **Doppler shift fluctuations σ_δ :** An anti-parallel alignment of the Rydberg laser beams, instead of the perpendicular configuration used currently, would reduce the magnitude of the effective wavevector $\mathbf{k}_{\text{eff}} = \mathbf{k}_R + \mathbf{k}_B$ by roughly a factor of three, which would reduce the fluctuation of the Doppler-induced frequency shift to $\sigma_\delta \simeq 2\pi \times 60 \text{ kHz}$, thereby significantly diminishing its effect on the dephasing of the oscillations.

Other parameters do also hold some potential for an enhancement of the coherence time, but are either more challenging to improve or their benefit is less immediate. The only way to reduce the fluctuations of the laser powers, for example, is improving their intensity stabilization, which is challenging, since the feedback loop spans two laboratories, causing the signal to travel a significant distance and making it prone to noise. Residual electric fields can have a significant impact on high- n Rydberg states, but installing field compensation would require a drastic modification of the vacuum chamber. A new version of the experiment that is currently being set up, however, will allow for the inclusion of such compensation plates. An alternative way of reducing the impact of fluctuations and inhomogeneities in the Rabi frequency is the implementation of an excitation scheme using stimulated Raman adiabatic passage (STIRAP) [151], which has been successfully implemented for a robust excitation to a Rydberg state that is insensitive to small variations in the coupling strength [90, 169]. This is useful when the goal is to prepare one or more atoms quickly and efficiently in a Rydberg state, as is important for the implementation of XY quantum magnets [43, 159], where ground-Rydberg state coherence is of less importance, as the coupling is only applied for preparation and read-out. For quantum gate operations [20, 38], or the mapping of Ising-type Hamiltonians to the system [39, 41, 42, 108, 143, 170], the ground-Rydberg coherence is of primary importance, however. For this application, an improvement of the laser system to reduce phase noise, as shown in [38], may become necessary.



6 Observation of Rydberg blockade and collective enhancement in the array

Having observed and characterized the coherent dynamics arising when driving the transition from the ground to the Rydberg state, the next step towards a two-qubit gate or the simulation of many-body physics consists of implementing controlled interactions between the atoms in the assembled array. As already mentioned in Chapter 2, the dominant type of interaction in the dipole trap array presented here is the van der Waals interaction $V_{\text{vdW}} = -C_6/R^6$. In this chapter, a first observation of partial and complete blockade between atoms in the array is documented for this experiment. It is structured as follows: The first section introduces the concept of Rydberg blockade and the effect it has on the coherent dynamics of the atoms, describing how the analysis of the measured Rabi oscillations allow to gain information regarding the underlying interactions. In the second section, first results are presented, documenting partial and complete blockade, while the third section is dedicated to analyzing imperfections and quantify effects that lead to a loss of coherence.

6.1 Rydberg interactions in the array

In order to understand the effect of the van der Waals interaction on the observable dynamics when driving Rydberg transitions in the array, it has to be studied in a more thorough approach than the simplified picture employed in Section 2.2.4, taking into account the anisotropy of the interaction and the geometry of the array. This is especially important when working in a partially blockaded regime, where the strength of the interaction is on the order of the Rabi frequency for nearest or next-nearest neighbors, while it can be neglected when working in a strongly blockaded regime. This section discusses both of these cases.

6.1.1 Angular dependence of the interaction

As the van der Waals interaction between two Rydberg atoms is a dipole-dipole interaction, its strength depends on the shape of the Rydberg orbitals and their relative orientation. The energy shift of the doubly-excited state caused by the interaction is given by second-order perturbation theory as

$$\Delta E = \sum_{r',r''} \frac{|\langle r',r'' | V_{\text{dd}}(\mathbf{R}) | rr \rangle|^2}{\Delta_{r',r''}}, \quad (6.1)$$

where the sum is taken over all pair states $|r',r''\rangle$ dipole-coupled to the target state $|rr\rangle$, and $\Delta_{r',r''} := E_{|r'\rangle} + E_{|r''\rangle} - 2E_{|r\rangle}$ is the energy difference between the respective pair states at infinite separation [171]. $V_{\text{dd}}(\mathbf{R})$ is the dipole-dipole operator introduced in Section 2.2.4 (Eq. (2.35)).

The geometry of this problem is illustrated in Fig. 6.1 (a). In the presence of a quantization field, the dipole moments $\mathbf{d}_{1,2}$ of the atoms are aligned parallel to it. Since the atoms are ordered in a two-dimensional structure in the array, the angle θ between the distance vector \mathbf{R} and the quantization axis is not always zero, as was assumed for the simplified picture in Section

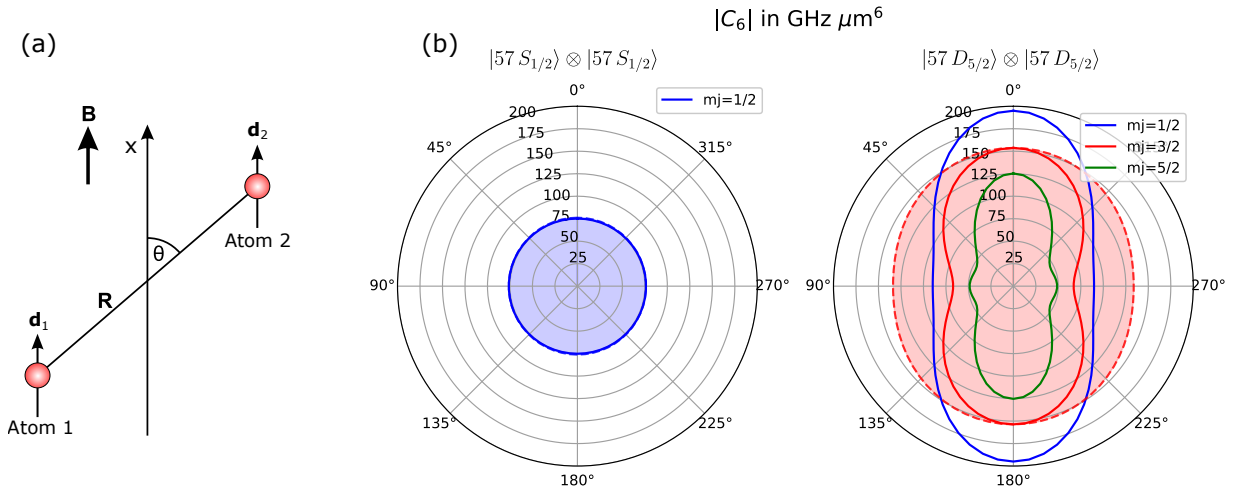


Figure 6.1.: Angular dependence of the van der Waals interaction. (a) In the 2D array, atom pairs generally have a non-zero angle θ between their internuclear axis and the quantization axis defined by the magnetic field \mathbf{B} . (b) For nD states, the van der Waals coefficient C_6 (solid lines) has a strong angular dependency, while being nearly isotropic for nS states. The blockade radius (shaded regions), due to its scaling with $\sqrt[6]{C_6}$, only exhibits a slight anisotropy, even for nD states. In the graphs, it is plotted in arbitrary units and normalized to the maximum of the corresponding C_6 data. For the $|57 D_{5/2}\rangle$ state, it is only drawn for the $|m_j| = 3/2$ sublevel, as this corresponds to the experimentally probed state.

2.2.4. The angular dependence of the interaction potential leads to an anisotropy of the van der Waals energy shift [171–173]. Figure 6.1 (b) shows a numerical calculation of this angular dependence, expressed in the coefficient $C_6 := \Delta E(R, \theta)/h \cdot |\mathbf{R}|^6$. The spherical symmetry of an S orbital leads to a nearly isotropic interaction for the $|57S_{1/2}\rangle \otimes |57S_{1/2}\rangle$ pair state, while the interaction between two atoms in the $|57D_{5/2}\rangle$ state is strongly anisotropic. A direct observation of this anisotropy was reported in [116, 174]. The blockade sphere, illustrated as shaded regions with arbitrary scaling to match the C_6 plot, only exhibits a minor anisotropy, due to the $\sqrt[6]{C_6}$ scaling of the blockade radius.

6.1.2 Collective enhancement through Rydberg blockade

While the van der Waals shift between two atoms is fairly simple to model and computationally tractable to quantify, the situation rapidly becomes more complex when increasing the number of atoms coupled by the interaction. This means that for a typical structure size prepared in the experiments presented in this thesis, the van der Waals shift experienced by an atom coupled to all other atoms in its vicinity is essentially impossible to calculate within a reasonable timeframe. A major benefit of the Rydberg blockade mechanism, and one of the reasons for its widespread use across many different systems, is its robustness against variations in the exact energy shift. For all atoms well inside the blockade sphere of a Rydberg atom, the condition $\Delta E \gg \hbar\Omega$ is met, which means that only a single atom can be excited to the Rydberg state at the same time. Consequently, while the Hilbert space originally contains 2^N states, the ensemble can be described as an effective two-level system in the N -atom Fock space. The ground state of the system,

$$|G\rangle := |g_1 g_2 \dots g_N\rangle, \quad (6.2)$$

is coupled to the superposition state

$$|\Psi_{1r}\rangle := \frac{1}{\sqrt{\sum_{i=1}^N |\Omega_i|^2}} \sum_{i=1}^N \Omega_i e^{i\mathbf{k}\cdot\mathbf{R}_i} |g_1 g_2 \dots r_i \dots g_N\rangle, \quad (6.3)$$

where the Rydberg excitation is shared among all atoms. Ω_i denotes the local Rabi frequency coupling atom i , while \mathbf{R}_i is its position and \mathbf{k} is the wavevector of the laser field. This entanglement of the ensemble leads to a collectively enhanced coupling strength

$$\Omega_N = \sqrt{\sum_{i=1}^N |\Omega_i|^2} \quad (6.4)$$

between $|G\rangle$ and $|\Psi_{1r}\rangle$, compared to the coupling of a single atom. This effect has been experimentally observed for the first time in [175]. In order to simplify the description, two assumptions shall be made, the validity of which will be discussed further below:

1. All atoms inside the blockade sphere are coupled with the same Rabi frequency $\Omega_i = \Omega$, such that the enhanced Rabi frequency can be written as

$$\Omega_N = \sqrt{N} \Omega. \quad (6.5)$$

2. The phase factors $e^{i\mathbf{k}\cdot\mathbf{R}_i}$ in Eq. (6.3) can be neglected, which is the case if the interatomic spacing is either small compared to the wavevector of the light field, or the vectors \mathbf{k} and $\mathbf{R}_{ij} = \mathbf{R}_i - \mathbf{R}_j$ are perpendicular to each other for all atom pairs (i, j) .

If these assumptions are valid, the excited Fock state corresponds to the maximally entangled state

$$|W\rangle := \frac{1}{\sqrt{N}} \sum_{i=1}^N |g_1 g_2 \dots r_i \dots g_N\rangle. \quad (6.6)$$

Both of the above assumptions are easier to fulfill the smaller one can make the interatomic distance, making optical lattice experiments perfect candidates for observing highly entangled multi-particle states in a single-atom trapping geometry¹. Accordingly, the creation of such a Rydberg "superatom" has been reported in [56], entangling more than 100 atoms. For the larger distances in a tweezer array, these requirements are more challenging to fulfill. Inhomogeneity of the Rabi frequency can lead to fast dephasing when driving the transition $|G\rangle \leftrightarrow |\Psi_{1r}\rangle$, as is the case for the system presented here. The first condition is only approximately valid for a small number of neighboring atoms, which can be addressed by restricting the size of the atom cluster. The phase factors, however, can not be neglected, since the effective wavevector $\mathbf{k}_{\text{eff}} = \mathbf{k}_R + \mathbf{k}_B$ is not perpendicular to the atom plane, but has a horizontal angle $\phi = \tan^{-1}(k_R/k_B)$ with the quantization axis. The different phases thus acquired by the components of $|\Psi_{1r}\rangle$ can lead to a reduction of the observed oscillation amplitude if they exhibit a time dependence, as caused by thermal motion of the atoms. A solution for this could either consist of aligning the red laser beam parallel or antiparallel to the blue beam², or in coupling the Rydberg state to the

¹ In ultracold gases, naturally a significantly larger number of atoms can be entangled because of the much smaller mean distances, as for example reported in [176].

² The latter would be much preferable, because of the accompanying significant reduction of the Doppler broadening.

second ground state, as demonstrated in [35]. The latter reduces the effective wavevector to that of the hyperfine splitting, which is orders of magnitude smaller than \mathbf{k}_{eff} , thus allowing for a robust entanglement of the ground states, which can then be selectively detected. It should also be noted that the enhanced Rabi frequency causes a slight reduction of the blockade radius, according to

$$R_b^{(N)} = \sqrt[6]{\frac{C_6}{\hbar\sqrt{N}\Omega}} = \frac{R_b}{\sqrt[12]{N}}. \quad (6.7)$$

This correction is not very large (it reduces the radius by $\sim 10\%$ for $N = 3$ atoms), but it has to be kept in mind when working in intermediate regimes not strongly blockaded.

6.1.3 Effect of imperfect blockade

So far, the dynamics of the system have either been considered in the non-interacting regime (Chapter 4) or, as in the previous subsection, in the strongly blockaded regime. In reality, for most measurements performed within the period documented in this thesis, the situation did not fully correspond to either of these regimes. Instead, the damping of the Rydberg oscillations presented in Chapter 4 suggests a non-negligible influence of interaction-induced energy shifts, and the strongly blockaded regime can only be achieved for a small number of atoms in the current setup. Unfortunately, an accurate prediction of the dynamics in this unblockaded interacting regime is extremely difficult, as calculating the interaction-induced shifts between multiple interacting particles is a highly non-trivial task. In [177], this has been done for a system of three atoms, yielding non-additive potentials due to strong state mixing.

6.2 Observation and analysis of partial and complete blockade

This section documents the first observation of Rydberg blockade in the experiment on which the work for this thesis was conducted. For all experiments presented in this chapter, an array with a pitch of $7.0(2)\mu\text{m}$ was used (ML2, see Table 2.1.2), as the smaller distance significantly facilitates the generation of blockaded clusters. The ability to assemble arbitrary structures, as introduced in Chapter 3, is utilized to build advantageous geometries for the observation of blockade.

6.2.1 Analysis of blockade strengths

The previously presented Rydberg measurements in this thesis all included an excitation of the $|57D_{5/2}\rangle$ state. The choice of this state was mainly due to historical reasons, as the laser system was aligned to work in the corresponding wavelength regime. Rydberg states in this region of n are commonly used for a first characterization of the system, as they represent a good compromise between coupling strength and state lifetime. For the observation of Rydberg blockade, however, higher-lying states ($n = 80..100$) are typically used [34, 105, 174, 178] in setups with comparable atomic distances as the $7\mu\text{m}$ pitch array used here, which exhibit appreciably stronger interactions, albeit at the cost of a reduced coupling strength. Figure 6.2 shows a comparison between the expected blockade strength for the $|57D_{5/2}\rangle$ and $|87D_{5/2}\rangle$ states. The latter was chosen, as its transition frequency has a similar offset with regard to the closest cavity fringe as the former, making it convenient to reach, only requiring alignment of the grating of the 960 nm laser. As interatomic axes between next neighbors in the array are either parallel

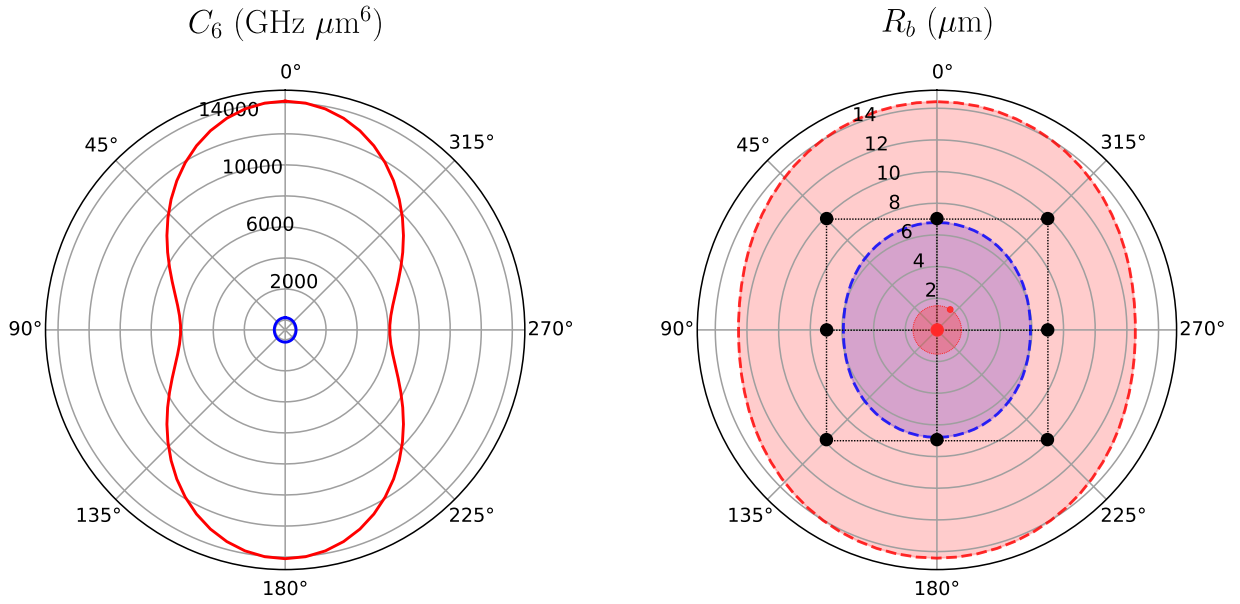


Figure 6.2.: Comparison of interaction strengths between the $|57 D_{5/2}\rangle$ (blue) and $|87 D_{5/2}\rangle$ (red) states, for $m_J = -3/2$. The left graph shows the angular dependence of vdW coefficient C_6 , obtained via a perturbative calculation, illustrating the 100-fold increase in interaction strength. The right graph shows the corresponding blockade radii for the two states. The grid of a $7 \mu\text{m}$ pitch array is drawn for scale. For $n = 87$, the blockade exerted by a Rydberg atom in the central trap extends appreciably further than one array pitch. Note that this perturbative calculation only serves to supply an estimate of the expected magnitude of blockade, a more accurate calculation is performed in Section 6.3.

or perpendicular to the quantization axis, those two angles have to be taken into account for the calculations, especially since the interaction strength along these two directions can differ significantly. A comparison of the blockade radii with the size of the array reveals an insufficient interaction strength for the $n = 57$ state, whereas the blockade exerted by a central atom in the $|87 D_{5/2}, m_J = -3/2\rangle$ state should easily cover all neighbors. The graphs were obtained by performing a perturbative calculation, which serves as an estimate of the magnitude of blockade and the anisotropy of the interaction, and is relatively fast to compute. For an accurate analysis, however, this is not sufficient, especially in the presence of a magnetic field. This will be discussed in Section 6.3.

6.2.2 Experimental observation of Rydberg blockade

Following the considerations above, the $n = 87$ Rydberg state was chosen for the measurements presented in this chapter. A blockade radius of $R_b \simeq 12 \mu\text{m}$ can be estimated as a lower bound. The largest structure in which a complete blockade can be expected to be observed is thus a 3×3 cluster, as indicated in Fig. 6.2. For the realization of two-qubit gates or the implementation of Ising- or XY-type Hamiltonians, this is enough, as all of these rely on pairwise interactions. The goal of the experiment presented in this section is the verification of Rydberg blockade via the observation of collectively enhanced Rabi oscillations, as well as via the suppressed excitation of more than one atom.

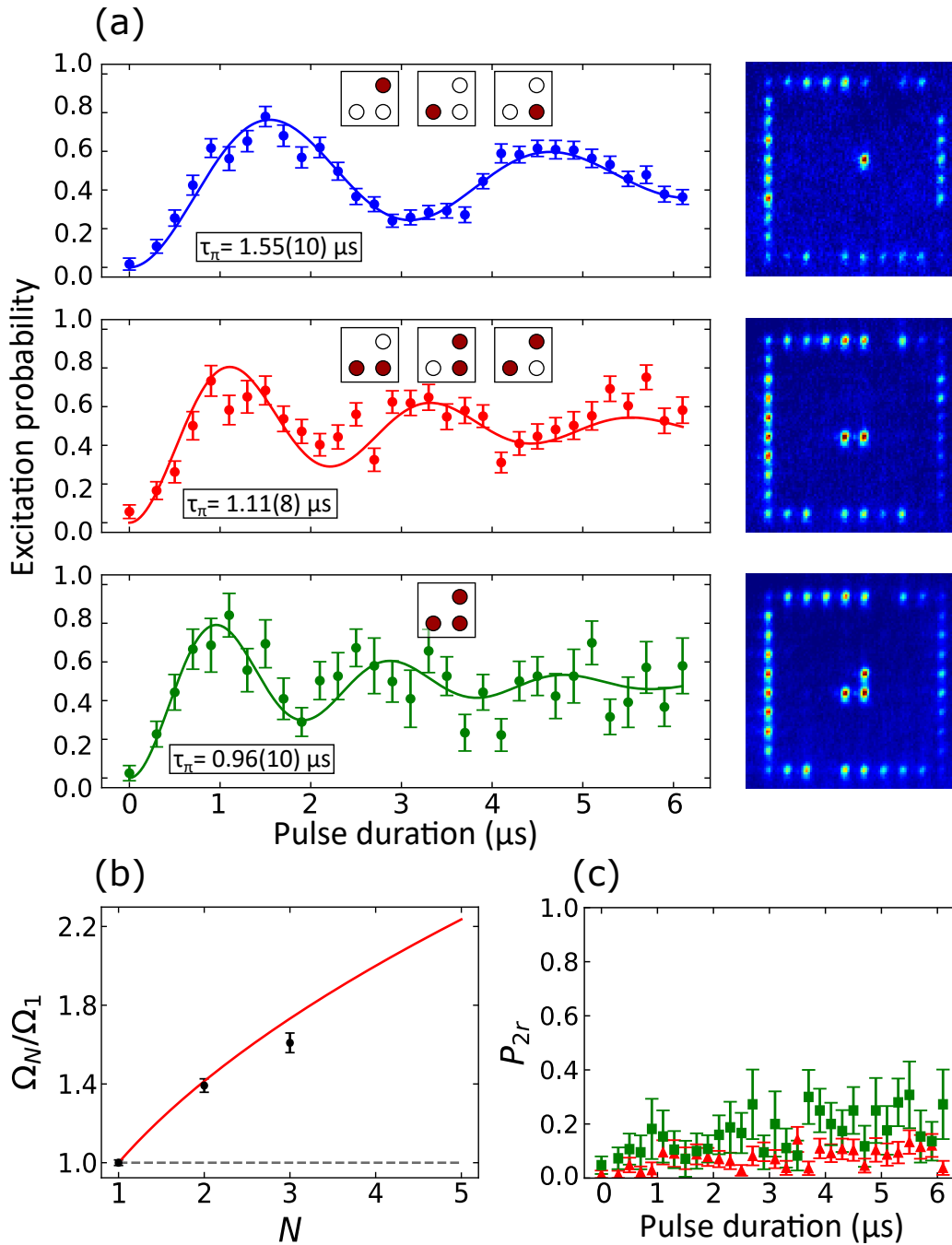


Figure 6.3.: Collective enhancement of the Rabi frequency through Rydberg blockade. (a) Probability of observing a single Rydberg excitation in a system of one, two and three atoms, respectively. The insets indicate the prepared geometries contributing to the signal, with exemplary fluorescence images shown on the right. Shots were post-selected for situations where a region of three traps in each direction from the central structure was empty, to exclude unwanted interactions. (b) As expected from Eq. (6.5), an enhancement of the Rabi frequency of the oscillation can be observed, in good agreement with a square root scaling. The grey dashed line corresponds to an unblocked situation. (c) Double excitation probability in the structures with two (red triangles) or three (green squares) atoms, indicating some blockade leakage in the triangular arrangement. Error bars correspond to statistical uncertainties.

The strong spatial variation of the Rabi frequency due to the small waist of the blue laser beam, however, makes it difficult to align the beam in a way that four atoms are coupled with the same strength³. Analyzing the Rabi oscillations for all atoms in the central 5×5 region of the array, a similar Rabi frequency could be detected for no more than three traps at the same time. As the beating of incommensurate Rabi frequencies within the blockaded ensemble would cause strong additional damping, the structure size is thus restricted to three atoms.

Figure 6.3 (a) shows Rabi oscillations in the probability of detecting a single $|87D_{5/2}, m_J = -3/2\rangle$ excitation in the prepared structure. From top to bottom, the number of atoms was increased, from one, to two, to three, with the corresponding combinations indicated in the insets. Exemplary fluorescence images of the structures are shown to the right. In order to rule out any residual interactions from atoms outside the target structure, a region consisting of three sites in each direction of the cluster was emptied prior to the application of the Rydberg excitation. Atoms in the surrounding "frame" and beyond served as a reservoir for reloading the structure after a Rydberg cycle.

The small size of the prepared cluster allowed for the repeated reconstruction within one experimental cycle, such that various Rydberg measurement cycles could be performed without having to reload the MOT. The closest distance to the "frame" is $4 \times d = 28 \mu\text{m}$, corresponding to an interaction strength of $< 30 \text{ kHz}$, which is less than the transform-limited linewidth of the excitation, even for the longest occurring pulse durations of $6 \mu\text{s}$. The data are normalized for static preparation and detection errors, as discussed in Chapter 5. Despite the near-deterministic preparation of the structures, the data were post-selected to only include measurements where the depicted initial configurations were achieved⁴.

Solid lines correspond to fits of Eq. (4.25) to the data. Even though the damping of the oscillation becomes more pronounced when more than one atom is present, the enhancement of the Rabi frequency is clearly visible and in good agreement with the expected scaling as $\Omega_N = \sqrt{N}\Omega$, as shown in Fig. 6.3 (b). Further evidence for the presence of blockade is the suppression of more than one excitation in the cluster. Figure 6.3 (c) shows the probability for detecting two simultaneous excitations, corrected for baseline atom loss and detection errors. While this probability is strongly suppressed for two atoms, there appears to be an imperfect blockade in the triangle. An analysis of the possible causes for this blockade leakage as well as the strong amplitude damping of the signal is performed in the next section.

6.3 Analysis of imperfections

In order to gain an understanding of the sources of oscillation damping and blockade leakage, the geometry of the experimental configuration and its influence on the blockade strength has to be analyzed in more detail. Particular attention has to be given to the modification of the Rydberg interaction potentials by an external magnetic field.

Influence of external fields

The application of an external magnetic field is necessary to guarantee a well-defined quantization axis and to lift the degeneracy of the Zeeman sublevels, which ensures both efficient optical pumping and the exclusive coupling to a single Rydberg state.

³ This is complicated by the fact that the blue spot is slightly elliptical.

⁴ Even though the preparation efficiency for just the three-atom target structure is practically 100%, the requirement of a completely empty region surrounding the structure reduces the overall preparation efficiency of the depicted configurations to less than unity, due to imperfections associated with finite atom removal efficiency and a small chance of recapture in neighboring traps after removal.

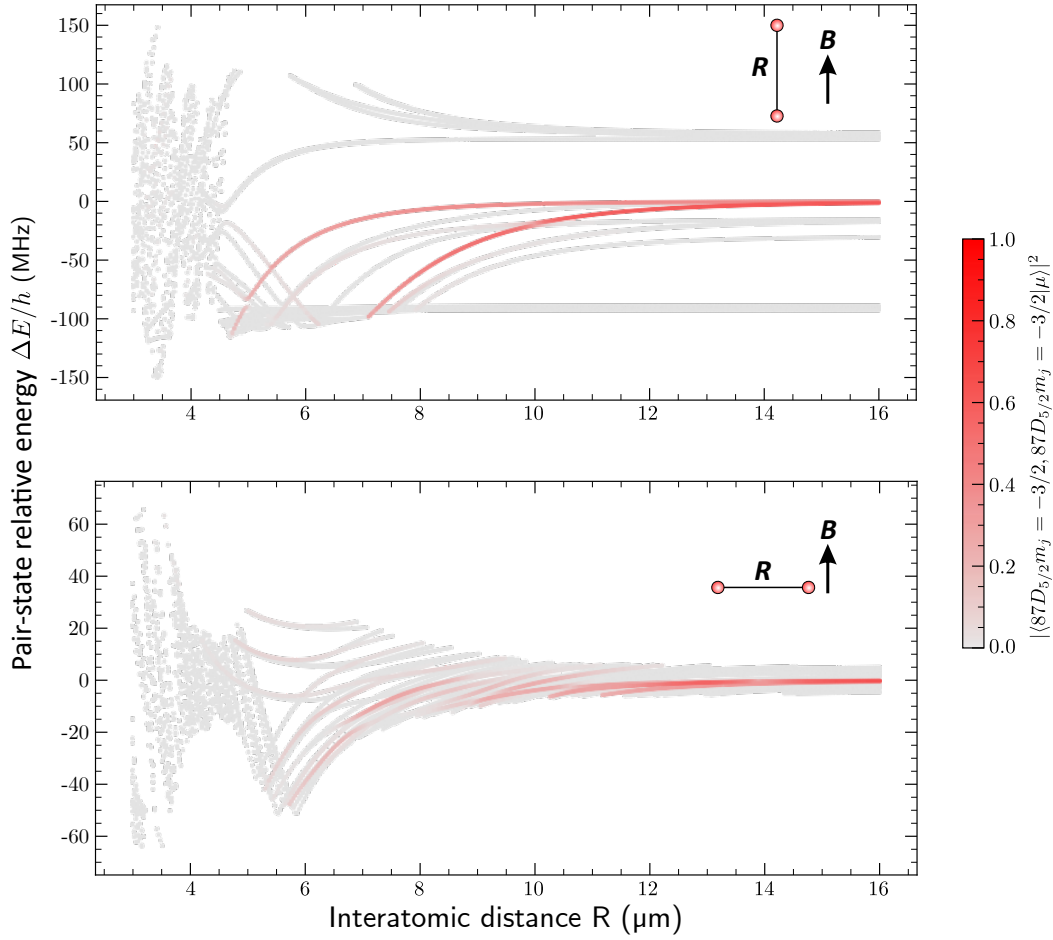


Figure 6.4.: Level diagrams of the $|87D_{5/2}, m_J = -3/2\rangle$ pair state in the presence of a $|\mathbf{B}| = 2.75$ G magnetic field, aligned parallel (top) or perpendicular (bottom) to the interatomic axis. The plots show the relative energy of the eigenstates of the interacting system, colored corresponding to the overlap with the unperturbed pair state. For discussion, see text. Calculations are based on the ARC library [103].

Since this Zeeman shift affects the entire manifold of Rydberg states, the strength of the vdW interaction between two Rydberg atoms can depend strongly on the magnetic field and its angle with respect to the interatomic axis [20]. This is especially true for Rydberg nD states, due to the multitude of Zeeman levels that can couple via the dipole-dipole interaction. Given the composition of the state $|87D_{5/2}, m_J\rangle$, with $m_J = \pm 1/2, \pm 3/2, \pm 5/2$, the Zeeman manifold of the $|87D_{5/2}, 87D_{5/2}\rangle$ pair state is composed of 36 sublevels. As they are all shifted corresponding to the respective value of $M = m_{J,1} + m_{J,2}$ in the presence of a magnetic field, where indices denote atom 1 and 2, this results in strong mixing with the Zeeman manifold of energetically close pair states, rendering the interaction strength extremely sensitive to external fields.

Figure 6.4 shows a comparison between the pair-state energies of two interacting Rydberg atoms for a parallel (top) and perpendicular (bottom) alignment of the interatomic axis with respect to a magnetic field of $|\mathbf{B}| = 2.75$ G. Levels are colored according to the contribution of the original pair state $|rr\rangle = |87D_{5/2}, m_J = -3/2\rangle \otimes |87D_{5/2}, m_J = -3/2\rangle$. If the interatomic axis is aligned parallel to the magnetic field, the Zeeman sublevels are degenerate with regard to the interaction, and only two eigenstates carry a significant contribution from the original state. At 90° to the magnetic field, the initial state is spread out across a multitude of non-degenerate Zeeman

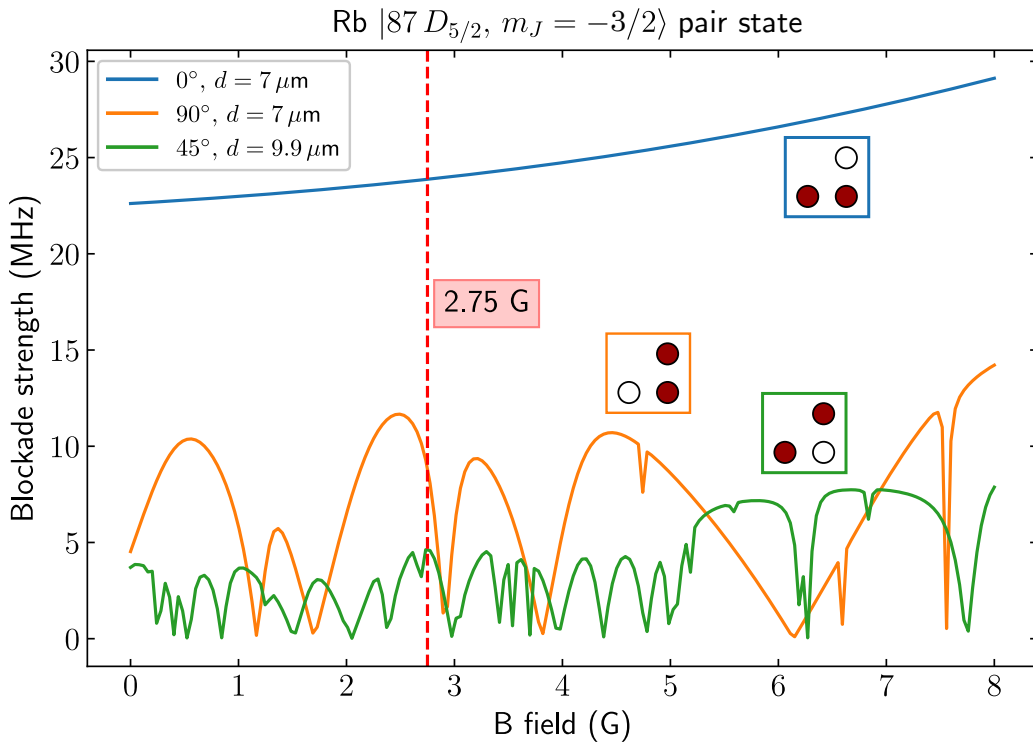


Figure 6.5.: Blockade strength in the presence of a magnetic field. If applied at an angle to the interatomic axis, the magnetic field lifts the degeneracy of the Zeeman levels, resulting in a rich level structure. Blockade strengths are calculated by diagonalizing the interaction Hamiltonian and weighting the resulting eigenstates by contribution of the initial pair state [179]. The three curves correspond to the distinct interatomic separations and angles in the array, as indicated by the inset. The red dashed line marks the magnetic field strength applied in the experiment.

levels, which generally weakens the interaction strength.

It should be noted here, that a calculation of the exact blockade interaction strength for the given system is far from trivial. The choice of $m_J = -3/2$ leads to the coupling with a multitude of $\Delta m_J = \pm 1$ states, initially separated by a few MHz, once the distance of the atoms gets small enough, which is the case even for distances far larger than $10 \mu\text{m}$, due to the high principal quantum number. The diagonalization of the interaction Hamiltonian thus only reaches convergence for a very large basis set, corresponding to long calculation times, and the value of the C_6 coefficient is difficult to determine as it typically relies on finding the state with the highest contribution of the unperturbed state and fitting its distance-dependent shift with a vdW-like function. If the original state is spread over too many eigenstates, this method is prone to errors. Depending on the state and interaction angle, one can expect a strong dependence of the blockade strength on external fields. This has been analyzed in [143, 159] for the $|62D_{3/2}, m_J = 3/2\rangle$ state, demonstrating that even the application of a small electric field of $E = 20 \text{ mV cm}^{-1}$ can lead to a breakdown of an otherwise strong blockade and illustrating the effect of the strength and sign of a magnetic field.

Performing similar calculations for the present experimental setup while varying the magnetic field (in the absence of an electric field), one obtains the graphs shown in Fig. 6.5, corresponding to the three distinct atomic distances and angles occurring in the measurement shown in

Fig. 6.3. Blockade strengths were calculated using the *Pair Interaction* library [179]⁵. Values range from 23 MHz for next neighbors along the quantization axis to 5 MHz for diagonal neighbors. The latter would still correspond to more than 10 times the Rabi frequency, even when considering the collective enhancement. However, the graph shows that a small change in magnetic field strength can lead to a situation where the shift can get down to 1 or 2 MHz, in which case the blockade condition would barely be satisfied. This could lead to a non-negligible double excitation probability, that can be estimated as $P_{2r} \simeq \Omega^2/(2B^2)$ [34], where B is the blockade strength. A similar effect was reported in [116], where the excitation probability of more than one atom was also higher than expected and ascribed to the geometry of the array.

A possible cause may lie in the interaction between all three atoms. In [180], it was shown how a third atom can break the Rydberg blockade in a triangular geometry with unequal interaction strengths, as is the case here, through the emergence of a three-atom dark state that does not experience an interaction shift. Similarly, the deformation of the blockade sphere in a system where the interatomic distance is on the order of the blockade radius, is analyzed in [181].

Discussion of amplitude damping

Comparing the signal shown in Fig. 6.3 (a) to single-atom Rydberg oscillations shown in Chapter 4 (see Fig. 4.9), one observes a significantly stronger damping of the amplitude in the interacting system when increasing the atom number. In an ideally blocked system, as discussed in Section 6.1, this increased damping can not be explained. Since a comprehensive simulation, as performed in [116, 174] would exceed the scope of this preliminary demonstration⁶, possible causes are only discussed qualitatively here. As mentioned previously, the individual Rabi frequencies with which the atoms are coupled to the Rydberg state vary because of the Gaussian profile of the Rydberg beams (see Section 4.3.3). The triangular structure for this measurement was chosen to minimize this inhomogeneity among the three atoms, but analyzing the excitation probability for every trap individually still yields a variation of $\pm 10\%$. This, given Eq. (6.4), does explain to some degree the slight discrepancy with regard to the \sqrt{N} scaling visible in Fig. 6.3 (b). The beating of multiple enhanced Rabi frequencies could also constitute a contribution to the damping in the two-atom case, where the signal was averaged over three different two-atom configurations. In the three-atom case, however, where the observed damping is strongest, it can not be explained that way, as the same enhanced Rabi frequency should have been present in every repetition. Comparing the experimental parameters with considerations made in [116], one can also rule out inhomogeneous detunings and atomic motion as a major cause of damping, which leaves imperfect blockade and thus fluctuating interaction strengths as the most probable cause, especially since the $nD_{5/2}$ states give rise to such a complex pair interaction potential landscape. Please note that the considerations of interatomic distance neglected variations of the axial position of the atoms in the traps, that is, in the direction perpendicular to the array plane. Given a Rayleigh range of $z_R = 8.3(12) \mu\text{m}$, however, one can expect the corresponding uncertainty in the axial position to "smear out" the blockade interaction strength between the atoms. Given the radial trap frequency ω_{\parallel} (Eq. (2.19)) for the lowered potential before switching off the trap, $U_0/k_B \approx 300 \mu\text{K}$, one obtains a standard deviation of the axial position of $\Delta x_{\parallel} = \sqrt{k_B T/m\omega_{\parallel}^2} \approx 2.4 \mu\text{m}$ [160]⁷. This can further weaken the interaction strength and is likely to contribute to the observed blockade leakage and damping of the amplitude.

⁵ <https://pairinteraction.github.io/pairinteraction/sphinx/html/index.html>

⁶ The comparison of a sophisticated model with the experiment requires more data.

⁷ The variation of the radial position is roughly a factor of 10 smaller and is thus neglected here.

An unexpectedly strong increase in damping has been observed in various experiments probing a fully blockaded ensemble [56, 116, 174, 182], and a quantitative explanation for this diminished coherence has yet to be found.

6.4 Conclusion

In this chapter, the first observation of Rydberg blockade in the present experiment was documented. This was done via the observation of a collective enhancement of the Rabi oscillation between the ground state and an entangled state with a single Rydberg excitation shared among two and three atoms, respectively. The observed scaling of the Rabi frequency with atom number is in good agreement with the expected \sqrt{N} law. Analysis of a residual double excitation probability reveals it to be higher than expected from calculated blockade strengths. This imperfect blockade, primarily occurring in the triangular geometry of three atoms for longer pulse durations, point to either an overestimation of the van der Waals strength or to the diminishment of the blockade through three-body interactions [180, 181]. The rich level structure of $nD_{5/2}$ states leads to a strong dependence of the blockade strength on external fields and interaction angle with respect to the quantization axis [173], even more so for three interacting atoms [177]. Similar effects may contribute to the unexpectedly strong damping of the oscillation amplitude, which was also observed in [56, 116]. These results underpin the notion that, in order to rely on a robust blockade mechanism in an array of Rydberg atoms, one has to carefully tune the experimental parameters when working with nD states. Alternatively, switching to nS states may be preferable, if the decrease in coupling strength can be compensated, as the blockade interaction for these states is far more robust and isotropic.



7 Discussion and Outlook

In the course of this thesis, the assembly of defect-free periodic clusters containing more than 100 neutral atoms could be demonstrated for the first time. This was accomplished by integrating a movable optical tweezer into the experiment and implementing a feedback control of the atomic occupation in the dipole trap array using a fast heuristic algorithm for the calculation of the atom rearrangement. Repeated cycles of assembly, in conjunction with a lifetime prolonging cooling effect caused by the associated imaging cycles, was shown to significantly increase the probability of defect-free filling in the presence of experimental imperfections such as transport losses. By the integration of a laser system for Rydberg excitation into the experimental setup, progress towards the implementation of a versatile quantum simulation architecture could be made, realizing coherent Rydberg excitation and controlled interactions in the assembled array. A detailed analysis of the limitations in the setup has been made in order to pinpoint sources of imperfections, which can be used as a reference for future improvements. At the time of writing this thesis, a new version of the experiment is being set up, with various improvements such as facilitated optical access, the possibility to include compensation plates for electric fields, and a larger, more stable magneto-optical trap.

In either of the two setups, the presented architecture lends itself to the investigation of countless physical problems spanning multiple areas of research in atomic physics and quantum optics [37, 96, 183]. These include quantum simulation and computation applications, examples being the implementation of topological quantum computing and quantum error correction [134, 135] based on Rydberg-mediated interactions [20, 30, 37] and the simulation of quantum physical systems [11, 13, 184]. Techniques developed here can be applied to the fields of quantum sensing and metrology, as having a large number of atoms in a periodic structure with tunable interactions holds potential for quantum-enhanced measurements and clock operation [185] using squeezed states and entanglement [186]. Scaling up the assembled atom array to more and more macroscopic sizes will provide abundant possibilities for the advancement of Rydberg-atom based sensors for electromagnetic fields [96, 167, 187]. Reduced trap separations pave the way to bottom-up engineering of quantum systems based on tunneling interactions [122, 188, 189]. While all results presented here are based on a quadratic grid, hexagonal MLAs are readily available and direct laser writing methods give access to user defined geometries [142, 190]. The trapping of atoms in the Talbot optical lattice introduced in Section 3.3.4 comes at no additional cost in terms of laser power and will allow for the expansion of the above-mentioned approaches into the third dimension.

Some of these applications require significant improvements and modifications of the presented setup and are thus more distant than others. In the following a brief outlook to two possible applications is given which can likely be implemented in the near future.

Parallelized two-qubit or multi-qubit gates

One of the logical next steps is to build on the above-mentioned advances to implement two-qubit gate operations between pairs of atoms. As has been shown in Chapter 6, an appropriate choice of Rydberg state leads to a strong nearest-neighbor blockade, which is a requirement for the implementation of the entangling operations that correspond to conditional logic gates on a quantum computer. One of the simplest forms of such an entangling operation is the conditional

phase gate C_Z . It corresponds to a sequence of three laser pulses on resonance between a qubit state $|1\rangle$ and a Rydberg state $|r\rangle$. The two atoms are referred to as *control atom* and *target atom*. The pulse sequence consists of a π pulse on the control atom, followed by a 2π pulse on the target atom, which is then followed by a second π pulse on the control atom. This sequence is illustrated in Fig. 7.1 for the target prepared in $|1\rangle$. If the control atom is initially in $|0\rangle$, it is not coupled to the Rydberg state and the target atom undergoes a 2π rotation, thereby acquiring a phase shift of π . If the control atom is in $|1\rangle$, the target is blockaded and its phase remains the same, but the control atom picks up a π phase shift. The only case where the two-atom state does not acquire a phase shift is if both atoms are initially in $|0\rangle$. In the two-atom basis $\{|00\rangle, |01\rangle, |10\rangle, |11\rangle\}$, this operation can be expressed as the matrix

$$C_Z = \begin{pmatrix} 1 & 0 & 0 & 0 \\ 0 & -1 & 0 & 0 \\ 0 & 0 & -1 & 0 \\ 0 & 0 & 0 & -1 \end{pmatrix}. \quad (7.1)$$

As the state of the target atom after the operation depends on the initial state of the control atom, this corresponds to the entanglement of the two atoms. Combining the C_Z gate with two $\pi/2$ rotations of the target atom before and after the interaction transforms the operation into a C_{NOT} gate [20, 34, 191].

There are different Zeeman sublevels that can be used as qubit states. The stretched states $|5S_{1/2}, F=2, m_F=-2\rangle =: |0\rangle$ and $|5S_{1/2}, F=3, m_F=-3\rangle =: |1\rangle$ are the most convenient choice in the current setup, as the transition $|1\rangle \leftrightarrow |r\rangle$ is already implemented. A second option would be the clock states with $m_F=0$ each, which have the advantage of increased qubit state coherence because of their reduced coupling to external magnetic fields and have been intensively used in earlier measurements [45, 47]. The site-selective excitation necessary for this operation can be accomplished by shifting one of the atoms out of resonance with the tweezer, as demonstrated in Chapter 4, or by site-selective illumination with the Rydberg lasers. The latter can be achieved by a two-dimensional AOD akin to the one used for the tweezer, which would have the added benefit of allowing for significantly higher Rabi frequencies and homogeneous coupling to all atoms within a large region. Rapid sequencing of pulses or multi-toning of the AODs would then allow for the parallelized application of entangling operations for multiple atom pairs in the array. Entanglement between more than two atoms, as shown in Chapter 6, also allows for the implementation of three-qubit gates, such as a C_{NOT} with multiple targets or a Toffoli gate [191]. While the fidelity of such gates can be expected to be limited by experimental imperfections [30], optimized pulse sequences using STIRAP [90, 151, 169] or optimal control [192] could lead to robust Rydberg gates [193], which presents in itself an interesting topic of research.

Synthesizing spin models

In addition to local entanglement operations, the periodic structure of the assembled atom array lends itself to the study of quantum magnetism, as the van der Waals interaction between Rydberg atoms can be mapped onto a system of interacting spins, where the two spin states are the ground state $|g\rangle = |\downarrow\rangle$ and the Rydberg state $|r\rangle = |\uparrow\rangle$. In the case of a strong laser drive Ω on the $|g\rangle \leftrightarrow |r\rangle$ transition, the resulting dynamics happen on a timescale much shorter than the thermal motion of the atoms, making this frozen Rydberg gas behave in an

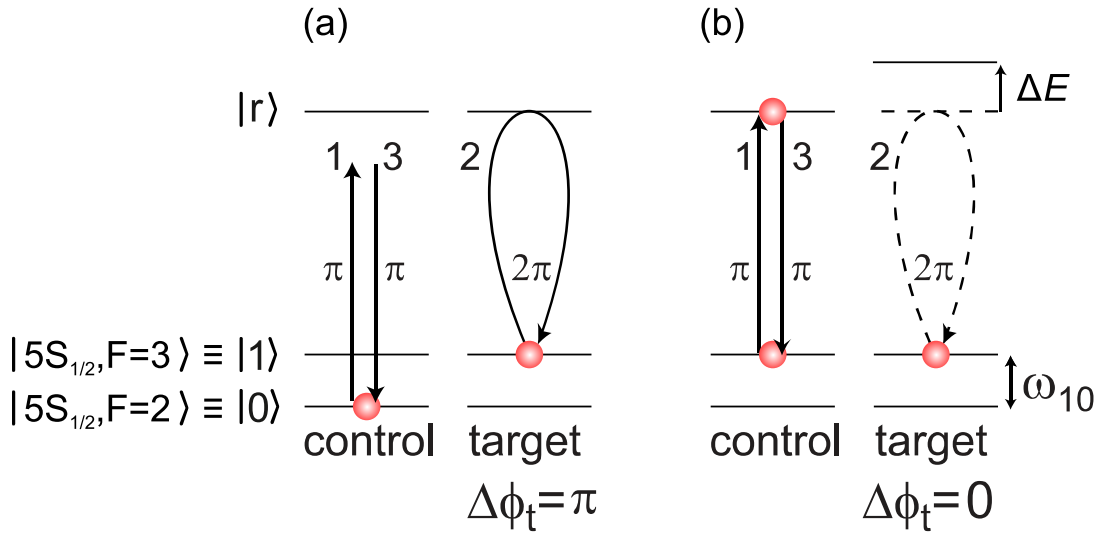


Figure 7.1.: Controlled phase (C_Z) gate. Depicted is the case where the target atom is initially in $|1\rangle$. (a) If the control atom is initially in $|0\rangle$, it is not coupled by the laser and the target undergoes a 2π rotation via the Rydberg state, acquiring a phase π . (b) In the case of the control being in the state $|1\rangle$, it is excited to the Rydberg state, shifting the two-atom Rydberg state by ΔE and thus blocking the excitation of the target atom, whose phase remains unchanged. Adapted from [20].

analogous way to a crystalline solid. The system can thus be described by the spin-1/2 Hamiltonian

$$H = \frac{\hbar\Omega}{2} \sum_i \sigma_i^x - \hbar\delta \sum_i n_i + \sum_{i \neq j} \frac{C_6}{R_{ij}^6} n_i n_j, \quad (7.2)$$

where $\sigma^x = |\uparrow\rangle\langle\downarrow| + |\downarrow\rangle\langle\uparrow|$ is the x Pauli matrix and $n_i = |\uparrow\rangle\langle\uparrow|_i$ is the projector on the Rydberg state for atom i . The first term in Eq. (7.2) therefore corresponds to the laser drive and the second to the detuning δ from the transition, as illustrated in Fig. 7.2 (a). The third term describes the van der Waals interaction V_{vdw} . Restricting interactions to approximately isotropic nearest-neighbor interactions¹ thus realizes an Ising-like model, where the first term takes the role of a transverse magnetic field $\propto \Omega$ and the second term that of a longitudinal field $\propto \delta$. For $C_{ij} > 0$ this gives rise to antiferromagnetic (AFM) order for certain values of (Ω, δ) . The corresponding phase diagram is shown in Fig. 7.2 (b), delineating the phase transition between the AFM and paramagnetic (PM) phase. The arising dynamics can be probed either by applying a sudden quench [41, 108, 143] or by adiabatically sweeping the system across a phase transition [40, 42] to study the slow buildup of correlations. The comprehensive control over the longitudinal and transverse fields, the interaction strength and, to a large extent, the topology of the system, will allow for the study of a plethora of rich physics in the presented setup. Implementing microwave transitions to a second Rydberg state would also give access to the implementation of XY-type Hamiltonians and the study of dipolar exchange interactions between the two Rydberg states, further expanding the range of explorable quantum phases [43]. The possibility for scaling this Rydberg simulator to hundreds or even thousands of atoms holds the potential for observing

¹ The requirement for isotropy suggests the use of a nS Rydberg state. Tuning the interatomic spacing in one dimension only, as has been done in [40] to accommodate the use of an anisotropic nD state, is not possible in the presented setup.

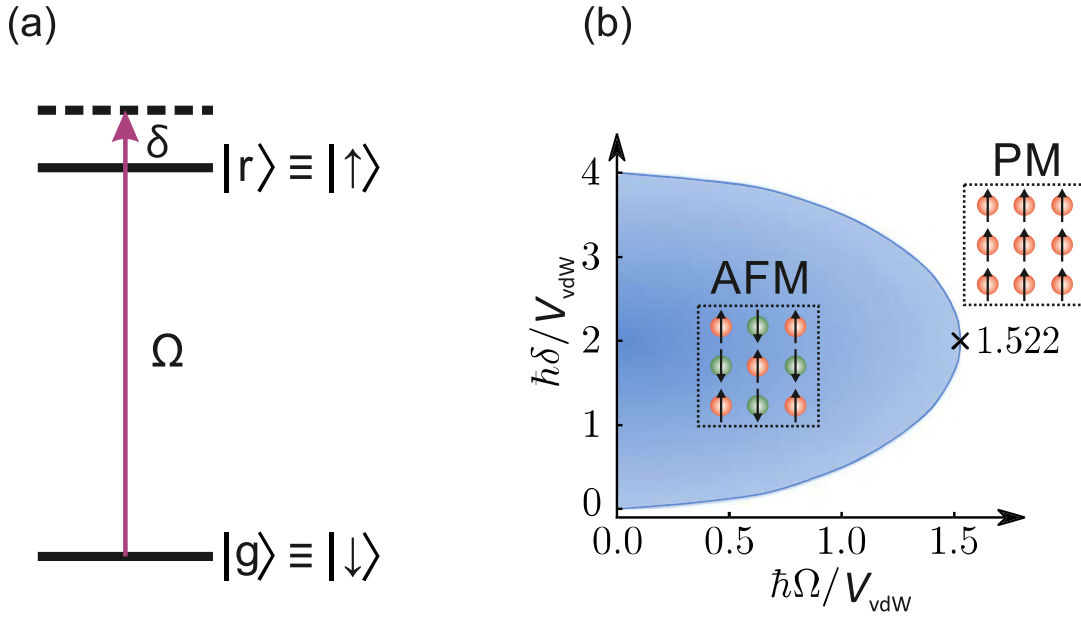


Figure 7.2.: Magnetic order arising in a frozen Rydberg gas. (a) The ground and Rydberg state of atoms trapped in a tweezer array can be mapped to spin states. The laser coupling Ω and detuning δ take the role of a transverse and longitudinal magnetic field in a quantum magnet, respectively. (b) Tuning the van der Waals interaction strength to only nearest-neighbor interactions realizes an effective Ising model, with antiferromagnetic (AFM) order manifesting within a critical region of the phase space spanned by Ω and δ , considered here in units of the interaction strength V_{vdW} . Outside of this region, the external drive dominates and the system behaves like a paramagnet (PM). Adapted from [40].

these correlations in ever larger systems, soon leaving the realm of classical tractability and entering the one of quantum supremacy [10, 11].

All of the above-mentioned applications will benefit from technical improvements of the setup. As is evident from the analysis performed in Chapter 5, higher Rabi frequencies will significantly increase the coherence of Rydberg dynamics, which would lead to both higher gate fidelities and more efficient state preparation. An upgrade of the blue laser system by installing a higher-power tapered amplifier (TA) would yield a power increase by an appreciable factor with commercially available TA chips. An alternative would be the implementation of a scheme utilizing the $6P_{3/2}$ state as intermediate state (see Fig. 2.9 (d)), in which the weakly coupled transition corresponds to an infrared wavelength, where much more powerful lasers are available. A potential switch to this scheme was already taken into account when coating the mirrors of the reference cavity. Another limitation of the coherence time of ground-Rydberg state dynamics is the thermal motion of the atoms, observable both as shot-to-shot dephasing and baseline loss when switching off the traps. Finite atom temperatures and mechanical forces caused by Rydberg interactions restrict the validity of the frozen Rydberg gas approximation, limiting quantum state fidelities and the available time for coherent Rydberg dynamics [59, 123]. This coherence time can be increased by cooling the atoms to the motional ground state of the dipole traps by Raman sideband cooling [194, 195] or by trapping the Rydberg atoms in a ponderomotive potential [196, 197], recently realized in a tweezer array experiment using a blue-detuned bottle-beam trap [198].

Potential measures to scale up the size of the assembled array have been analyzed in Chapter 3. Most of these are contingent on an increase in available dipole laser power. However, as the simulations show, an increase in initial loading rate would significantly benefit the assembly of larger arrays as well and might even become crucial at some point. Adopting a gray-molasses loading scheme as presented in [85] could thus be a key factor for scaling the system to thousands of atoms.

The experimental results presented in this thesis hint at the suitability of this setup for advancing quantum technologies as well as our knowledge about the rules that govern the behaviour of matter at the fundamental level.



A Properties of ^{85}Rb

A detailed compilation of the atomic properties of ^{85}Rb can be found in [101]. A selection of data relevant for the QUIPS experiment is shown in Table A.1.

Figure A.1 shows an extract from the energy level scheme of ^{85}Rb including the ground state $5^2S_{1/2}$ and the first two excited states $5^2P_{1/2}$ and $5^2P_{3/2}$. The right hand side depicts transitions driven by the lasers introduced in this thesis (excluding Raman and Rydberg lasers).

Atomic properties of ^{85}Rb		
Atomic number	Z	37
Total nucleons	$Z + N$	85
Atomic mass	m	$1.40999 \times 10^{-25} \text{ kg}$
Nuclear spin	I	$5/2$
Nucl. Landé factor	g_I	-2.936400×10^{-4}
Electr. Landé factor	g_J	$\simeq \frac{3}{2} + \frac{S(S+1) - L(L+1)}{2J(J+1)}$
Properties of the $5^2S_{1/2}$ ground state		
Electr. Landé factor	g_J	2.00233113(20)
HFS splitting	ω_{HFS}	$2\pi \cdot 3035.732439 \text{ MHz}$
Quadr. Zeeman effect	$\Delta\omega_{0 \rightarrow 0}$	$2\pi \cdot 1293.98 \text{ Hz G}^{-2} \cdot B^2$
Properties of the ^{85}Rb D1 line and the excited state $5^2P_{1/2}$		
Wavelength	λ	794.979014933 nm
Transition frequency	ω_0	$2\pi \cdot 377.107385690 \text{ THz}$
Natural linewidth	Γ	$2\pi \cdot 5.7500 \text{ MHz}$
Properties of the ^{85}Rb D2 line and the excited state $5^2P_{3/2}$		
Wavelength	λ	780.241368271 nm
Transition frequency	ω_0	$2\pi \cdot 384.230406373 \text{ THz}$
Natural linewidth	Γ	$2\pi \cdot 6.0666 \text{ MHz}$
Saturation intensity	I_0	1.66932 mW/cm^2
Doppler temperature	T_D	$145.57 \mu\text{K}$
Recoil temperature	T_R	370.47 nK

Table A.1.: Physical properties of ^{85}Rb . Data taken from [101].

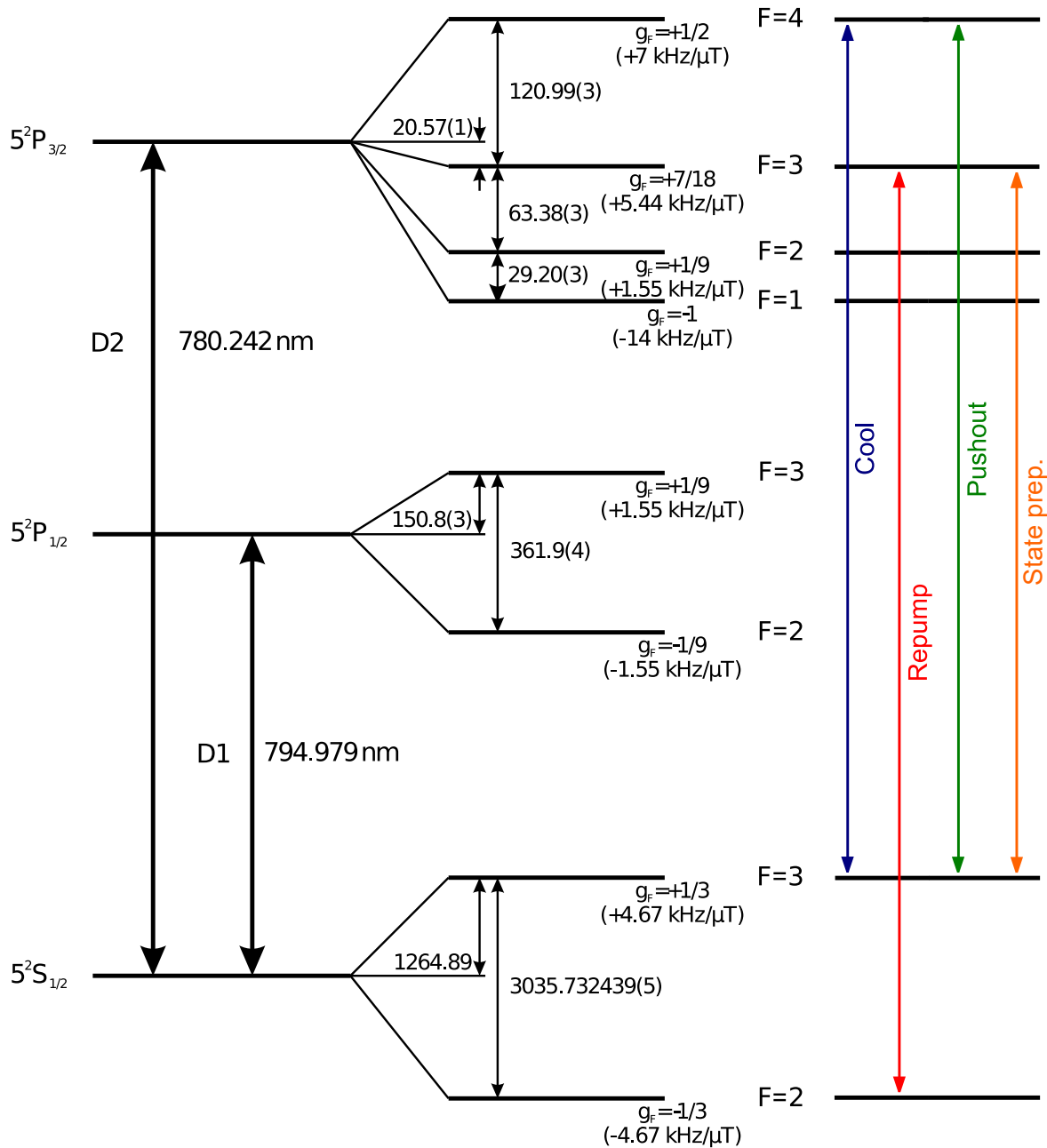


Figure A.1.: Energy level scheme of the ^{85}Rb D line states. The hyperfine splitting is given in MHz. Besides the g_F factor, the Zeeman splitting of the m_F states is indicated. On the right hand side the D2 line transitions driven by the lasers in the QUIPS experiment are drawn (excluding lasers driving the Raman and Rydberg transitions).

B Monte-Carlo simulation of atom-structure assembly

Figures 3.13 and 3.15 show the result of Monte-Carlo simulations of the atom assembly procedure, with a single array and interleaved arrays acting as a reservoir, respectively. The code uses the GridMover class written by J. Werkmann [86, 133] and is given in the following (The code for the functions `pad_rows_cols` and `grid_generators` was provided by J. Werkmann):

```
1 import numpy as np
2 from qutils.GridMover import GridMover
3 import matplotlib.pyplot as plt
4
5 def pad_rows_cols(arr, pad=(1, 1), offset=(0, 0)):
6     """
7     Generates an interleaved array from the given array, padded with zeros.
8
9     Parameters:
10    arr (np.array): Original array that is to be padded.
11    pad (tuple of int): Numbers of rows and columns that are to be padded between
12    each row and column of arr.
13    offset (tuple of int): Offset defining the position of the original array
14    inside the padded one.
15
16    Returns:
17    arr (np.array): Original array, padded with rows and columns of zeros.
18    """
19    shape = arr.shape
20
21    if pad[0] < offset[0] or pad[1] < offset[1]:
22        raise Exception('offset can not be larger than the padding')
23
24    rows = np.split(arr, shape[0], axis=0)
25    arr = np.zeros((shape[0] * (1 + pad[0]), shape[1]), dtype=np.int)
26    for i, row in enumerate(rows):
27        arr[i * (pad[0] + 1) + offset[0]] = row
28
29    cols = np.split(arr, shape[1], axis=1)
30    arr = np.zeros((shape[0] * (1 + pad[0]), shape[1] * (1 + pad[1])), dtype=np.int)
31    for i, col in enumerate(cols):
32        arr[:, i * (pad[1] + 1) + offset[1]] = col.flatten()
33
34    return arr
35
36 def grid_generators(width, width_res, n_grids=1, p=0.5):
37     """
38     Provides generators for a random initial (reservoir) array and a target (result)
39     array. Restricted to quadratic arrays.
40     Allows for interleaved arrays.
```

```

39 Parameters:
40 width (int): Width (and height) of the workspace grid.
41 width_res (int): Width (and height) of the target grid, centered in the
workspace.
42 n_grids (int): Number of interleaved reservoir grids (max. 4).
43 p (float or np.array): Loading rate, can be either global (float) or site-
specific (np.array).
44
45 Returns:
46 reservoir_grid_factory: Generator function that can be called to provide a
random reservoir array.
47 padded_res_grid_factory: Generator function that can be called to provide a
padded target array.
48 """
49 if n_grids < 0 or n_grids > 4:
50     raise Exception('Number of grids needs to be > 0 and < 5.')
51 if width_res > width:
52     raise Exception('The width of the result grid needs to be smaller than the
start grid.')
53
54 def reservoir_grid_factory():
55     if n_grids > 1:
56         reservoir = np.zeros((width * 2, width * 2))
57         for i in range(n_grids):
58             if np.isscalar(p):
59                 grid = np.random.choice([0, 1], size=(width, width),
60                                         p=[1 - p, p])
61             elif p.shape == (width, width):
62                 grid = (np.random.uniform(0, 1, size=(width, width)) < p)
63                     .astype(int)
64             else:
65                 raise Exception('Loading rate array does not have the right
size!')
66         reservoir += pad_rows_cols(grid, pad=(1, 1), offset=(i // 2, i % 2)
)
67     else:
68         if np.isscalar(p):
69             reservoir = np.random.choice([0, 1], size=(width, width),
70                                         p=[1 - p, p])
71         elif p.shape == (width, width):
72             reservoir = (np.random.uniform(0, 1, size=(width, width)) < p)
73                 .astype(int)
74         else:
75             raise Exception('Loading rate array does not have the right size!')
76
77     return reservoir
78
79 def padded_res_grid_factory():
80     diff = width - width_res
81     res_grid = np.ones((width_res, width_res), dtype=np.int)
82     res_grid = np.pad(res_grid, ((diff - diff // 2, diff // 2),
83                               (diff - diff // 2, diff // 2)), 'constant',
84                       constant_values=(0))
85
86     if n_grids > 1:
87         res_grid = pad_rows_cols(res_grid, pad=(1, 1), offset=(0, 0))
88     return res_grid
89

```



```

90     return reservoir_grid_factory, padded_res_grid_factory
91
92
93 def simulate_assembly(name, grid_factory, res_grid_factory, n_sim=1000,
94                       transport_eff=0.75, n_sorts=20, img_time=0.05,
95                       lifetime_arr=13, rise_time=300e-6, fall_time=300e-6,
96                       wait_time=200e-6, tweezers_ramp_speed=1200,
97                       wait_time_beginning=0.045):
98     """
99     Simulates the repeated assembly of a target structure. Averaging the results
100    over n_sim realizations yields a corresponding success probability.
101
102    Parameters:
103    name: Printed at the beginning, useful for keeping track of the current
104    simulation.
105    grid_factory, res_grid_factory: Functions to generate a random initial grid as
106    well as a target (result) grid. Provided by the function 'grid_generators'.
107    n_sim (int): Number of simulations, over which the results will then be
108    averaged. Corresponds to the number of experimental cycles.
109    transport_eff (float or iterable): Transport efficiency of the tweezers. If
110    passed as a tuple, the second index corresponds to the uncertainty.
111    n_sorts (int): Number of assembly cycles within a single experimental cycle.
112    img_time (float): Duration of the fluorescence imaging in seconds.
113    lifetime_arr (float or np.array): Atom lifetime in the array. Can be either
114    global (float) or site-specific (np.array).
115    rise_time, fall_time, wait_time (float): Intensity ramp durations for an
116    elementary atom move and wait time in between two moves in seconds.
117    tweezers_ramp_speed (float): Average speed of a transport ramp in nodes per
118    second.
119    wait_time_beginning (float): Wait time at the beginning of each assembly cycle,
120    given by the 'downtime' of the EMCCD.
121
122    Returns:
123    sort_num (list): List of indices corresponding to assembly repetitions.
124    ind_prob (list): List of individual success probabilities, with indices
125    corresponding to sort_num.
126    cum_prob (list): List of cumulative success probabilities, with indices
127    corresponding to sort_num.
128    fillfac (list): List of filling fractions, with indices corresponding to
129    sort_num.
130
131    """
132    print(name)
133    # Implement a randomly fluctuating transport efficiency by drawing from a
134    normal distribution:
135    if type(transport_eff) == tuple:
136        transport_eff = np.random.normal(transport_eff[0], transport_eff[1], n_sim)
137    # If no uncertainty is given, keep it static:
138    elif type(transport_eff) == float or type(transport_eff) == int:
139        transport_eff = [transport_eff for i in range(n_sim)]
140    else:
141        pass
142
143    success = {n:[] for n in range(0, n_sorts + 1)}
144    fill_factor = {n:[] for n in range(0, n_sorts + 1)}
145    cumulative_success = {n:[] for n in range(0, n_sorts+1)}
146    # Create an instance of the GridMover class:
147    mover = GridMover()

```

```

135 for j in range(n_sim):
136     # Build grid
137     done = False
138     tries = 0
139     while not done:
140         grid = grid_factory().astype(int)
141         res_grid = res_grid_factory().astype(int)
142         # Check if there are enough atoms in the reservoir to fill the target:
143         done = np.sum(res_grid) <= np.sum(grid)
144         tries += 1
145         if tries >0: # Set this greater than zero if some kind of initial
selection based on the number of loaded atoms shall be simulated
146             break
147         # The success marker is True once the structure is assembled
148         success_marker = ((res_grid & grid) == res_grid).all()
149         success[0].append(success_marker)
150         fill_factor[0].append(np.sum(res_grid & grid)/np.sum(res_grid))
151         cumulative_success[0].append(success_marker)
152
153         current_grid = grid
154         # Loop over assembly cycles:
155         for sort in range(1, n_sorts+1):
156             # Apply the sorting algorithm to calculate a series of reordering moves
, moving obstacles out of the way:
157             moves = mover.find_route(current_grid.copy(), res_grid,
158                                     trivial_movement=False, compress=False,
159                                     remove_mode='default')
160
161             # Ramp of the form 0bxyz
162             # x: is removal move
163             # y: falling ramp
164             # z: rising ramp
165             paths = []
166             # Split the moves onto individual paths
167             for i, (from_node, to_node, ramps) in enumerate(moves):
168                 if ramps == 0b011: # Rising and falling ramp.
169                     paths.append((from_node, to_node, ramps))
170                 elif ramps == 0b001: # Only rising ramp, in that case join with the
next elementary move. Corresponds to the path having a 90 degree turn.
171                     from_node2, to_node2, ramps2 = moves[i+1]
172                     paths.append((from_node, to_node2, 0b011))
173                 else:
174                     pass
175             # Keep track of time to implement time-dependent losses:
176             sort_time = wait_time_beginning + img_time
177             for (from_node, to_node, ramps) in paths:
178                 # Add the ramp and wait times:
179                 sort_time += rise_time + fall_time + wait_time
180                 # Add the time necessary for the current movement
181                 sort_time += (np.abs(to_node[0] - from_node[0])
182                             + np.abs(to_node[1] - from_node[1]))
183                             /tweezer_ramp_speed
184                 chance = np.random.uniform(0,1)
185                 # Implement random loss due to finite transport efficiency:
186                 if chance < transport_eff[j]:
187                     # Update grid if atom is not lost:
188                     _, current_grid = mover.perform_moves(from_node, [to_node],
189                                                         current_grid)
189                 else:

```

```

190         # Remove atom:
191         row_from, col_from = from_node
192         current_grid[row_from, col_from] = 0
193
194     # Implement random atom loss according to lifetime
195     survival_prob = np.exp(-(np.float64(sort_time))
196                             /np.float64(lifetime_arr))
197     temp_grid = np.random.uniform(0, 1, size=grid.shape)
198     loss_mask = temp_grid < survival_prob
199     current_grid = current_grid & loss_mask
200     # Store results:
201     success[sort].append(((res_grid & current_grid) == res_grid).all())
202     fill_factor[sort].append(np.sum(res_grid & current_grid)
203                             /np.sum(res_grid))
204     success_marker = success_marker or ((res_grid & current_grid)
205                                         == res_grid).all()
206     cumulative_success[sort].append(success_marker)
207
208 # Average over all simulations and return final results:
209 sort_num, ind_prob, cum_prob, fillfac = [],[],[],[]
210 for key, value in success.items():
211     sort_num.append(key)
212     ind_prob.append(np.mean(value))
213     cum_prob.append(np.mean(cumulative_success[key]))
214     fillfac.append(np.mean(fill_factor[key]))
215
216 return sort_num, ind_prob, cum_prob, fillfac

```



C Simulation of Rydberg dynamics

In the following, the code used for the Monte-Carlo simulations in Chapter 5 is given. It uses the Master equation solver provided by the *QuTiP* package [165], as well as the *ARC* library for atomic properties [103]. In the presence of only one decay channel, as is the default, the implemented Hamiltonian and Lindblad dissipator correspond to Eq. (5.7) and Eq. (5.8), respectively.

```
1 import numpy as np
2 import matplotlib.pyplot as plt
3 # Import the QuTiP package:
4 from qutip import*
5 # Import the ARC library for calculating Rabi frequencies:
6 from arc import*
7
8 # Basic definitions:
9 atom = Rubidium85()
10 # Decay rate of the intermediate state:
11 Gamma = 2 * np.pi * 6.0666e6
12
13 # n, L, J, mJ
14 rydberg_state = [57, 2, 2.5, -1.5]
15
16 # Experimental parameters:
17 waist_red = 550e-6
18 waist_blue = 19e-6
19 power_red = 500e-6
20 power_blue = 0.04
21
22 power_uncert_red = 0.02
23 power_uncert_blue = 0.05
24
25 Omega_B = atom.getRabiFrequency(5, 1, 1.5, -1.5, *rydberg_state[:3], 0,
26                                 power_blue, waist_blue)
27 Omega_R = atom.getRabiFrequency(5, 0, 0.5, -0.5, 5, 1, 1.5, -1,
28                                 power_red, waist_red)
29
30 Delta = 2 * np.pi * 417e6
31
32 # Measured static errors:
33 prep_eff = 0.96
34 baseline_loss = 0.05
35 det_err = 0.19
36
37 # Take the light shift into account for the effective detuning:
38 delta = - (Omega_R**2 - Omega_B**2) / (4 * Delta)
39
40 # Introduce Doppler Broadening of the resonance:
41 doppler = 2 * np.pi * 170e3
42
43
44
45
```

```

46 def get_rydberg_state_pop(Omega_R, Omega_B, Delta, delta, times, Gamma,
47                             doppler, prep_eff):
48
49     """
50     Uses the QuTiP Master equation solver to obtain the population in the Rydberg
51     state for a set of time steps given by 'times',
52     for a three level system with two possible decay channels.
53
54     Returns:
55     result.expect[0]: List of expectation values of a Rydberg state projection
56     measurement for all time steps in 'times'
57     """
58
59     # The state g' corresponds to a second decay channel from the intermediate state
60     # not coupled to the Rydberg state,
61     # leading to an asymmetric damping of the dynamics. However, in all experiments
62     # presented in this thesis,
63     # it was not present due to using the stretched intermediate state mF=-4
64     Gamma_g = Gamma
65     Gamma_gprime = 0
66
67     # Define the basis. For the sake of generality, the state g' is included in the
68     # basis:
69     ket_gprime = np.array([[1], [0], [0], [0]])
70     bra_gprime = np.array([[1, 0, 0, 0]])
71
72     ket_g = np.array([[0], [1], [0], [0]])
73     bra_g = np.array([[0, 1, 0, 0]])
74
75     ket_e = np.array([[0], [0], [1], [0]])
76     bra_e = np.array([[0, 0, 1, 0]])
77
78     ket_r = np.array([[0], [0], [0], [1]])
79     bra_r = np.array([[0, 0, 0, 1]])
80
81     # Define the collapse operators corresponding to dissipation via the intermediate
82     # state:
83     c_g = Qobj(np.sqrt(Gamma_g) * ket_g * bra_e)
84     c_gprime = Qobj(np.sqrt(Gamma_gprime) * ket_gprime * bra_e)
85
86     # Draw a random effective detuning from the Doppler broadened distribution:
87     delta_eff = delta + np.random.normal(0, doppler)
88
89     # Define the Hamiltonian and initial state:
90     H = Qobj([[0, 0, 0, 0], [0, 0, Omega_R / 2, 0],
91              [0, Omega_R / 2, -Delta, Omega_B / 2], [0, 0, Omega_B / 2, -delta_eff]])
92     psi0 = prep_eff * basis(4, 1) + (1 - prep_eff) * basis(4, 0)
93
94     # Use the QuTiP Master equation solver to evolve the system:
95     result = mesolve(H, psi0, times, c_ops=[c_g, c_gprime],
96                     e_ops=[Qobj(ket_r * bra_r)])
97
98     return result.expect[0]
99
100 def simulate_dynamics(times, Omega_R, Omega_B, delta, Delta=Delta, n_sim=100,
101                       baseline_loss=baseline_loss, prep_eff=prep_eff,
102                       det_err=det_err, include_scattering=True,

```

```

98         include_dephasing=True, doppler=doppler, Gamma=Gamma,
99         include_power_uncerts=True, power_uncert_red=power_uncert_red
100     ,
101         power_uncert_blue=power_uncert_blue):
102     """
103     Returns a list of Rydberg state evolutions, corresponding to multiple
104     experimental realizations.
105     This way, dephasing effects can be modelled, such as Doppler broadening and
106     fluctuating laser power.
107     """
108     r_pops = []
109     for i in range(n_sim):
110         doppler = doppler if include_dephasing else 0
111         Gamma = Gamma if include_scattering else 0
112
113         # Model a fluctuating laser power by drawing the Rabi frequencies from a
114         # normal distribution:
115         O_R = np.random.normal(Omega_R, power_uncert_red*Omega_R/2) if
116             include_power_uncerts else Omega_R
117         O_B = np.random.normal(Omega_B, power_uncert_blue*Omega_B/2) if
118             include_power_uncerts else Omega_B
119
120         # Obtain the Rydberg populations and introduce static errors to model
121         # experimental limitations:
122         r_state_pop = get_rydberg_state_pop(O_R, O_B, Delta, delta, times, Gamma,
123             doppler, prep_eff)
124         r_state_pop = r_state_pop * (1-baseline_loss) + baseline_loss
125         r_state_pop = r_state_pop * (1 - det_err)
126         r_pops.append(r_state_pop)
127
128     return r_pops

```




D List of publications

D. Ohl de Mello, D. Schäffner, J. Werkmann, T. Preuschoff, L. Kohfahl, M. Schlosser and G. Birkel
Defect-Free Assembly of 2D Clusters of More Than 100 Single-Atom Quantum Systems, Phys. Rev. Lett. **122**, 203601 (2019).

M. Schlosser, S. Tichelmann, D. Schäffner, D. Ohl de Mello, M. Hambach and G. Birkel
Large-scale multilayer architecture of single-atom arrays with individual addressability, submitted for publication, arXiv preprint (2019), arXiv:1902.05424.

M. Schlosser, D. Ohl de Mello, D. Schäffner, T. Preuschoff, L. Kohfahl and G. Birkel
Assembled arrays of Rydberg-interacting atoms, submitted for publication in J. Phys. B.



Bibliography

- [1] E. Schrödinger, *ARE THERE QUANTUM JUMPS? PART II*, The British Journal for the Philosophy of Science **III**, 233 (1952).
- [2] S. Chu, *Nobel Lecture: The manipulation of neutral particles*, Rev. Mod. Phys. **70**, 685 (1998).
- [3] C. N. Cohen-Tannoudji, *Nobel Lecture: Manipulating atoms with photons*, Rev. Mod. Phys. **70**, 707 (1998).
- [4] W. D. Phillips, *Nobel Lecture: Laser cooling and trapping of neutral atoms*, Rev. Mod. Phys. **70**, 721 (1998).
- [5] E. A. Cornell und C. E. Wieman, *Nobel Lecture: Bose-Einstein condensation in a dilute gas, the first 70 years and some recent experiments*, Rev. Mod. Phys. **74**, 875 (2002).
- [6] W. Ketterle, *Nobel lecture: When atoms behave as waves: Bose-Einstein condensation and the atom laser*, Rev. Mod. Phys. **74**, 1131 (2002).
- [7] S. Haroche, *Nobel Lecture: Controlling photons in a box and exploring the quantum to classical boundary*, Rev. Mod. Phys. **85**, 1083 (2013).
- [8] J. M. Raimond, M. Brune und S. Haroche, *Manipulating quantum entanglement with atoms and photons in a cavity*, Rev. Mod. Phys. **73**, 565 (2001).
- [9] D. J. Wineland, *Nobel Lecture: Superposition, entanglement, and raising Schrödinger's cat*, Rev. Mod. Phys. **85**, 1103 (2013).
- [10] R. Feynman, *Simulating physics with computers*, International Journal of Theoretical Physics **21**, 467 (1982).
- [11] I. M. Georgescu, S. Ashhab und F. Nori, *Quantum simulation*, Rev. Mod. Phys. **86**, 153 (2014).
- [12] S. Somaroo, C. H. Tseng, T. F. Havel, R. Laflamme und D. G. Cory, *Quantum Simulations on a Quantum Computer*, Phys. Rev. Lett. **82**, 5381 (1999).
- [13] C. Gross und I. Bloch, *Quantum simulations with ultracold atoms in optical lattices*, Science **357**, 995 (2017).
- [14] S. Lloyd, *Universal Quantum Simulators*, Science **273**, 1073 (1996).
- [15] D. Deutsch, *Quantum Theory, the Church-Turing Principle and the Universal Quantum Computer*, Proceedings of the Royal Society of London. A. Mathematical and Physical Sciences **400**, 97 (1985).
- [16] L. K. Grover, *Quantum Mechanics Helps in Searching for a Needle in a Haystack*, Phys. Rev. Lett. **79**, 325 (1997).
- [17] P. Shor, *Polynomial-Time Algorithms for Prime Factorization and Discrete Logarithms on a Quantum Computer*, SIAM Journal on Computing **26**, 1484 (1997).

-
- [18] S. Boixo, S. V. Isakov, V. N. Smelyanskiy, R. Babbush, N. Ding, Z. Jiang, M. J. Bremner, J. M. Martinis und H. Neven, *Characterizing quantum supremacy in near-term devices*, Nat. Phys. **14**, 595 (2018).
- [19] T. D. Ladd, F. Jelezko, R. Laflamme, Y. Nakamura, C. Monroe und J. L. O'Brien, *Quantum computers*, Nature **464**, 45 (2010).
- [20] M. Saffman, T. G. Walker und K. Mølmer, *Quantum information with Rydberg atoms*, Rev. Mod. Phys. **82**, 2313 (2010).
- [21] C. Monroe und J. Kim, *Scaling the Ion Trap Quantum Processor*, Science **339**, 1164 (2013).
- [22] M. H. Devoret und R. J. Schoelkopf, *Superconducting Circuits for Quantum Information: An Outlook*, Science **339**, 1169 (2013).
- [23] F. Arute *et al.*, *Quantum supremacy using a programmable superconducting processor*, Nature **574**, 505 (2019).
- [24] C. H. Bennett, D. P. DiVincenzo, J. A. Smolin und W. K. Wootters, *Mixed-state entanglement and quantum error correction*, Phys. Rev. A **54**, 3824 (1996).
- [25] D. Gottesman, *An Introduction to Quantum Error Correction and Fault-Tolerant Quantum Computation*, arXiv:0904.2557 (2009).
- [26] R. Laflamme, C. Miquel, J. P. Paz und W. H. Zurek, *Perfect Quantum Error Correcting Code*, Phys. Rev. Lett. **77**, 198 (1996).
- [27] T. Kleinjung *et al.*, *Factorization of a 768-bit RSA modulus*, Cryptology ePrint Archive, Report 2010/006 (2010).
- [28] J. A. Smolin, G. Smith und A. Vargo, *Oversimplifying quantum factoring*, Nature **499**, 163 (2013).
- [29] D. P. DiVincenzo, *The Physical Implementation of Quantum Computation*, Fortschritte der Physik **48**, 771 (2000).
- [30] M. Saffman, *Quantum computing with atomic qubits and Rydberg interactions: progress and challenges*, Journal of Physics B: Atomic, Molecular and Optical Physics **49**, 202001 (2016).
- [31] M. Schlosser, S. Tichelmann, J. Kruse und G. Birkel, *Scalable architecture for quantum information processing with atoms in optical micro-structures*, Quantum Information Processing **10**, 907 (2011).
- [32] D. Jaksch, J. I. Cirac, P. Zoller, S. L. Rolston, R. Côté und M. D. Lukin, *Fast Quantum Gates for Neutral Atoms*, Phys. Rev. Lett. **85**, 2208 (2000).
- [33] M. D. Lukin, M. Fleischhauer, R. Cote, L. M. Duan, D. Jaksch, J. I. Cirac und P. Zoller, *Dipole Blockade and Quantum Information Processing in Mesoscopic Atomic Ensembles*, Phys. Rev. Lett. **87**, 037901 (2001).
- [34] L. Isenhower, E. Urban, X. L. Zhang, A. T. Gill, T. Henage, T. A. Johnson, T. G. Walker und M. Saffman, *Demonstration of a Neutral Atom Controlled-NOT Quantum Gate*, Phys. Rev. Lett. **104**, 010503 (2010).

-
- [35] T. Wilk, A. Gaëtan, C. Evellin, J. Wolters, Y. Miroshnychenko, P. Grangier und A. Browaeys, *Entanglement of Two Individual Neutral Atoms Using Rydberg Blockade*, Phys. Rev. Lett. **104**, 010502 (2010).
- [36] H. Weimer, M. Müller, I. Lesanovsky, P. Zoller und H. P. Büchler, *A Rydberg quantum simulator*, Nat Phys **6**, 382 (2010).
- [37] A. Browaeys, D. Barredo und T. Lahaye, *Experimental investigations of dipole-dipole interactions between a few Rydberg atoms*, Journal of Physics B: Atomic, Molecular and Optical Physics **49**, 152001 (2016).
- [38] H. Levine, A. Keesling, A. Omran, H. Bernien, S. Schwartz, A. S. Zibrov, M. Endres, M. Greiner, V. Vuletić und M. D. Lukin, *High-Fidelity Control and Entanglement of Rydberg-Atom Qubits*, Phys. Rev. Lett. **121**, 123603 (2018).
- [39] A. Omran *et al.*, *Generation and manipulation of Schrödinger cat states in Rydberg atom arrays*, Science **365**, 570 (2019).
- [40] V. Lienhard, S. de Léséleuc, D. Barredo, T. Lahaye, A. Browaeys, M. Schuler, L.-P. Henry und A. M. Läuchli, *Observing the Space- and Time-Dependent Growth of Correlations in Dynamically Tuned Synthetic Ising Models with Antiferromagnetic Interactions*, Phys. Rev. X **8**, 021070 (2018).
- [41] E. Guardado-Sanchez, P. T. Brown, D. Mitra, T. Devakul, D. A. Huse, P. Schauß und W. S. Bakr, *Probing the Quench Dynamics of Antiferromagnetic Correlations in a 2D Quantum Ising Spin System*, Phys. Rev. X **8**, 021069 (2018).
- [42] A. Keesling *et al.*, *Quantum Kibble–Zurek mechanism and critical dynamics on a programmable Rydberg simulator*, Nature **568**, 207 (2019).
- [43] S. de Léséleuc, V. Lienhard, P. Scholl, D. Barredo, S. Weber, N. Lang, H. P. Büchler, T. Lahaye und A. Browaeys, *Observation of a symmetry-protected topological phase of interacting bosons with Rydberg atoms*, Science **365**, 775 (2019).
- [44] A. Lengwenus, J. Kruse, M. Schlosser, S. Tichelmann und G. Birkl, *Coherent Transport of Atomic Quantum States in a Scalable Shift Register*, Phys. Rev. Lett. **105**, 170502 (2010).
- [45] M. Schlosser, *Preparation and coherent control of single-atom quantum systems in two-dimensional quantum processing architectures*, Ph.d. thesis, Technische Universität Darmstadt, (2013).
- [46] D. Ohl de Mello, *Experimental demonstration of 100+ qubit registers and fast atom transport*, Master thesis, TU Darmstadt, (2014).
- [47] J. Kruse, *Neutral atoms in a dipole trap array for quantum information processing*, Ph.d. thesis, Technische Universität Darmstadt, (2010).
- [48] M. Greiner, O. Mandel, T. Esslinger, T. W. Hansch und I. Bloch, *Quantum phase transition from a superfluid to a Mott insulator in a gas of ultracold atoms*, Nature **415**, 39 (2002).
- [49] J. F. Sherson, C. Weitenberg, M. Endres, M. Cheneau, I. Bloch und S. Kuhr, *Single-atom-resolved fluorescence imaging of an atomic Mott insulator*, Nature **467**, 68 (2010).
- [50] W. S. Bakr, A. Peng, M. E. Tai, R. Ma, J. Simon, J. I. Gillen, S. Fölling, L. Pollet und M. Greiner, *Probing the Superfluid-to-Mott Insulator Transition at the Single-Atom Level*, Science **329**, 547 (2010).

-
- [51] P. T. Brown, D. Mitra, E. Guardado-Sanchez, P. Schauß, S. S. Kondov, E. Khatami, T. Paiva, N. Trivedi, D. A. Huse und W. S. Bakr, *Spin-imbalance in a 2D Fermi-Hubbard system*, Science **357**, 1385 (2017).
- [52] D. Barredo, S. de Léséleuc, V. Lienhard, T. Lahaye und A. Browaeys, *An atom-by-atom assembler of defect-free arbitrary two-dimensional atomic arrays*, Science **354**, 1021 (2016).
- [53] M. Endres, H. Bernien, A. Keesling, H. Levine, E. R. Anschuetz, A. Krajenbrink, C. Senko, V. Vuletic, M. Greiner und M. D. Lukin, *Atom-by-atom assembly of defect-free one-dimensional cold atom arrays*, Science **354**, 1024 (2016).
- [54] H. Kim, W. Lee, H.-g. Lee, H. Jo, Y. Song und J. Ahn, *In situ single-atom array synthesis using dynamic holographic optical tweezers*, Nature Communications **7**, 13317 EP (2016), article.
- [55] A. Kumar, T.-Y. Wu, F. Giraldo und D. S. Weiss, *Sorting ultracold atoms in a three-dimensional optical lattice in a realization of Maxwell's demon*, Nature **561**, 83 (2018).
- [56] J. Zeiher, P. Schauß, S. Hild, T. Macrì, I. Bloch und C. Gross, *Microscopic Characterization of Scalable Coherent Rydberg Superatoms*, Phys. Rev. X **5**, 031015 (2015).
- [57] J. Zeiher, R. van Bijnen, P. Schauß, S. Hild, J. yoon Choi, T. Pohl, I. Bloch und C. Gross, *Many-body interferometry of a Rydberg-dressed spin lattice*, Nat. Phys. **12**, 1095 (2016).
- [58] E. A. Goldschmidt, T. Boulier, R. C. Brown, S. B. Koller, J. T. Young, A. V. Gorshkov, S. L. Rolston und J. V. Porto, *Anomalous Broadening in Driven Dissipative Rydberg Systems*, Phys. Rev. Lett. **116**, 113001 (2016).
- [59] S. de Léséleuc, D. Barredo, V. Lienhard, A. Browaeys und T. Lahaye, *Analysis of imperfections in the coherent optical excitation of single atoms to Rydberg states*, Phys. Rev. A **97**, 053803 (2018).
- [60] T. M. Graham, M. Kwon, B. Grinkemeyer, Z. Marra, X. Jiang, M. T. Lichtman, Y. Sun, M. Ebert und M. Saffman, *Rydberg-Mediated Entanglement in a Two-Dimensional Neutral Atom Qubit Array*, Phys. Rev. Lett. **123**, 230501 (2019).
- [61] F. Nogrette, H. Labuhn, S. Ravets, D. Barredo, L. Béguin, A. Vernier, T. Lahaye und A. Browaeys, *Single-Atom Trapping in Holographic 2D Arrays of Microtraps with Arbitrary Geometries*, Phys. Rev. X **4**, 021034 (2014).
- [62] H. J. Metcalf und P. van der Straten, *Laser Cooling and Trapping* (Springer, New York, 1999).
- [63] R. Grimm, M. Weidemüller und Y. B. Ovchinnikov, *Optical dipole traps for neutral atoms*, Molecular and Optical Physics **42**, 95 (2000).
- [64] D. A. Steck, *Quantum and Atom Optics*, published online, <http://steck.us/teaching>, 2012.
- [65] G. Grynberg, A. Apect und C. Fabre, *Introduction to Quantum Optics: From the Semi-classical Approach to Quantized Light* (Cambridge University Press, Cambridge, UK, 2010).
- [66] A. Lengwenus, *Manipulation der internen und externen Freiheitsgrade neutraler Atome in optischen Mikropotentialen*, Ph.d. thesis, TU Darmstadt, (2008).
- [67] B. Besold und N. Lindlein, *Fractional Talbot effect for periodic microlens arrays*, Optical Engineering **36**, 1099 (1997).

-
- [68] J. Wen, Y. Zhang und M. Xiao, *The Talbot effect: recent advances in classical optics, nonlinear optics, and quantum optics*, Adv. Opt. Photon. **5**, 83 (2013).
- [69] M. Schlosser, S. Tichelmann, D. Schöffner, D. O. de Mello, M. Hambach und G. Birkl, *Large-scale multilayer architecture of single-atom arrays with individual addressability*, arXiv:1902.05424 (2019).
- [70] J. Sattler, *Planung und Aufbau eines Experiments zur Manipulation einzelner neutraler Atome*, Master thesis, TU Darmstadt, (2008).
- [71] S. Chu, L. Hollberg, J. E. Bjorkholm, A. Cable und A. Ashkin, *Three-dimensional viscous confinement and cooling of atoms by resonance radiation pressure*, Phys. Rev. Lett. **55**, 48 (1985).
- [72] E. L. Raab, M. Prentiss, A. Cable, S. Chu und D. E. Pritchard, *Trapping of Neutral Sodium Atoms with Radiation Pressure*, Phys. Rev. Lett. **59**, 2631 (1987).
- [73] J. Dalibard und C. Cohen-Tannoudji, *Laser cooling below the Doppler limit by polarization gradients: simple theoretical models*, J. Opt. Soc. Am. B **6**, 2023 (1989).
- [74] X. Baillard, A. Gauguet, S. Bize, P. Lemonde, P. Laurent, A. Clairon und P. Rosenbusch, *Interference-filter-stabilized external-cavity diode lasers*, Optics Communications **266**, 609 (2006).
- [75] T. Preuschoff, M. Schlosser und G. Birkl, *Optimization strategies for modulation transfer spectroscopy applied to laser stabilization*, Optics Express **26**, 24010 (2018).
- [76] S. J. M. Kuppens, K. L. Corwin, K. W. Miller, T. E. Chupp und C. E. Wieman, *Loading an optical dipole trap*, Phys. Rev. A **62**, 013406 (2000).
- [77] N. Schlosser, G. Reymond, I. Protsenko und P. Grangier, *Sub-poissonian loading of single atoms in a microscopic dipole trap*, Nature **411**, 1024 (2001).
- [78] N. Schlosser, G. Reymond und P. Grangier, *Collisional Blockade in Microscopic Optical Dipole Traps*, Phys. Rev. Lett. **89**, 023005 (2002).
- [79] B. Ueberholz, S. Kuhr, D. Frese, D. Meschede und V. Gomer, *Counting cold collisions*, Journal of Physics B: Atomic, Molecular and Optical Physics **33**, L135 (2000).
- [80] Y. R. P. Sortais, A. Fuhrmanek, R. Bourgain und A. Browaeys, *Sub-Poissonian atom-number fluctuations using light-assisted collisions*, Phys. Rev. A **85**, 035403 (2012).
- [81] A. V. Carpentier, Y. H. Fung, P. Sompet, A. J. Hilliard, T. G. Walker und M. F. Andersen, *Preparation of a single atom in an optical microtrap*, Laser Physics Letters **10**, 125501 (2013).
- [82] P. Schauß, *Characterization of dipole trap arrays for quantum information processing with neutral atoms*, Master thesis, TU Darmstadt, (2009).
- [83] J.-N. Schmidt, *Two-photon Rydberg excitation and analysis of an atom-loss detection scheme for atoms in dipole-trap arrays*, Master thesis, TU Darmstadt, (2017).
- [84] Y. H. Fung und M. F. Andersen, *Efficient collisional blockade loading of a single atom into a tight microtrap*, New Journal of Physics **17**, 073011 (2015).

-
- [85] M. O. Brown, T. Thiele, C. Kiehl, T.-W. Hsu und C. A. Regal, *Gray-Molasses Optical-Tweezer Loading: Controlling Collisions for Scaling Atom-Array Assembly*, Phys. Rev. X **9**, 011057 (2019).
- [86] J. Werkmann, *Control Systems and Optical Tweezers for Quantum Information Processing*, Master thesis, TU Darmstadt, (2018).
- [87] T. F. Gallagher, *Rydberg Atoms* (Cambridge University Press, New York, NY, USA, 2005).
- [88] R. Heidemann, U. Raitzsch, V. Bendkowsky, B. Butscher, R. Löw und T. Pfau, *Rydberg Excitation of Bose-Einstein Condensates*, Phys. Rev. Lett. **100**, 033601 (2008).
- [89] P. Schauß, M. Cheneau, M. Endres, T. Fukuhara, S. Hild, A. Omran, T. Pohl, C. Gross, S. Kuhr und I. Bloch, *Observation of spatially ordered structures in a two-dimensional Rydberg gas*, Nature **491**, 87 (2012).
- [90] G. Higgins, F. Pokorny, C. Zhang, Q. Bodart und M. Hennrich, *Coherent Control of a Single Trapped Rydberg Ion*, Phys. Rev. Lett. **119**, 220501 (2017).
- [91] J. Vogel, W. Li, A. Mokhberi, I. Lesanovsky und F. Schmidt-Kaler, *Shuttling of Rydberg Ions for Fast Entangling Operations*, Phys. Rev. Lett. **123**, 153603 (2019).
- [92] T. Kazimierczuk, D. Fröhlich, S. Scheel, H. Stolz und M. Bayer, *Giant Rydberg excitons in the copper oxide Cu₂O*, Nature **514**, 343 (2014).
- [93] A. Paris-Mandoki, C. Braun, J. Kumlin, C. Tresp, I. Mirgorodskiy, F. Christaller, H. P. Büchler und S. Hofferberth, *Free-Space Quantum Electrodynamics with a Single Rydberg Superatom*, Phys. Rev. X **7**, 041010 (2017).
- [94] A. V. Gorshkov, J. Otterbach, M. Fleischhauer, T. Pohl und M. D. Lukin, *Photon-Photon Interactions via Rydberg Blockade*, Phys. Rev. Lett. **107**, 133602 (2011).
- [95] Q.-Y. Liang, A. V. Venkatramani, S. H. Cantu, T. L. Nicholson, M. J. Gullans, A. V. Gorshkov, J. D. Thompson, C. Chin, M. D. Lukin und V. Vuletić, *Observation of three-photon bound states in a quantum nonlinear medium*, Science **359**, 783 (2018).
- [96] C. S. Adams, J. D. Pritchard und J. P. Shaffer, *Rydberg atom quantum technologies*, Journal of Physics B: Atomic, Molecular and Optical Physics **53**, 012002 (2019).
- [97] J. R. Rydberg, *XXXIV. On the structure of the line-spectra of the chemical elements*, The London, Edinburgh, and Dublin Philosophical Magazine and Journal of Science **29**, 331 (1890).
- [98] C.-J. Lorenzen und K. Niemax, *Quantum Defects of the $n^2P_{1/2,3/2}$ Levels in $^{39}\text{K I}$ and $^{85}\text{Rb I}$* , Physica Scripta **27**, 300 (1983).
- [99] W. Li, I. Mourachko, M. W. Noel und T. F. Gallagher, *Millimeter-wave spectroscopy of cold Rb Rydberg atoms in a magneto-optical trap: Quantum defects of the ns, np, and nd series*, Phys. Rev. A **67**, 052502 (2003).
- [100] J. Han, Y. Jamil, D. V. L. Norum, P. J. Tanner und T. F. Gallagher, *Rb nf quantum defects from millimeter-wave spectroscopy of cold ^{85}Rb Rydberg atoms*, Phys. Rev. A **74**, 054502 (2006).
- [101] D. A. Steck, *Rubidium 85 D line data*, <http://steck.us/alkalidata>, 2012.

-
- [102] I. I. Beterov, I. I. Ryabtsev, D. B. Tretyakov und V. M. Entin, *Quasiclassical calculations of blackbody-radiation-induced depopulation rates and effective lifetimes of Rydberg nS , nP , and nD alkali-metal atoms with $n \leq 80$* , Phys. Rev. A **79**, 052504 (2009).
- [103] N. Šibalić, J. Pritchard, C. Adams und K. Weatherill, *ARC: An open-source library for calculating properties of alkali Rydberg atoms*, Computer Physics Communications **220**, 319 (2017).
- [104] D. A. Anderson, A. Schwarzkopf, R. E. Sapiro und G. Raithel, *Production and trapping of cold circular Rydberg atoms*, Phys. Rev. A **88**, 031401 (2013).
- [105] A. M. Hankin, Y.-Y. Jau, L. P. Parazzoli, C. W. Chou, D. J. Armstrong, A. J. Landahl und G. W. Biedermann, *Two-atom Rydberg blockade using direct $6S$ to nP excitation*, Phys. Rev. A **89**, 033416 (2014).
- [106] M. Saffman, X. L. Zhang, A. T. Gill, L. Isenhower und T. G. Walker, *Rydberg state mediated quantum gates and entanglement of pairs of neutral atoms*, Journal of Physics: Conference Series **264**, 012023 (2011).
- [107] L. S. Theis, F. Motzoi, F. K. Wilhelm und M. Saffman, *High-fidelity Rydberg-blockade entangling gate using shaped, analytic pulses*, Phys. Rev. A **94**, 032306 (2016).
- [108] H. Labuhn, D. Barredo, S. Ravets, S. de Léséleuc, T. Macrì, T. Lahaye und A. Browaeys, *Tunable two-dimensional arrays of single Rydberg atoms for realizing quantum Ising models*, Nature **534**, 667 EP (2016).
- [109] D. Barredo, H. Labuhn, S. Ravets, T. Lahaye, A. Browaeys und C. S. Adams, *Coherent Excitation Transfer in a Spin Chain of Three Rydberg Atoms*, Phys. Rev. Lett. **114**, 113002 (2015).
- [110] S. de Léséleuc, D. Barredo, V. Lienhard, A. Browaeys und T. Lahaye, *Optical Control of the Resonant Dipole-Dipole Interaction between Rydberg Atoms*, Phys. Rev. Lett. **119**, 053202 (2017).
- [111] E. Urban, T. A. Johnson, T. Henage, L. Isenhower, D. D. Yavuz, T. G. Walker und M. Saffman, *Observation of Rydberg blockade between two atoms*, Nat. Phys. **5**, 110 (2009).
- [112] W. R. Anderson, J. R. Veale und T. F. Gallagher, *Resonant Dipole-Dipole Energy Transfer in a Nearly Frozen Rydberg Gas*, Phys. Rev. Lett. **80**, 249 (1998).
- [113] T. G. Walker und M. Saffman, *Zeros of Rydberg–Rydberg Förster interactions*, Journal of Physics B: Atomic, Molecular and Optical Physics **38**, S309 (2005).
- [114] S. Ravets, H. Labuhn, D. Barredo, L. Béguin, T. Lahaye und A. Browaeys, *Coherent dipole–dipole coupling between two single Rydberg atoms at an electrically-tuned Förster resonance*, Nat. Phys. **10**, 914 (2014).
- [115] S. Ravets, H. Labuhn, D. Barredo, T. Lahaye und A. Browaeys, *Measurement of the angular dependence of the dipole-dipole interaction between two individual Rydberg atoms at a Förster resonance*, Phys. Rev. A **92**, 020701 (2015).
- [116] H. Labuhn, *Rydberg excitation dynamics and correlations in arbitrary 2D arrays of single atoms*, Ph.d. thesis, Université Paris-Saclay, (2016).
- [117] N. R. Cooper, J. Dalibard und I. B. Spielman, *Topological bands for ultracold atoms*, Rev. Mod. Phys. **91**, 015005 (2019).

-
- [118] G. K. Brennen, C. M. Caves, P. S. Jessen und I. H. Deutsch, *Quantum Logic Gates in Optical Lattices*, Phys. Rev. Lett. **82**, 1060 (1999).
- [119] A. Mazurenko, C. S. Chiu, G. Ji, M. F. Parsons, M. Kanász-Nagy, R. Schmidt, F. Grusdt, E. Demler, D. Greif und M. Greiner, *A cold-atom Fermi–Hubbard antiferromagnet*, Nature **545**, 462 (2017).
- [120] C. S. Chiu, G. Ji, A. Mazurenko, D. Greif und M. Greiner, *Quantum State Engineering of a Hubbard System with Ultracold Fermions*, Phys. Rev. Lett. **120**, 243201 (2018).
- [121] C. Robens, J. Zopes, W. Alt, S. Brakhane, D. Meschede und A. Alberti, *Low-Entropy States of Neutral Atoms in Polarization-Synthesized Optical Lattices*, Phys. Rev. Lett. **118**, 065302 (2017).
- [122] B. J. Lester, N. Luick, A. M. Kaufman, C. M. Reynolds und C. A. Regal, *Rapid Production of Uniformly Filled Arrays of Neutral Atoms*, Phys. Rev. Lett. **115**, 073003 (2015).
- [123] H. Bernien *et al.*, *Probing many-body dynamics on a 51-atom quantum simulator*, Nature **551**, 579 (2017).
- [124] D. Barredo, V. Lienhard, S. De Léséleuc, T. Lahaye und A. Browaeys, *Synthetic three-dimensional atomic structures assembled atom by atom*, Nature **561**, 79 (2018).
- [125] D. Ohl de Mello, D. Schöffner, J. Werkmann, T. Preuschoff, L. Kohfahl, M. Schlosser und G. Birkl, *Defect-Free Assembly of 2D Clusters of More Than 100 Single-Atom Quantum Systems*, Phys. Rev. Lett. **122**, 203601 (2019).
- [126] F. Mayer, *Design of Algorithms for Efficient Relocation of Atoms in a Quantum Register*, mathesis, TU Darmstadt, (2015).
- [127] Y. Ambach, *System for the two-dimensional transport of neutral Atoms in dipole traps*, mathesis, TU Darmstadt, (2015).
- [128] S. Tichelmann, *Coherent transport of atomic quantum states in a shift register of dipole traps*, Master thesis, TU Darmstadt, (2010).
- [129] F. Schmaltz, *Charakterisierung von Transportverfahren für Dipolfallenregister*, Bachelor thesis, TU Darmstadt, (2011).
- [130] M. Schlosser, J. Kruse, C. Gierl, S. Teichmann, S. Tichelmann und G. Birkl, *Fast transport, atom sample splitting and single-atom qubit supply in two-dimensional arrays of optical microtraps*, New Journal of Physics **14**, 123034 (2012).
- [131] D. Hucul, M. Yeo, S. Olmschenk, C. Monroe, W. K. Hensinger und J. Rabchuk, *On the Transport of Atomic Ions in Linear and Multidimensional Ion Trap Arrays*, Quantum Info. Comput. **8**, 501 (2008).
- [132] B. Bohmeier, *Control of a digital synthesizer with a FPGA*, Bachelor thesis, TU Darmstadt, (2014).
- [133] J. Werkmann, *Grid Routing Github Repository*, <https://github.com/PhyNerd/GridRouting>, 2019.
- [134] A. G. Fowler, M. Mariantoni, J. M. Martinis und A. N. Cleland, *Surface codes: Towards practical large-scale quantum computation*, Phys. Rev. A **86**, 032324 (2012).

-
- [135] H. Bombin und M. A. Martin-Delgado, *Statistical mechanical models and topological color codes*, Phys. Rev. A **77**, 042322 (2008).
- [136] S. Weber, S. de Léséleuc, V. Lienhard, D. Barredo, T. Lahaye, A. Browaeys und H. P. Büchler, *Topologically protected edge states in small Rydberg systems*, Quantum Sci. Technol. **3**, 044001 (2018).
- [137] A. M. Kaufman, B. J. Lester, M. Foss-Feig, M. L. Wall, A. M. Rey und C. A. Regal, *Entangling two transportable neutral atoms via local spin exchange*, Nature **527**, 208 EP (2015).
- [138] M. Hambach, *Towards the implementation of quantum gates in optical dipole trap arrays*, Master thesis, TU Darmstadt, (2012).
- [139] D. Frese, B. Ueberholz, S. Kuhr, W. Alt, D. Schrader, V. Gomer und D. Meschede, *Single Atoms in an Optical Dipole Trap: Towards a Deterministic Source of Cold Atoms*, Phys. Rev. Lett. **85**, 3777 (2000).
- [140] A. Cooper, J. P. Covey, I. S. Madjarov, S. G. Porsev, M. S. Safronova und M. Endres, *Alkaline-Earth Atoms in Optical Tweezers*, Phys. Rev. X **8**, 041055 (2018).
- [141] J. P. Covey, I. S. Madjarov, A. Cooper und M. Endres, *2000-Times Repeated Imaging of Strontium Atoms in Clock-Magic Tweezer Arrays*, Phys. Rev. Lett. **122**, 173201 (2019).
- [142] D. Schäffner, T. Preuschoff, S. Ristok, L. Brozio, M. Schlosser, H. Giessen und G. Birkl, *Arrays of optical tweezers based on 3D-printed microlens arrays*, arXiv:1905.06929 (2019).
- [143] S. de Léséleuc, S. Weber, V. Lienhard, D. Barredo, H. P. Büchler, T. Lahaye und A. Browaeys, *Accurate Mapping of Multilevel Rydberg Atoms on Interacting Spin-1/2 Particles for the Quantum Simulation of Ising Models*, Phys. Rev. Lett. **120**, 113602 (2018).
- [144] L. Kohfahl, *Two-Photon Rydberg Excitation of Neutral Atoms in Optical Dipole-Trap Arrays*, Master thesis, TU Darmstadt, (2017).
- [145] M. Fleischhauer, A. Imamoglu und J. P. Marangos, *Electromagnetically induced transparency: Optics in coherent media*, Rev. Mod. Phys. **77**, 633 (2005).
- [146] J. D. Pritchard, *Cooperative Optical Non-linearity in a blockaded Rydberg Ensemble*, Ph.d. thesis, Durham University, (2011).
- [147] S. Albrecht, *A laser system for the spectroscopy on highly charged ions, tellurium molecules, and Rydberg states of rubidium atoms*, Ph.d. thesis, TU Darmstadt, (2014).
- [148] B. E. King, *Angular Momentum Coupling and Rabi Frequencies for Simple Atomic Transitions*, arXiv:0804.4528 (2008).
- [149] R. W. P. Drever, J. L. Hall, F. V. Kowalski, J. Hough, G. M. Ford, A. J. Munley und H. Ward, *Laser phase and frequency stabilization using an optical resonator*, Applied Physics B **31**, 97 (1983).
- [150] E. D. Black, *An introduction to Pound–Drever–Hall laser frequency stabilization*, American Journal of Physics **69**, 79 (2001).
- [151] N. V. Vitanov, A. A. Rangelov, B. W. Shore und K. Bergmann, *Stimulated Raman adiabatic passage in physics, chemistry, and beyond*, Rev. Mod. Phys. **89**, 015006 (2017).
- [152] K. C. Younge, B. Knuffman, S. E. Anderson und G. Raithel, *State-Dependent Energy Shifts of Rydberg Atoms in a Ponderomotive Optical Lattice*, Phys. Rev. Lett. **104**, 173001 (2010).

-
- [153] R. Löw, H. Weimer, J. Nipper, J. B. Balewski, B. Butscher, H. P. Büchler und T. Pfau, *An experimental and theoretical guide to strongly interacting Rydberg gases*, Journal of Physics B: Atomic, Molecular and Optical Physics **45**, 113001 (2012).
- [154] R. Loudon, *The quantum theory of light*, Oxford science publications, 3rd ed. (Oxford University Press, Oxford, NY, USA, 2000).
- [155] J. Kruse, C. Gierl, M. Schlosser und G. Birkl, *Reconfigurable site-selective manipulation of atomic quantum systems in two-dimensional arrays of dipole traps*, Phys. Rev. A **81**, 060308 (2010).
- [156] C. Weitenberg, M. Endres, J. F. Sherson, M. Cheneau, P. Schauß, T. Fukuhara, I. Bloch und S. Kuhr, *Single-spin addressing in an atomic Mott insulator*, Nature **471**, 319 EP (2011), article.
- [157] J. H. Lee, E. Montano, I. H. Deutsch und P. S. Jessen, *Robust site-resolvable quantum gates in an optical lattice via inhomogeneous control*, Nature Communications **4**, 2027 (2013).
- [158] H. Labuhn, S. Ravets, D. Barredo, L. Béguin, F. Nogrette, T. Lahaye und A. Browaeys, *Single-atom addressing in microtraps for quantum-state engineering using Rydberg atoms*, Phys. Rev. A **90**, 023415 (2014).
- [159] S. de Léséleuc, *Quantum simulation of spin models with assembled arrays of Rydberg atoms*, Ph.d. thesis, Université Paris-Saclay, (2018).
- [160] C. Tuchendler, A. M. Lance, A. Browaeys, Y. R. P. Sortais und P. Grangier, *Energy distribution and cooling of a single atom in an optical tweezer*, Phys. Rev. A **78**, 033425 (2008).
- [161] F. Stopp, *Setup and characterization of a phase-stabilized laser system for coherent manipulation of cold rubidium atoms*, Master thesis, TU Darmstadt, (2014).
- [162] M. Werner, *Kohärente Manipulation von kalten Atomen mit phasenstabilisierten Lasersystemen*, Master thesis, TU Darmstadt, (2017).
- [163] M. Saffman und T. G. Walker, *Analysis of a quantum logic device based on dipole-dipole interactions of optically trapped Rydberg atoms*, Phys. Rev. A **72**, 022347 (2005).
- [164] Y. Miroshnychenko, A. Gaëtan, C. Evellin, P. Grangier, D. Comparat, P. Pillet, T. Wilk und A. Browaeys, *Coherent excitation of a single atom to a Rydberg state*, Phys. Rev. A **82**, 013405 (2010).
- [165] J. Johansson, P. Nation und F. Nori, *QuTiP: An open-source Python framework for the dynamics of open quantum systems*, Computer Physics Communications **183**, 1760 (2012).
- [166] A. Osterwalder und F. Merkt, *Using High Rydberg States as Electric Field Sensors*, Phys. Rev. Lett. **82**, 1831 (1999).
- [167] H. Fan, S. Kumar, J. Sedlacek, H. Kübler, S. Karimkashi und J. P. Shaffer, *Atom based RF electric field sensing*, Journal of Physics B: Atomic, Molecular and Optical Physics **48**, 202001 (2015).
- [168] L. Béguin, *Measurement of the van der Waals interaction between two Rydberg atoms*, Ph.d. thesis, Université Paris-Saclay, (2013).

-
- [169] T. Cubel, B. K. Teo, V. S. Malinovsky, J. R. Guest, A. Reinhard, B. Knuffman, P. R. Berman und G. Raithel, *Coherent population transfer of ground-state atoms into Rydberg states*, Phys. Rev. A **72**, 023405 (2005).
- [170] H. Kim, Y. Park, K. Kim, H.-S. Sim und J. Ahn, *Detailed Balance of Thermalization Dynamics in Rydberg-Atom Quantum Simulators*, Phys. Rev. Lett. **120**, 180502 (2018).
- [171] A. Reinhard, T. C. Liebisch, B. Knuffman und G. Raithel, *Level shifts of rubidium Rydberg states due to binary interactions*, Phys. Rev. A **75**, 032712 (2007).
- [172] T. J. Carroll, K. Claringbould, A. Goodsell, M. J. Lim und M. W. Noel, *Angular Dependence of the Dipole-Dipole Interaction in a Nearly One-Dimensional Sample of Rydberg Atoms*, Phys. Rev. Lett. **93**, 153001 (2004).
- [173] B. Vermersch, A. W. Glaetzle und P. Zoller, *Magic distances in the blockade mechanism of Rydberg p and d states*, Phys. Rev. A **91**, 023411 (2015).
- [174] D. Barredo, S. Ravets, H. Labuhn, L. Béguin, A. Vernier, F. Nogrette, T. Lahaye und A. Browaeys, *Demonstration of a Strong Rydberg Blockade in Three-Atom Systems with Anisotropic Interactions*, Phys. Rev. Lett. **112**, 183002 (2014).
- [175] A. Gaëtan, Y. Miroshnychenko, T. Wilk, A. Chotia, M. Viteau, D. Comparat, P. Pillet, A. Browaeys und P. Grangier, *Observation of collective excitation of two individual atoms in the Rydberg blockade regime*, Nat. Phys. **5**, 115 (2009).
- [176] R. McConnell, H. Zhang, J. Hu, S. Ćuk und V. Vuletić, *Entanglement with negative Wigner function of almost 3,000 atoms heralded by one photon*, Nature **519**, 439 (2015).
- [177] D. Cano und J. Fortágh, *Nonadditive potentials between three Rydberg atoms*, Phys. Rev. A **86**, 043422 (2012).
- [178] M. Ebert, A. Gill, M. Gibbons, X. Zhang, M. Saffman und T. G. Walker, *Atomic Fock State Preparation Using Rydberg Blockade*, Phys. Rev. Lett. **112**, 043602 (2014).
- [179] S. Weber, C. Tresp, H. Menke, A. Urvoy, O. Firstenberg, H. P. Büchler und S. Hofferberth, *Tutorial: Calculation of Rydberg interaction potentials*, J. Phys. B: At. Mol. Opt. Phys. **50**, 133001 (2017).
- [180] T. Pohl und P. R. Berman, *Breaking the Dipole Blockade: Nearly Resonant Dipole Interactions in Few-Atom Systems*, Phys. Rev. Lett. **102**, 013004 (2009).
- [181] J. Qian, X.-D. Zhao, L. Zhou und W. Zhang, *Anisotropic deformation of the Rydberg-blockade sphere in few-atom systems*, Phys. Rev. A **88**, 033422 (2013).
- [182] M. Ebert, M. Kwon, T. G. Walker und M. Saffman, *Coherence and Rydberg Blockade of Atomic Ensemble Qubits*, Phys. Rev. Lett. **115**, 093601 (2015).
- [183] A. Acín *et al.*, *The quantum technologies roadmap: a European community view*, New Journal of Physics **20**, 080201 (2018).
- [184] E. Altman *et al.*, *Quantum Simulators: Architectures and Opportunities*, arXiv:1912.06938 (2019).
- [185] A. D. Ludlow, M. M. Boyd, J. Ye, E. Peik und P. O. Schmidt, *Optical atomic clocks*, Rev. Mod. Phys. **87**, 637 (2015).

-
- [186] V. Giovannetti, S. Lloyd und L. Maccone, *Quantum-Enhanced Measurements: Beating the Standard Quantum Limit*, Science **306**, 1330 (2004).
- [187] A. Tauschinsky, R. M. T. Thijssen, S. Whitlock, H. B. van Linden van den Heuvell und R. J. C. Spreeuw, *Spatially resolved excitation of Rydberg atoms and surface effects on an atom chip*, Phys. Rev. A **81**, 063411 (2010).
- [188] S. Murmann, A. Bergschneider, V. M. Klinkhamer, G. Zürn, T. Lompe und S. Jochim, *Two Fermions in a Double Well: Exploring a Fundamental Building Block of the Hubbard Model*, Phys. Rev. Lett. **114**, 080402 (2015).
- [189] M. R. Sturm, M. Schlosser, R. Walser und G. Birkl, *Quantum simulators by design: Many-body physics in reconfigurable arrays of tunnel-coupled traps*, Phys. Rev. A **95**, 063625 (2017).
- [190] T. Gissibl, S. Thiele, A. Herkommer und H. Giessen, *Sub-micrometre accurate free-form optics by three-dimensional printing on single-mode fibres*, Nature Communications **7**, 11763 EP (2016).
- [191] M. A. Nielsen und I. L. Chuang, *Quantum computation and quantum information* (Cambridge University Press, New York, NY, USA, 2000).
- [192] M. M. Müller, M. Murphy, S. Montangero, T. Calarco, P. Grangier und A. Browaeys, *Implementation of an experimentally feasible controlled-phase gate on two blockaded Rydberg atoms*, Phys. Rev. A **89**, 032334 (2014).
- [193] M. H. Goerz, E. J. Halperin, J. M. Aytac, C. P. Koch und K. B. Whaley, *Robustness of high-fidelity Rydberg gates with single-site addressability*, Phys. Rev. A **90**, 032329 (2014).
- [194] A. M. Kaufman, B. J. Lester und C. A. Regal, *Cooling a Single Atom in an Optical Tweezer to Its Quantum Ground State*, Phys. Rev. X **2**, 041014 (2012).
- [195] J. D. Thompson, T. G. Tiecke, A. S. Zibrov, V. Vuletić und M. D. Lukin, *Coherence and Raman Sideband Cooling of a Single Atom in an Optical Tweezer*, Phys. Rev. Lett. **110**, 133001 (2013).
- [196] S. E. Anderson, K. C. Younge und G. Raithel, *Trapping Rydberg Atoms in an Optical Lattice*, Phys. Rev. Lett. **107**, 263001 (2011).
- [197] L. Li, Y. O. Dudin und A. Kuzmich, *Entanglement between light and an optical atomic excitation*, Nature **498**, 466 (2013).
- [198] D. Barredo, V. Lienhard, P. Scholl, S. de Léséleuc, T. Boulier, A. Browaeys und T. Lahaye, *Three-dimensional trapping of individual Rydberg atoms in ponderomotive bottle beam traps*, arXiv:1908.00853 (2019).

Acknowledgments

Last but not least I would like to thank all the people who have contributed to the success of this work, supported me during the last ten years and with whom I share many precious memories of that time.

An erster Stelle danke ich meinem Doktorvater Herrn Prof. Dr. Gerhard Birkl für die Möglichkeit, acht Jahre lang in diesem spannenden Feld forschen zu können. Von Bachelorarbeit bis Promotion konnte ich immer eine exzellente Betreuung und ein motivierendes Arbeitsklima genießen inklusive unzähliger hilfreicher Diskussionen und Ratschläge.

Gleichermaßen geht mein Dank an alle Mitglieder der Arbeitsgruppe Atome-Photonen-Quanten, die das Institut für mich in all dieser Zeit wie zu einem zweiten Zuhause gemacht haben. Ein solch produktives Arbeitsumfeld, in dem man sich stets gegenseitig unterstützt und alle an einem Strang ziehen, ist keine Selbstverständlichkeit. Es waren aber auch gerade die nicht-physikalischen Aktivitäten, die mich meine Zeit hier sehr haben genießen lassen.

Im Besonderen bedanke ich mich bei meinen (aktuellen und ehemaligen) Kollegen und Betreuern im QUIPS-Team: Malte und Sascha, Ihr habt mich als Bachelorstudent aufgenommen und in mir die Faszination für dieses aufregende Experiment geweckt. Malte, Du hast mich seit meinem ersten Tag hier bis zum Ende meiner Promotion mit Rat und Tat unterstützt, auf Dich war immer Verlass.

Mein spezieller Dank geht an Dominik, meinem langjährigen Doktoranden-Kollegen am Experiment, ohne Dich wäre diese Arbeit nicht möglich gewesen. Zusammen haben wir alle guten und schwierigen Phasen im Labor durchlebt, uns unzählige Nächte im Labor um die Ohren geschlagen und auch neben der Arbeit einiges erlebt. Du bist jetzt der Nächste; ich wünsche Dir viel Erfolg!

Lars und Tilman, auf Eure Unterstützung konnte ich immer zählen. Insbesondere Eure Arbeit am Rydberg-Lasersystem war eine riesige Hilfe. Viel Erfolg mit der neuen Generation des Experiments!

Danke an alle Bachelor- und Masterstudenten, mit denen ich über die Jahre zusammenarbeiten durfte: Jan, Deine Programmier-Expertise hat uns enorm weitergebracht. Jan-Niklas und Max, danke für die Unterstützung am Experiment. Danke auch an René Kolb, Friedel Spindler, Patrick Reh, Lukas Brozio, Felix Stopp, Kathrin Luksch und Tobias Schreiber. Tobi, bei Dir wird das Experiment auch in Zukunft in guten Händen sein.

Auch experimentübergreifend möchte ich mich noch bei meinen Doktorandenkollegen Felix und Patrick für die ständige Unterstützung bedanken, sowohl bei Problemen im Labor als auch beim Bier nach Feierabend.

Ebenso geht mein Dank an Gabi und Nathalie für den steten Rückhalt und die aufmunternden Worte und Gesten in stressigen Zeiten.

Des Weiteren möchte ich mich bei den Teams der Elektronik- und Feinmechanik-Werkstätten für die angenehme und produktive Zusammenarbeit bedanken.

Mein herzlicher Dank geht auch an Herrn Prof. Dr. Thomas Walther für die unkomplizierte Übernahme des Zweitgutachtens sowie an Herrn Prof. Dr. Gernot Alber und Herrn Prof. Dr. Markus Roth für die Teilnahme an meiner Disputation.

I would also like to thank Dr. Trey Porto for letting me spend six highly instructive and enjoyable months in his group at the Joint Quantum Institute in Maryland, as well as all the people at JQI who made my time there unforgettable. Special thanks go to the lunch club crew. You made me feel right at home and I will always remember the amazing trips and good times we had!

Ein ganz besonderer Dank geht an meine Darmstädter Freunde Christoph, Bernhard, Felix, Kristian, Lena, Lydia, Marc, Marian, Max, Tim und Tobi. Mit den meisten von Euch habe ich seit dem ersten Semester alle schwierigen Phasen des Studiums durchlitten und vor allem außerhalb der Vorlesungen Unzähliges erlebt. Sei es bei den Skatrunden in der Uni und den Abenden in der Kneipe, oder bei Fahrradtouren und kleinen bis großen Ausflügen und Reisen, Ihr alle habt die Zeit hier unvergesslich werden lassen und habt mich in jeder Situation unterstützt.

Regina, Dir danke ich für Deine Geduld, Dein Vertrauen und die Unterstützung in den letzten Jahren, vor allem in der stressigen Endphase. Ich freue mich auf alles, was jetzt kommt!

Und zu guter Letzt geht mein tiefster Dank an meine Eltern und Großeltern für die Liebe, die Unterstützung und den unerschütterlichen Rückhalt in all den Jahren. Ohne Euch wäre ich niemals so weit gekommen. Vielen Dank.

Curriculum Vitae

Personal data *Not included in the online version for reasons of data protection*

Graduation

05/2015–02/2020 Graduation in the group of Prof. Dr. Gerhard Birkl, Institut für Angewandte Physik, Technische Universität Darmstadt
Thesis title: *Rydberg interactions in a defect-free array of single-atom quantum systems*

University education

10/2009–11/2014 Studies of physics, Technische Universität Darmstadt

11/2014 Master of Science, Technische Universität Darmstadt

10/2013–11/2014 Master thesis in the group of Prof. Dr. Gerhard Birkl, Institut für Angewandte Physik, Technische Universität Darmstadt
Thesis title: *Experimental demonstration of 100+ qubit registers and fast atom transport*
Awarded with the Harald Rose prize

10/2012 Bachelor of Science, Technische Universität Darmstadt

06/2012–09/2012 Bachelor thesis in the group of Prof. Dr. Gerhard Birkl, Institut für Angewandte Physik, Technische Universität Darmstadt
Thesis title: *Dynamical positioning of arrays of optical microtraps*

Research stay

05/2016–10/2016 Visiting researcher at the Joint Quantum Institute (JQI), College Park, MD (USA), group of Prof. Dr. Trey Porto,
Project: *Cold Atoms in Optical Lattices*

School education

08/2000–06/2009 Abitur at the Albert-Einstein-Gymnasium, Maintal, Germany



Erklärung zur Dissertation

Hiermit versichere ich, die vorliegende Dissertation ohne Hilfe Dritter nur mit den angegebenen Quellen und Hilfsmitteln angefertigt zu haben. Alle Stellen, die aus Quellen entnommen wurden, sind als solche kenntlich gemacht. Diese Arbeit hat in gleicher oder ähnlicher Form noch keiner Prüfungsbehörde vorgelegen.

Darmstadt, den 28.01.2020

(Daniel Ohl de Mello)